Numerical assessment of aerodynamic and aeroelastic effects of pressure gain combustion in axial compressors

vorgelegt von
Eng. Mecânico (Universidade Federal de Juiz de Fora)
Victor Bicalho Civinelli de Almeida

an der Fakultät V - Verkehrs- und Maschinensysteme
der Technischen Universität Berlin
zur Erlangung des akademischen Grades

Doktor der Ingenieurwissenschaften
- Dr.-Ing. -

genehmigte Dissertation

Promotionsausschuss:

Vorsitzender: Prof. Dr.-Ing. Flávio José Silvestre
Gutachter: Prof. Dr.-Ing. Dieter Peitsch
Gutachter: Prof. Tekn. Dr. Damian Vogt
Tag der wissenschaftlichen Aussprache: 26. Juli 2022

Berlin 2022

Acknowledgments

Concluding this work was only possible with the help of several people. First of all, I express my deepest gratitude to Professor Peitsch, who since the beginning of my time at the Chair for Aero Engines provided all necessary resources, along with valuable technical advice.

I am also grateful to Professor Vogt, who kindly accepted to be a reviewer, as well as Professor Silvestre, chair of the examination committee.

Many others at the Chair for Aero Engines played a decisive role in my path. Nothing would have been possible without the initial encouragement of Yury, Alex and Christine. The invaluable scientific insight provided by the aeroelastic team, namely Leonie, Patrick and Valentina, coupled with laid-back coconut tasting cannot be underestimated. I am also grateful to all exchanges with Nico, Dominik, Jan, Mario and other colleagues, be they in the form of constructive suggestions or amusing stories with a sip of coffee in the C-Lab. I also appreciate the assistance and endless patience of Christian and Astrid, who never let me down.

I would like to additionally acknowledge the financial support from the Berlin International Graduate School in Model and Simulation based Research and the Prof. Dr. Manfred Fricke Stiftung.

The emotional support from my family (despite the distance) and friends was fundamental to the completion of my PhD, including all the prior steps leading me here. Finally, thank you Irina, for unconditionally being there whenever needed.

Abstract

Reducing fuel consumption of aero engines and stationary gas turbines currently requires breakthrough technologies able to offer radical improvements in efficiency. One such approach involves the substitution of conventional constant-pressure combustion with processes delivering an increase in pressure. The so-called pressure gain combustion (PGC) provides higher thermal efficiency, however at the cost of unsteady fuel burning. This modification challenges the adjacent turbomachinery components, introducing additional unsteadiness into the turbine and compressor.

This thesis contributes to better understanding the effects of PGC upstream of the combustor, namely in the compressor system. More specifically, unsteady aerodynamics and aeroelasticity numerical investigations were employed to assess the fluid dynamics and solid mechanics responses of two high pressure compressors subjected to PGC disturbances. An analytical formulation was proposed to model the change in amplitude of the disturbance waves propagating through the engine. When applied to the case studies, this metric, termed here "unsteady damping", identified an amplification of the PGC for low disturbance frequencies. The depreciation in performance was assessed for multirow setups, as a function of the form, frequency and amplitude of PGC disturbances. Data-driven methods, including proper orthogonal and dynamic mode decompositions, revealed a spread of energy and coherence into high-order modes, as well as the subsuming of baseline flow features in the PGC-disturbed scenario. These methods also helped expound which flow phenomena could be directly linked to the observed increase in stage losses. The forced response investigations indicated a substantial increase in vibration and stress levels on rotor blades when subjected to PGC disturbances. The augmented structural loading was also examined considering the interaction of unsteady forcing, data-driven decompositions and modal analyses.

Keywords:
Unsteady aerodynamics, aeroelasticity, high pressure compressor, data-driven decomposition, pressure gain combustion

Kurzfassung

Um den Treibstoffverbrauch von Luftfahrtantrieben und stationären Gasturbinen weiter zu reduzieren, sind neuartige Technologien erforderlich, die eine erhebliche Wirkungsgradsteigerung ermöglichen. Einer dieser Ansätze besteht darin, die herkömmliche Gleichdruckverbrennung durch eine Verbrennung mit Drucksteigerung (engl. pressure gain combustion, PGC) zu ersetzen. Die sogenannte druckerhöhende Verbrennung erzielt einen höheren thermischen Wirkungsgrad, allerdings mit dem Nachteil eines höchst instationären Verbrennungsprozesses. Dieses Verfahren stellt eine Herausforderung für die angrenzenden Turbomaschinenkomponenten dar, da dabei zusätzliche Druck- und Geschwindigkeitsschwankungen in Verdichter und Turbine induziert werden.

Die vorliegende Arbeit leistet einen Beitrag zum besseren Verständnis über die Auswirkungen der PGC auf den stomaufliegenden Verdichter. Zu diesem Zweck wurden numerische Untersuchungen zur instationären Aerodynamik und Aeroelastik durchgeführt, um die strömungs- und strukturmechanischen Reaktionen von zwei Hochdruckverdichtern zu bewerten, die den Störungen der PGC ausgesetzt sind. Es wurde eine analytische Formulierung entwickelt, um die Änderung der Amplitude der sich durch das Triebwerk ausbreitenden Störwellen zu modellieren. Dieser Ansatz ermöglichte es, eine Anfachung der Amplitude der PGC-Störungen bei niedrigen Verbrennungsfrequenzen zu identifizieren. Die Einbußen in der Verdichterleistung für vielstufige Konfigurationen wurde in Abhängigkeit der Frequenz, Amplitude und Gestalt der PGC-Störung bewertet. Datenbasierte Ansätze, einschließlich der proper orthogonal decomposition und der dynamic mode decomposition, zeigten eine Streuung von Energie und Kohärenz in höhere Modenordnungen sowie Unterschiede von spezifischen Strömungsmerkmalen zwischen dem stationär durchströmten Verdichter und dem Vergleichsfall mit PGC. Darüber hinaus konnte festgestellt werden, welche Strömungsphänomene unmittelbar mit dem identifizierten Anstieg der Stufenverluste zusammenhängen. Die Untersuchungen zu erzwungenen Schwingungen zeigten einen signifikanten Anstieg des

Schwingungs- und Spannungsniveaus an den Rotorschaufeln, wenn diese den PGC-Störungen ausgesetzt sind. Die erhöhte strukturelle Belastung wurde auch unter Einsatz der Kombination von instationärer Anregung, datengesteuerter Zerlegungen und der Modalanalyse untersucht.

Schlagworte:
Instationäre Aerodynamik, Aeroelastik, Hochdruckverdichter, Datengesteuerte Zerlegung, Druckerhöhende Verbrennung

CONTENTS

Nomenclature

Abbreviations

ALE	Arbitrary lagrangian-eulerian
AP	Axial plane
BPF	Blade passing frequency
CFD	Computational fluid dynamics
CSM	Computational solid mechanics
DDT	Deflagration to detonation transition
DMD	Dynamic mode decomposition
EEE	NASA Energy Efficient Engine
EO	Engine order
FEM	Finite element method
FSI	Fluid-structure interaction
GCI	Grid convergence index
HCF	High-cycle fatigue
HPC	High pressure compressor
IBPA	Interblade phase angle
ICM	Influence coefficient method
LES	Large eddy simulation
ND	Nodal diameter
NHB	Nonlinear harmonic balance
NSV	Non-synchronous vibrations
PDE	Pulse detonation engine
PGC	Pressure gain combustion
POD	Proper orthogonal decomposition
RANS	Reynolds-averaged Navier–Stokes equations
RDC	Rotating detonation combustion
SDOF	Single degree of freedom
SEC	Shockless explosion combustion
SVD	Singular value decomposition
TWM	Traveling wave mode
VPF	Vane passing frequency
WRC	Wave rotor combustion
ZND	Zeldovich/von Neumann/Döring

Greek letters

$\boldsymbol{\alpha}$	DMD mode amplitude
$\boldsymbol{\Phi}$	DMD complex mode
$\boldsymbol{\phi}$	Mode shape
$\boldsymbol{\Theta}$	DMD mode phase
ϕ	General state variable
$\boldsymbol{\delta}$	Kronecker delta tensor
$\boldsymbol{\sigma}$	Cauchy stress tensor
$\boldsymbol{\Sigma}$	Singular value matrix
$\boldsymbol{\tau}$	Stress tensor
$\boldsymbol{\varepsilon}$	Deformation tensor
ε	Unsteady damping, Kinetic energy dissipation
η	Isentropic efficiency, Damping loss factor
$\hat{\varepsilon}$	Homogeneous unsteady damping
λ	Discrete-system eigenvalue, Lamé parameter
λ_2	Vortex identification criterion
μ	Continuous-system eigenvalue, Dynamic viscosity, Mass ratio, Lamé parameter
μ_ν	Volumetric viscosity
μ_t	Turbulent eddy viscosity
ν	Poisson coefficient
ω	Angular frequency, Total pressure loss
ω_0	Natural frequency
ψ	Phase angle
ρ	Density
σ	Interblade phase angle
σ_{vm}	Von-Mises (equivalent) stress
θ	Phase angle, Circumferential coordinate, Generic scalar
ξ	Viscous damping coefficient
ζ	Critical damping ratio
${}^n\varepsilon$	Unsteady damping for station n ($\varepsilon_{n+1,n} \triangleq {}^n\varepsilon$)

Superscripts

n	Variable at time step n

Subscripts

0	Reference value
∞	Free stream
a	Alternating
d	Disturbance
f	Fluid
m	Mean
p	Pulse
r	Rotor, Resonance
s	Stator, Solid
t	Total (stagnation)

Mathematical symbols

$\bar{\mathbf{f}}$	Low-rank approximation of matrix $\mathbf{f}$
$\bar{f}$	Time-average of variable f
$\boldsymbol{\nabla}$	Nabla diferential operator
Δ	Finite variation
$\hat{\mathbf{f}}$	Fourier transform of variable $\mathbf{f}$, Unit vector $\mathbf{f}$, Effective
$\mathbf{f}^*$	Conjugate (Hermitian) transpose of tensor $\mathbf{f}$
$\mathbf{f}^+$	Moore-Penrose inverse of tensor $\mathbf{f}$
f'	Fluctuation (small perturbation) of variable f
$tr(\mathbf{f})$	Trace of tensor $\mathbf{f}$
$\dot{f}$	Partial derivative of f with respect to time
$\partial f/\partial x$	Partial derivative of f with respect to x

General symbols

$\mathbf{b}$	Body force, DMD initial coefficients vector
$\mathbf{d}$	Symmetric part of the velocity gradient
$\mathbf{P}$	Piola–Kirchhoff stress tensor
$\mathbf{q}$	Heat flux
$\mathcal{X}$, $\mathcal{Y}$, $\mathcal{Z}$	Snapshot matrices
$\mathbf{A}$	Linear time-shift operator
$\mathbf{n}$	Normal vector
$\mathbf{u}$	Displacement
$\mathbf{U}$, $\mathbf{V}$	Left and right singular vectors
$\mathbf{v}$	Velocity

$\mathbf{w}$	Weight functions
$\mathbf{X}$	Spatial coordinates in the material reference frame
$\mathbf{x}$	Spatial coordinates in the spatial reference frame
A	Amplitude
c	Chord, Damping coefficient, Speed of sound
c_d	Dilatational wave speed
c_p	Pressure coefficient
c_s	Shear wave speed
d_m	Nodal diameter
E	Modulus of elasticity
e	Internal energy per unit mass
f	Linear frequency, forcing
J	Jacobian
k	Reduced frequency, Stiffness, Kinetic energy
L	Representative system length
m	Mass
Ma	Mach number
N	Number of rotationally periodic substructures
n	Safety factor
n_c	Circumferential order
N_h	Number of harmonics
N_s	Number of rotationally periodic excitation units
p	Pressure
q	Scaling factor
R	Specific gas constant
r	Radius
s	Entropy
S_e	Endurance strength
S_{ut}	Ultimate tensile strength
S_y	Yield strength
St	Strouhal number
T	Temperature, Period
t	Time
W_{aero}	Aerodynamic work
y^+	Nondimensional wall distance

List of Figures

LIST OF TABLES

1

Introduction

Alarming scientific reports have been published in the last decades by international and intergovernmental groups concerning the dire consequences of global warming, especially in the Global South. These macro-scale changes are directly linked to anthropogenic greenhouse gas (GHG) emissions [1].

On the one hand, concrete efforts are being made to curb overall GHG emissions from all sectors, including power generation and aviation. On the other hand, political and technical challenges prevent their swift decarbonization.

This is particularly the case for civil aviation. Ramping globalization signals steady increase in GHG emissions from air transport. While in 2016 aviation was responsible for 3.6% of the European GHG emissions, a larger percentage is expected in the next years, despite decarbonization initiatives. Namely, the European Environment Agency predicts an increase in CO_2 emissions from air transport in Europe of at least 21% by 2040 [2]. As shown in Fig. 1.1, this trend is global, with 4.1% compound annual growth rate in revenue passenger-kilometer until 2045, as forecast by the International Civil Aviation Organization [3]. Although these assessments were made prior to the COVID-19 pandemic, the trend is expected to resume in the next years.

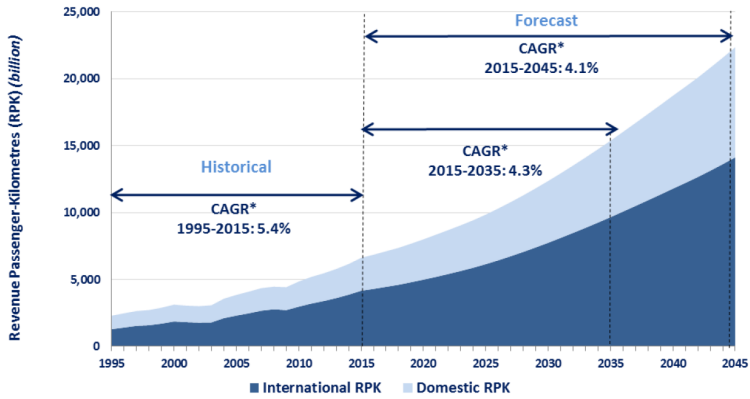

Figure 1.1: Forecast of growth in the air transport sector, according to the International Civil Aviation Organization [3]. CAGR stands for the compound annual growth rate.

In response to these predictions, challenging goals are being set by policymakers, such as a 75% reduction in aviation emissions in 2050 compared to 2000 [4]. To achieve such ambitious targets, strategic transport policies and a decrease in its overall volume are urgent. Additionally, marginal improvement in traditional technology will not suffice. This is especially true for gas turbines used in power generation and air transport: former improvements in efficiency have reached a saturation plateau. Instead, novel, radical concepts are necessary to tackle the issue.

Among several emerging approaches, pressure gain combustion (PGC) promises to substantially increase the thermal efficiency of gas turbines. However, such fuel burning processes come with the price of additional flow unsteadiness, which must be endured by turbomachinery components adjacent to the combustion chamber. In other words, PGC is expected to adversely influence aerodynamics and performance of the compressor and turbine, at the same time aeroelastically challenging the blading structure.

Therefore, the application of PGC into gas turbines is directly dependent on its successful integration with the upstream and downstream components. Considering the turbomachinery, two key conditions must be independently met:

- additional performance losses from PGC should be limited, so as not to hinder the overall thermodynamic gain;
- the structure is not allowed to fail.

This thesis addresses these aspects in depth. More specifically, unsteady aerodynamic and aeroelastic effects from PGC on high pressure compressors will be numerically assessed. The simulations are based on the state-of-the-art research on PGC and aim at shedding light on the fundamental fluid dynamics and solid mechanics response of compressor blades and vanes to novel PGC approaches.

1.0 Thesis scope

This work is articulated in the following manner. Chapter 2 presents the fundamentals of aeroelasticity in turbomachinery. The main concepts necessary to understand the aeroelastic phenomena investigated are introduced and discussed.

Subsequently, chapter 3 provides the theory and numerical methods employed in this thesis. The necessary equations to model the solid and fluid domain, as well as their interaction, are described. The numerical approach schemes to solve each domain are outlined. Finally, the data-driven decompositions applied to thoroughly analyze the unsteady flow are introduced.

Chapter 4 develops the PGC framework described above in more detail. Although combustion modeling is not the main focus of this thesis, it is crucial to understand the interaction of novel PGC concepts with turbomachinery components.

Selected results are then delivered in chapter 5. Analytical considerations about the propagation of PGC waves through turbomachinery are followed by two case studies employing modern high pressure compressors. Unsteady aerodynamic and aeroelastic assessments are presented. The interrelation between fluid dynamics and solid mechanics assessments is also discussed.

At this point, the fundamental unsteady effects of PGC on turbomachinery performance and aeroelastic response will be summarized in chapter 6, along with a brief outlook for future work.

2

Aeroelasticity in turbomachines

This chapter presents the main concepts and methods employed in the aeroelastic analyses

2.1 Background

Gas turbines and aero engines are designed to operate under rigorous safety criteria. However, efficiency and costs are also main development drivers, which tighten the safety margins of every component, often aiming at saving mass and space. The proper tuning of engine efficiency, operation safety and maintenance executability constraints is one of the biggest design challenges.

One of the most decisive determiners of design constraints is the transdisciplinary field of aeroelasticity. Before diving deeper into its physical description, it is important to mention the potential consequences of underestimating its relevance. To briefly cite a recent case, in 2018 a CFM International CFM56-7B turbofan engine experienced a structural failure, prompting an emergency landing of a Boeing 737-7H4 in Philadelphia, USA. One fatality occurred, when the window next to passenger Jennifer R. was destroyed by a cowl fragment. Additionally, eight people were injured. Detailed root-cause analysis [5] indicated that fatigue led to a blade-off event and consequentially engine total loss (Fig. 2.1). Several other accidents may be traced back to turbomachinery vibration issues [6–9].

Indeed, among other failure modes, fatigue alone is responsible for more than 75% of turbine blade failures, according to [10]. Specifically concerning high-cycle fatigue (HCF), besides being the largest cause of failure, it is mostly concentrated on blades, followed by vanes [11]. Ref. [12] indicates that, although more than 90% of HCF potential issues may be exposed during testing, the remaining part is accountable for up to 30% of development costs. When assessing heavy-duty and aeroderivative gas turbines, [13] showed that the percentual damage costs related to blading HCF amounts respectively to 24% and 9.5%. Furthermore, [14] inform that between 40% and 50% of land-based gas turbines outages occur due to blade fatigue.

In essence, excessive vibration leading to structural failure are of utmost importance in the development and maintenance of

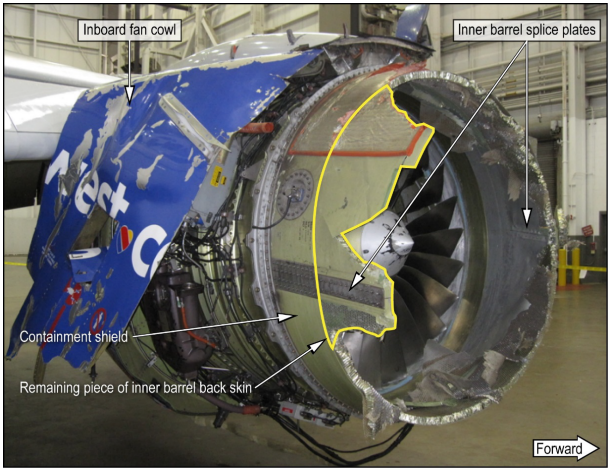

(a) Engine damaged by blade-off event

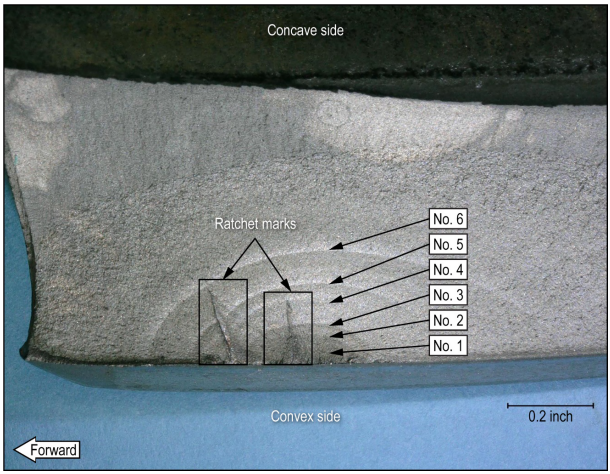

(b) Fatigue crack close to the fan's blade dovetail

Figure 2.1: Representative aeroelasticity (fatigue) failure [5].

gas turbines and aero engines. Not only lives may be directly at stake, but secondarily the reliable generation of energy, the trustworthiness of air transport, the execution of several industrial

processes and high component costs.

Other causes of blade failure are also worth researching, such as sucking of foreign object damage, corrosion, erosion or creep. The frequency and severity of these phenomena depend directly on the type of component, operation and maintenance regimes. Although they are not within the scope of the present work, it is relevant to notice that these failure modes oftentimes occur concurrently, so that multidisciplinary analyses may be required.

2.2 Main concepts

The field of aeroelasticity comprises a highly complex set of phenomena which span over multiple disciplines. One classic description of aeroelasticity was originally proposed by [15] as the interaction between three types of forces, namely aerodynamic, elastic and inertia. It became known as the Collar triangle. A more recent reading of these field interactions is depicted in Fig. 2.2, where the three vertices of the triangle now stand for the disciplines of fluid mechanics, dynamics and structural mechanics. The main phenomena arising from the interaction of these subjects are also shown inside the triangle, and will be discussed in detail in the next sections.

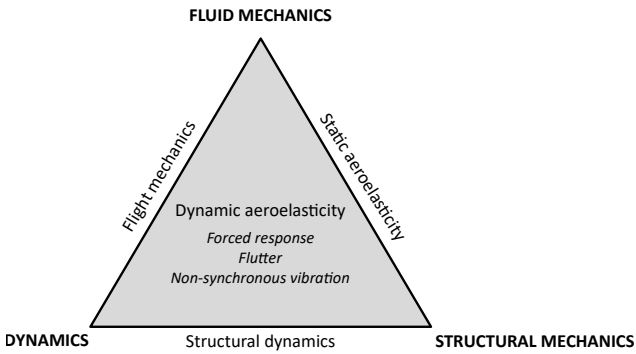

Figure 2.2: Simplified aeroelasticity triangle, based on [15].

Other denominations and phenomena are also found in the general aeroelasticity literature, including static divergence, buffeting, galloping, reversal control, gusts etc. They will not be discussed in detail here, since the main focus lies on turbomachinery vibration. Additionally, thermal and control effects may also be considered, giving rise to the respective fields of aerothermoelasticity and aeroservoelasticity.

2.2.1 Aeroelastic parameters

Before describing aeroelastic phenomena, it is important to define some parameters that will be used throughout this work. The list is not exhaustive, and the reader is encouraged to consult aeroelastic texts for further relevant parameters.

2.2.1.1 Interblade phase angle (IBPA) and nodal diameter (ND)

These related concepts describe how a substructure (or sector) of a rotationally periodic structure dynamically behaves with respect to another substructure. Figure 2.3 shows a sample compressor rotor, where each of the blades (substructures) vibrates in the first bending mode with the same frequency but at different phase. The dashed lines represent the NDs, corresponding to inflexion lines, where no infinitesimal movement takes place (directly related to regions with null displacement in a modal decomposition). While Fig. 2.3(a) depicts a case with a single ND (corresponding IBPA of $\pi/7$), in Fig. 2.3(b) every blade is completely out of phase with the adjacent blades (i.e., IBPA of π).

The maximum number of NDs, here represented by d_m, for rotationally periodic structures with odd and even number of substructure is given by Eq. (2.1)

$$d_{m,max} = \lfloor N/2 \rfloor, \tag{2.1}$$

where the symbol $\lfloor \cdot \rfloor$ stands for the floor function. That is, $\lfloor \phi \rfloor$ computes the highest integer lower than or equal to ϕ.

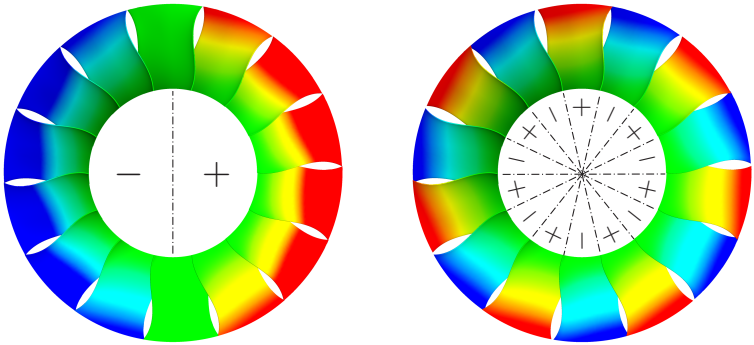

(a) 1 ND (b) 7 NDs

Figure 2.3: Color representation of the interblade phase angle in a compressor rotor with blades vibrating in the first bending mode. The dashed lines indicate the nodal diameters.

The IBPA can be understood either spatially or temporally, due to its unsteady manifestation in substructures. For a rotationally periodic structure with N identical substructures (say, blades), the IBPA, here represented by σ, is directly related to d_m as described in Eq. (2.2)

$$\sigma_{forward} = \frac{2\pi\, d_m}{N}, \tag{2.2a}$$

$$\sigma_{backward} = \frac{2\pi\,(N - d_m)}{N}, \tag{2.2b}$$

where $\sigma_{forward}$ and $\sigma_{backward}$ are usual conventions for forward and backward traveling waves. The use of the term *traveling* indicates that the ND pattern can be thought of as rotating in the circumferential direction. The existence of two σ for each d_m is due to the fact that the NDs can be regarded as rotating in both directions on the axial plane. Although each of the substructures vibrate with the same frequency, the angular velocity of each of these traveling modes is not the same, but higher for lower d_m.

In fact, every pair of forward and backward traveling modes can be understood as a complex mode, so that the wave *motion* is obtained by varying the phase angle of the complex variable (see, e.g., [16]). In other words, these two modes consist in a degenerate orthogonal pair of eigenvectors with the same eigenfrequency. Two special cases are not perceived as a traveling wave: (i) $d_m = 0 \Rightarrow \sigma = 0$, where the substructures vibrate in perfect phase; (ii) $d_m = N/2 \Rightarrow \sigma = \pi$, where every substructure is exactly out of phase with the adjacent sector.

In general, axisymmetrical structures present not only ND as inflexion lines, but also nodal circles. These are less relevant than NDs in practical turbomachinery and will not be discussed in this work.

2.2.1.2 Reduced frequency and Strouhal number

The reduced frequency is defined here as a nondimensional quantity representing the unsteadiness of an oscillating airfoil or blade. On a chord basis, it is given by Eq. (2.3)

$$k \triangleq \frac{\omega\, c}{U_\infty} = \frac{2\pi f\, c}{U_\infty}, \tag{2.3}$$

where c stands for the airfoil chord, U_∞ for the free stream velocity and $\omega = 2\pi f$ for the angular oscillation speed, with f being the ordinary oscillation frequency (e.g. one of the natural frequencies of the structure under analysis). Sometimes the reduced frequency is given on a half-chord basis.

One simple way to interpret the reduced frequency is as a metric proportional to the ratio between the time a fluid particle takes to travel the chord length to the time it takes for the structure to undergo one vibration cycle. Lower k values indicate a quasi-steady flow while higher values magnify the importance of unsteady phenomena.

The Strouhal number is another nondimensional quantity involving frequency, historically linked to vortex shedding [17]. It is defined here by Eq. (2.4)

$$St \triangleq \frac{f\,L}{U_\infty}, \tag{2.4}$$

where L is a representative length in the system (e.g. diameter, chord) and f usually represents a frequency unrelated to the structure eigenfrequencies, such as vortex shedding or general external excitation.

Although historically the reduced frequency and the Strouhal number emerged separately to explain different phenomena, they are both nondimensional frequencies[1]. When employed in this text, all nondimensional quantities will be explicitly defined.

2.2.1.3 Mass ratio

This nondimensional parameter relates the mass of the airfoil or blade to the mass of a virtual fluid cylinder surrounding it, as given by Eq. (2.5)

$$\mu \triangleq \frac{m_{blade}}{m_{fluid}} = \frac{4\,m_s}{\pi c^2 \rho_f}, \tag{2.5}$$

where ρ_f stands for the fluid density and m_s stands for the airfoil mass per unit length in a 2D case.

Usually μ is much higher in solid turbomachinery blades than composite blades or wings. This implies that solid turbomachinery blades (such as the ones analyzed in this work) tend to exhibit aeroelastic phenomena such as flutter linked to a single natural mode. That is, typical bending-torsion coupling present in wing flutter is not expected to occur here [19]. Additionally, a high μ value hints that aerodynamic forces acting on the structure are not expected to change its vibration pattern significantly; in other words, the influence of the fluid on the structure – for example when determining the natural modes – can be considered negligible [20, 21].

[1]Some authors use both quantities as synonyms (see, e.g., [18]).

2.2.1.4 Damping parameters

In the solid dynamics context, damping describes how the oscillations of a system decrease in time, so that the motion energy dissipates into other forms such as heat generation. It is a key concept in aeroelasticity, since the energy exchange between fluid flow and solid motion directly determines the structure's displacement levels, and whether or not a dangerous power imbalance takes place.

Although detailed solid mechanics equations for multiple degrees of freedom will be presented in section 3.2.1, a brief mention of single-degree-of-freedom (SDOF) oscillation systems is insightful. These represent the dynamics of a body in time domain as given by Eq. (2.6)

$$m\ddot{u} + c\dot{u} + ku = f, \tag{2.6}$$

where m, c and k stand respectively for the mass, (viscous) damping coefficient and stiffness coefficient. The body's displacement is given by u. External time-dependent forcing is represented by f. If $f = 0$ the system is denominated unforced; otherwise it is a forced oscillator. The overdot notation indicates time derivative ($\dot{u} \triangleq \partial u/\partial t$, $\ddot{u} \triangleq \partial^2 u/\partial t^2$ and so on).

At this point, it is enough to mention that the damping coefficient c is the sole parameter on the left hand side of Eq. (2.6) responsible for changing the displacement amplitude *in time*. If $c > 0$, the displacement amplitude decreases with time, while if $c < 0$, it increases indefinitely. $c = 0$ defines the threshold where no amplification or attenuation occur: the system is then considered an undamped oscillator.

The parameters m and k are related to physical properties of solids, such as density, elastic modulus and poisson ratio. They determine the natural frequency ω_0 with which the system oscillates, namely at $\omega_0 = \sqrt{k/m}$ for the undamped oscillator. In the case when $c \neq 0$, the effective oscillation frequency becomes $\omega = \sqrt{\omega_0^2 - c^2/(4m^2)}$, which is always less than ω_0.

Even in the case of $c < 0$, no real system oscillates with unbounded energy, due to inherent physical limitations.

However, negative damping, or even enough time in a regime with small positive damping may already be enough to cause destructive vibration in structures. These are key concepts in flutter and forced response, respectively, and will be further discussed in detail.

Damping is not only described by the damping coefficient c, but also by related parameters. Some of the most common nondimensional damping quantities are the *critical damping ratio* ζ, the *loss factor* η, the *logarithmic decrement* δ and the *quality factor* Q, which, for small damping values, are related to each other according to Eq. (2.7)

$$\zeta = \frac{c}{2\,m\,\omega_0} = \frac{\eta}{2} = \frac{\delta}{2\pi} = \frac{1}{2Q}. \tag{2.7}$$

These parameters describe damping in general, and may be employed in experimental and numerical analyses. The types of damping according to their source will be outlined in section 2.4.

2.2.1.5 Resonance frequency

Another relevant concept to be mentioned from the SDOF oscillator is the resonance frequency ω_r. It exists only in forced systems ($f \neq 0$), and corresponds to the forcing frequency at which the maximum power is externally supplied to the oscillator [22]. Interestingly, in the damped case, the resonance frequency is not the frequency that provides the maximum displacement – that being $\omega_0\sqrt{1-2\zeta^2}$. For undamped oscillators, the resonance frequency indeed equals the natural frequency, that is, $\omega_r = \omega_0$.

This fact motivates the need to keep the forcing frequencies far enough from natural frequencies to prevent high supply of power to the oscillator, which will be discussed in detail in section 2.3. Finally, models with multiple degrees of freedom have correspondingly multiple resonance frequencies (while continuous systems have infinite frequencies). However, not all of these resonance frequencies present actual danger, which is usually restricted to the smallest frequencies or the ones directly related to forcing elements.

2.3 Forced response

This section presents the fundamentals of forced response in turbomachinery, including the most useful diagrams. The numerical workflow employed here to compute forced response will be presented in depth in section 3.2.3.

Referring to Eq. (2.6) without loss of generality for multiple degrees of freedom, forced response corresponds to dynamics where $f \neq 0$ on the RHS[2]. That is, one or more external, motion-independent phenomena play an important role in determining the structure response, in addition to the parameters on the LHS of Eq. (2.6). Examples of external forcing in a turbomachinery context are the presence of adjacent blade or vane rows, struts, inlet distortions or unsteady combustion excitation.

Since turbomachinery components consist in an alternating series of rotating and stationary elements, unsteady excitation is often directly related to the rotational velocity of the axis (or axes) in the engine. The excitation frequency is usually presented in a nondimensional form, as a multiple of the engine order (EO), which corresponds to the engine's rotational velocity.

2.3.1 Campbell diagram

One of the most helpful representations assisting turbomachinery mechanical design is the Campbell diagram, originally introduced by [25]. A sample depiction is shown in Fig. 2.4, where the horizontal axis depicts the rotor speed and the vertical axis depicts frequencies of both natural modes and relevant aeroelastic phenomena. The first three natural modes are shown with continuous red lines. The straight dashed black lines starting from the origin are the EO lines, which simply correspond to multiples of the fundamental rotor frequency.

[2]This is the classic description of forced response for structural mechanics. From the aeroelastic perspective, this forcing may be presented as motion-dependent and motion-independent, respectively f_{md} and f_{mi}, with $f = f_{md} + f_{mi}$. If the forcing on the RHS of Eq. (2.6) is directly and solely dependent on the body's motion, i.e., $f = f_{md}(u, \dot{u}, \ddot{u})$, it may be brought to the LHS, as in a typical flutter analysis [23, 24]. This section considers cases where $f_{mi} \neq 0$.

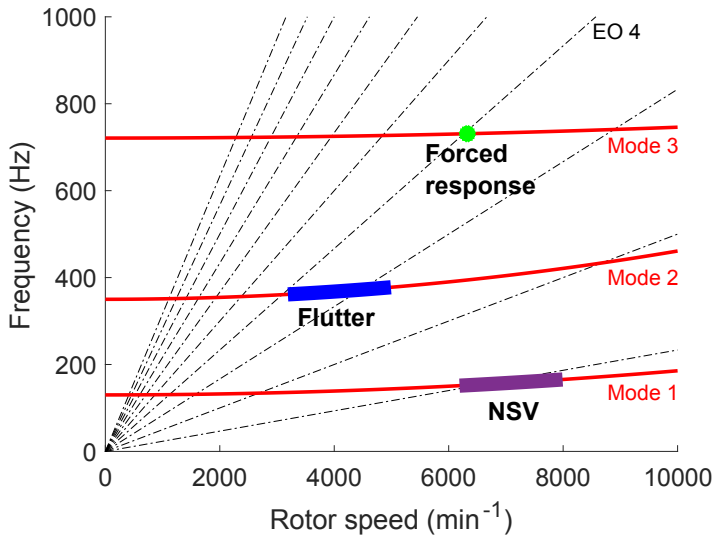

Figure 2.4: Sample Campbell diagram, depicting three main aeroelasticity phenomena: forced response, flutter and non-synchronous vibration (NSV). Natural modes are depicted by the red curves, while engine order lines are represented with black dashes.

Three of the main aeroelasticity mechanisms are indicated in Fig. 2.4. Forced response takes place in general at the crossing of EO lines with the structure natural modes (e.g. in Fig. 2.4, mode 3 with EO 4). Design attention is drawn particularly to crossings which occur close to operating speeds, where the engine stays for relative longer periods (such as cruise or idle states). Additionally, crossings corresponding to vane or strut passing frequencies (and a few higher harmonics) should also be avoided in the final design.

Although the other aeroelasticity phenomena depicted in Fig. 2.4 will be discussed in further sections, a brief word on the difference between flutter and non-synchronous vibration (NSV) may be insightful. Flutter is usually presented within a stability framework, describing self-excited vibrations which halt in the

absence of blade motion. NSV, in turn, describes a phase locking between a blade natural mode and pressure fluctuations due to one or more aerodynamic phenomena [26]. It is important to remark that Fig. 2.4 is not an exhaustive depiction of aeroelasticity issues that may occur in turbomachinery, exposing only the most predominant ones.

Also portrayed in Fig. 2.4 is the change in the natural frequencies as a function of the rotational speed. This occurs in fast-spinning turbomachinery mainly due to the so-called centrifugal stiffening effect. The increase in the perceived stiffness of the blades is in general modeled with the Southwell coefficient [27]. This effect is usually more pronounced for modes with bending predominance [28]. Sometimes, a decrease in the natural frequencies at high rotational speeds occurs in high pressure turbines, due to the direct increase in the material temperature and therefore decline in stiffness [29].

2.3.2 Interference diagram

Although the Campbell diagram consists of a highly helpful tool when searching for potential forced response issues, it is only a necessary – but not sufficient – condition for resonance in rotationally periodic structures. In fact, the Campbell diagram is able to show when exactly the external forcing frequency and the natural frequency of a blade match and resonance becomes *possible*. However, matching of forcing shape is also necessary to induce forced response.

Therefore, in addition to the Campbell, the interference diagram is necessary to assess forced response issues in turbomachinery. It has been originally proposed by [30], and is also known as SAFE or Zig-Zag diagram. An interference diagram is presented in Fig. 2.5 for a representative blisk. The diagram displays in the horizontal axis the ND count, and in the vertical axis frequency or engine order. In fact, both the Campbell and the interference diagrams are 2D cuts of a 3D general diagram relating rotor speed, nodal diameters and natural modes. For the purposes of the current work, 2D visualization provides enough clarity.

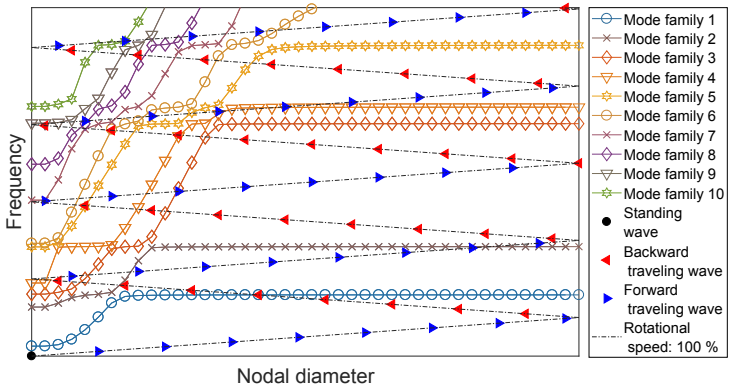

Figure 2.5: Interference diagram for a simulated blisk, showing the first 10 mode families and a representative speed line. Forward and backward traveling waves are shown according to the convention from Eq. (2.2).

A few comments are meaningful with respect to the interference diagram. The modal families shown in Fig. 2.5 are the outcome of the modal analysis of a blisk (section 3.2.1.2). Since for blisks the blades and the disk consist of a single part, every eigenmode may, in the general case, contain both disk and blade participation. The denomination "family" corresponds to the aggregation of eigenvectors linked to the same blade natural mode. For example, mode family 1 in Fig. 2.5 comprises all eigenvectors whose blade displacement are the first bending mode.

The speed line shown in Fig. 2.5 is constructed by linking all the nodal diameter which are susceptible to a particular combination of excitable and excitation units (e.g. rotor blades and stator vanes respectively). No detailed explanation on how to graphically construct an interference diagram will be provided here, the reader being referred to, e.g., [31] for an in-depth analysis.

The fundamental relation conveyed by the speed line in the interference diagram is given by Eq. (2.8)

$$d_m = \left| nN_s - N \lfloor \left(nN_s + \lfloor N/2 \rfloor \right) / N \rfloor \right| , \tag{2.8}$$

where, as usual, d_m and N are the number of nodal diameters and blade count. N_s stands for the number of excitation units (for example, the stator vane count or combustor modules), while n is a positive integer. Equation (2.8) is a closed-form relation determining the exact nodal diameter that will be excited by any combination of N, N_s and n. Figure 2.6 depicts a sample interference diagram for a case with $N = 13$ rotor blades, with two curves for different numbers of stator vanes N_s. One notices firstly that the interference diagram is periodic, repeating itself every N harmonics, since $d_n(n + N) = d_n(n)$. Secondly, for each period N, the lines are symmetric at the axis $N/2$.

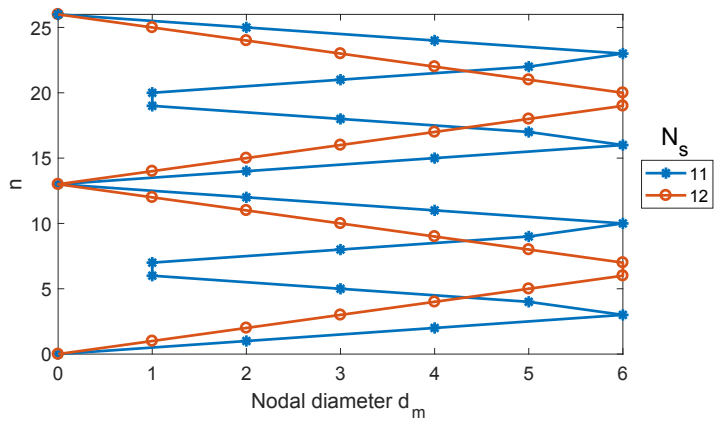

Figure 2.6: Illustrative interference diagram for a case with $N = 13$ blades, with curves for two stator configurations with different vane count N_s. The forcing engine order is given by n.

Another common way Eq. (2.8) is portrayed is given by

$$\frac{nN_s \pm d_m}{N} = \text{integer}. \tag{2.9}$$

This condition requiring shape matching is nothing more than an aliasing phenomenon. That is, although the forcing may have arbitrarily high angular frequency (conveyed here by nN_s), a reduction in sampling occurs from the rotor perspective, due to

a limitation of N rotor blades. Therefore, even for high forcing frequencies, only NDs up to $d_{m,max}$ (Eq. (2.1)) are excitable. This aliasing phenomena is a manifestation of the Nyquist-Shannon-Kotelnikov theorem [31]. Lastly, although the denomination for rotor and stator has been respectively employed for N and N_s, they are generally interchangeable for frames rotating with respect to each other.

2.4 Flutter

This work will focus on the dynamic nature of flutter (see Fig. 2.2) in the turbomachinery context, the reader being referred to [18, 28] for a broader overview on other flutter modes. This section presents the fundamentals of flutter in turbomachinery, including the main equations, types of damping and occurrence in a compressor map. The numerical approaches to compute flutter stability will be presented in section 3.2.2.3.

Referring back to Eq. (2.6), flutter generally occurs independently from the (strictly external) forcing f on the RHS (see footnote 2 in section 2.3). Common definitions consider flutter a self-excitation or instability phenomenon. For practical purposes, instability is interpreted here as a trajectory in a dynamical system which changes significantly (even becoming unbound) under small perturbations. For the SDOF system described in Eq. (2.6), instability takes place when the damping parameter c becomes strictly negative. In fact, the name *damping* even loses meaning, since for $c < 0$ the amplitude of the displacement u only increases in time, and the larger the value of $|c|$, the higher the amplification in u will be.

Therefore, there is high interest in determining the existing damping in a system, not only to assess whether or not instabilities are expected, but also to estimate the maximum level of forced response, as discussed in section 2.3.

In the turbomachinery context (here restricted to blades and vanes), the main sources of damping are the structural, aerodynamic and material damping. Other damping mechanisms may be implemented, such as piezoelectric elements, eddy

current, air film etc. Only the main sources will be discussed here. In the general case, all these mechanisms may add up nonlinearly, turning the analysis of each one independently into a very complex task.

2.4.1 Material damping

The material damping is a physical property of the blading material. It is determined experimentally by measuring the energy dissipated during cyclic stressing of homogeneous samples. Since these cycles are in fact hysteresis loops, the material damping is also known as hysteretic damping. It is related to the vibration energy internally dissipated into heat.

For typical turbomachinery materials and specifically the ones employed in this work, the material damping is usually negligible in comparison to other damping sources [12, 14, 32]. For example, [33] reports for titanium and stainless steel (materials often employed in HPC) values of loss factor η in the order of 10^{-4}. Similar values of $\eta \approx 0.0003$ were reported by [32] for a titanium alloy used in turbomachinery. These figures are one to three orders of magnitude smaller than aerodynamic or structural damping, and can be safely disregarded here.

For completeness, a representative relation for the loss factor linked to material damping is given in Eq. (2.10)

$$\eta = \frac{1}{2\pi}\frac{E_d}{E_s}, \tag{2.10}$$

where E_d and E_s stand respectively for the dissipated energy and the maximum strain energy during one hysteresis vibration cycle [32].

2.4.2 Structural damping

This type of damping, sometimes referred to as friction damping, is related to the complex interaction between each blade and the adjacent structures it comes in contact with (disk, shroud and other blades, in case snubbers are present). A

common practice is the addition of a third metal element between platforms or shrouds of adjacent blades, introducing rubbing and therefore dissipating vibration energy. The structural damping is, therefore, intrinsically linked to the friction taking place at these metal-to-metal interfaces. Naturally, platform-blade friction damping is absent in one-piece blisk designs.

The structural damping is a highly nonlinear interaction, mostly due to the intermittent contact between surfaces (e.g. stick-slip behavior). It is also dependent on the normal pressure experienced by contact surfaces, rotational speed, friction coefficient, mode shape, presence of external damping elements among other factors.

Analytical models for friction damping have been developed based on Coulomb's law of friction, making use for example of a harmonic balance numerical approach [34, 35]. Numerically modeling the structure and external dampers explicitly is also a possibility, having been extensively explored for wedge, seal wire and strip dampers by [36]. However, the practical prediction of structural damping still relies heavily on experiments.

It is out of the scope of this work to research or model friction damping in detail. Except for the blisk case (where no contact friction is present), the structural damping will be estimated based on literature estimates, as common practice (see, e.g., [37–39]). Detailed reviews on structural damping can be found, for instance, in [40, 41].

2.4.3 Aerodynamic damping

This type of damping is directly related to the interaction between the structure and the fluid surrounding it. The higher the aerodynamic damping, the more energy is transferred from the structure motion to the flow. By convention, a positive aerodynamic damping implies that the vibration experienced by the structure loses energy and eventually dampens out. Conversely, a negative value means that energy is transferred from the flow to the structure motion, provoking an increase in displacement with potentially drastic consequences.

This reasoning has been initially implemented by [42], in the well-established energy method for flutter prediction. The key idea is conveyed by the aerodynamic work W_{aero}, given by

$$W_{aero} = \int_{t}^{t+T} \int_{\ell} p \; \mathbf{v} \cdot \hat{\mathbf{n}} \; d\ell \; dt, \tag{2.11}$$

where p is the static pressure, $\mathbf{v}$ the wall velocity vector and $\hat{\mathbf{n}}$ the normal unit vector pointing outwards from the wall. The surface integral takes place along the blade walls ℓ. The aerodynamic power is integrated in time t during one period T, yielding W_{aero}. For $W_{aero} < 0$, energy is being fed from the blade motion to the fluid stream, in a stable fashion; for $W_{aero} > 0$, energy is being transferred from the fluid to the structure, indicating instability.

The modal damping ratio ζ_{modal} is related to the aerodynamic work according to Eq. (2.12)

$$\zeta_{modal} = \frac{-W_{aero}}{2\,\pi\,\omega^2\,q^2}, \tag{2.12}$$

where $\omega = 2\pi f$ is the angular vibration frequency of the blade (obtained from a pre-stressed modal analysis), and q is the scaling factor of the natural mode shape for the computational fluid dynamics (CFD) simulation (including the modal scaling, in case mode shapes are obtained as mass normalized). Relation (2.12) is valid for lightly damped systems, which is a good approximation for typical turbomachinery blades [24]. More details about modal analysis will be given in section 3.2.1.2.

Furthermore, the energy method just described has been extended to a traveling wave mode (TWM) formulation (see [24, 43]). In this approach, all the blades in the row vibrate with the same frequency and mode shape, but with an interblade phase angle, as described in section 2.2.1.1. The same Eq. (2.11) is employed to determine flutter stability.

In addition to the TWM formulation, another way to determine aeroelastic (in)stability is the so-called aerodynamic influence coefficient method (ICM). This time-linearized frequency domain approach can be traced back to the work of [44], and in the

turbomachinery context is presented as follows: only a single blade (termed reference blade) oscillates, and the unsteady forcing on the other blades is measured and transformed into aerodynamic influence coefficients. Afterwards, a generalized eigenvalue problem is solved and stability is determined by assessing each eigenvalue. An insightful interpretation of the ICM is that each coefficient obtained represents the forcing on one blade due to the motion of another ([45] having shown that the reference being self-damped is a necessary but not sufficient condition for cascade stability). Differently from the TWM approach, a single experiment or computation is enough to determine the aeroelastic stability of the system.

Indeed, both formulations, TWM and ICM, have shown to be equivalent when representing the aeroelastic system [24]. They are simply different function bases for the modal coordinates representing the blade displacement. While the ICM uses the typical solid mechanics modal base, which facilitates the inclusion of, e.g., mistuning, the TWM employs a function base dictated by the IBPA shape functions. Other function bases have been described in the aeroelastic literature (see [24, 46] for an overview).

2.4.4 Occurrence of flutter

Self-excitation in turbomachinery is usually confined to fans, front and middle compressor blades and low pressure turbines. It is however a highly complex phenomenon, which motivated the search for nondimensional parameters that hint where flutter occurrence might be expected. One of them is the reduced frequency k (section 2.2.1.2), which empirically indicates flutter occurrence: for bending modes $k < 0.8$ and for torsion modes $0.8 < k < 1.4$, according to [20]. Sometimes, even lower reduced frequencies, namely $k < 0.4$ for bending modes, are required to incur flutter [47][3]. A broader occurrence range is suggested by [48], namely between $0.1 \leq k \leq 1$ for turbomachinery blades.

[3]The definition of reduced frequency employed by [20, 47] makes use of half the chord. In this work, the reduced frequency will always be converted to the definition from Eq. (2.3), considering the entire chord.

On a similar note, blades with rather reduced mass ratios (2.2.1.3) would be in higher risk of flutter [29] (however without broad, precise values known in the turbomachinery literature). This is directly related to the fact that low mass ratios increase the aeroelastic coupling in the system.

Flutter occurrence in a compressor map is depicted in Fig 2.7. Typical flutter boundaries are shown, according to numerous experimental reports in the turbomachinery history. They will not be discussed in detail in this work, with in-depth information made available by [29, 49].

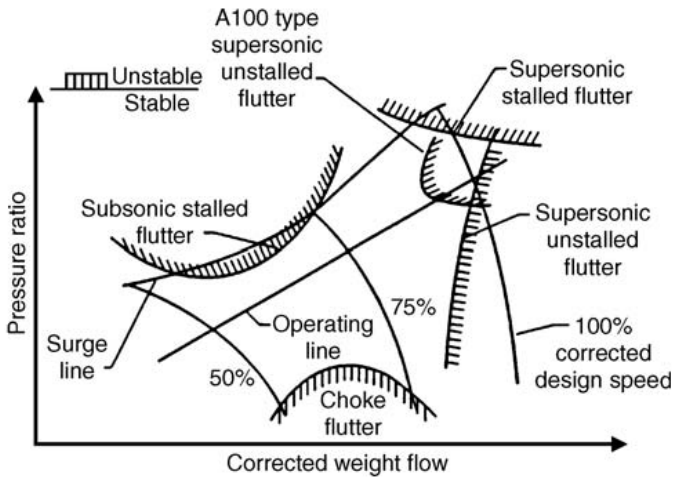

Figure 2.7: Occurrence of flutter in a compressor showing several stability boundaries [29].

A representative operating line is also displayed in Fig 2.7, crossing into the unstable boundary for high corrected mass flow. The goal of an aeroelastically properly designed component is to keep all possible operation states within stable regions, that is, flutter free. Differently from forced response, where during acceleration a "brief" period close to a resonance frequency may be endured, flutter may very fast lead to destructive vibration issues. Therefore, an adequate aeroelastic design should keep the system as far as practicable from these unstable zones. That means securing large flutter margins for the entire operating range.

2.5 Non-synchronous vibrations

Besides the traditional forced response and flutter phenomena usually considered as main aeroelastic issues in turbomachinery, non-synchronous vibrations (NSV) have also been reported in the recent literature[4]. Differently from separated flow vibrations, which manifest as an instability with a broad spectrum, NSV take usually form with a dominant frequency [51]. Typically, a lock-in between a flow phenomenon and a blade natural mode occurs.

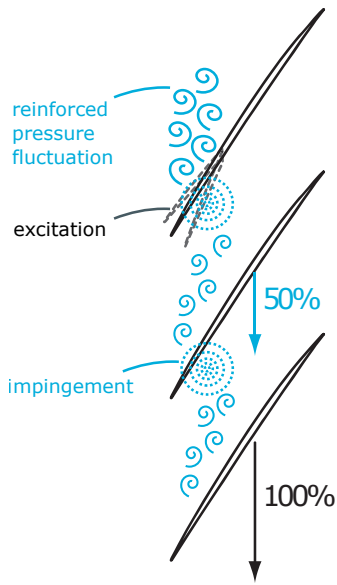

Figure 2.8: Representation of non-synchronous vibration caused by rotating instabilities [26].

[4]Strictly speaking, NSV would correspond to any vibration issue which is not directly traceable to the fundamental engine rotational frequency, possibly including flutter (see [50] for a broad overview). However, NSV is typically reported in the literature excluding flutter issues, as presented in this work.

Flow behavior leading to NSV may include unsteady tip clearance flow, vortex shedding, rotating stall, among other flow instabilities. The main frequency of these phenomena is not a priori related to integral multiples of the rotational speed of the rotor, therefore the name NSV.

As a representative case, rotating instabilities with a periodicity of approximately half the rotor speed have induced NSV in a transonic compressor blisk [26]. The flow instability arose from high pressure fluctuations due to enlarged tip gaps, and is sketched in Fig. 2.8. Further experiments with non-uniform casing eccentricity yielded an amplitude reduction in NSV, at the expense of a potential increase in synchronous vibration (forced response) [52]. This trade-off hints that taking all aeroelasticity issues into account is often a technically challenging task.

2.6 Mistuning

Up to now, no consideration has been made about how each turbomachinery element may differ from one another. This situation is referred to as mistuning. Up to now, all blades or vanes have been assumed to be equal for a specific row, concerning geometric and material properties. This is in fact not the case in a real machine, due to variability in manufacturing and finishing tolerances but also operation and (usually random) wear reasons.

The effects of structural mistuning on aeroelasticity phenomena vary. For flutter, an increase in mistuning usually promotes more aeroelastic stability, whereas for forced response, typically higher [20, 29, 53–55] but sometimes lower [56, 57] vibration amplitudes occur. The groundwork in turbomachinery mistuning was laid by [58, 59], who investigated, among other topics, the actual change in vibration amplitude. In fact, [59] has provided an analytical upper bound for vibration amplification due to mistuning, namely, of $\frac{1}{2}(1+\sqrt{N})$ for a rotor with N blades. It was however recognized that this limit is rarely reached in real cases (see [60] for further analytical considerations).

For forced response, mistuning may lead to mode localization. This happens when the propagation of energy externally injected in the vibrating system does not occur freely, leading to energy confinement close to the forcing source and possibly excessive stresses. Additionally, the splitting of single modes into closely-spaced multiple eigenfrequencies due to mistuning makes the task of measuring and modeling the structure vibration much more challenging [61].

Since the increase in forced response amplitude occurs nonlinearly [62], researchers have sought optimal mistuning levels and patterns. Ref. [63] have shown that the sensibility of a rotor to random mistuning can be decreased in the presence of intentional mistuning. Direct mistuning optimization has been successfully employed by [64], with an approach specially designed to be used with large finite element models. Other attempts at reducing forced vibration with premeditated mistuning have considered grouping or *packeting* of shrouded blades [65] and implementation of alternating patterns of strongly and weakly mistuned blades [66].

Exploiting intentional mistuning has also been sought to enhance flutter stability. For example, [45] employed constrained optimization to find ideal intentional mistuning patterns, obtaining increase in stability margin with an "almost alternate" pattern. A linearized asymptotic mistuning model was proposed by [67], enabling increase in flutter stability for unstable low pressure turbine rotors.

In essence, structural mistuning makes solid mechanics analyses more complex. However, although vibration levels may indeed change in the presence of mistuning, it is usually not included in preliminary assessments. Mistuning can then be added to workflows once they have been proven to adequately represent virtually tuned systems and particularly to circumstances where substantial inhomogeneity is present (e.g. end-of-life components) or high-precision estimations are necessary.

2.7 Failure criteria

Once the static and dynamic stresses caused by the aeroelastic phenomena described until now have been measured or estimated, the next question is how to assess whether or not the loads are tolerable or excessive. Since gas turbine components are constantly subjected to steady and unsteady loads, simple static criteria such as yield limits are not enough to ensure fatigue-free operation. Therefore, adequate failure criteria should be chosen, according to the desired factor of safety (here denoted by n). The considerations in this section are valid for ductile metals (representing most alloys employed in gas turbines), while brittle materials require different approaches (see, e.g., [68]).

A typical fatigue failure diagram (also known as Goodman-Haigh) employed for metals is shown in Fig. 2.9. The diagram depicts both mean and alternating stresses, respectively given by σ_m and σ_a. It is here restricted to tensile mean stresses (by convention positive). This representation, originally proposed by [69], is valid for a single material (specimen) at a specific temperature.

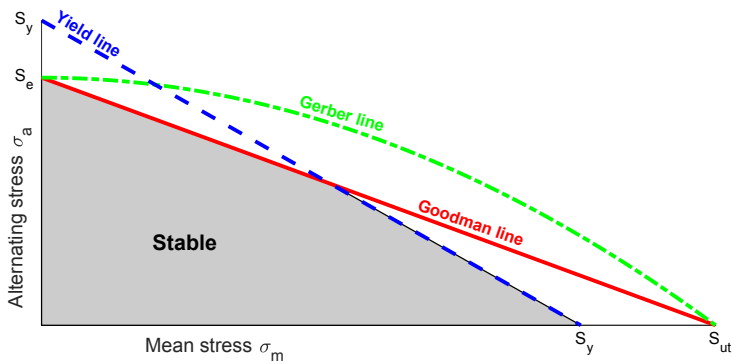

Figure 2.9: Representative failure diagram for fatigue depicting a stable region and typical failure criteria.

In practice, failure criteria are computed from a few solid mechanics properties empirically determined. Several failure thresholds have been historically suggested, whereas discussing all formulations in detail is out of the scope of this work. Three of the most common failure criteria are depicted in Fig. 2.9:

- Yield (Langer) line: it is constructed simply by joining the yield strength S_y for both mean and alternating stresses. It is described by the relation

$$\sigma_m + \sigma_a = \frac{S_y}{n} \tag{2.13}$$

- (Modified) Goodman line: it is constructed by joining the endurance strength S_e (obtained from infinite-life tests) to the ultimate tensile strength S_{ut}. It is given by the relation

$$\frac{\sigma_m}{S_{ut}} + \frac{\sigma_a}{S_e} = \frac{1}{n} \tag{2.14}$$

- Gerber line: it is a parabola given by the relation

$$\left(\frac{n\sigma_m}{S_{ut}}\right)^2 + \frac{n\sigma_a}{S_e} = 1 \tag{2.15}$$

A stable area (ideally free of fatigue failure) is also depicted in Fig. 2.9, roofed by the yield and the Goodman lines. It allows the designer to estimate the trade-off between mean and alternating stresses for a component. It is important to notice that this stability area is not strictly deterministic, due to the variability intrinsic to empirical methods. It provides, nevertheless, an effective and simple basis to judge for failure expectation, being constructed from readily available material properties. Detailed information about failure criteria is given, e.g., by [68].

3

Theory and methods

This chapter develops some of the fundamental concepts from chapter 2, their numerical implementation and additional methods employed in this work

3.1 Physical description

This section will present the general physical formulation and main equations for the solid and fluid domains. These theories derived from continuum mechanics are the basis for every aeroelastic model, since the interaction between flow and structure can only be adequately modeled once the independent formulations for each domain are precisely defined.

Some fundamental concepts have already been mentioned in Chapter 2. A formal and general approach will be provided here for both solid and fluid domains. It will be precise enough to understand the numerical methods in section 3.2, however confined to the necessary applied concepts used throughout the work. All equations will be presented in Cartesian coordinates for simplicity, while cylindrical or spherical coordinates are readily available in the accompanying literature suggestions.

3.1.1 Solid domain

The solid domain is modeled in this work as a continuous elastodynamic medium. The main equations governing the model will be described, while a more theoretical and rich approach may be found, e.g., in [70, 71].

Three simplifying hypothesis will be employed when deriving the solid domain equations: isotropic medium, generalized Hooke's law and relatively small deformation gradients. In this work, the elastodynamic equations will be described in the Lagrangian, or "material reference frame". That is, the observer follows each material particle located in the initial configuration at coordinates $\mathbf{X} = (X, Y, Z)$[1].

The unknowns to be determined are the displacements $\mathbf{u} = \mathbf{u}(\mathbf{X}, t)$, the Cauchy stresses $\boldsymbol{\sigma} = \boldsymbol{\sigma}(\mathbf{X}, t)$ and the deformations $\boldsymbol{\varepsilon} = \boldsymbol{\varepsilon}(\mathbf{X}, t)$. These variables are defined for a particle located at material coordinates $\mathbf{X} \in \Omega$ for an instant $t \in [0, \infty)$. The spatial domain $\Omega \subset \mathbb{R}^n$ $(n = 1, 2, 3)$ has as

[1] Uppercase spatial coordinates (X, Y, Z) indicate the material reference frame, whereas lowercase coordinates (x, y, z) indicate the spatial reference frame.

boundaries the set $\Gamma \subset \mathbb{R}^{n-1}$, with $\Gamma = \Gamma_1 \cup \Gamma_2$. Γ_1 stands for Dirichlet boundary conditions (first type or essential) and Γ_2 stands for Neumann boundary conditions (second type, or natural), and $\Gamma_1 \cap \Gamma_2 = \emptyset$. A weighted combination of Dirichlet and Neumann bounds is known as Robin boundary condition.

Starting with the mass continuity equation, it assumes a very simple form when described in the Lagrangian reference frame, namely given by Eq. (3.1)

$$\rho|J| = \rho_0, \tag{3.1}$$

where ρ is the particle density, with value ρ_0 at time t_0. $|J|$ stands for the absolute value of the Jacobian J, which is the determinant of the deformation gradient tensor. Since for positive masses $J > 0$, the absolute operator is often dropped. For any deformation gradient, the change in density is automatically determined by Eq. (3.1). Therefore, density itself does not appear as an unknown in the solid domain equations, when written in the Lagrangian reference frame.

The conservation of linear momentum in the differential form is given by Eq. (3.2)

$$\rho \frac{\partial^2 \mathbf{u}}{\partial t^2} = \rho \mathbf{b} + \boldsymbol{\nabla} \cdot \boldsymbol{\sigma}, \tag{3.2}$$

where $\mathbf{b}$ are domain forces per unit mass (e.g., gravitational force), and $\boldsymbol{\sigma}$ the Cauchy stress tensor. The del or nabla operator is defined as $\boldsymbol{\nabla} \triangleq (\frac{\partial}{\partial x}, \frac{\partial}{\partial y}, \frac{\partial}{\partial z})$ for a 3D Cartesian case. Accordingly, the gradient, divergence and curl of a generic field $\mathbf{f}$ are given respectively by $\boldsymbol{\nabla}\mathbf{f}$, $\boldsymbol{\nabla} \cdot \mathbf{f}$ and $\boldsymbol{\nabla} \times \mathbf{f}$.

Using the isotropic and Hooke's hypotheses, the Cauchy stress tensor can be written as in Eq. (3.3) (also known as Hooke's law)

$$\boldsymbol{\sigma} = \lambda \, tr(\boldsymbol{\varepsilon}) \, \boldsymbol{\delta} + 2\mu \, \boldsymbol{\varepsilon}, \tag{3.3}$$

where $\boldsymbol{\delta}$ stands for the Kronecker delta tensor and the trace operator is given by $tr(\boldsymbol{\varepsilon}) = \varepsilon_{xx} + \varepsilon_{yy} + \varepsilon_{zz}$. Indeed, Eq. (3.3) is a linear constitutive relation between forces and displacements, or more precisely in this case, between tensions and deformations

respectively. The scalars λ and μ are the Lamé parameters, which specific to each solid material. They relate to more commonly known material properties, namely the modulus of elasticity E and the Poisson coefficient ν, according to Eqs. (3.4)

$$\lambda = \frac{E\,\nu}{(1+\nu)(1-2\nu)}, \tag{3.4a}$$

$$\mu = \frac{E}{2(1+\nu)}. \tag{3.4b}$$

The relation between deformation and displacement is given by Eq. (3.5)

$$\boldsymbol{\varepsilon} = \frac{1}{2}\left(\boldsymbol{\nabla}\mathbf{u} + \boldsymbol{\nabla}\mathbf{u}^T\right). \tag{3.5}$$

To obtain the Navier-Cauchy equations, we substitute Eq. (3.5) in Eq. (3.3) and then the result in Eq. (3.2), obtaining Eq. (3.6)

$$\rho\frac{\partial^2\mathbf{u}}{\partial t^2} = \rho\mathbf{b} + (\lambda+\mu)\,\boldsymbol{\nabla}(\boldsymbol{\nabla}\cdot\mathbf{u}) + \mu\boldsymbol{\nabla}^2\mathbf{u}, \tag{3.6}$$

where the Laplace operator is given by $\boldsymbol{\nabla}^2 = \boldsymbol{\nabla}\cdot\boldsymbol{\nabla}$ (divergence of the gradient). The Navier-Cauchy equations can also be rewritten as

$$\frac{\partial^2\mathbf{u}}{\partial t^2} = \mathbf{b} + \left(c_d^2 - c_s^2\right)\boldsymbol{\nabla}(\boldsymbol{\nabla}\cdot\mathbf{u}) + c_s^2\boldsymbol{\nabla}^2\mathbf{u}, \tag{3.7}$$

where the dilatational c_d and shear wave c_s speeds are given as a function of the Lamé parameters or material properties by Eqs. (3.8)

$$c_d^2 = \frac{\lambda+2\mu}{\rho} = \frac{E\,(1-\nu)}{\rho\,(1+\nu)\,(1-2\nu)}, \tag{3.8a}$$

$$c_s^2 = \frac{\mu}{\rho} = \frac{E}{2\rho\,(1-\nu)}. \tag{3.8b}$$

A viscous damping force proportional to the particle velocity is usually included in the momentum equation. It is here given by $\xi \frac{\partial \mathbf{u}}{\partial t}$, where ξ is the viscous damping coefficient. Then, the final form of the momentum conservation is given by Eq. (3.9)

$$\frac{\partial^2 \mathbf{u}}{\partial t^2} = \frac{\xi}{\rho} \frac{\partial \mathbf{u}}{\partial t} + \mathbf{b} + \left(c_d^2 - c_s^2\right) \boldsymbol{\nabla}(\boldsymbol{\nabla} \cdot \mathbf{u}) + c_s^2 \boldsymbol{\nabla}^2 \mathbf{u}. \tag{3.9}$$

Finally, the balance of energy can also be written for solid domains in the Lagrangian reference frame. It becomes particularly relevant to describe system changes in the presence of nonmechanical effects, such as substantial heat flux, viscoelastic or plastic deformations. The balance of internal energy is given by Eq. (3.10)

$$\rho_0 \frac{\partial e}{\partial t} = -\boldsymbol{\nabla} \cdot \mathbf{q} + \mathbf{P} : \mathbf{d}, \tag{3.10}$$

where e is the internal energy per unit mass and $\mathbf{q}$ is the heat flux vector (e.g., related to temperature gradients). $\mathbf{P}$ stands for the Piola–Kirchhoff stress tensor and $\mathbf{d}$ for the symmetric part of the velocity gradient, i.e., $\mathbf{d} = \frac{1}{2}\left(\boldsymbol{\nabla}\mathbf{v} + \boldsymbol{\nabla}\mathbf{v}^T\right)$, $\mathbf{v}$ being the particle velocity. The double contraction represented by $\mathbf{P} : \mathbf{d}$ is known as stress power (per unit volume). Other therms such as radiation energy may also be included in Eq. (3.10), according to modeling requirements.

3.1.2 Fluid domain

The fluid domain modeled in this work is restricted to monophasic, newtonian and isotropic descriptions. These assumptions are very accurate for the type of fluid present in turbomachinery components of gas turbines. Additionally, no chemical reaction mechanisms are implemented, since computing combustion is not in the scope of this work. Also for the fluid domain, only the main equations will be shown, while the reader can refer, e.g., to [71–73] for detailed discussions.

Differently from the typical Lagrangian description of solid domains, now an Eulerian approach is employed. That means that the observer does not follow each fluid particle, but obtains data from fixed points in space, where different fluid particles travel through. These stationary points are located at coordinates $\mathbf{x} = (x, y, z)$. This idea of obtaining and computing data for a fixed location in space traversed by different fluid elements is conveyed by the material (or total) derivative, given for a generic (scalar or vector) field $\mathbf{f}$ by Eq. (3.11)

$$\frac{\mathrm{D}\mathbf{f}}{\mathrm{D}t} = \frac{\partial \mathbf{f}}{\partial t} + \mathbf{v} \cdot \boldsymbol{\nabla} \mathbf{f}. \tag{3.11}$$

The first term on the RHS of Eq. (3.11) accounts for the classic partial derivative with respect to time for a single particle, while the second term includes the convection effect due to the velocity field $\mathbf{v}$. The nonlinear relation given by Eq. (3.11) actually links the Lagrangian and Eulerian descriptions of continuum media.

The unknowns to be determined now are the fluid velocity $\mathbf{v} = \mathbf{v}(\mathbf{x}, t)$, density $\rho = \rho(\mathbf{x}, t)$, pressure $p = p(\mathbf{x}, t)$ and temperature $T = T(\mathbf{x}, t)$. Other variables such as the internal energy e may be derived from the previous quantities. These variables are defined for a particle located at spatial coordinates $\mathbf{x} \in \Omega$ for an instant $t \in [0, \infty)$. The spatial domain $\Omega \subset \mathbb{R}^n$ ($n = 1, 2, 3$) has as boundaries the set $\Gamma \subset \mathbb{R}^{n-1}$, with $\Gamma = \Gamma_1 \cup \Gamma_2$. Γ_1 stands for Dirichlet boundary conditions (first type or essential) while Γ_2 stands for Neumann boundary conditions (second type, or natural), and $\Gamma_1 \cap \Gamma_2 = \emptyset$. Typical boundary conditions are the flow velocity and thermodynamic state, but more complex and mixed combinations may arise for involved problems.

The starting point is the mass continuity equation (analogous to Eq. (3.1)), now written in the Eulerian description in Eq. (3.12)

$$\frac{\mathrm{D}\rho}{\mathrm{D}t} + \rho \boldsymbol{\nabla} \cdot \mathbf{v} = 0. \tag{3.12}$$

Subsequently, analogously to Eq. (3.2), the Cauchy equation for conservation of linear momentum is given by Eq. (3.13)

$$\rho \frac{\mathrm{D}\mathbf{v}}{\mathrm{D}t} = \rho \mathbf{b} + \boldsymbol{\nabla} \cdot \boldsymbol{\tau}, \tag{3.13}$$

where $\mathbf{b}$ are body forces and $\boldsymbol{\tau}$ the stress tensor on the fluid particles. For isotropic media, the stress tensor can be written as

$$\boldsymbol{\tau} = -p\boldsymbol{\delta} + \mu \left(\boldsymbol{\nabla}\mathbf{v} + \boldsymbol{\nabla}\mathbf{v}^T \right) + \left(\mu_\nu - \frac{2}{3}\mu \right) \left(\boldsymbol{\nabla} \cdot \mathbf{v} \right) \boldsymbol{\delta}, \tag{3.14}$$

where μ and μ_ν stand respectively for the dynamic and volumetric fluid viscosities. The first term on the RHS of Eq. (3.14) corresponds to the inviscid stresses, directly related to the thermodynamic pressure. The last two terms are the viscid components, related respectively to the symmetric part of the velocity gradient tensor and the volumetric strain rate ($\boldsymbol{\nabla} \cdot \mathbf{v}$). Analogously to Eq. (3.3) for the solid domain, Eq. (3.14) is the constitutive equation for the fluid medium. That is, it relates stresses with deformation rates of fluid particles.

Plugging the constitutive relation Eq. (3.14) into the Cauchy equation Eq. (3.13), we obtain the conservation of linear momentum for a Newtonian fluid, commonly known as Navier-Stokes equations

$$\rho \frac{\mathrm{D}\mathbf{v}}{\mathrm{D}t} = -\boldsymbol{\nabla} p + \rho \mathbf{b} + \boldsymbol{\nabla} \cdot \left[\mu \left(\boldsymbol{\nabla}\mathbf{v} + \boldsymbol{\nabla}\mathbf{v}^T \right) + \left(\mu_\nu - \frac{2}{3}\mu \right) \left(\boldsymbol{\nabla} \cdot \mathbf{v} \right) \boldsymbol{\delta} \right]. \tag{3.15}$$

The conservation of energy is also needed to describe compressible flows, being directly derived from the first law of thermodynamics. One way to write it is given by Eq. (3.16)

$$\frac{\mathrm{D}e}{\mathrm{D}t} = -p \frac{\mathrm{D}}{\mathrm{D}t} \left(\frac{1}{\rho} \right) + \frac{1}{\rho} \boldsymbol{\sigma} : \mathbf{d} - \frac{1}{\rho} \boldsymbol{\nabla} \cdot \mathbf{q}, \tag{3.16}$$

where e is the internal energy per unit mass and $\mathbf{q}$ is the heat flux vector[2]. The symmetric part of the velocity gradient tensor is

[2]The heat flux is usually expanded by the Fourier's law as $\mathbf{q} = -k\boldsymbol{\nabla}T$, for heat conductivity k and temperature T.

given by $\mathbf{d} = \frac{1}{2}\left(\boldsymbol{\nabla}\mathbf{v} + \boldsymbol{\nabla}\mathbf{v}^T\right)$. The double contraction represented by $\boldsymbol{\sigma} : \mathbf{d}$ is known as stress power (per unit volume), and is directly related to the kinetic energy dissipation per unit mass, given by $\varepsilon = \frac{1}{\rho}\boldsymbol{\sigma} : \mathbf{d}$.

The kinetic energy dissipation ε also appears in the entropy equation. It is derived from Eq. (3.16) and is given here for completeness by Eq. (3.17)

$$\frac{\mathrm{D}s}{\mathrm{D}t} = -\frac{1}{\rho T}\boldsymbol{\nabla}\cdot\mathbf{q} + \frac{\varepsilon}{T} = \frac{1}{\rho}\boldsymbol{\nabla}\cdot\left(\frac{k}{T}\boldsymbol{\nabla}T\right) + \frac{k}{\rho T^2}\left(\boldsymbol{\nabla}T\right)^2 + \frac{\varepsilon}{T}, \quad (3.17)$$

where s and T stand respectively for the fluid entropy and temperature. It is clear from Eq. (3.17) that an increase in entropy is directly related to heat transfer and how much kinetic energy is dissipated, including by viscous means.

The second law of thermodynamics does not have to be explicitly included in computations, since requiring the heat conductivity k, the dynamic viscosity μ and the volumetric viscosity μ_ν to be non-negative suffices to ensure that the entropy given by Eq. (3.17) never decreases (for a closed system).

Additionally, a state equation relating pressure and density is also necessary for closure. A typical model is the ideal gas relation, given by Eq. (3.18)

$$p = \rho R T, \quad (3.18)$$

where R is the specific gas constant. With the mass, momentum and energy conservation equations (Eqs. (3.12), (3.15) and (3.16)), and a state equation (Eq. (3.18)), closure is obtained, and all fluid variables can be (theoretically) computed, in the presence of suitable boundary conditions.

3.1.2.1 Special forms of equations

A couple of special cases are worth mentioning briefly. In case of low flow velocities (usually taken as Ma < 0.3), the flow is said to be incompressible. In this case, the fluid density does not

change with pressure[3], that is,

$$\frac{\mathrm{D}\rho}{\mathrm{D}t} = 0 \Rightarrow \boldsymbol{\nabla} \cdot \mathbf{v} = 0. \tag{3.19}$$

The last result was obtained by plugging the incompressibility relation into the mass continuity Eq. (3.12). That is, for incompressible flows, no infinitesimal compression or expansion of fluid particles takes place. Indeed, it is not possible to determine an absolute pressure for incompressible fluids, only its gradients. Plugging Eq. (3.19) into the Navier-Stokes Eq. (3.15), we obtain their incompressible version

$$\rho \frac{\mathrm{D}\mathbf{v}}{\mathrm{D}t} = -\boldsymbol{\nabla} p + \rho \mathbf{b} + \boldsymbol{\nabla} \cdot \left(\mu \left(\boldsymbol{\nabla} \mathbf{v} + \boldsymbol{\nabla} \mathbf{v}^T \right) \right). \tag{3.20}$$

Finally, when viscous effects are negligible, the Navier-Stokes Eq. (3.15) reduces to the Euler Eq. (3.21)

$$\rho \frac{\mathrm{D}\mathbf{v}}{\mathrm{D}t} = -\boldsymbol{\nabla} p + \rho \mathbf{b}. \tag{3.21}$$

In fact, under the conditions leading to Eq. (3.21), there is no further need to solve the conservation of energy. This happens because for inviscid, incompressible flows, the internal energy is constant along every flow line, making the computation less expensive than compressible, viscid cases.

3.1.2.2 Acoustics

Another relevant fluid dynamics domain is the field of acoustics. Only a couple of comments will be made about it in this section.

The main relation representing the propagation of acoustic waves in a medium can be derived by a linearization of the mass (Eq. (3.12)) and Euler (Eq. (3.21)) equations. The final result is the wave equation of second order, given by Eq. (3.22)

$$\boldsymbol{\nabla}^2 p' - \left(\frac{1}{c^2} \right) \frac{\partial^2 p'}{\partial t^2} = 0, \tag{3.22}$$

[3]That does not necessarily mean that $\rho = constant$ in the entire spatial domain (which would still be a particular but not the general solution of $\frac{\mathrm{D}\rho}{\mathrm{D}t} = 0$).

where p' represent pressure fluctuations around a reference pressure value. The constant c is the wave propagation speed (termed speed of sound), obtained by Eq. (3.23)

$$c^2 = \left(\frac{\partial p}{\partial \rho}\right)_s , \tag{3.23}$$

where the subscript s indicates an isentropic process. Equation (3.22) is a hyperbolic equation on the pressure fluctuations p', meaning that, if a disturbance is introduced in the system, not all points in space experience it at the same time. Indeed, the disturbances propagate with fixed speed given by Eq. (3.23).

Note that for incompressible flows, (Eqs. (3.19) and (3.20)), the density does not vary with changes in pressure; according to Eq. (3.23), that implies a speed of sound tending to infinity. Finally, although not shown here, acoustic damping may be included in the wave equation, usually proportional to variations of pressure in time, i.e., $\frac{\partial p'}{\partial t}$.

3.1.2.3 Turbulence

Up to now, no consideration of turbulence has been made when deriving the fluid domain equations. They are indeed valid for laminar and turbulent flows, and if solved with enough discretization precision, no turbulence modeling would be necessary. The main issue is the computational cost needed to solve all relevant spatial and temporal scales, which rapidly exceeds modern processing power for most practical problems.

The study of turbulence is a highly complex field in itself, being out of the present scope to theoretically discuss it in depth. However, since almost all macroscopic flows in nature are turbulent, the development and use of adequate models are highly important. Some comments will be made about turbulent phenomena in general, and how they relate to the equations derived until now. Section 3.2.2.4 will present the numerical implementation of turbulence models, particularly those suitable for turbomachinery. For a broader overview, see e.g. [74, 75].

Turbulence is in general associated with high enough Reynolds numbers. Fluid flows are called laminar due to the fact the flow layers do not mix with each other and are well organized. Once the Reynolds number reaches a so-called transition range, complex eddy behavior ensues, and further increase in the Reynolds number implies a fully-turbulent regime.

According to [72], in contrast to laminar flows, the main characteristics of turbulent regimes are: (i) the presence of fluctuations (even when boundary conditions are steady); (ii) nonlinearity; (iii) constant change in vorticity ($\boldsymbol{\nabla} \times \mathbf{v}$), manifested in identifiable coherent structures, called eddies; (iv) dissipation of kinetic energy through viscosity, vortex stretching being responsible for the energy and vorticity transfer from higher to smaller spatial scales; (v) high diffusivity of species, momentum and heat, yielding large mixing rates.

Employing statistical tools, turbulence is typically modeled by computing mean state variables and their respective deviations. For example, a time-dependent, fluctuating pressure p is decomposed as $p = \bar{p} + p'$, where $\bar{p}$ stands for the mean pressure, and p' represents the unsteady pressure variation (with zero mean). Performing the same decomposition for other flow variables and then plugging them into the instantaneous conservation equations derived in section 3.1.2, and finally averaging, a new system of equations for mean quantities arises. This process is known as "Reynolds averaging".

The most relevant difference between the instantaneous and the Reynolds averaged equations is the presence of the so-called Reynolds stresses, given by $\boldsymbol{\tau}^R \triangleq \rho\, \mathbf{v}' \otimes \mathbf{v}'$. This correlation tensor consists in a new set of unknowns, not present in the original instantaneous equations. The challenge now becomes solving the problem including these second order correlations. Each of the second order correlation components would theoretically have its own conservation equation, involving third order correlations. Each of the third order correlation components would then require fourth order correlations, and so on. This is known as the closure problem in turbulence.

One approach to deal with this issue is the Reynolds-averaged Navier–Stokes (RANS) closure modeling. It works by stopping this endless equation cascade at some point and employing numerical and experimental models to determine the Reynolds stresses. These approximating models, although consciously neglecting some of the spatial scales of the problem, have produced fairly reliable results when compared with experiments for most engineering applications.

Another approach would be to directly solve the time-dependent conservation equations in very fine spatial and temporal scales and only afterwards perform the Reynolds averaging. This computationally expensive technique is known as direct numerical simulation. Other approaches falling between RANS modeling and direct numerical simulation exist, such as large eddy simulations, which explicitly solves the flow field up to certain physical scales and models the smallest eddies with sub-grid scale models.

3.1.3 Fluid-structure interaction

The equations modeling the solid and fluid domains have been described in detail in sections 3.1.1 and 3.1.2. The key question for aeroelastic analyses is how these media interplay, in the field known as fluid-structure interaction (FSI).

The interface between fluid and solid domains must obey two compatibility conditions, namely

i. Kinematic constraint:

$$\mathbf{v} = \frac{\partial \mathbf{u}}{\partial t} \tag{3.24}$$

ii. Dynamic constraint:

$$\boldsymbol{\sigma}_f \cdot \mathbf{n} = \boldsymbol{\sigma}_s \cdot \mathbf{n} \tag{3.25}$$

where, as usual, $\mathbf{v}$ stands for the fluid velocity and $\mathbf{u}$ for the solid displacement. The stress tensors $\boldsymbol{\sigma}_f$ and $\boldsymbol{\sigma}_s$ are given respectively by Eqs. (3.14) and (3.3). $\mathbf{n}$ is the vector normal to the FSI interface.

The kinematic constraint given by Eq. (3.24) corresponds to the Dirichlet type of boundary conditions previously discussed (Γ_1 in section 3.1.1). It ensures that no slip and no penetration takes place between domains. That is, both independent boundaries should produce the same displacements and velocities at all times.

The dynamic constraint given by Eq. (3.25) on the other hand corresponds to the Neumann type of boundary conditions (Γ_2 in section 3.1.1). It ensures that the fluid and solid forces match at the common interface, with opposite sign. Both pressure and viscous forces are contained in the fluid stress tensor $\boldsymbol{\sigma}_s$.

When considering domains described in different reference frames (such as in the current case, with Lagrangian solid and Eulerian fluid descriptions), mixed formulations are employed to match the equations. For example, in the Arbitrary Lagrangian-Eulerian (ALE) approach, both the observer and the reference frame can move arbitrarily [76]. To illustrate this effect on the equations, the total time derivative described by Eq. (3.11) in the Eulerian frame can be written in the ALE referential as

$$\frac{\mathrm{D}\mathbf{f}}{\mathrm{D}t} = \frac{\partial \mathbf{f}}{\partial t} + (\mathbf{v} - \mathbf{v}_g) \cdot \boldsymbol{\nabla}\mathbf{f} = \frac{\partial \mathbf{f}}{\partial t} + \mathbf{v}_c \cdot \boldsymbol{\nabla}\mathbf{f}, \tag{3.26}$$

where $\mathbf{v}_g$ stands for the grid velocity and $\mathbf{v}_c = \mathbf{v} - \mathbf{v}_g$ for the convective velocity. Note that if $\mathbf{v}_g = 0$, Eq. (3.11) is recovered for an Eulerian approach; conversely, if $\mathbf{v}_c = 0$, the simple Lagrangian frame derivative is obtained. All transport equations may be written in the ALE formulation, when boundary motion is relevant for the problem.

More comments about how to model coupled fluid and solid domains numerically and the challenges that arise from it will be given in section 3.2.3.

3.2 Numerical approach

This section will provide the numerical models employed in this work to solve the solid and fluid domains. These models represent the state of the art for turbomachinery simulation and bear wide acceptance in industry and academia. This does not mean that these methods are universally optimal for all problems, while other existing numerical approaches may be more or less suitable from case to case.

The general numerical models will be initially described, followed by specific analysis approaches in computational solid mechanics and fluid dynamics.

3.2.1 Computational solid mechanics

As mentioned in section 3.1.1, the structure is modeled here in the Lagrangian reference frame. Additionally, a variational formulation is employed, minimizing an error functional with the help of weight functions. Several approaches may be obtained with a variational technique, but the one employed in this work is the finite element method (FEM), more specifically in its Galerkin formulation. Mathematical descriptions of the FEM are given in detail by, e.g., [77], while a solid mechanics approach is presented by [78, 79]. The solver employed for the structural computations and solid meshing is Ansys Mechanical version 19.2 [80].

The FEM approach starts from the Cauchy relation given by Eq. (3.2) with viscous damping included

$$\rho \frac{\partial^2 \mathbf{u}}{\partial t^2} + \xi \frac{\partial \mathbf{u}}{\partial t} - \rho \mathbf{b} = \boldsymbol{\nabla} \cdot \boldsymbol{\sigma}. \tag{3.27}$$

Subsequently, to obtain the weak form of Eq. (3.27), we multiply it by a weight function $\mathbf{w} = \mathbf{w}(\mathbf{X})$ and integrate over the spatial domain Ω. Then, employing Green's first identity, we obtain

$$\int_\Omega \boldsymbol{\sigma} : \boldsymbol{\nabla} \mathbf{w} \, d\Omega + \int_\Omega \left(\rho \frac{\partial^2 \mathbf{u}}{\partial t^2} + \xi \frac{\partial \mathbf{u}}{\partial t} - \rho \mathbf{b} \right) \cdot \mathbf{w} \, d\Omega = \int_{\Gamma_2} \boldsymbol{\tau}_n \cdot \mathbf{w} \, d\Gamma, \tag{3.28}$$

where both domain (Ω) and boundary (Γ) integrals are present. $\boldsymbol{\tau}_n = \boldsymbol{\sigma} \cdot \mathbf{n}$ are the traction forces normal to the boundary. One notices that only Γ_2 is present as a boundary integral in Eq. (3.28), since, by construction of the Galerkin FEM, the residuals $\mathbf{w}$ vanish on Dirichlet boundaries (Γ_1). If all terms in Eq. (3.28) are sent to the LHS, we obtain the typical averaged weighted-residual Galerkin form.

The solution candidates for $\mathbf{u}$ are approximated as linear combinations of shape (or basis) functions $\mathbf{N} = \mathbf{N}(\mathbf{X})$ as in Eq. (3.29)[4]

$$\mathbf{u}(\mathbf{X}, t) \approx \mathbf{N}(\mathbf{X})^T \mathbf{U}(t), \tag{3.29}$$

where the vector $\mathbf{U}$ contains the temporal coefficients multiplying the shape functions $\mathbf{N}$. Additionally, the Galerkin approach employs the same expressions to compute both the weight and trial functions (respectively the arrays $\mathbf{N}$ and $\mathbf{U}$). Plugging the approximation from Eq. (3.29) into the weighted residuals Eq. (3.28) and reorganizing the terms, we obtain the system dynamics equation, written in matrix form as:

$$\mathbf{M}\ddot{\mathbf{U}} + \mathbf{C}\dot{\mathbf{U}} + \mathbf{K}\mathbf{U} = \mathbf{F}. \tag{3.30}$$

Here, $\mathbf{M}$, $\mathbf{C}$ and $\mathbf{K}$ stand respectively for the mass, damping and stiffness matrices. The vector $\mathbf{F}$ stands for the forcing, while the dots over the displacement $\mathbf{U}$ indicate time derivative in Newton's notation ($\dot{\mathbf{U}} \triangleq \partial \mathbf{U}/\partial t$, $\ddot{\mathbf{U}} \triangleq \partial^2 \mathbf{U}/\partial t^2$ and so on). Note the direct similarity with the dynamics equation for the SDOF system (Eq. (2.6) in chapter 2).

[4]Since this and the following equations in this section are directly implementable in a numerical code, they are written in classic matrix multiplication notation.

The matrices displayed in Eq. (3.30) are given by

$$\mathbf{M} = \bigcup_e \int_{\Omega_e} \mathbf{N}\, \rho\, \mathbf{N}^T \, d\Omega, \tag{3.31a}$$

$$\mathbf{C} = \bigcup_e \int_{\Omega_e} \mathbf{N}\, \xi\, \mathbf{N}^T \, d\Omega, \tag{3.31b}$$

$$\mathbf{K} = \bigcup_e \int_{\Omega_e} \mathbf{B}\, \mathbf{D}\, \mathbf{B}^T \, d\Omega, \tag{3.31c}$$

$$\mathbf{F} = \bigcup_e \left(\int_{\Gamma_e} \mathbf{N}\, \boldsymbol{\tau}_n \, d\Gamma + \int_{\Omega_e} \rho\, \mathbf{N}\, \mathbf{b}\, d\Omega \right), \tag{3.31d}$$

where **B** stands for the deformation matrix and **D** for the elasticity matrix. The symbol $\bigcup_e$ indicates the assembly procedure, where matrices constructed for each finite element are clustered in the global system. These integrals are in general performed numerically, so that even complex, high-order analytical expressions for the shape functions are easily computed. General information about the assembly process can be found, e.g., at [78, 81].

The shape functions contained in matrix **N** are organized as

$$\mathbf{N}^T = \begin{bmatrix} N_1 & 0 & 0 & N_2 & 0 & 0 & \cdots & N_J & 0 & 0 \\ 0 & N_1 & 0 & 0 & N_2 & 0 & \cdots & 0 & N_J & 0 \\ 0 & 0 & N_1 & 0 & 0 & N_2 & \cdots & 0 & 0 & N_J \end{bmatrix}, \tag{3.32}$$

for a 3D finite element with J nodes. The functions N_j, $j = 1, \cdots, J$ are constructed as linearly independent from each other. The deformation matrix **B** is obtained by operating with derivatives on the shape functions according to

$$\mathbf{B}^T = \begin{bmatrix} \partial/\partial x & 0 & 0 \\ 0 & \partial/\partial y & 0 \\ 0 & 0 & \partial/\partial z \\ 0 & \partial/\partial z & \partial/\partial y \\ \partial/\partial z & 0 & \partial/\partial x \\ \partial/\partial y & \partial/\partial x & 0 \end{bmatrix} \mathbf{N}. \tag{3.33}$$

Finally, the elasticity matrix **D** relating stresses and strains for an isotropic material is given (in Voigt notation) by Eq. (3.34)

$$\mathbf{D} = \frac{E}{d} \begin{bmatrix} (1-\nu) & \nu & \nu & 0 & 0 & 0 \\ \nu & (1-\nu) & \nu & 0 & 0 & 0 \\ \nu & \nu & (1-\nu) & 0 & 0 & 0 \\ 0 & 0 & 0 & \frac{(1-2\nu)}{2} & 0 & 0 \\ 0 & 0 & 0 & 0 & \frac{(1-2\nu)}{2} & 0 \\ 0 & 0 & 0 & 0 & 0 & \frac{(1-2\nu)}{2} \end{bmatrix}, \tag{3.34}$$

where $d = (1+\nu)(1-2\nu)$. Then, we have

$$\boldsymbol{\sigma} = \mathbf{D}\,\boldsymbol{\varepsilon} \Rightarrow \begin{bmatrix} \sigma_{xx} \\ \sigma_{yy} \\ \sigma_{zz} \\ \tau_{xy} \\ \tau_{yz} \\ \tau_{zx} \end{bmatrix} = \mathbf{D} \begin{bmatrix} \varepsilon_{xx} \\ \varepsilon_{yy} \\ \varepsilon_{zz} \\ \gamma_{xy} \\ \gamma_{yz} \\ \gamma_{zx} \end{bmatrix}, \tag{3.35}$$

where σ stands for normal stress and τ for shear stress. Similarly, normal strain is given by ε and shear strain by γ.

Figure 3.1 shows a sample rotor blade modeled with finite elements. Although only one type of element was employed

(namely 10-node tetrahedron), combinations are possible, with adequate treatment on boundaries between different types of elements. Additionally, high-order elements may include more internal nodes to accommodate more complex shape functions, demanding naturally more memory and computation time.

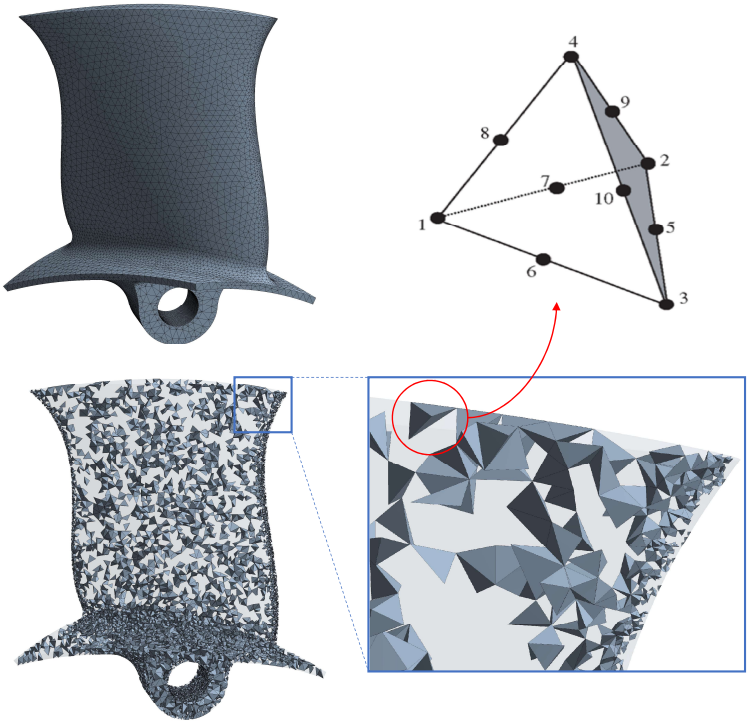

Figure 3.1: Sample rotor blade modeled with finite elements. Top left: elements outer surface; bottom left: selected 3D elements; bottom right: zoom on blade tip; Top right: diagram of a 10-node tetrahedron element.

3.2.1.1 Static analysis

Static analyses do not take transient or unsteady phenomena in consideration. Referring back to Eq. (3.30), it simplifies to

$$\mathbf{KU} = \mathbf{F}. \tag{3.36}$$

Several different types of load may be included in the RHS of Eq. (3.36), such as gravity, pressure or thermal. In turbomachinery applications, typical static analyses take into account mean flow loads and centrifugal loads (such as rotational velocity for rotors).

The results obtained from static analyses correspond to the static loads in failure assessments. For example, in Fig. 2.9, the static stresses would be indicated in the horizontal axis. Even when static loads in a component are far enough from static limits, the presence of alternating loads actually reduces the safety margins considerably. That is, for the aeroelastic designer, high static loads decreases the tolerable dynamic load range. However, the static loads usually stem from aerodynamic design, with modern trends towards high mean pressure and rotational speed.

3.2.1.2 Modal analysis

Modal analyses are key to determine inherent characteristics of dynamic systems, including natural frequencies and modes. The multiple-degree-of-freedom system in the time domain is transformed into the frequency domain by assuming that the whole structure vibrates harmonically with a constant angular frequency ω for each mode. This is accomplished by considering, without loss of generality, that

$$\mathbf{U} = \boldsymbol{\phi}\, e^{i\omega t}, \tag{3.37}$$

where the vector $\boldsymbol{\phi}$ contains the so-called mode shapes or natural modes of the structure. The result obtained by plugging Eq. (3.37) into the unforced and undamped[5] version of Eq. (3.30), ignoring trivial solutions, is given by

$$\left(\mathbf{K} - \omega^2 \mathbf{M}\right) \boldsymbol{\phi} = \mathbf{0}. \tag{3.38}$$

This turns out to be a generalized eigenvalue problem, with eigenvalue ω^2 and eigenvector $\boldsymbol{\phi}$. As will be showed later, these

[5]This procedure generates the so-called undamped eigenvectors. If damping is retained, it is still possible to find eigenvalues, which in the general case becomes complex variables. The dynamic system becomes then coupled. The

eigenvectors may also be used to reduce the order of the system, both in harmonic and transient analysis (sections 3.2.1.3 and 3.2.1.4).

As an illustration, the modal displacement of the first three natural modes of a rotor blade is shown in Fig. 3.2. Mode 1 is a typical bending mode, while mode 2 indicates blade torsion. For high-order modes such as number 3, and especially for 3D blade designs, mixed patterns often occur, where a clear mode designation becomes impractical.

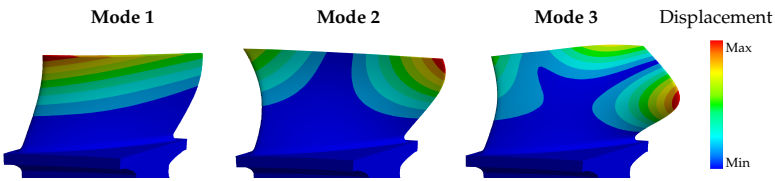

Figure 3.2: Sample rotor natural modes from modal analyses.

Since Eq. (3.38) can always be multiplied by a real constant without changes in the eigenvalue, every multiple of an eigenvector ϕ is also an eigenvector. Therefore, there is no unique way to present mode shapes of a structure. A typical way they are exhibited is normalized by the mass matrix, so that

$$\phi^T \mathbf{M} \phi = 1. \tag{3.39}$$

As previously discussed in section 2.2.1.1, when solving the eigenvalue problem for rotationally periodic structures, paired or repeated eigenvalues/eigenvectors arise. They represent the same spatial form, but with a phase difference. Therefore, two paired modes may also be understood as a complex mode with amplitude and phase. This leads to the concept of traveling waves discussed beforehand, which consist in nothing more than a pair of eigenvectors with the same eigenvalue. Algorithms to efficiently compute the eigenvalue decomposition of a rotationally periodic structure are readily available, and are not

two main models when computing eigenvectors including damping are the viscous and the structural [82]. They will not be discussed in detail here.

discussed in detail here (see, e.g., [83]). A modal analysis example for a structure with rotational periodicity is contained in the interference diagram for a blisk in Fig. 2.5, where the mode families refer to eigenvectors linked to the same blade mode shape.

3.2.1.3 Harmonic analysis

A harmonic analysis is a linear frequency-domain approach, in which all loads and displacements of a structure vary at the same known frequency, but not necessarily in phase. It starts from an assumption similar to Eq. (3.37), now including a phase angle θ for the displacement, such as

$$\mathbf{U} = \left(\mathbf{u}_{max}\, e^{i\theta}\right) e^{i\omega t}, \tag{3.40}$$

where $\mathbf{u}_{max}$ is the maximum displacement (amplitude) vector. A corresponding relation is given for the load vector, with the same temporal frequency ω, however with a different phase angle ψ, so that

$$\mathbf{F} = \left(\check{\mathbf{F}}\, e^{i\psi}\right) e^{i\omega t}, \tag{3.41}$$

where $\check{\mathbf{F}}$ is the vector of force modal amplitudes. Plugging Eqs. (3.40) and (3.41) into the dynamics Eq. (3.30) and simplifying, we obtain

$$\left(-\omega^2\mathbf{M} + i\omega\mathbf{C} + \mathbf{K}\right) \boldsymbol{\phi}\, e^{i\theta} = \check{\mathbf{F}}\, e^{i\psi}. \tag{3.42}$$

Equation (3.42) is indeed a complex system (due to the phase angles), which can also be subdivided into real and imaginary parts. Since in general the maximum amplitude and stresses are sought, a phase sweep on θ (or ψ) is common practice. Additionally, the phase angle at which the load lags the response is $\phi - \psi$.

A typical and very convenient approach in harmonic analyses is to reduce the model order by employing only a subset of the available natural modes. In this context, reduced order means that instead of directly solving the large system conveyed by

Eq. (3.42), only a few equations are considered. This is accomplished by properly selecting some of the natural modes ϕ previously obtained in the eigenvalue decomposition. Subsequently, a linear combination of the individual contribution of each of the selected modes provides the final displacement, velocity and so forth. This procedure is named here mode-superposition analysis. In general, the lower frequencies contain most of the vibration energy and represent the most relevant dynamics. That is, employing only the first natural modes is usually enough for precise results with considerably less computational resources. Additionally, several algorithms to extract a subset of eigenvalues optimally are available (see, e.g., [84]).

The number of modes to choose to span the solution space should ensure that frequencies relevant to the problem are present. Typically, one should include natural frequencies of at least one and a half times the maximum external forcing frequency [80]. Additional indexes may also be employed, such as the modal participation factor or the cumulative mass fraction. They will not be discussed in detail here, but have been duly considered in the computations to ensure reliable and accurate results.

3.2.1.4 Transient analysis

It is also possible to solve the dynamic system posed by Eq. (3.30) directly in the time domain. Indeed, Eq. (3.30) is numerically constructed for a single time step, here denoted[6] with a superscript n, so that

$$\mathbf{M}\ddot{\mathbf{U}}^n + \mathbf{C}\dot{\mathbf{U}}^n + \mathbf{K}\mathbf{U}^n = \mathbf{F}^n. \tag{3.43}$$

The next step is to choose an adequate time march, which approximates the time derivatives in Eq. (3.43). Since transient analysis modeling is not the primary focus of this work, no involved description of time discretization schemes will be

[6] Employing a superscript as time step notation is typical in solid mechanics. The superscript n does *not* indicate the nth power of a matrix when referring to transient analyses.

presented, but only a few comments, which will also be valuable for section 3.2.2. To illustrate, the central difference method employs the finite difference approximations

$$\ddot{\mathbf{U}}^n \approx \frac{1}{\Delta t^2}\left(\mathbf{U}^{n-1} - 2\mathbf{U}^n + \mathbf{U}^{n+1}\right), \tag{3.44a}$$

$$\dot{\mathbf{U}}^n \approx \frac{1}{2\Delta t}\left(-\mathbf{U}^{n-1} + \mathbf{U}^{n+1}\right), \tag{3.44b}$$

where $\Delta t = t^n - t^{n-1}$ is the time step employed. Plugging these approximations into Eq. (3.43), we obtain the recursive numerical form

$$\widehat{\mathbf{M}}\mathbf{U}^{n+1} = \widehat{\mathbf{F}}^n, \tag{3.45}$$

with effective mass matrix $\widehat{\mathbf{M}}$ and effective load vector $\widehat{\mathbf{F}}$ given by

$$\widehat{\mathbf{M}} = \left(\frac{1}{\Delta t^2}\mathbf{M} + \frac{1}{2\Delta t}\mathbf{C}\right), \tag{3.46a}$$

$$\widehat{\mathbf{F}}^n = \mathbf{F}^n + \left(\frac{2}{\Delta t^2}\mathbf{M} - \mathbf{K}\right)\mathbf{U}^n - \left(\frac{1}{\Delta t^2}\mathbf{M} - \frac{1}{2\Delta t}\mathbf{C}\right)\mathbf{U}^{n-1}. \tag{3.46b}$$

Equation (3.45) allows computing the displacement $\mathbf{U}^{n+1}$ considering only the information already available from the last time steps $\mathbf{U}^n$, $\mathbf{U}^{n-1}$ and $\mathbf{F}^n$. Time marches may be classified into explicit and implicit according to how the effective mass matrix $\widehat{\mathbf{M}}$ is constructed. Explicit time marches are the ones where the stiffness matrix $\mathbf{K}$ is not present on the LHS of the recursive form (Eq. (3.45)), so that the effective mass matrix can be made diagonal by condensing the terms properly. This diagonalization decouples all degrees of freedom, so that no full inversion of $\widehat{\mathbf{M}}$ is needed to advance the time steps. However, explicit time marches are in general conditionally stable, meaning that a large enough Δt makes the solution unstable (blow up) and invalid[7].

[7]For completeness, the central difference method illustrated here is stable when the time step is chosen so that $\Delta t < \Delta t_{crit} = 2/\omega_{max}$, where ω_{max} is the maximum natural frequency of all finite elements present in the mesh [78].

On the other hand, implicit time marches can be constructed as being unconditionally stable, that is, feasible irrespective of the Δt choice. This is a great advantage for the general user, who does not have to worry about numerical instability (at least due to the time discretization). Implicit marches require, however, at least one full matrix inversion at every time step. Some of the most common implicit integration techniques employed in elastodynamics are the Newmark [85] and the generalized alpha [86] methods. More complex approaches aiming at optimally reduce undesired (often termed "spurious") numerical oscillations are also available, both in explicit and implicit forms (see, e.g., [87]).

Discretization schemes also possess an accuracy order, in both time and space. It is related to the precision with which the discretization solves the equations. If a scheme is said to be of order $\mathcal{O}(\Delta t^p)$ accurate in time, it means that changes in the numerical error vary with power p of the time step Δt. For example, for $\mathcal{O}(\Delta t^2)$, halving the time step produces errors which are four times smaller.

In summary, transient analyses make no a priori linear approximation to the dynamics problem and are able to model complex unsteady phenomena. However, they come with their own hurdles, such as high processing and memory costs, initialization challenges and the possible presence of numerical, non-physical oscillations. Just like for harmonic analyses (section 3.2.1.3), transient computations can also be carried out in a subspace spanned by the structure eigenvectors. Mode superposition may then be a good strategy to perform unsteady simulations in feasible computation time. Nonetheless, the computational resources needed are still much higher than when performing harmonic analyses.

3.2.2 Computational fluid dynamics

The discretization employed for the fluid domain is the finite volume method. It is based on the integral form of the transport equations presented in section 3.1.2, which are enforced on a local

level, namely on finite volumes. Simply described, these units consider averaged values of the solution within each local cell. Additionally, finite-element shape functions are also used when approximating the solution at integration points and calculating gradients. The solver employed for the fluid dynamics computations is Ansys CFX version 19.2 [80].

Each of the terms present in the transport equations (advection, diffusion, gradients, transient) requires specific discretization techniques. Their mathematical description will not be shown here in detail, except for a couple of practical comments. The main types of CFD simulations employed in this work will be described in the following sections.

3.2.2.1 Steady state

Steady state solutions are desired when transient phenomena are unimportant. In turbomachinery, they are often used to obtain performance maps, as well as mean state quantities, such as flow profiles or pressure distributions. They are also employed as initial conditions for transient simulations.

The discretization of the advection terms ($\mathbf{v} \cdot \nabla \mathbf{f}$) in the conservation equations is solved with a blended scheme. This approach combines the robustness of the first-order upwind scheme close to steep gradients, with second-order accuracy of the central difference scheme in other regions (see, e.g., [88]). With that, the blending scheme avoids artificial diffusion and non-physical oscillations in the solution.

Although steady state solutions have no time dependency, they are typically solved with a pseudo time march, so to accelerate convergence. All steady state computations in this work are performed so that high numerical accuracy is obtained. That means specifically double machine precision, imbalances of at most $5 \cdot 10^{-6}$ for the conservation equations and root-mean-square residuals always less than 10^{-5}.

The software employed in this work to obtain the turbomachinery grids is AutoGrid5 version 13.1, developed by Numeca [89]. Multi-block, structured hexaedra meshes are

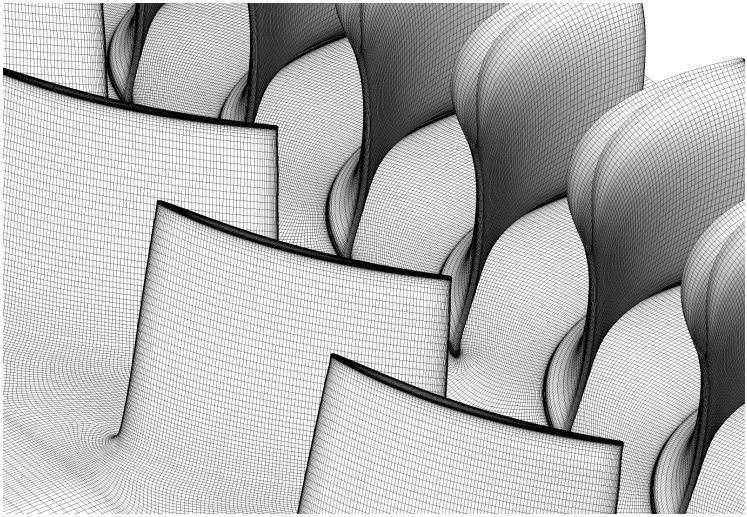

Figure 3.3: Sample CFD grid with rotor and stator, with surface of finite volumes visible.

generated, with blade-to-blade topology O4H. A sample mesh for a stage is shown in Fig. 3.3, where edges of the finite volumes on solid surfaces are drawn with black lines.

A relevant aspect when simulating viscid flow is the modeling of boundary layers. Although other types of boundary layers exist (such as thermal or species concentration), we will concentrate the analyses on the velocity field. Due to high velocity gradients close to walls, adequate treatment of flow quantities and grid generation in these areas is critical. Following Fig. 3.4, multiple experiments, mostly based on Couette flows, have assessed the relation between the normalized velocity parallel to smooth walls (U^+) and its normal distance to the wall (y^+).

Three specific regions in Fig. 3.4 are of interest: (i) the viscous sublayer, where $y^+ < 5$ and the shear stress is approximately constant; (ii) a transition or buffer layer, roughly for $5 < y^+ < 30$; (iii) the log-law layer, for $y^+ > 30$, where the following empirical relation is generally employed

$$U^+ = \frac{1}{\kappa}\ln(E\,y^+), \tag{3.47}$$

where the von-Kármán coefficient $\kappa \approx 0.4$ and $E \approx 9.8$ are constants for turbulent flows past smooth walls [90].

Customarily in CFD, two approaches are employed concerning boundary layer flow. The first one requires no detailed grid modeling of the boundary layer, the velocity close to the walls being bridged with functions such as Eq. (3.47). For that, the first grid cell should be located in the log-law layer; placing it in the buffer layer hinders the solution's quality, since no reliable model is available for this region. It is clear that this strategy saves memory and processing resources by reducing the size and complexity of the numerical domain.

In the second approach, the boundary layer is solved in detail and no direct correction must be applied. It comes, however, with higher computational efforts and meshing requirements such as

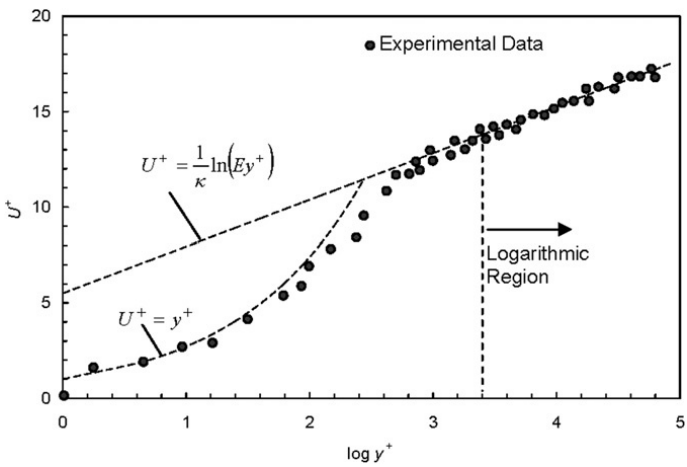

Figure 3.4: Turbulent boundary layer and models for flows close to smooth walls. U^+ and y^+ are respectively the normalized velocity parallel to the wall and the normal distance to the wall. Here, $U^+ = U/u_\tau$ and $y^+ = y\rho u_\tau/\mu$, with the wall friction velocity given by $u_\tau = \sqrt{\tau_w/\rho}$, for wall shear stress τ_w [90].

an adequate amount of near-wall cells, a small expansion ratio etc. Here, the first cell should be located in the viscous sublayer, with a good-practice nondimensional wall distance of $y^+ \approx 2$ or less. All simulations performed in this work model all boundary layers in detail, in order to obtain high-quality results especially when extracting wall loads for aeroelastic analyses.

3.2.2.2 Transient analysis

The time march employed in the fluid solver is a combination of second and first order backward Euler methods. Both schemes are implicit, unconditionally stable and conservative in time. That means that no discretization parameter (such as the CFL number [91]) must be explicitly constrained to ensure stability. Second order backwards Euler is employed most of the time for higher accuracy. However, since it is not monotonic, variables that must remain bounded, such as turbulent quantities, are solved with the first order discretization.

Similarly to the discussion leading to the recursive form for time marches in the solid domain, an analogous relation to Eq. (3.45) is obtained for the fluid, based on the transient conservation equations derived in section 3.1.2. This relation is encapsulated by

$$\mathbf{AX} = \mathbf{b}, \tag{3.48}$$

where $\mathbf{X}$ contains the fluid independent state variables, $\mathbf{A}$ is the coefficient matrix and $\mathbf{b}$ a load vector. The solver employed in this work is a coupled solver, meaning that Eq. (3.48) is directly solved employing matrix factorization techniques. This direct approach contrasts with segregated solvers, which initially solve, e.g., the momentum equations with a guessed pressure, whose value is then corrected in a second computation step. Segregated solvers require substantially more iterations to achieve final convergence than coupled methods.

3.2.2.3 Fourier transformation and nonlinear harmonic balance

When a specific known frequency is present in a turbomachinery problem (such as blade passing or vibration), the Fourier transformation[8] and the nonlinear harmonic balance (NHB) methods may be employed to reduce computational efforts significantly. They allow not only the modeling of fewer passages (sometimes only two, instead of the whole annulus), but also a substantial reduction in convergence time.

The Fourier transformation "time-domain" approach for turbomachinery employed in this work is based on the method proposed by [92]. It assumes a harmonic variation of the flow quantities on the periodic boundaries of the modeled blade/vane sector. Afterwards, an update procedure is carried out at every time step, until Fourier convergence in these periodic boundaries is achieved. Extensions of the technique for multiple disturbances with uncorrelated frequencies were presented by [93, 94], among others.

Differently from the Fourier transformation, the NHB works in the frequency domain. [95] developed the first application of the NHB method for oscillating blades, decomposing the flow as

$$\mathbf{X} = \bar{\mathbf{X}} + \mathbf{X}', \tag{3.49}$$

where the vector with independent variables $\mathbf{X}$ is split into a time-averaged part $\bar{\mathbf{X}}$ and a small-perturbation part $\mathbf{X}'$. After this approximation is substituted into the conservation equations, and the time average is taken, new terms appear (similar to the Reynolds stresses $\mathbf{v}' \otimes \mathbf{v}'$ described in section 3.1.2.3, for RANS turbulence models). These new terms, named "unsteady" or "deterministic stresses" [96], are evaluated by solving the system of equations for the perturbations $\mathbf{X}'$, assuming that the perturbations themselves vary harmonically.

[8] What is meant by "Fourier transformation" in this section is not simply a Fourier transform of the transient solution. It indeed employs Fourier transforms, however in a more involved way, which will not be detailed in this work.

This NHB approach solves the closely-coupled time-averaged and perturbation equations simultaneously. This is achieved by employing typical pseudo time marches readily available in steady state CFD codes. That is, through the NHB, a single system of unsteady flow equations is broken down into several "steady state" systems, which are then solved until the desired convergence criteria. The number of systems to be solved is related to the number of harmonics chosen. More specifically, if N_h harmonics are desired, the total number of "steady state" systems in the corresponding NHB computation will be $2N_h + 1$. This increases memory requirements but decreases the processing time substantially.

Finally, the NHB formulation employed here was implemented following the framework from [97]. In comparison to the method from [95], the cross coupling terms between different perturbation harmonics are retained. This approach not only increases the accuracy of the solution by considering high-order coupling effects, but also makes the evaluation of turbulence transport equations easier.

For both the Fourier transformation and the NHB methods, proper convergence must be achieved. In the Fourier transformation case, periodic convergence criteria similar to transient analyses are employed. For the NHB case, since it consists of parallel steady state computations, corresponding residuals and imbalances are adequately controlled. In both cases, independence studies are performed to make sure the discretizations are good enough.

More specifically for aerodynamic work computations, similar assessments must be conducted regarding the chosen blade displacement level in the CFD simulations. On the one hand, no excessive, unfeasible mesh deformation should occur, which would lead to negative-volume cells and invalid results. On the other hand, for modal normalization, the mesh displacement scaling factor must fall within the quadratic range (given by q in Eq. (2.12)). Therefore, care was also taken when selecting the mesh displacement scaling factor.

3.2.2.4 Turbulence modeling

Section 3.1.2.3 has provided the general characteristics of turbulence and delineated the major numerical approaches of dealing with turbulent flows. This section briefly presents a couple of turbulent models relevant for turbomachinery flows. This list is far from exhaustive, with new models and improvements on existing ones being constantly published in the turbulence research community. It is out of the scope of this work to discuss all turbulence models and their equations in depth, with valuable references given in section 3.1.2.3.

Some of the turbulence models most commonly employed for turbomachinery are based on the Boussinesq assumption for the eddy viscosity [98]. It states that the Reynolds stress tensor $\boldsymbol{\tau}^R$ is linearly related to the traceless strain rate tensor, that is,

$$\boldsymbol{\tau}^R = \mu_t \left(\boldsymbol{\nabla}\mathbf{v} + \boldsymbol{\nabla}\mathbf{v}^T - \frac{2}{3} \left(\boldsymbol{\nabla} \cdot \mathbf{v} \right) \boldsymbol{\delta} \right) - \frac{2}{3} \rho k \boldsymbol{\delta}, \tag{3.50}$$

where the linear constant μ_t stands for the turbulent eddy viscosity.

The Spalart-Allmaras model, originally proposed by [99] for wall-bounded flows, computes one extra transport equation to account for the eddy viscosity μ_t. Its implementation simplicity and good performance makes it a very popular model in aerospace and turbomachinery applications.

Other models employ two equations concerning the turbulence transport. The k-ε model from [100] casts one transport equation for the turbulent kinetic energy k and another for its dissipation rate ε. This approach attempts to improve on mixing-length models, working well for planar shear layer flows. However, areas with large adverse pressure gradients are not accurately modeled.

The k-ω model also computes the turbulent kinetic energy k, but employs the specific rate of dissipation ω as the second transport equation, which corresponds to the frequency of the large eddies [101]. This model has good predicting capabilities for large adverse pressure gradients and separated flow.

An attempt to achieve "the best of both worlds" was the development of the shear stress transport (SST) model by [102]. It combines the good capabilities of the k-ε model, for flows far from the walls, with the advantages of the k-ω model, for low-Reynolds areas close to walls and separating flow. The shear stress transport model is used throughout this work, due to its flexibility when modeling complex unsteady flow, and wide acceptance in the turbomachinery community (see, e.g., [103–108]).

More involved closure models avoiding the eddy-viscosity assumption given by Eq. (3.50) compute all components of the Reynolds stress tensor with dedicated transport equations. These models are termed Reynolds stress models and are able to include turbulence anisotropy. However, they require much more computational resources and are in general still dependent on (empirical) closure constants.

Finally, models demanding even more computational resources, such as large eddy simulation (LES), slowly find their way into the turbomachinery research community. They employ a filtered version of the Navier-Stokes equations, consequently selecting specific large spatial scales to be numerically solved, while the small scales and eddies are modeled. The Smagorinsky–Lilly subgrid-scale approach [109, 110] is a common choice, where the grid length itself is used to construct the filters. Hybrid setups combining RANS and LES seem to be a feasible strategy to avoid the high costs of LES in high Reynolds regimes (e.g. [111]).

3.2.3 Computational fluid-structure interaction

The underlying equations connecting the fluid and solid domains were presented in section 3.1.3. Namely, two constraints are necessary for domain compatibility: *kinematics*, matching the interface displacements/velocities and *dynamics*, matching the interface forces. Focusing specifically on aeroelastic phenomena in turbomachinery, chapter 2 also mentioned how the structural dynamics are affected by the flow field (and potentially vice-versa).

From the computational modeling point of view, different approaches to dealing with unsteady multiple domains are possible. They vary in the physical interpretation of the problem and implementation complexity, with the availability of computational resources playing a decisive role. A couple of terms regarding the classification of FSI problems will be initially clarified. In general, these terms describe strict time-domain FSI techniques.

A FSI setup is called monolithic[9] when the discretization method is the same for both fluid and solid domains [112]. In this approach, both domains are solved simultaneously, in a single global equation system. One the one hand, the solver implementation is simplified and stability is enhanced by marching all domains in time simultaneously [113]. On the other hand, the global system matrix becomes often ill-conditioned, due to the different order of magnitude stiffness present in both domains [114]. Typically, the structure requires smaller time steps than the fluid, since the wave propagation velocities for the solid (Eqs. (3.8)) are higher than for the fluid domain (Eq. (3.23)). Employing different time steps (subcycling) is also not convenient for monolithic setups. Finally, memory requirements may be higher, since both systems' unknowns must be simultaneously stored.

In contrast, FSI partitioned[10] schemes aim at combining the advantages of structural and fluid solvers in the same simulation. Due to the availability of optimized methods tuned for each of the domains, a partitioned approach seeks "the best of both worlds" by flexibly solving each domain separately and then employing fixed-point iteration at each time step to ensure numerical convergence [19]. Temporal subcycling may be then straightforwardly employed. Additionally, the mesh for each domain can be independently generated, suiting as best as possible the physics and numerics of each media.

[9] Sometimes termed direct or simultaneous.
[10] Also known as iterative, staggered, segregated or time-lagged.

Partitioned schemes are further characterized as loose or tight, or conversely weak or strong. When two domains are solved staggered, there is no a priori guarantee that the initial guess (within a single time step) for the solution on the boundary between fluid and solid is indeed the correct guess. A FSI scheme is termed loose/weak when there is no procedure guaranteeing that these predicted values are indeed correct at every time step. Loose schemes may accumulate errors and should be used with care to prevent instabilities [115]. In contrast, tight/strong approaches usually implement after the "prediction" step a "correction" loop within every time step to guarantee, up to a predetermined convergence level, that the solved values in the common boundaries match [116, 117]. The discussed FSI denominations may vary in the literature, especially when explicit/implicit descriptors are taken into account.

Regarding FSI in turbomachinery environments, monolithic approaches are rarely employed. Furthermore, the use of partitioned, strongly coupled schemes is still notably restricted to selected research endeavors, still far from the established design practices in the industry. A much more common approach is the so-called one-way coupling, which consists in a special case of loosely coupled schemes. One-way FSI assumes that the solution for one of the domains (e.g., the solid) is affected by the other (the fluid), but not vice-versa. In contrast, a two-way coupling constantly considers the boundary interaction between both domains.

3.2.3.1 Harmonic forced response

A specific approach to deal with the interactions between fluid and solid in turbomachinery environments will be delineated in this section. It is called here harmonic forced response, although it may assume different denominations in the literature. Focus is given to this setup since it will be employed in this work to assess the aeroelastic effects of PGC on the compressor blades.

Differently from the two-way, strongly-coupled FSI techniques described above, the fluid and solid domains are modeled

separately, employing both time- and frequency-domain methods. Figure 3.5 shows the harmonic forced response workflow employed in this work.

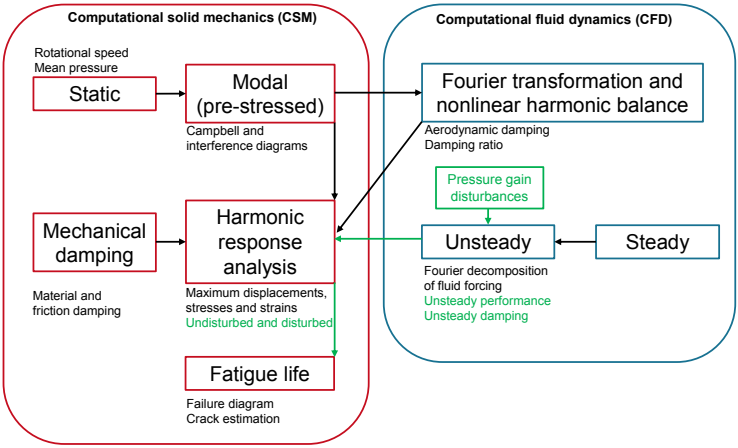

Figure 3.5: Harmonic forced response workflow employed in this work.

Methods from both CSM and CFD are employed at different steps. Once adequate geometries and operating conditions are available, the starting point are static analyses (section 3.2.1.1), which include mean flow loads and centrifugal forces from rotation. The results are then transferred to (pre-stressed) modal analyses (section 3.2.1.2), which provide the natural frequencies and modes for the simulated case, commonly presented in Campbell and interference diagrams (sections 2.3.1 and 2.3.2).

The natural frequencies and modes are then used as input to perform Fourier transformation and nonlinear harmonic balance computations (section 3.2.2.3). Here, the blades are set in periodic motion matching specific natural modes. For these computations, it is assumed that the fluid exerts no unsteady influence in changing the blade eigenfrequencies, which is a typical hypothesis for solid metal blades (as the ones modeled in this work), possessing much higher stiffness than the surrounding

fluid [118]. This step estimates the aerodynamic work (Eq. (2.11)), and with it the aerodynamic damping.

In parallel, steady state CFD simulations (section 3.2.2.1) are followed by unsteady runs (section 3.2.2.2), which generate the transient loads on the blade surface. The blades are treated here as rigid bodies, not being displaced by the fluid loads. The unsteady loads are then cast in the frequency domain by using Fourier transforms. Here, the unsteady performance of the turbomachinery component and the unsteady damping (to be discussed in section 5.1) are also evaluated. The unsteady data may also be interpreted in detail with data-driven decompositions (presented in sections 3.3.2 and 3.3.3).

At this point, harmonic response analyses (section 3.2.1.3) can be performed. They need three inputs from the previous steps: (i) the natural modes, so that mode-superposition can be used to reduce the model order; (ii) aerodynamic damping in the form of modal damping ratio (Eq. (2.12)); (iii) loads in the frequency domain from unsteady CFD. Additionally, when present, mechanical damping (sections 2.4.1 and 2.4.2) may also be included in the total damping.

As results from harmonic response analyses, we obtain the displacements, strains and stresses experienced by the blade subject to the simulated operating conditions, damping and unsteady loads. Usually, the maximum values obtained by phase sweeps are the most relevant quantities.

Finally, following failure criteria considerations (section 2.7), Goodman and similar relations enable an estimate of the blade life in operation, particularly under the unsteady loads simulated. The results presented in this work, however, do not focus on failure criteria. Ultimately, crack estimation, among other methods, can be performed numerically and experimentally to aid in optimally operating and maintaining the engine. Of course, if fatigue issues arise, which are not tolerable in operation, redesign of the system or loads may be necessary.

Since one of the goals of this work is to assess how PGC influences the unsteady operation and aeroelastic behavior of

turbomachinery, its implementation is indicated in green in Fig. 3.5. Specifically, PGC disturbances are introduced as boundary conditions into the unsteady CFD computations, changing performance results, but also the loads for harmonic response analyses. Along this work, unsteady results at undisturbed (or baseline) and PGC-disturbed conditions will be constantly contrasted.

The methodology described here and summarized in Fig. 3.5 employs most of the mathematical and numerical models described more extensively in the previous chapters and sections. Although well established when estimating forced response in turbomachinery, this approach is not the only one available. Another one is the energy method for forced response, developed by [39, 119]. This method assumes a linear scaling of the forcing work (performed by the fluid on the blade) with vibration amplitude and a quadratic scaling of the damping work at resonance. Once these two quantities are computed, an equilibrium may be found, which yields the final vibration amplitude of the blade. The energy method for forced response has been validated with satisfactory results (see, for instance, [21, 120, 121]).

3.3 Data-driven decompositions

3.3.1 Fourier analysis

Fourier analyses are employed in several phases in this work. Not only they play an elemental role in more involved techniques (such as the Fourier transformation and the harmonic balance techniques shown in section 3.2.2.3), they also are used to obtain the harmonic loads of unsteady force distributions for harmonic forced response (section 3.2.3.1). Additionally, Fourier analyses are indispensable whenever the frequency signature of a time-domain signal is necessary.

For a function $f(t)$, where the variable t is often but not necessarily the time, its continuous, direct Fourier transform $\hat{f}$ is customarily defined by

$$\hat{f}(\omega) \triangleq \int_{-\infty}^{\infty} f(t)\, e^{-i\omega t}\, dt, \tag{3.51}$$

where ω is the angular frequency. The inverse Fourier transform recovers the original function, and is given by

$$f(t) = \frac{1}{2\pi} \int_{-\infty}^{\infty} \hat{f}(\omega)\, e^{i\omega t}\, d\omega. \tag{3.52}$$

For numerical data, a discrete version of the Fourier transform is utilized, where the integrals in Eqs. (3.51) and (3.52) are substituted by finite sums over limited periodic intervals. Several methods able to efficiently perform discrete Fourier transforms are available. They are known as fast Fourier transform (FFT) algorithms (see, e.g., [122]), and are always employed in this work when Fourier transforms are executed.

Since Fourier analyses are commonplace in most engineering workflows, no exhaustive discussion will take place here. Mathematical aspects such as existence, properties and aliasing considerations are given, e.g., by [123].

3.3.2 Proper orthogonal decomposition

The proper orthogonal decomposition (POD) optimally extracts spatially orthogonal modes from a field. The data can stem either from experiments or simulations. POD was introduced in different research areas and times independently, and is also known as principal component analysis in statistics, Karhunen-Loève decomposition, singular system analysis, empirical orthogonal functions, among several other denominations [124–129]. It was specifically engaged in assessing turbulence and coherent structures by [130], whereas the reader is referred to [131, 132] for comprehensive theoretical aspects.

The POD algorithm implemented in this work starts with the construction of a snapshot matrix $\boldsymbol{\mathcal{X}} \in \mathbb{C}^{m \times n}$ for a specific state variable (e.g., pressure p, velocity $\mathbf{v}$ or vorticity $\boldsymbol{\nabla} \times \mathbf{v}$). If desired, the temporal mean flow can be subtracted from each row of $\boldsymbol{\mathcal{X}}$, to work only with the field fluctuations. Differently from the transient notation given in section 3.2.1.4, the time step index is written in this section as a subscript. That is, each column $\mathbf{X}_j$ contains the field $\mathbf{X}$ arranged as a vector[11], at time step (or snapshot) j, so that

$$\boldsymbol{\mathcal{X}} \triangleq \begin{bmatrix} | & & | & & | \\ \mathbf{X}_1 & \cdots & \mathbf{X}_j & \cdots & \mathbf{X}_n \\ | & & | & & | \end{bmatrix}, \tag{3.53}$$

where $j = 1, \ldots, n$ and n is the total number of time steps in the analyzed data batch. The amount of rows m corresponds to the number of discrete spatial points in the field. In sequence, a singular value decomposition (SVD) of $\boldsymbol{\mathcal{X}}$ is performed as

$$\boldsymbol{\mathcal{X}} = \mathbf{U}\boldsymbol{\Sigma}\mathbf{V}^*, \tag{3.54}$$

where the left singular vectors $\mathbf{U} \in \mathbb{C}^{m \times m}$ are the POD spatial modes (*topos*), $\boldsymbol{\Sigma} \in \mathbb{C}^{m \times n}$ the singular values in diagonal form and the right singular vectors $\mathbf{V} \in \mathbb{C}^{n \times n}$ the temporal structures

[11] For vectorial state variables (e.g. velocity), each of their components may be subsequentially allocated in the same vector $\mathbf{X}$.

(*chronos*) [133]. The superscript * indicates conjugate transpose. If the mean is not subtracted, the first row of $\mathbf{U}$ contains the average flow of the analyzed data, corresponding to the largest singular value of $\mathbf{\Sigma}$, which is customarily at least one order of magnitude higher than the other singular values. The matrices $\mathbf{U}$ and $\mathbf{V}$ are unitary, that is,

$$\mathbf{U}^* = \mathbf{U}^{-1}, \qquad \mathbf{V}^* = \mathbf{V}^{-1}. \tag{3.55}$$

In some situations, the method of snapshots [134] is preferred. For that, first we construct the correlation matrix $\boldsymbol{\mathcal{X}}^T\boldsymbol{\mathcal{X}}$ and then an eigenvalue problem is solved, obtaining as eigenvectors the same matrix $\mathbf{V}$ and eigenvalues $\lambda_j = \Sigma_{jj}^2$. Conversely with the "classic method", an eigendecomposition of $\boldsymbol{\mathcal{X}}\boldsymbol{\mathcal{X}}^T$ yields as eigenvectors $\mathbf{U}$, sharing the same eigenvalues λ_j. Since in most cases the number of spatial points is much higher than the number of snapshots (i.e., $m \gg n$), $\boldsymbol{\mathcal{X}}^T\boldsymbol{\mathcal{X}}$ is usually much smaller than $\boldsymbol{\mathcal{X}}\boldsymbol{\mathcal{X}}^T$, favoring the use of the snapshot method over the classic[12].

Employing either the SVD or correlation matrices approach, it is in general possible to obtain a reduced number of singular values (and therefore a subset of eigenvectors). In the SVD case, this concept is called *economy-sized SVD*. This not only makes the computation of the POD modes substantially faster, but also enables a reconstruction of the original field in a lower rank manifold. The reconstructed (or approximated, if a lower rank $n' < n$ is adopted) field $\overline{\boldsymbol{\mathcal{X}}} \in \mathbb{C}^{m\times n}$ is obtained by

$$\overline{\boldsymbol{\mathcal{X}}} = \overline{\mathbf{U}}\left(\overline{\mathbf{U}}^*\,\boldsymbol{\mathcal{X}}\right) = \overline{\mathbf{U}}\,\mathbf{C}, \tag{3.56}$$

where $\mathbf{C} \triangleq \overline{\mathbf{U}}^*\,\boldsymbol{\mathcal{X}} \in \mathbb{C}^{n'\times n}$ is the time coefficient matrix, multiplying the (low-rank) POD modes $\overline{\mathbf{U}} \in \mathbb{C}^{m\times n'}$. Note that $n' = n \Rightarrow \overline{\boldsymbol{\mathcal{X}}} = \boldsymbol{\mathcal{X}}$ and $\overline{\mathbf{U}} = \mathbf{U}$. The formulation given by Eq. (3.56) encapsulates the straightforward field reconstruction idea behind the POD. Additionally, the orthogonality of the spatial modes is very attractive for Galerkin approximations (see, e.g., [135]).

[12] The double j in Σ_{jj} refers simply to matrix indexing, specifically the terms in the diagonal of $\mathbf{\Sigma}$. That is, this expression implies no repeated-index summation.

The denomination "data-driven" arises from the fact that the POD is applied in a post-processing fashion, independently on how the original data was measured or computed. That is, no prior knowledge of the system operator is needed as input. Among all possible low-rank approximations, the POD is the linear decomposition that retains the most energy as possible in the generated subspace (i.e., it is optimal in the L_2 sense [131]).

Indeed, if $\boldsymbol{\mathcal{X}}$ represents a turbulent velocity field, λ_j corresponds to twice the average kinetic energy of mode j. If $\boldsymbol{\mathcal{X}}$ is the vorticity field, then ranked enstrophy is obtained, shedding light into energy cascades in large-scale turbulence and the transfer of vorticity intensity among wavenumbers [136]. The POD L_2 optimality can be harvested to identify relevant flow structures, which are in general discernible in the first (highly energetic) POD modes.

Although velocity and vorticity fields are typically decomposed (due to their direct relation to intuitive physical functionals), assessing other fields such as pressure, mass flow or helicity enables us to enhance our understanding of important flow features described by diverse state variables, and with which energetic intensity these features "decay" in a POD.

In summary, obtaining a reduced number of singular values (and corresponding modes) sorted by magnitude – which is straightforward with modern subspace decomposition techniques – promotes a deep understanding of the most significant flow features; it also enables reconstructing the unsteady flow retaining the most energy as possible from all linear decompositions.

3.3.3 Dynamic mode decomposition

Like the POD, the dynamic mode decomposition (DMD) is also a data-driven decomposition, often employed to analyze unsteady fluid dynamics. It may be understood as a numerically-oriented development of the Koopman spectral theory [137]. It was initially defined as an algorithm by [138], whereas the connection to the Koopman operator under certain

conditions was provided by [139]. Rich theoretical and numerical discussions about the DMD are presented by [132, 140, 141].

The "standard" definition of the DMD will be provided here, whereas a more comprehensive framework has been suggested by [141]. Referring back to the POD snapshot matrix from Eq. (3.53), the DMD requires the assembling of two similar matrices, shifted by one time step. They are given here by

$$\mathcal{Y} \triangleq \begin{bmatrix} | & & | & & | \\ \mathbf{X}_1 & \cdots & \mathbf{X}_j & \cdots & \mathbf{X}_{n\text{-}1} \\ | & & | & & | \end{bmatrix}, \tag{3.57a}$$

$$\mathcal{Z} \triangleq \begin{bmatrix} | & & | & & | \\ \mathbf{X}_2 & \cdots & \mathbf{X}_j & \cdots & \mathbf{X}_n \\ | & & | & & | \end{bmatrix}. \tag{3.57b}$$

Observe that the matrix $\mathcal{Y} \in \mathbb{C}^{m\times(n\text{-}1)}$ is defined here simply as the POD snapshot matrix $\mathcal{X}$ (Eq. (3.53)) lacking the last column $\mathbf{X}_n$. Similarly, $\mathcal{Z} \in \mathbb{C}^{m\times(n\text{-}1)}$ corresponds to $\mathcal{X}$ with the first column $\mathbf{X}_1$ removed.

The relation between $\mathcal{Y}$ and $\mathcal{Z}$ is conveyed by a "time-shift operator" $\mathbf{A} \in \mathbb{C}^{m\times m}$, which in the linear time-invariant case represents a tangent approximation, so that

$$\mathbf{X}_{j+1} = \mathbf{A}\,\mathbf{X}_j \qquad \text{or} \qquad \mathcal{Z} = \mathbf{A}\,\mathcal{Y}. \tag{3.58}$$

Indeed, the DMD can be defined (see [141]) as computing the best-fit linear operator $\mathbf{A}$ for Eqs. (3.58), equivalently to

$$\mathbf{A} = \mathcal{Z}\,\mathcal{Y}^{+}, \tag{3.59}$$

where the superscript $^{+}$ represents the Moore-Penrose inverse, a generalization of matrix inversion [142]. What is meant by best fit is that the operator $\mathbf{A}$ given by Eq. (3.59) is the optimal solution when minimizing the error $||\mathcal{Z} - \mathbf{A}\,\mathcal{Y}||_F$ in the Frobenius norm [143].

Two procedures to obtain the DMD modes will be mentioned:

(i) QR-decomposition: the DMD construction originally given by [138] defines the full snapshot matrix $\boldsymbol{\mathcal{X}}$ as a Krylov sequence [144], which can be written as $\boldsymbol{\mathcal{X}} = \left[\mathbf{X}_1, \mathbf{A}\mathbf{X}_1, \mathbf{A}^2\mathbf{X}_1, \ldots, \mathbf{A}^{n\text{-}1}\mathbf{X}_1\right]$. This relation is based on the assumption of a constant mapping $\mathbf{A}$ between snapshots $\mathbf{X}_j$. Additionally, increasing the number of snapshots (columns of $\boldsymbol{\mathcal{X}}$) will improve the dynamic characterization of the system up to a certain "saturation point", when the vectors $\mathbf{X}_j$ become linearly dependent. However, before they become linearly dependent, a residual $\mathbf{r}$ vector can be according to the expression

$$\boldsymbol{\mathcal{Z}} = \mathbf{A}\boldsymbol{\mathcal{Y}} = \boldsymbol{\mathcal{Y}}\mathbf{S} + \mathbf{r}\,\mathbf{e}_{n\text{-}1}^T, \tag{3.60}$$

where $\mathbf{e}_{n\text{-}1}$ is the unit vector. $\mathbf{S}$ is a companion matrix containing the linear dependency coefficients relating the last snapshot to all previous snapshots. Subsequentially, we cast the snapshot matrix in the form $\boldsymbol{\mathcal{Y}} = \mathbf{QR}$ and then perform a QR decomposition as $\mathbf{AQ} \approx \mathbf{QH}$, with $\mathbf{H} = \mathbf{RSR}^{\text{-}1}$. Now we can obtain the companion matrix $\mathbf{S} = \mathbf{R}^{\text{-}1}\mathbf{Q}^T\mathbf{QR} = \mathbf{R}^{\text{-}1}\mathbf{Q}^T\boldsymbol{\mathcal{Y}}$, and then compute its eigendecomposition. The main idea is that the eigenvalues (Ritz values) of $\mathbf{S}$ approximate some of the eigenvalues of $\mathbf{A}$. The eigenvectors of $\mathbf{S}$, given here by $\mathbf{W}$, are projected into the snapshot matrix $\boldsymbol{\mathcal{Y}}$ to obtain the DMD modes $\boldsymbol{\Phi}$ from

$$\boldsymbol{\Phi} = \boldsymbol{\mathcal{Y}}\,\mathbf{W}. \tag{3.61}$$

(ii) SVD: this approach aims at improving potential ill-conditioning arising from the QR-decomposition (i). We start by employing an economy-sized SVD (Eq. (3.54))[13] to the snapshot matrix $\boldsymbol{\mathcal{Y}}$, i.e., $\boldsymbol{\mathcal{Y}} = \mathbf{U}\boldsymbol{\Sigma}\mathbf{V}^*$. Substituting this expression in Eq. (3.60) we obtain

$$\boldsymbol{\mathcal{Z}} = \mathbf{AU}\boldsymbol{\Sigma}\mathbf{V}^*, \tag{3.62}$$

[13]The overbar for low-rank matrices (see Eq. (3.56)) will be dropped for simplicity.

which can be premultiplied by $\mathbf{U}^*$ and postmultiplied by $\mathbf{V}\boldsymbol{\Sigma}^{-1}$. Due to the orthogonality of $\mathbf{U}$ and $\mathbf{V}$ (Eqs. (3.55)) and the fact that $\boldsymbol{\Sigma}\boldsymbol{\Sigma}^{-1} = \boldsymbol{\delta}$, we obtain

$$\mathbf{U}^*\mathbf{A}\mathbf{U} = \mathbf{U}^*\mathcal{Z}\mathbf{V}\boldsymbol{\Sigma}^{-1} \triangleq \tilde{\mathbf{S}}, \tag{3.63}$$

where the newly defined matrix $\tilde{\mathbf{S}} \in \mathbb{C}^{n' \times n'}$ is related to $\mathbf{A}$ and $\mathbf{S}$ via similarity transformations[14]. This is the key idea behind this similarity transformation, which allows us to work with a low-dimensional matrix $\tilde{\mathbf{S}}$ instead of the high-dimensional original operator $\mathbf{A}$.

Additionally, Eq. (3.63) allow us to understand $\tilde{\mathbf{S}}$ as the correlation between the POD spatial modes $\mathbf{U}$ with their time-shifted counterpart $\mathbf{AU}$. Thus, the intrinsic properties of $\tilde{\mathbf{S}}$ directly characterize the system dynamics.

Similarly to the procedure with the companion matrix $\mathbf{S}$, an eigendecomposition of $\tilde{\mathbf{S}}$ is performed, obtaining eigenvalues λ_j (diagonal entries of $\boldsymbol{\Lambda}$) and eigenvectors $\tilde{\mathbf{w}}_j$ (columns of $\tilde{\mathbf{W}}$). Finally, the so-called *projected DMD modes* are given by

$$\boldsymbol{\Phi} = \mathbf{U}\tilde{\mathbf{W}}. \tag{3.64}$$

The SVD formulation to obtain the DMD modes has been employed in this work, to improve robustness. However, computing the residual $\mathbf{r}$ from the QR-decomposition (Eq. (3.60)) is also helpful when determining how converged or "saturated" the dynamic system is, and whether or not more snapshots may be necessary[15].

[14] Matrices related by similarity transformations share the same eigenvalues and eigenvectors (although the eigenvectors are given in different coordinate systems). Note that the main advantage of employing an economy-sized SVD with $n' \ll n$ is elegantly reflected in the reduced size of $\tilde{\mathbf{S}}$, which will then represent the system dynamics instead of $\mathbf{A}$.

[15] A supplementary definition provided by [141], known as *exact DMD modes*, is given by $\boldsymbol{\phi}_j = \lambda_j^{-1}\mathcal{Z}\mathbf{V}\boldsymbol{\Sigma}^{-1}\tilde{\mathbf{w}}_j$, valid only for $\lambda_j \neq 0$. Although it may be more flexible for some special types of input, it produces the same DMD modes as Eq. (3.64) when the column spaces of $\mathcal{Y}$ and $\mathcal{Z}$ coincide.

Once the DMD modes have been obtained by Eq. (3.64), relevant information about the dynamics of the system is also available. The discrete-system eigenvalues of $\tilde{\mathbf{S}}$, organized in the diagonal matrix $\mathbf{\Lambda}$, indicate the stability of the dynamical system. They are complex variables, and if $|\lambda_j| > 1$, the corresponding DMD mode $\boldsymbol{\phi}_j = \boldsymbol{\mathcal{Y}}\tilde{\mathbf{w}}_j$ is termed unstable, i.e., its amplitude grows in time. Conversely, stability is expected if $|\lambda_j| < 1$. The neutrally stable case when $|\lambda_j| = 1$ refers to so-called "saturated" modes, which cluster around the unit disk, indicating that the nonlinear process manifested in the analyzed data converges towards a linear representation [145].

The DMD discrete system can also be cast in a corresponding continuous counterpart. For that, the continuous-system eigenvalues μ_j correlate to the discrete-system eigenvalues λ_j as

$$\mu_j = \frac{\log(\lambda_j)}{\Delta t}. \tag{3.65}$$

When employing continuous-system eigenvalues, the stability criteria change accordingly. Stability is achieved if their real part is negative, i.e., $\Re(\mu_j) < 0$. Conversely, instability is presumed for $\Re(\mu_j) > 0$. The liminal case becomes $\Re(\mu_j) = 0$. Additionally, the linear frequency f_j (e.g. in Hz) of DMD mode j is extracted from the imaginary part of the continuous-system eigenvalues as

$$f_j = \frac{\Im(\mu_j)}{2\,\pi}. \tag{3.66}$$

Equation (3.66) indicates that each DMD mode has one single frequency f_j. That is, the spatial structure $\boldsymbol{\phi}_j$ linked to the mode j oscillates (with a decay or growth rate) with a specific periodicity. This is a special feature of the DMD, contrasting with the POD modes $\mathbf{U}$ which, although orthogonal in space, oft accommodate mixed frequencies in their spectra.

To illustrate these properties, sample continuous- and discrete-system eigenvalues are depicted in Fig. 3.6, for a decomposition of a representative turbomachinery unsteady CFD case. Since both representations are equivalent, from now on only the continuous-system eigenvalues will be displayed. Each DMD mode is represented by a sphere, whose position indicate the frequency and level of dynamic (in)stability. More specifically, in the continuous case (left plot), the more towards the left, the higher the stability; in the discrete case (right plot), stability increases towards the origin of the unit circle. The symmetry in the imaginary plane is due to the fact that the snapshot data itself is real [138]. Additionally, according to Eq. (3.66), the imaginary part of the continuous-system eigenvalues can be also understood (or plotted) as the DMD mode frequency.

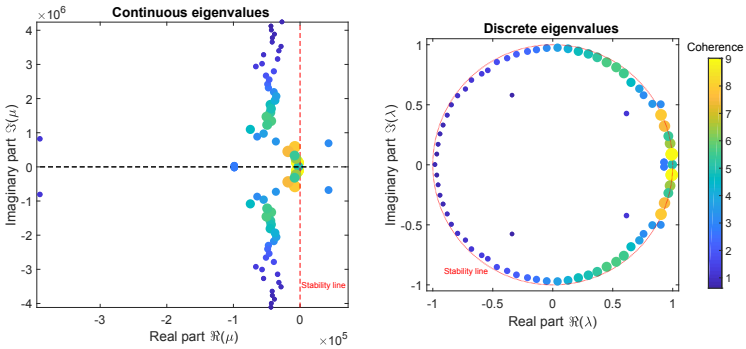

Figure 3.6: DMD eigenvalues depicted on the complex plane for a representative turbomachinery unsteady CFD computation. Left: continuous-system eigenvalues λ. Right: discrete-system eigenvalues μ. The coherence metric is computed as the projection of each DMD mode into the POD spatial modes.

The color and size of each DMD mode in Fig. 3.6 depict the modal coherence metric. Spatiotemporal coherent structures are (usually large-scale) flow features that persist long enough to be statistically measured, and typically contain high energy. They reveal relevant information arising for instance from turbulent behavior, flow instabilities or stable eddies (see, e.g., [131] for a

rich discussion). The DMD modal coherence metric employed in this work is computed for mode j as $||\phi_j^T \mathbf{U}||$, that is, the DMD modes ϕ are projected into the POD spatial modes $\mathbf{U}$, and the norm is taken [138]. The coherence absolute magnitude will not be shown in the results, since the most significant information is the relative value between the DMD modes.

For completeness, just like the POD, the DMD also allows field reconstruction with the obtained modes. This is achieved with the discrete data as

$$\mathbf{X}_j \approx \sum_{k=1}^{n'} \phi_k \lambda_k^{j\text{-}1} b_k = \mathbf{\Phi} \mathbf{\Lambda}^{j\text{-}1} \mathbf{b}, \tag{3.67}$$

where $\mathbf{b}$ is a vector with initial coefficients (i.e., initial coordinates of $\mathbf{X}$), which is computed as $\mathbf{b} = \mathbf{\Phi}^+ \mathbf{X}_1$. The exponentiation matrix of the DMD eigenvalues $\mathbf{\Lambda}^{j\text{-}1}$ is known as the Vandermonde matrix. Note that the summation stops at the desired reduced order rank n', with $n' \leq n$.

Analogously to Eq. (3.67), it is possible to write a continuous form of the DMD reconstruction as

$$\mathbf{X}(t) \approx \sum_{k=1}^{n'} \phi_k e^{\mu_k t} b_k = \mathbf{\Phi} e^{(\boldsymbol{\mu} t)} \mathbf{b}, \tag{3.68}$$

which allows the computation of the best-fit linear dynamics $\mathbf{X}_{j+1} = \mathbf{A}\,\mathbf{X}_j$ for arbitrary time t. Equation (3.68) is indeed the general solution for the continuous flow map $d\mathbf{x}/dt = \mathcal{A}\,\mathbf{x}$, for a linear operator $\mathcal{A}$.

4

Pressure gain combustion

This chapter presents the state of the art in pressure gain combustion and considerations about its integration with gas turbines

4.1 Background

The conventional thermodynamic model of a gas turbine or aero engine includes a steady constant-pressure (isobaric) heat addition process, encompassed by the Brayton (or Joule) ideal cycle. In reality, the stagnation pressure losses observed in actual operation of combustion chambers show that the real heat addition is rather a pressure-loss process (approximately 4% to 7% of the total stagnation pressure [146]), decreasing the overall efficiency of the engine.

These losses linked to the combustion process are acknowledged by [147] to be the main exergy destruction source for long-range turbofans. That is, an improvement potential even higher than diminishing losses in the core exhaust or bypass flow can be achieved by enhancing the efficiency of heat addition.

Therefore, the replacement of typical pressure-loss combustion by approaches increasing the total pressure has regained much attention recently. In this work, these methods will be broadly termed *pressure gain combustion* (PGC). Although the concept has long been present in the gas turbine development (as in the pioneer Holzwarth "explosion" engine [148]), several new research initiatives have been recently established to dominate PGC and develop technological applications.

A working definition for PGC has been given by [149] and further adapted as

> [a] fundamentally unsteady process whereby gas expansion by heat release is constrained, causing a rise in stagnation pressure and allowing work extraction by expansion to the initial pressure [150].

One of the two key aspects in this definition is the spatial constraint during the heat release process. It can be ideally achieved by either fixing the expansion volume (isochoric combustion) or accelerating the process so intensely so that not enough time for gas expansion is available (e.g., with detonation waves) [151].

Before presenting some of the contemporary PGC-specific approaches in section 4.2, some introductory qualitative remarks about their thermodynamic efficiency are fruitful. As a motivation, we start by comparing the standard thermodynamic ideal cycle for gas turbines with novel PGC methods. Figure 4.1 presents, beyond the classic Joule, the Humphrey and the Zeldovich/von Neumann/Döring (ZND) cycles in a T-s diagram. These surrogate respectively an isochoric and a detonation combustion.

The Humphrey cycle, due to the isochoric heat addition, increases the effective divergence rate between the heat addition (states 3 to 4) and heat removal (states 10 to 0) curves. This change amplifies the area contained within the state lines, increasing work extraction. When modeling PGC with the ZND model, even higher efficiencies may be achieved, due to lower entropy production during the combustion process.

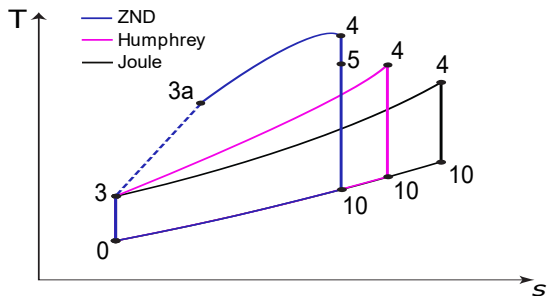

Figure 4.1: Thermodynamic cycles modeling gas turbine operation in a temperature-entropy (T-s) diagram, including PGC. Numbering of thermodynamic states based on [152].

The second critical aspect of the previously presented PGC definition [150] is its unsteadiness. To date, all practical attempts to achieve a pressure gain in combustion employed unsteady mechanisms, in contrast to steady combustion with constant injection of fuel in traditional gas turbines. Unsteady combustion, however, brings several challenges. Not only from the

aerodynamic, but also from the aeroelastic point of view, since the whole engine structure must withstand the arising vibrations. Furthermore, the safe operation of all engine components must be ensured under these novel unsteady combustion regimes.

4.2 State of the art

Four selected PGC genres, more intensively pursued by researches in the last decades, will be outlined in the next sections: pulse detonation combustion, rotating detonation combustion, shockless explosion combustion and wave rotor combustion.

4.2.1 Pulse detonation combustion

Before properly linking the use of detonation combustion concepts with gas turbines, it is important to mention the classic pulse detonation engine (PDE) as a thrust propulsion system itself. In contrast to conventional aeronautical engines such as turbojets or turbofans, which employ a deflagration combustion process, the PDE is characterized by a detonation mechanism. A detonation (as opposed to deflagration[1]) generates supersonic shock waves that propagate through a reactive mixture with a velocity ranging from 1 km/s to 4 km/s [153]. Indeed, the energy that maintains the shock wave is obtained from the highly exothermic chemical reactions. As a second main characteristic, PDEs are inherently unsteady; in fact, [154] have shown that trying to stabilize a detonation as a stationary wave is not practicably feasible for propulsion.

An introductory description of the pulse detonation cycle is given here, whilst further details can be found on referenced work. Figure 4.2 depicts the three main phases of a descriptive detonation cycle: fill, fire and purge. In the first phase, a fuel-air mixture is laded into the tube (the combustion chamber); the duration of this process depends on the volume of the tube, inlet

[1]The PDE differs from the well-known pulsejet engine, in the sense that the pulsejet employs a deflagration combustion process, although still unsteady.

pressure, among other parameters. The second phase can be split into four sub-phases: ignition, deflagration to detonation transition (DDT), detonation and blow down; now, fuel characteristics and the DDT mechanism are the major determiners of time scales. Finally, the purge phase follows, acting as an exhaust step in the cycle.

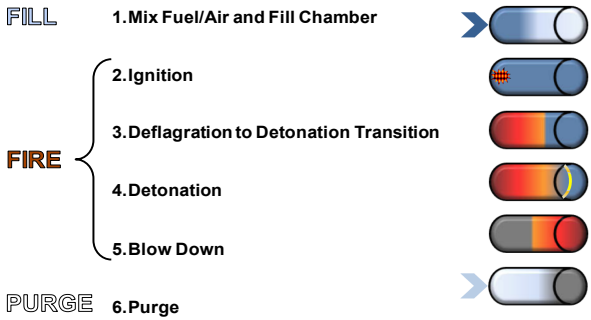

Figure 4.2: General description of a pulse detonation cycle [155].

A broad review on the PDC propulsion topic and its historical and technological evolution is given by [156], including physical and chemical descriptions. Considerations are given for gaseous and heterogeneous detonations, DDT achievement, detonability limits and nonideal cycle losses, including supporting experimental studies performed so far. Several design concepts have been proposed, among which valved and valveless, with predetonator, multitube and resonator, but also some unusual configurations, such as pulse-blasting, stratified charge and dual fuel. [156] also highlight some of the challenges still to be overcome by the PDC for propulsion purposes, for instance: detonation initiation with low-energy sources, proper mixing enhancement of the fuel with the oxidizer, control mechanisms, cooling methods and integration of the combustor with inlets and nozzles. Particularly, the authors point out the potential structural complications that arise from high-frequency loading, including combustion disturbances that might travel upstream to the inlet of the PDC. Among the experimental results with

unsteady combustion listed, the frequency per tube ranges from less than 1 Hz up to the kHz order [157].

[158] provides a general review of detonation waves employed in propulsion applications, ranging from the early 1940s research studies that started to link detonation with propulsion, until more recent achievements, such as laser-supported detonations, oblique detonation wave engines and the PDE itself. It is also mentioned by [158] that issues such as heat transfer, noise and vibrations have to be properly addressed to grant feasibility to propulsive detonation technology. In a following work, [159] highlights recent progress in PDC development for both airbreathing and rocket applications, remarking however that inlets and nozzles are still challenges to be overcome. Other practical difficulties faced by PDCs are the achievement of a smooth DDT without the use of very long tubes, noise reduction and damping of high amplitude vibrations.

In a similar fashion, [160] presents an extensive summary on the PDC topic with both experimental and numerical considerations. Some practical issues regarding detonation initiation, wave propagation and heat transfer are discussed.

A comprehensive review considering several R&D applications besides power generation and propulsion is provided by [161]. In addition to presenting pulse combustion analytical models, fuel sensibility and mechanical aspects such as the suitability of different valves are addressed.

A myriad of studies have corroborated the potential thermodynamic gains of PDC in comparison to the Joule cycle. The seminal work of [152] provides a concise analytical description of pressure-gain processes, determining the PDC ideal efficiency and contrasting it with the Joule and Humphrey cycles. The heat addition in the pulsed detonation cycle is modeled by [152] with a normal detonation (ZND) wave with Chapman–Jouguet constraints. Loss considerations are also taken into account for the three compared cycles, concluding that the PDC nonideal cycle efficiency clearly exceeds the Joule and Humphrey efficiencies for flight $Ma < 3$.

With an exergetic approach, cycle assessments were performed by [147]. Employing the pioneer exergy metric from [162], based on the first and second laws of thermodynamics, three radically improved aircraft engine designs were analyzed, namely: open rotor, intercooled recuperated and pulse detonation core setups. In all configurations, the combustor played the larger roll on exergy destruction, indicating the pulse detonation core as a very interesting approach to reduce specific fuel consumption (SFC) for future propulsion power plants. Overall, a 18% reduction on SFC was reported for the PDC operation (together with intercooling and recuperation) in comparison to the conventional turbofan engine setup expected in 2050. More recent studies from the same group analyzed similar performance designs, such as non-precooled, intercooled and intercooled-aftercooled PDC integration [163]. Once again, reduction in uninstalled fuel consumption and improvements in thermal efficiency were obtained by both a one-dimensional performance model and CFD results.

Further results modeling the pressure-gain process with a Fickett-Jacobs cycle were obtained by [164]. Also here the PDC outperformed the isobaric and isochoric counterparts. The numerical values differ slightly from [152], since the specific heat ratio employed by [164] was lower, in order to represent the combustion products more accurately. Concerning the specific modeling of gas turbines with PDC, [165] also employed the Fickett-Jacobs cycle, yielding a higher efficiency than the corresponding Joule, for both ideal and nonideal cases.

Several other analytical, numerical and experimental studies underline the efficiency increase obtained with PDC [163, 166–171], not only focused on propulsion applications, but also on power generation or marine transport. It is relevant to mention that the increase in efficiency is directly linked to the complexity of the cycle (e.g., intercooling, pre-heating) but also to project constraints (e.g., weight, material limits).

Even though a gain in thermodynamic efficiency is expected with the implementation of PDC in gas turbines, concerns about its integration with other engine components can be traced back to its recasting as a candidate to performance improvement. For instance, the early work of [172] already forewarned about unwanted pressure pulsations and backflow from the so-called "pulse combustor".

Since then, several researchers tried to shed light on the adverse impacts of PDC unsteadiness in the adjacent components, especially the downstream turbine. Considering linear cascades, [173] conducted unsteady experimental and numerical studies in a row of stationary turbine blades. As depicted in Fig. 4.3, both shadowgraph and CFD images showed strong reflected shocks upstream the turbine and weak shocks transmitted downstream the blade cascade.

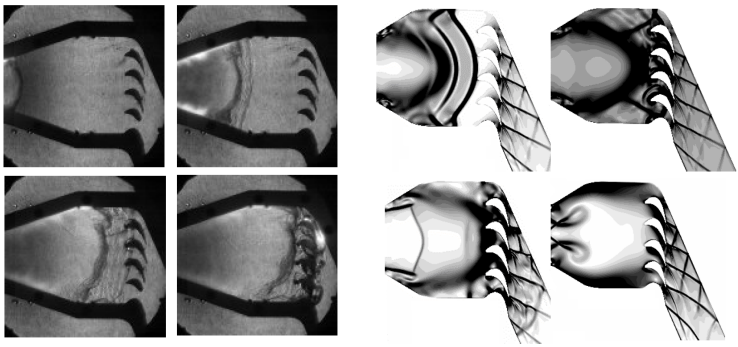

(a) Detonation wave on shadowgraph (b) CFD prediction of shock wave

Figure 4.3: Experimental and numerical results of a 2D cascade impinged by a PGC shock wave [173].

Many studies coupled PDC with radial turbines, particularly from turbochargers. For instance, [174] drove a turbine from a Garrett T3 turbocharger with a self-aspirated PDE with two tubes firing simultaneously. Subsequent work from [175] span the turbocharger at 130,000 rpm with operating combustion frequencies from 20 Hz to 40 Hz, reporting high turbine losses but also attenuation in the detonation shock waves.

In a similar track, [176] have employed a single detonation tube to drive an automotive turbocharger using a Shchelkin spiral. Later research from [177] added a second detonation tube out of phase achieving a combined firing frequency of 80 Hz, though with lower thermal efficiency than the single-tube setup.

[178] report the use of a turbocharger radial flow turbine with a PDC tube firing between 1 Hz and 10 Hz, employing liquid C_8H_{16} as fuel. After more than 12,000 detonations there was no visible sign of pitting or discoloration on the turbine. The peak pressure reported at the PDC exit roamed between 2 MPa and 3 MPa.

Also employing a radial turbine, [155] coupled a Garret automotive turbocharger with a PDE fueled with hydrogen. Up to 30% increase in average specific work was obtained for firing frequencies between 10 Hz and 25 Hz. Temporary reverse flow in the turbine inlet was reported. Subsequent studies from [179] with a similar PDC-turbocharger configuration considered temporary mass accumulation in the efficiency computation. This time, firing frequencies ranged between 20 Hz and 30 Hz. Performance was improved for higher PDC frequencies.

As a last PDC application with turbochargers, [180] discharged the flow of a PDC firing at low-frequencies into a single-stage radial turbine. Once the PDC operation was initiated with air from a dedicated high-pressure reservoir, the outflow from the turbocharger compressor was the sole air supply to the turbine. With that, a complete coupling between compressor, PDC and turbine was achieved. The thrust produced exceeds the Joule cycle counterpart. Backward-propagating waves reached pressure peaks of 6 bar, which amount to 30% of the corresponding pressure downstream of the combustor. Valves located further upstream attenuated these pressure peaks to 0.3 bar, a value which represents the fluctuations to which the upstream-positioned compressor was subjected. However, the presence of long channels between the compressor and PDC inlet together with the turbocharger's off-design condition hint that a higher variability in PDC-upstream conditions is to be expected, when considering its integration with gas turbines.

Axial turbines have also been simulated with PDC configurations. A parametric performance study was conducted by [181] using the Numerical Propulsion Systems Simulation code for a hybrid PDE cycle, which coupled a high-thrust class turbofan with a detonation tube. This engine setup increased the thrust by 2% and lowered the SFC by up to 10% at cruising conditions, compared to normal operation.

Another group of researchers [182] have set up a test rig with an axial turbine rated for 90 hp and 60,400 rpm output, coupled to a six-tube PDC burning ethylene with oxygen. The firing frequency was 20 Hz. This preliminary study analyzed the pressure reduction after the detonation wave travels through the turbine blades, with and without bypass air. Focusing on acoustic attenuation of detonation waves by turbines, further studies by [183] indicated that the reduction of wave peak pressure is highly dependent on the initial strength of the wave. This strength variation could be achieved by interchangeably varying the fill fraction, equivalence ratio or nitrogen dilution.

Subsequent experiments with the same test rig assessed the performance of the multitube PDC [184]. The main conclusion was that the efficiency of the integrated PDC-turbine system was quantitatively comparable to the efficiency of a steady-burner driven turbine. This was observed across the turbine operating map from low load up to approximately 67% of its nominal capacity. A rich summary of the major results obtained by this work group was organized by [185].

Subsequently, [186] conducted experiments with a power generation turbine subject to both cold and combustion pulsating flow, with four different frequencies (ranging from 5 Hz to 20 Hz) and three operating points. Mass-average and work-averaged efficiencies presented very similar values, both being acceptable for the unsteady computations. Finally, pressure perturbations due to firing of adjacent tubes were measured, indicating a harmonic dependence on the number of combustion units.

As one of a series of published results, [187] set up a PDC with eight tubes in a can-annular display, firing into single-stage axial

turbine from a locomotive-scale turbocharger. The system is depicted in Fig. 4.4. The firing frequencies per tube reached 30 Hz and different firing patterns were employed. Secondary air controlled independently was supplied by external compressors to be mixed with the PDC exhaust gases, in order to cool the tubes. Further experiments were conducted in the same test rig by [188], this time with twelve high-temperature strain gauges mounted on the stators, in the interest of assessing vane deflections. The reported pressure rise at the combustor inlet reached 18 bar, at 20 Hz firing frequency. Probes located in the upstream plenum measured a peak pressure of approximately 5 bar. The measured strain reached only 8% of the stator material yielding point. Furthermore, different tube firing patterns were experimented, namely: single tube, all tubes simultaneously, counter and co-rotating ignition sequences; the simultaneous firing produced the highest strain, while the single tube mode yielded the lowest value.

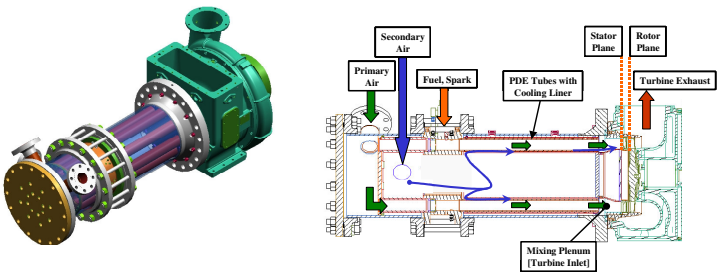

Figure 4.4: 8-tube PDC-turbine setup from [188].

Following the experimental setup from [187], further results were provided by [189]. This time, no valve was used to control the air inflow. Transducers installed upstream of the detonation tubes indicate a variation in the peak pressure of approximately 5 bar and 2.4 bar for simultaneous and sequential firing, respectively. Such upstream pressure measurements, although still scarce in the literature, are insightful when evaluating in which way the PDC disturbances propagate throughout the

compressor. [189] also addressed the interaction of pressure waves among adjacent tubes and its effect on optimum engine operation. Misfiring was reported, particularly for the sequential firing mode, leading to the hypothesis of intensive pressure wave interplay between adjacent detonation tubes and reverse flow conditions, imparting instability to the system.

Acoustic attenuation results from the same working group have been reported. [190] measured a 20 dB peak pressure attenuation and 10 dB attenuation over a broadband acoustic spectrum, using a similar turbine setup as [187, 188]. It was argued by [190] that noise issues should not be a critical barrier for the integration of PDC with gas turbines.

Higher PDC firing frequencies have been reached in the last years. Although for a setup with small dimensions, [157] was able to achieve stable operation at almost 2 kHz with a single PDC tube. Another research group focusing on rocket propulsion experimented with hypergolic propellants, sustaining PDC with pressure oscillations between 200 Hz and 700 Hz [191].

Specifically from the numerical front, [192] have simulated the attenuation and reflection effect of a PDC pulse on an axial turbine, with a 3D viscous code in the time domain. The numerical domain consisted in $1/8^{th}$ annulus with a unitary pitch ratio. No chemical kinetics were modeled, but instead 1D gas dynamics simulated the pressure and temperature distribution of the detonation. An average pressure attenuation of approximately 15 dB was observed. Temporary reverse flow occurred in a region right upstream of the vanes.

Numerical computations were also carried out by [193], in which a conceptual PDE discharges on an axial turbine stator row. The model includes 1D irreversible single-step chemical kinetics calculations in the detonation tubes, coupled to a 3D fluid domain surrounding the combustor and stators. The detonation frequency simulated corresponds to 50% of the turbine rotation frequency. Once again, the pressure perturbations caused by the PDC are reported to be substantially reduced with the presence of the zero-turning axial cascade.

Among the few existing investigations on PGC waves propagating upstream through the compressor, research conducted at the Chair for Aero Engines at Technische Universität Berlin is worth mentioning. A low-speed annular test rig was built including a rotating choking disk designed to generate PGC-like aerodynamic disturbances [194]. This disk is located downstream of the compressor stator vanes as depicted in Fig. 4.5. The periodic throttling of the compressor is therefore achieved according to the disk geometry design, choice of rotational speed and direction.

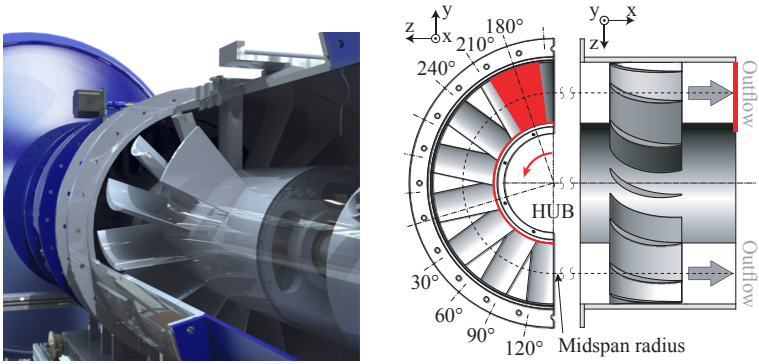

(a) Test section showing choking disk and stator vanes

(b) Choking disk marked in red, located downstream of the stator row

Figure 4.5: Low-speed test rig at the Chair for Aero Engines designed to simulate PGC disturbances in an axial compressor stage [195].

Various assessments at the annular test rig characterized the stator flow in the presence of upstream-propagating disturbances generated by the choking disk. Additionally, active flow control was implemented to reduce or mitigate the adverse effects of flow unsteadiness on the compressor aerodynamics [194–196]. It was shown by [196] that lower disturbance frequencies generated by the choking disk had a larger impact on the vane suction side flow dynamics than higher ones. Forthcoming experiments including rotor blades (designed by [197]) are expected to shed light into the complex interaction between choking disk, stator

and rotor rows. Numerical simulations as shown in Fig. 4.6 disclose the clear spectral signature due to the choking disk on the rotor blade pressure distribution, much stronger than the vane passing excitation. Such outcome indicates that not only unsteady aerodynamic, but also potential aeroelastic challenges are associated with the integration of PGC within gas turbines.

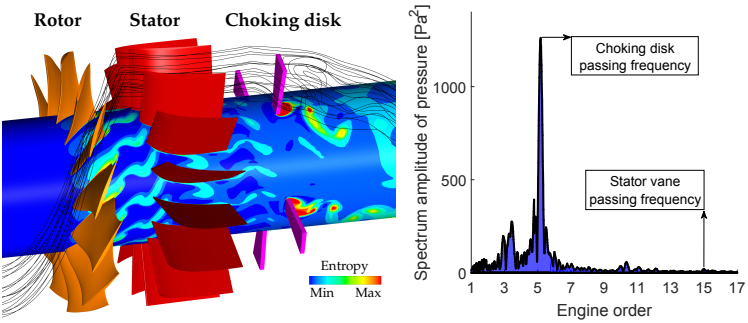

Figure 4.6: CFD sample result from the low-speed annular test rig at the Chair for Aero Engines. Left: numerical setup comprising the compressor stage and a four-sector choking disk simulating PGC aerodynamics. Right: spectrum of mean pressure on the rotor blade.

4.2.2 Rotating detonation combustion

The rotating detonation combustion (RDC) working principle differs from the typical PDE mainly in the following aspects: the detonation wave now travels circumferentially in an annular rotating chamber and the unsteady frequency is much higher (in the kHz order). Figure 4.7 depicts a concept rotor in which a detonation wave propagates circumferentially. In the RDC, the filling and purging phases occur at the same time, however at different locations. Some of the potential advantages of RDC in contrast to the PDE are the "lighter" unsteadiness (due to the higher frequencies), higher power density, self-sustained operation and no DDT challenges. Some of the drawbacks include the stability and control of a rotating detonation wave, as well as proper cooling capacity of the rotor [198, 199].

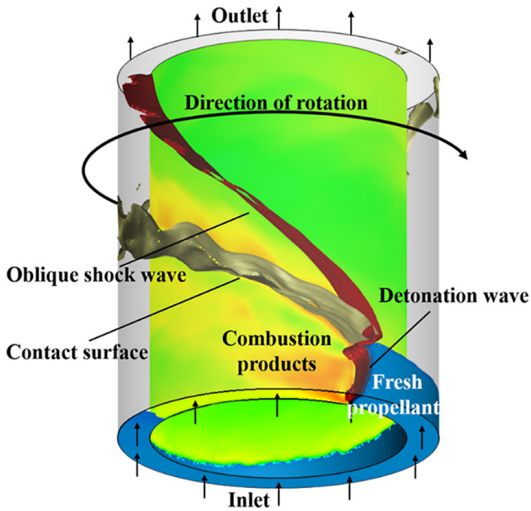

Figure 4.7: Rotating detonation combustion concept from [200].

Increase in thermodynamic efficiency with RDC has been predicted, e.g., by [201–203]. From several research initiatives, a couple are worth mentioning. Building on pioneer RDC research, [204] summarizes the progress in the chemistry understanding of the so-called "continuous spin detonation", including the successful application of hydrogen and hydrocarbon fuels.

A large body of results by another group investigating RDC was compiled by [205]. Variation in combustion and geometry parameters was thoroughly assessed, both for annular and hollow setups. Different RDC operating modes were also identified. The plenum-combustor coupling is expected to play a crucial role in RDC performance and stability.

Further endeavors analyzed in detail the behavior of RDC waves [206]. Single- and counter-rotating patterns have been experimentally characterized [207], considering different injection schemes. Later studies applied dynamic mode decomposition to better assess the unsteadiness of these phenomena [208], concluding that this data-based technique was a powerful tool to identify and reconstruct flow dynamics specific to RDC.

The interaction of the RDC with adjacent components has also been pondered by several researchers. A hypothetical integration with a gas turbine is depicted in Fig. 4.8, where the RDC radius coincides with the adjacent components size. However, it may also be the case that several smaller RDC units take the place of typical can-type combustors distributed around the annulus.

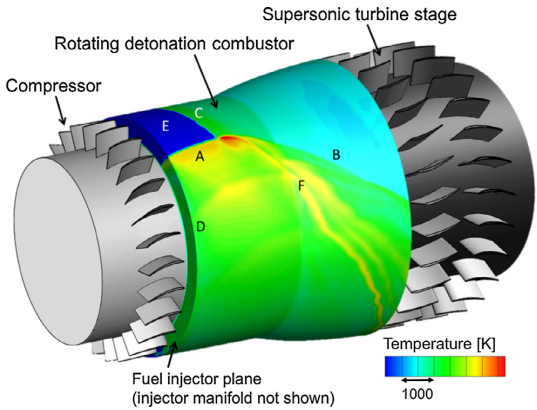

Figure 4.8: Hypothetical integration of RDC with a gas turbine [203].

Specific design and operation parameters play a critical part when estimating the perturbations expected in the compressor and turbine. For instance, [209] obtained high fluctuation values of the pressure feedback into the RDC mixture plenum, warning about the potential impact on the compressor located upstream.

The unsteady effects downstream the RDC have also been underscored. Guide vanes aft the combustor were analyzed experimentally by [210]. Further numerical assessments by [211–213] quantified the impact of blade setting angle, solidity and profile on the aerodynamic losses in the presence of RDC. Wave amplitude damping through the guide vanes was reported.

4.2.3 Shockless explosion combustion

In order to overcome the main challenges related to PDC, a new mechanism was proposed by [214], namely the shockless

explosion combustion (SEC). The concept addresses two difficulties related to PDC: high pressure peaks due to shock waves and DDT losses. In order to tackle these challenges, properly tuned smooth resonant pressure waves in a tube handle the fuel recharging process, analogously to a pulsejet combustor[2]. Figure 4.9 illustrates the SEC cycle. The reflection of PGC waves leaving the combustion tube creates a pressure gradient, which in turn is responsible for sucking in fresh air and exhausting the burnt gases. In the sequence, fuel is injected into the fresh air to provide a homogeneous charge compression ignition process, which theoretically boosts the combustion efficiency. More details about the chemistry, operation and mechanical design are given by [151, 214, 217].

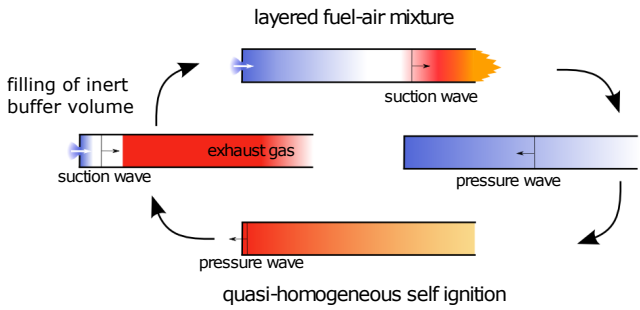

Figure 4.9: Shockless explosion combustion cycle as proposed by [214].

Thermodynamic efficiency gain with SEC has been shown by [218], where SEC exceeded the Joule cycle by a few percentage points. More involved gas turbine topologies were accessed by [219], with focus on steam injection in the Humphrey cycle. Not all configurations resulted in realistic lengths for the isochoric combustor. Further studies by [220] included a recuperator in the Humphrey cycle, yielding up to five percentage points increase in efficiency.

[2]The pulsejet was actually considered a "conceptual precursor" of the SEC [215]. However, the pulsejet operation is assumed to provide enough time for expansion of the burned gases, therefore not effectively achieving isochoric combustion [216].

Further encouraging results with SEC have been obtained. [215] have simulated the chemical kinetics and showed its theoretical feasibility without the onset of detonations. With respect to ignition delay control, [216] have developed a discrete extremum seeking controller in an atmospheric test rig; although working with a rather low firing frequency of $\frac{4}{3}$ Hz, the proposed methodology showed to be promising for further tests with higher frequency and pressure levels. Additional results were obtained by [217] with a more instrumented setup and validate the previously developed controller.

The SEC concept, however, carries also some implementation obstacles, mostly related to the ignition onset. First, proper fine mixing should be achieved in order to profit from the high efficiency of a homogeneous charge compression ignition process. Secondly, the control of ignition delay with respect to residence time is critical to ensure an homogeneous autoignition. Furthermore, the hot surfaces of the walls and exhaust gases must not be in contact with the fuel-air mixture to prevent ignition at an inappropriate moment; therefore the necessity of inert air volumes. The misfiring issue pointed out for multiple-tube PDC is also found in SEC. Lastly, extremely fast valves must be employed to guarantee correct filling of the tube with hot gas and at high frequency, regime which is so far not tolerated by current mechanical valve systems; fluidic valves could be a good alternative [214].

While the novel concept of SEC builds upon homogeneous combustion (as from internal combustion engines), another approach seeking isochoric combustion has also been considered in the last years. This older concept, commonly known as pulsejet, is also termed resonant pulse combustion (RPC).

Measured total pressure gain of 3.5% was reported by [221], employing an off-the-shelf pulsejet working at 220 Hz. The temperature ratio was approximately 2.3, similar to gas turbine values. Additionally, thrust was successfully produced and quantified with the test rig.

A subsequent step was the introduction of a turbocharger in the experimental setup [222]. The compressor discharge was connected to the pulsejet inlet and the turbine to the pulsejet outlet (see Fig. 4.10). That is, except for the bypassing air, a complete coupling turbocharger-pulsejet was obtained. Short but stable operation was reported, with approximately 20 dB attenuation in noise by the turbine. The rapid failure of reed valves was one of the main mechanical issues. To address this problem, other valve concepts such as poppet have been recently proposed and assessed [223].

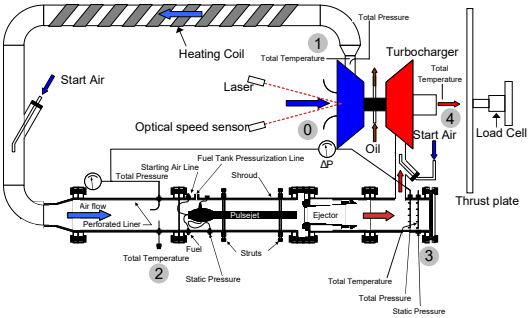

Figure 4.10: Resonant pulse combustor coupled to a turbocharger [222].

Other research groups are also active in the research of RPC (see for instance [224, 225]). Further investigation is still needed to fully understand the combustion fundamentals within RPC, as well as effective and safe integration into gas turbines.

4.2.4 Wave rotor combustion

Another attempt to harness the thermodynamic efficiency increase of isochoric combustion is the wave rotor combustion (WRC). Indeed, two main applications of wave rotors coupled with gas turbines have been recently proposed: using the rotor as a topping spool to increase cycle efficiency or using the rotor as an isochoric combustion chamber itself.

In the topping spool approach, the wave rotor is employed as a supercharger for the Joule cycle, without modifying the

combustion process itself. Here, after leaving the compressor, the air flows twice through the wave rotor before reaching the turbine. Figure 4.11 depicts a conceptual wave rotor and a burner for this type of application. The air leaving the compressor is further compressed inside the wave rotor (first passing); then, it is energized at the combustion chamber; it subsequently expands inside the wave rotor (second passing) before arriving at the turbine. The efficiency gain expected is due to the fact that the gases arrive at the turbine at the same temperature they would arrive if the wave rotor was not present (thus not requiring stronger heat-resistant turbine material), but at a slightly higher pressure. Thus, the thermal efficiency and the output power are increased. Ongoing design and testing of wave rotor as a topping spool are reported, e.g., by [226, 227].

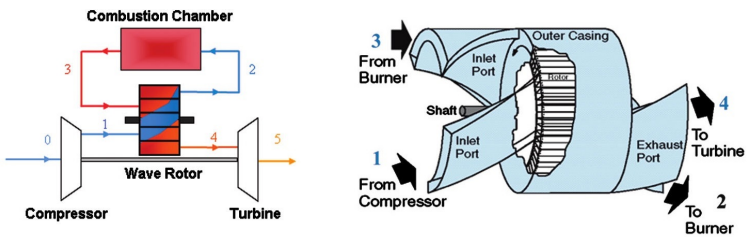

Figure 4.11: Wave rotor as a pressure-exchange system, adapted from [228].

The second application of the wave rotor discussed here aims at modifying the isobaric combustion regime to an isochoric process. Figure 4.12 depicts such a wave rotor combustor. It consists of a rotating drum in which the circumferentially distributed channels now function as multiple small combustion chambers. Two stationary endplates are located at the inlet and outlet of the rotor and act as passive controllers of fluid flow through the channels. The compression and expansion of the fuel-air mixture is achieved by the closing and opening of the rotating channel with the ports, coupled with a continuous ignition system. In principle, quick deflagration has been

considered when using WRC with gas turbines; however, larger engines could make use of detonation to reduce the cycle period and minimize weight. Two propagation regimes could be designed, based on the igniter location: in the "forward" mode, the flame travels from the inlet to the outlet end of the channel (thus the igniter is mounted in the inlet section), while in the "backward" mode, the flame travels from the outlet to the inlet end of the channel (igniter located in the outlet section) [228].

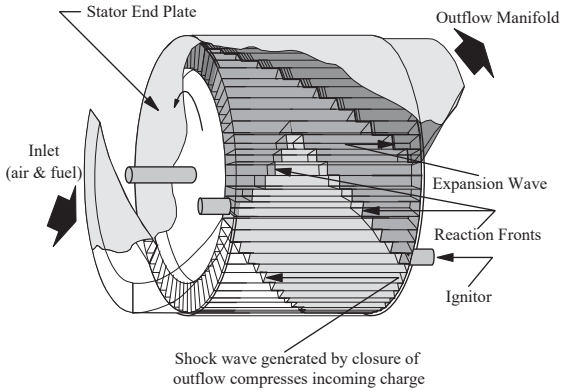

Figure 4.12: Wave rotor combustion setup from [229].

Preliminary validation of WRC against experiments has shown promising results [229, 230]. At the same time, novel design approaches are being proposed, such as rotors with non-axial channels [231].

One of the potential advantages of the WRC among PGC concepts is that a high number of channels would grant a semi-steady combustion process, at least as perceived by the upstream and downstream turbomachinery components. Additionally, enough cooling should be automatically provided by the periodic exchange of hot and cold gases within each cycle, for every channel. Some of the drawbacks of the system include proper fuel provision for rotating combustion chambers, rapid ignition methods and overall control of the combustion process [228, 229].

The impact of WRC on adjacent components is expected to be less pronounced than other PGC approaches, such as PDC. This is mostly related to the high rotational frequency perceived by the compressor and turbine. However, it comes at the price of spatial non-uniformity, due to the way the endplates are positioned circumferentially.

4.3 Summary

Although combustion modeling is out of the scope of this work, the previous sections briefly introduced some of the recently pursued PGC approaches. The work of a few research groups towards the implementation of PGC in gas turbines was also presented. This review is definitely not exhaustive, with new studies being constantly presented to the scientific communities.

Additionally, no attention was given to other PGC concepts, such as the composite (piston) topping cycle [232, 233], the radial wave engine [234] or the nutating disk [235]. All these approaches promise to deliver higher thermodynamic efficiency, and therefore lower fuel consumption of present (and future) gas turbines. Even though several features are shared, the differences among the PGC approaches will be responsible for selecting the ones most suitable for integration with turbomachinery in large scale.

What all the aforementioned devices clearly have in common is their fundamental unsteadiness. That is, the steady state combustion found it traditional gas turbines should make way for (or be combined with) novel approaches imparting fluctuations to the flow. These additional flow variations will be termed "disturbances" throughout this work[3]. They impose new technical challenges, especially when considering the integration of PGC with gas turbines.

Aerodynamic and performance issues on both compressor and turbine have been acknowledged by numerous researchers working on this integration [158, 159, 169, 209, 212, 236–242]. There are also plentiful comments and warnings about potential

[3]Not to be confused with the meaning of "disturbance" in control theory.

structural damage linked to turbomachinery vibration caused by PGC unsteadiness [170, 198, 212, 237, 243–245].

A key aspect determining the main features of the PGC disturbances are the plena (or accumulators), located between the combustor and adjacent components. Although recognized as crucial when estimating the unsteadiness strength expected by the compressor or turbine, very few studies tackle this topic in depth [209, 246, 247]. Part of this unpredictability is related to the fact that such a plenum geometry is deeply associated with the PGC and the gas turbine specifications, including mass flow rates, spatial and time scales, combustion residence time etc. Since no fully-integrated prototypes are yet available, further development regarding PGC-gas turbine integration is crucial to assess the impact the disturbances will have on the efficient and safe operation of turbomachinery components. Useful data should include the operating characteristics of PGC disturbances, their amplitude, frequency, circumferential distribution, as well as transient profiles.

In spite of this uncertainty, the simulations performed in this work deal with PGC disturbance primarily from the turbomachinery perspective (more specifically, from the compressor side). Although the physical characteristics and scales of PGC waves are based on the aforementioned references, they are cast according to parameters relevant for turbomachinery. For example, combustion frequencies are normalized by figures such as the Strouhal number or the blade passing frequency; disturbance amplitudes are standardized to mean state variables at chosen axial stations. This approach allows the direct comparison of simulations with diverse PGC excitation patterns employing different engine geometries. More details about the modeling of PGC will be given in dedicated sections in chapter 5.

5

Selected results and discussion

In this chapter, the most important results obtained with the methods described in chapters 2 and 3 are presented and discussed. First, section 5.1 provides analytical formulations for the general problem of PGC waves traveling axially. Subsequently, unsteady aerodynamics and aeroelastic assessments of two high pressure compressors subjected to PGC oscillations are given in sections 5.2 and 5.3

5.1 Unsteady damping formulation

The computations performed in this work simulate the fluid dynamics and aeroelastic effects of pressure gain combustion (PGC) in gas turbine axial compressors. As presented in detail in chapter 4, the key idea behind PGC is to increase the thermodynamic efficiency of gas turbine cycles by substituting the classic constant-pressure (or rather pressure-loss) combustion with an unsteady process that yields total pressure gain. This fundamental change in the combustion mechanism has explicit effects on the compressor.

Particularly, the boundary conditions downstream the compressor's last stage – generally assumed constant in the design phase – experience continuous change in the presence of PGC. The exact way the boundary conditions change is strictly dependent on the particular gas turbine-PGC design (processes of filling, burning, purging etc.) and on the integrating volumes between turbomachinery components and combustor (plena).

Not only the flow conditions at the very outlet of the compressor are important, but also how these changes caused by PGC unsteadiness propagate further upstream. From the turbomachinery viewpoint, the main open questions are: how exactly do the PGC disturbances affect the flow for each row/stage? How many rows are in practice subjected to these PGC disturbances? How are the losses and efficiencies affected? How does the structure react to these additional aeroelastic loads? What changes with respect to compressor stability?

This section aims at answering one of these questions, namely how the PGC disturbances travel further upstream in the compressor. Consider a representative stage as shown in Fig. 5.1, where the main flow goes from left to right, while the PGC disturbances travel upstream from right to left. The rotor blades move from the bottom upwards in Fig. 5.1(a). Also depicted are axial planes (APs), ranging from AP A to AP E. The APs have a fixed axial coordinate with varying radius and the circumferential coordinates.

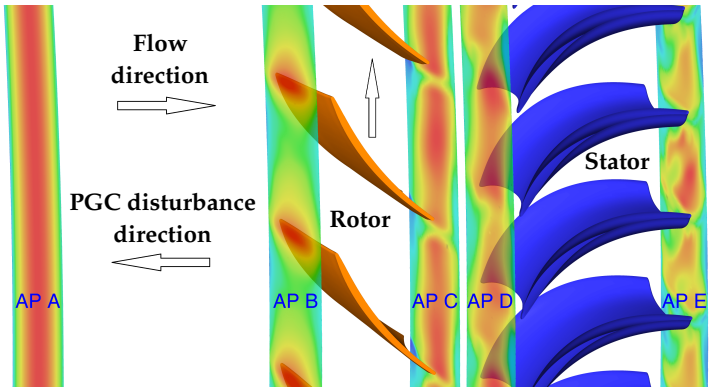

(a) 3D view

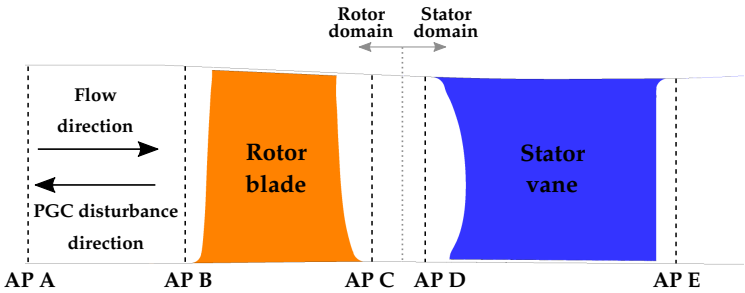

(b) Meridional view

Figure 5.1: Representative compressor stage showing axial planes (APs) employed for unsteady analyses. APs A, B and C are located in the rotor numerical domain, while APs D and E are located in the stator numerical domain. A PGC device would be positioned farther on the right, downstream of the stage.

An integrated PGC combustor (with an adequate plenum geometry) would be located right downstream the stage shown in Fig. 5.1. Suppose that, due to PGC, arbitrary fluctuations occur in the outlet boundary conditions, say on plane AP E. A reasonable question is whether or not these fluctuations will be perceived on the other APs located upstream. For that, the single-domain and cumulative unsteady damping will be now defined.

5.1.1 Single-domain unsteady damping

Consider the unsteady fluctuation of a generic variable ϕ (e.g. pressure, temperature), properly averaged in space. Sample variation scenarios for this quantity are shown in Fig. 5.2. The disturbance travels in this illustrative case from station 2 to station 1 (e.g. through the rotor domain from AP C to AP B in Fig. 5.1). Attenuation of the signal occurs in Fig. 5.2(a) (wave amplitudes goes from 10 to 5), whereas amplification takes place in Fig. 5.2(b) (amplitude goes from 10 to 20).

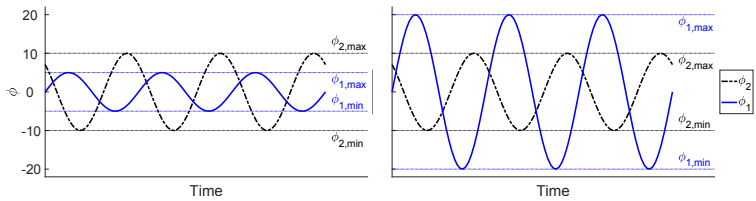

(a) Attenuation behavior ($\varepsilon_{2,1} = 0.5$) (b) Amplification behavior ($\varepsilon_{2,1} =$ -1.0)

Figure 5.2: Sample fluctuation of generic variable ϕ for two axial positions, considering a wave traveling from station 2 to 1. The unsteady damping ε is computed for each case.

In order to numerically determine the magnitude of this change in wave amplitude, we define here the *single-domain unsteady damping* $\varepsilon_{2,1}$ as

$$\Delta\phi \triangleq \frac{\phi_{max} - \phi_{min}}{\phi_{mean}}, \tag{5.1a}$$

$$\varepsilon_{2,1} \triangleq \frac{\Delta\phi_2 - \Delta\phi_1}{\Delta\phi_2}. \tag{5.1b}$$

Per construction, $-\infty < \varepsilon_{2,1} \leq 1$. Equation (5.1a) represents the nondimensional variation in the wave amplitude for one single station, normalized by its mean[1]. Equation (5.1b) then computes

[1]Note that the mean value ϕ_{mean} should be nonzero. In Fig. 5.2, the fluctuations of the generic variable ϕ occur around a "reference zero" for visualization simplicity, which is equivalent to setting ϕ_{mean} as unitary.

the unsteady damping between two arbitrary stations 2 and 1. These stations can be any two axial planes, located between rows, stages, cavities etc. This concept has been presented, e.g., by [248] when assessing the unsteady performance of an axial turbine to flow fluctuations.

Notice that, according to the definitions from Eqs. (5.1), amplitude attenuation or damping from station 2 to 1 implies $\varepsilon_{2,1} > 0$ (see Fig. 5.2(a)); conversely, amplitude increase yields $\varepsilon_{2,1} < 0$ (see Fig. 5.2(b)). Finally, perfect attenuation entails $\varepsilon_{2,1} = 1$, meaning that no flow fluctuation is perceived at station 1 (i.e., the curve for ϕ_1 becomes flat).

5.1.2 Cumulative unsteady damping

This work contributes further to the unsteady damping concept by introducing the *cumulative unsteady damping*. Specifically, it consists in an extended version of Eq. (5.1b) for multiple domains[2] sequentially stacked (e.g., several row or stages). That is, we assess how the unsteady damping ε behaves cumulatively for n stations.

For clarity, the following notation with left superscript will be employed here: between stations 2 and 1, we define $\varepsilon_{2,1} \triangleq {}^{1}\varepsilon$. Likewise, between stations $n+1$ and n, we have $\varepsilon_{n+1,n} \triangleq {}^{n}\varepsilon$. In the general case, the left superscript i_k on ${}^{i_k}\varepsilon$ lies in the range $i_1, \ldots, i_k \in \{1, \ldots, n\}$, where $k \leq n$ (the positive integer k is simply a summation index).

Now consider that the wave travels initially one more domain, namely located between stations 3 and 2. Similarly to Eq. (5.1b) for ${}^{1}\varepsilon$, we may compute another single-domain unsteady damping as

$$ {}^{2}\varepsilon \triangleq \varepsilon_{3,2} = \frac{\Delta\phi_3 - \Delta\phi_2}{\Delta\phi_3}. \tag{5.2} $$

We may then construct the cumulative damping between stations 3 and 1 as

$$ \varepsilon_{3,1} = \frac{\Delta\phi_3 - \Delta\phi_1}{\Delta\phi_3}. \tag{5.3} $$

[2]What is meant by *domain* in this context is a wave-carrying fluid medium between two axial stations.

Isolating $\Delta\phi_1$ from Eq. (5.1b) and $\Delta\phi_3$ from Eq. (5.2), and then substituting their values into Eq. (5.3), we obtain

$$\begin{aligned}\varepsilon_{3,1} = {}^1\varepsilon + {}^2\varepsilon - {}^1\varepsilon\,{}^2\varepsilon &= 1 - (1-\varepsilon_{2,1})\,(1-\varepsilon_{3,2}) \\ &= 1 - \left(1 - {}^1\varepsilon\right)\,\left(1 - {}^2\varepsilon\right), \qquad (5.4)\end{aligned}$$

which relates $\varepsilon_{3,1}$ directly and only to ${}^1\varepsilon$ and ${}^2\varepsilon$. Proceeding in the same manner for n stations, the closed formula for the cumulative damping $\varepsilon_{n+1,1}$ (between stations $n+1$ and 1) is given by

$$\varepsilon_{n+1,1} = \sum_{k=1}^{n} \sum_{\substack{i_1,\ldots,i_k \in \{1,\ldots,n\} \\ i_1 < \cdots < i_k}} (-1)^{k+1} \prod_{j=1}^{k} {}^{i_j}\varepsilon \qquad (5.5a)$$

$$= 1 - \prod_{k=1}^{n} (1 - {}^k\varepsilon). \qquad (5.5b)$$

Equation (5.5a) is a sum of unsteady damping products[3], including all the stations between ${}^1\varepsilon$ and ${}^n\varepsilon$. It represents a nonlinear relation between all single-domain unsteady damping values in the system. The equivalence between Eqs. (5.5a) and (5.5b) is formally derived in appendix A.2.

5.1.2.1 Homogeneous unsteady damping

The cumulative unsteady damping given by Eqs. (5.5) is complex to treat analytically due to the intricate nonlinear relation between all single-domain unsteady damping values. Therefore, a special case may be worth analyzing to better understand how ε behaves for practical values.

Suppose that ${}^1\varepsilon = {}^2\varepsilon = \cdots = {}^n\varepsilon \triangleq \hat{\varepsilon}$, i.e., there is a homogeneous unsteady damping $\hat{\varepsilon}$ for all domains. Accordingly, Eqs. (5.5) assume a simpler binomial form, given by Eqs. (5.6)

[3]Note that the strict inequalities in the second summation ($i_1 < \cdots < i_k$) in Eq. (5.5a) imply that the products of ${}^{i_k}\varepsilon$ do not contain repeated indexes i_k.

(note that the right superscript indicates as usual an exponent, not a domain).

$$\varepsilon_{n+1,1} = \sum_{k=1}^{n} (-1)^{k+1} \binom{n}{k} \hat{\varepsilon}^{\,k} \tag{5.6a}$$

$$= 1 - (1 - \hat{\varepsilon})^n \tag{5.6b}$$

To exemplify the analytical computation of the cumulative unsteady damping, Tab. 5.1 shows the expressions for both the general case (Eqs. (5.5)) and the homogeneous case (Eqs. (5.6)), for the first $n = 5$ domains. We notice that the cumulative unsteady damping is a polynomial of order n equal to the number of staggered domains. Additionally, the terms with odd powers of $\hat{\varepsilon}$ always contribute to the cumulative unsteady damping proportionally to the sign of $\hat{\varepsilon}$, whereas the terms with even powers, negatively.

A visual representation of the last column from Tab. 5.1 is given in Fig. 5.3. It depicts namely the cumulative unsteady damping as a function of the single-domain homogeneous value $\hat{\varepsilon}$. The number of domains vary from $n = 1, \ldots, 10$, i.e., 2 to 11 stations. This situation could represent a multistage compressor or turbine whose single-domain (for example, one stage) unsteady damping values do not change significantly among each other. For example, we can estimate from Eqs. (5.6) that if $\hat{\varepsilon} = 0.75$ for one row, three rows are already enough to produce a cumulative unsteady damping of $\varepsilon_{4,1} = 0.98$, practically imperceptible by upstream domains. On the other hand, if $\hat{\varepsilon} = -0.26$, a slightly negative value, three rows yield a twofold increase in wave amplitude for the unsteady variable ϕ, i.e., $\varepsilon_{4,1} = -1.0 \Rightarrow \Delta\phi_4 = 2\Delta\phi_1$. This large sensitivity in the range $\hat{\varepsilon} < 0$ is related to the negative sign terms multiplying even powers in Eqs. (5.6).

Table 5.1: Analytical expressions for the cumulative unsteady damping $\varepsilon_{n+1,1}$. Shown for first $n = 5$ domains.

Number of domains, n	Number of stations, $n+1$	Cumulative ε $\varepsilon_{n+1,1}$	General cumulative case Eqs. (5.5)	Homogeneous case Eqs. (5.6)
1	2	$\varepsilon_{2,1}$	${}^{1}\varepsilon$	$\hat{\varepsilon}$
2	3	$\varepsilon_{3,1}$	${}^{1}\varepsilon + {}^{2}\varepsilon - {}^{1}\varepsilon\,{}^{2}\varepsilon$	$2\hat{\varepsilon} - \hat{\varepsilon}^2$
3	4	$\varepsilon_{4,1}$	${}^{1}\varepsilon + {}^{2}\varepsilon + {}^{3}\varepsilon - {}^{1}\varepsilon\,{}^{2}\varepsilon$ $-{}^{1}\varepsilon\,{}^{3}\varepsilon - {}^{2}\varepsilon\,{}^{3}\varepsilon + {}^{1}\varepsilon\,{}^{2}\varepsilon\,{}^{3}\varepsilon$	$3\hat{\varepsilon} - 3\hat{\varepsilon}^2 + \hat{\varepsilon}^3$
4	5	$\varepsilon_{5,1}$	${}^{1}\varepsilon + {}^{2}\varepsilon + {}^{3}\varepsilon + {}^{4}\varepsilon - {}^{1}\varepsilon\,{}^{2}\varepsilon - {}^{1}\varepsilon\,{}^{3}\varepsilon$ $-{}^{1}\varepsilon\,{}^{4}\varepsilon - {}^{2}\varepsilon\,{}^{3}\varepsilon - {}^{2}\varepsilon\,{}^{4}\varepsilon - {}^{3}\varepsilon\,{}^{4}\varepsilon$ $+{}^{1}\varepsilon\,{}^{2}\varepsilon\,{}^{3}\varepsilon + {}^{1}\varepsilon\,{}^{2}\varepsilon\,{}^{4}\varepsilon + {}^{1}\varepsilon\,{}^{3}\varepsilon\,{}^{4}\varepsilon$ $+{}^{2}\varepsilon\,{}^{3}\varepsilon\,{}^{4}\varepsilon - {}^{1}\varepsilon\,{}^{2}\varepsilon\,{}^{3}\varepsilon{}^{4}\varepsilon$	$4\hat{\varepsilon} - 6\hat{\varepsilon}^2 + 4\hat{\varepsilon}^3 - \hat{\varepsilon}^4$
5	6	$\varepsilon_{6,1}$	${}^{1}\varepsilon + {}^{2}\varepsilon + {}^{3}\varepsilon + {}^{4}\varepsilon + {}^{5}\varepsilon - {}^{1}\varepsilon{}^{2}\varepsilon - {}^{1}\varepsilon{}^{3}\varepsilon$ $-{}^{1}\varepsilon{}^{4}\varepsilon - {}^{1}\varepsilon{}^{5}\varepsilon - {}^{2}\varepsilon{}^{3}\varepsilon - {}^{2}\varepsilon{}^{4}\varepsilon - {}^{2}\varepsilon{}^{5}\varepsilon$ $-{}^{3}\varepsilon{}^{4}\varepsilon - {}^{3}\varepsilon{}^{5}\varepsilon - {}^{4}\varepsilon{}^{5}\varepsilon + {}^{1}\varepsilon{}^{2}\varepsilon{}^{3}\varepsilon + {}^{1}\varepsilon{}^{2}\varepsilon{}^{4}\varepsilon$ $+{}^{1}\varepsilon{}^{2}\varepsilon{}^{5}\varepsilon + {}^{1}\varepsilon{}^{3}\varepsilon{}^{4}\varepsilon + {}^{1}\varepsilon{}^{3}\varepsilon{}^{5}\varepsilon + {}^{1}\varepsilon{}^{4}\varepsilon{}^{5}\varepsilon$ $+{}^{2}\varepsilon{}^{3}\varepsilon{}^{4}\varepsilon + {}^{2}\varepsilon{}^{3}\varepsilon{}^{5}\varepsilon + {}^{2}\varepsilon{}^{4}\varepsilon{}^{5}\varepsilon + {}^{3}\varepsilon{}^{4}\varepsilon{}^{5}\varepsilon$ $-{}^{1}\varepsilon{}^{2}\varepsilon{}^{3}\varepsilon{}^{4}\varepsilon - {}^{1}\varepsilon{}^{2}\varepsilon{}^{3}\varepsilon{}^{5}\varepsilon - {}^{1}\varepsilon{}^{2}\varepsilon{}^{4}\varepsilon{}^{5}\varepsilon$ $-{}^{1}\varepsilon{}^{3}\varepsilon{}^{4}\varepsilon{}^{5}\varepsilon - {}^{2}\varepsilon{}^{3}\varepsilon{}^{4}\varepsilon{}^{5}\varepsilon + {}^{1}\varepsilon{}^{2}\varepsilon{}^{3}\varepsilon{}^{4}\varepsilon{}^{5}\varepsilon$	$5\hat{\varepsilon} - 10\hat{\varepsilon}^2$ $+10\hat{\varepsilon}^3 - 5\hat{\varepsilon}^4 + \hat{\varepsilon}^5$

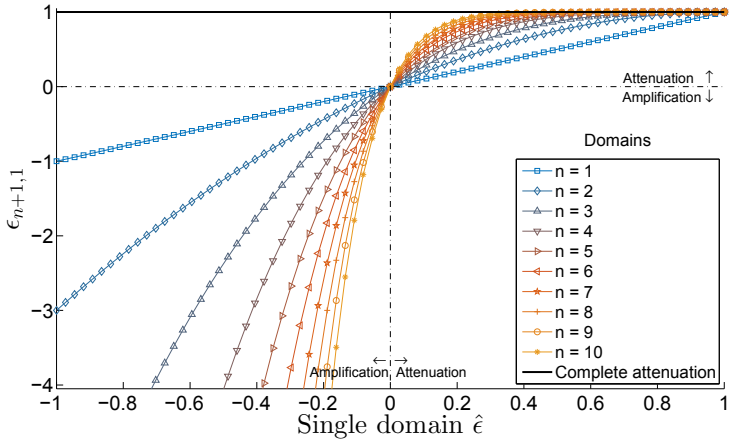

(a) $-1 \leq \hat{\varepsilon} \leq 1$

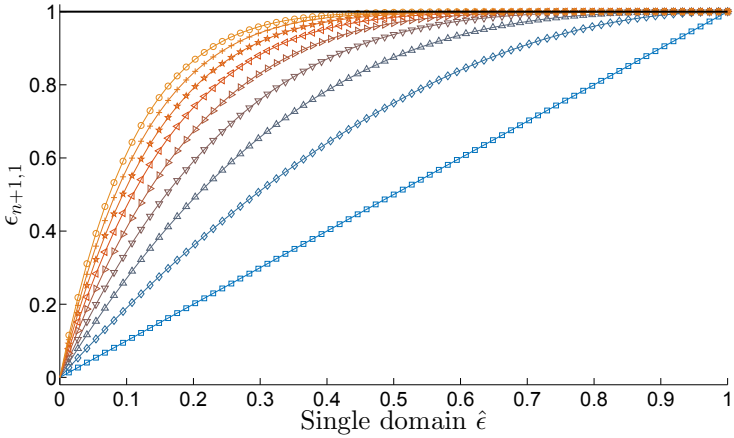

(b) Zoom into $\hat{\varepsilon} \geq 0$

Figure 5.3: Cumulative unsteady damping $\varepsilon_{n+1,1}$ (Eqs. (5.6)), as a function of the homogeneous single-domain $\hat{\varepsilon}$. Several numbers of domains n are shown.

It is also interesting to investigate the sensitivity of the cumulative unsteady damping $\varepsilon_{n+1,1}$ with respect to the number

of stations n. This can be done by computing the partial derivative with respect to n, as in Eq. (5.7)[4]

$$\frac{\partial(\varepsilon_{n+1,1})}{\partial n} = (\varepsilon_{n+1,1} - 1) \cdot \ln(1-\hat{\varepsilon}) = -(1-\hat{\varepsilon})^n \cdot \ln(1-\hat{\varepsilon}) \,. \tag{5.7}$$

Figure 5.4 shows the corresponding plot for Eq. (5.7). Focusing on the first quadrant ($\hat{\varepsilon} \geq 0$), which is the case of interest for attenuation purposes, Fig. 5.4(b) shows that all values of the derivative are positive. This means that the addition of further rows/stages for a homogeneous $\hat{\varepsilon} > 0$ will always enhance the cumulative unsteady damping. Increase in the number of domains n flattens the curve towards complete attenuation.

Additionally, the loci of maxima is also shown in Fig. 5.4, whose analytical coordinates are given by

$$\left(\hat{\varepsilon}_{max}\,,\ \frac{\partial(\varepsilon_{n+1,1})_{max}}{\partial n}\right) = \left(1 - \frac{1}{e^n}\,,\ \frac{1}{n\,e}\right). \tag{5.8}$$

From Eq. (5.8), $\hat{\varepsilon}_{max}$ has its upper limit at $n = 1$ (namely with a value of approximately 0.6321), considering only integer numbers of domains. That is, the maximum sensitivity in attenuation gain always decreases with the stacking of further domains, approaching zero monotonically as $n \to \infty$.

5.1.2.2 Alternating unsteady damping

The homogeneous unsteady damping discussed in section 5.1.2.1 can be quite restrictive by assuming the same value for all domains. A more flexible approach would be to have alternating unsteady damping for every other domain. As an example suitable for turbomachinery multirow setups, an alternating pattern may arise if the rotor rows are expected to provide more/less damping than the stator rows in a uniform manner.

[4]Equation (5.7) is strictly defined only for $\hat{\varepsilon} < 1$. This is almost always the case from the definition range of ε, except for the trivial case $\hat{\varepsilon} = 1$.

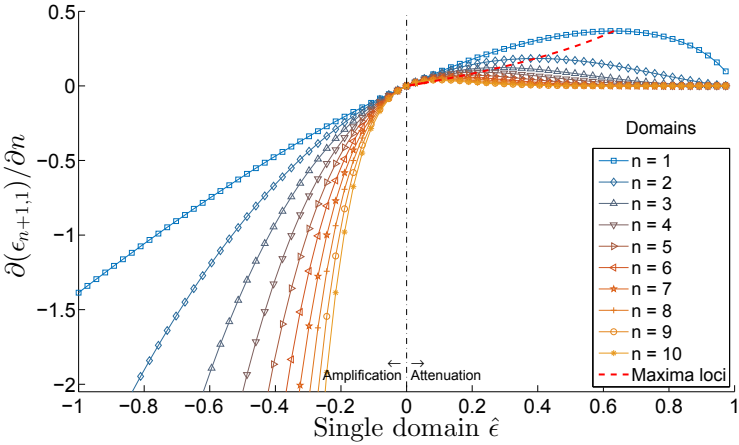

(a) $-1 \leq \hat{\varepsilon} < 1$

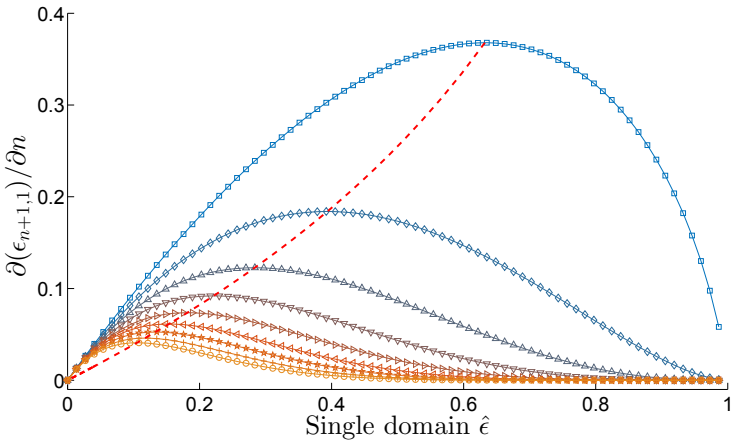

(b) Zoom into $\hat{\varepsilon} \geq 0$

Figure 5.4: Sensitivity of cumulative unsteady damping $\varepsilon_{n+1,1}$ (Eq. (5.7)), as a function of the homogeneous single-domain $\hat{\varepsilon}$. Several numbers of domains n are shown.

Now we define the unsteady damping for domains with odd and even indexes respectively as ${}^{ODD}\varepsilon$ and ${}^{EVEN}\varepsilon$. Then, Eq. (5.5b) becomes

$$\varepsilon_{n+1,1} = 1 - \left[\left(1 - {}^{ODD}\varepsilon\right)\left(1 - {}^{EVEN}\varepsilon\right)\right]^{\frac{n-1}{2}} \left(1 - {}^{ODD}\varepsilon\right) \qquad \text{for } n \text{ odd} \tag{5.9a}$$

$$\varepsilon_{n+1,1} = 1 - \left[\left(1 - {}^{ODD}\varepsilon\right)\left(1 - {}^{EVEN}\varepsilon\right)\right]^{\frac{n-1}{2}} \qquad \text{for } n \text{ even} \tag{5.9b}$$

The effect of alternating pattern on the cumulative unsteady damping can be seen in Fig. 5.5, where only 1 to 3 domains are shown for clarity. The ratio between the odd and even unsteady damping values is given by the factor $f = {}^{ODD}\varepsilon / {}^{EVEN}\varepsilon$. This formulation might be useful when the designer has a better idea of how the disturbances change in amplitude along specific domains.

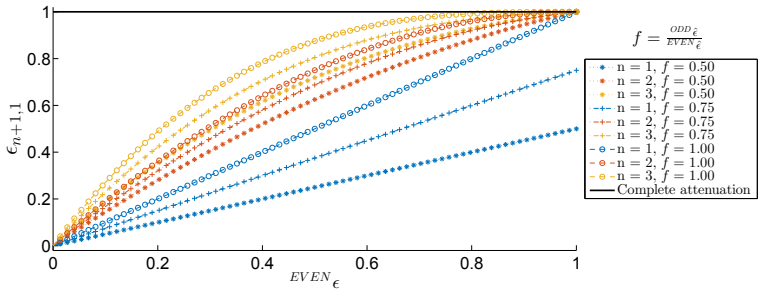

(a) ${}^{ODD}\varepsilon \leq {}^{EVEN}\varepsilon$

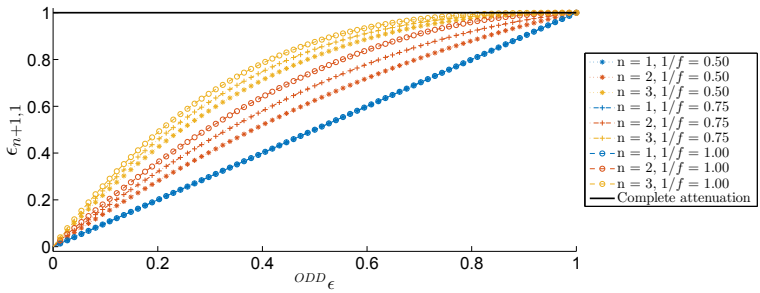

(b) ${}^{ODD}\varepsilon \geq {}^{EVEN}\varepsilon$

Figure 5.5: Cumulative unsteady damping $\varepsilon_{n+1,1}$ for alternating case. Odd and even single-domain unsteady damping are given respectively by ${}^{ODD}\varepsilon$ and ${}^{EVEN}\varepsilon$.

5.1.3 Conclusions

This section provided a rather simple analytical model to quantitatively assess how waves traveling axially through fluid domains experience changes in their amplitude. The introduction of the "unsteady damping" in section 5.1.1 as described by Eqs. (5.1) enables the empirical determination of whether the amplitude of a periodically varying quantity (such as pressure) remains constant, increases or decreases as the wave travels axially through a fluid domain (row, stage etc.) in a turbomachine.

Moreover, the formulation for a single domain was extended to multiple instances in section 5.1.2. For that, the cumulative unsteady damping has been derived, as given by Eqs. (5.5). These general expressions apply to cases with arbitrary values of unsteady damping at each domain, which are then combined into a final figure representing all the analyzed domains as one single instance.

Two special cases have been derived from the general cumulative unsteady damping formulation. Firstly, the homogeneous unsteady damping was presented in section 5.1.2.1, considering a fixed value for the single-domain unsteady damping. This procedure results in the simple expressions given by Eqs. (5.6), illustrated in Fig. 5.3. This simplification is advantageous e.g. in the preliminary design phase of turbomachinery components which shall be subject to PGC disturbances, especially if no detailed information on flow response to combustion unsteadiness is available. Unsteady damping records from other experiments and numerical estimations (such as the ones presented in this work) may serve as ballpark figures for the aerodynamics and aeroelastic designers.

A second special case of the cumulative damping relaxes the homogeneous assumption by considering an alternating pattern. This is conveyed by Eqs. (5.9) and shown in Fig. 5.5. Such a situation could represent turbomachinery components such as multistage compressors and turbines, which are predominantly

arranged with successive alternating rotor and stator rows. Additionally, some aerodynamic designs employ very similar blade profiles for adjacent stages, while slightly rescaling the geometries to account for constant mass flow. If empirically observed or numerically estimated that each type of domain produces rather uniform values along the machine, the alternating formulation comes in handy for initial assessments.

Other modeling strategies are of course possible, apart from the homogeneous and alternating unsteady damping approaches. Once more simulations and empirical results are available in the literature regarding unsteady fluid dynamics in turbomachinery, a road map to more detailed and precise modeling may be drawn expanding the understanding of the effects of flow fluctuations originated from PGC on compressors and turbines. The present work starts this inquiry by numerically applying the unsteady damping concepts presented in this section to two high pressure compressors subjected to PGC disturbances in sections 5.2 and 5.3.

5.2 Case study 1

5.2.1 Case description

This work aims at numerically analyzing how PGC disturbances affect turbomachinery components (more specifically the HPC) with respect to unsteady fluid dynamics and aeroelastic aspects. So as to assess these effects as reliably as practicable with the information existing in this day and age, we have chosen to simulate modern industrial (aero) engines.

The first case study presented here employs a research highly-loaded core compressor developed for modern aero engines. It was designed focusing on the future generation of medium thrust range engines. The first six stages feature titanium blisks, while the last three comprise conventional bladed disk arrangements. Figure 5.6 shows a reference engine integrated with case study 1 core compressor.

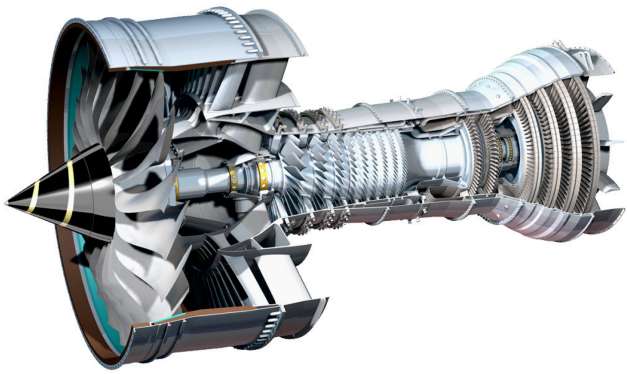

Figure 5.6: Hypothetical integration of case study 1 core compressor into a reference aero engine [249].

For the simulations, pre-validated operating conditions from cruise altitude have been chosen, delivering large overall pressure ratio and high efficiency. Additionally, since we focus on the aeroelastic behavior subject to PGC, the last blisk stage has been selected for the analyses (although more rows have been also

modeled, as discussed later). This is justified by the fact that blisk rotors lack platform-blade friction damping (as reviewed in section 2.4.2). Since material (hysteretic) damping is considered negligible for titanium parts, the only damping source left is the aerodynamic.

5.2.2 Numerical aspects

The case study 1 configurations simulated here are shown in Tab. 5.3. Not only the last blisk rotor (R6) is modeled, but also the entire sixth stage (R6-S6) and also a last configuration with one more stage downstream (R6-S6-R7-S7). This is important to compare the significance of PGC disturbances traveling upstream with the unsteadiness already present in the system due to rotor-stator interactions. Comments about the number of passages modeled and cells will be provided later.

Table 5.3: Domain configurations for case study 1 numerical model.

Configuration	Rows	Modeled passages	Millions of cells
R6	1	1	0.8
R6-S6	2	7	4.8
R6-S6-R7-S7	4	9	6.2

Grid independence studies have been performed to ensure reliable numerical results. Two main criteria have been employed to determine when a mesh is coarse/fine enough when representing the model. They are: (i) quantitative comparison of scalar quantities representing the whole flow; (ii) the grid convergence index (GCI) [250], whose detailed methodology is presented in appendix A.1.

Numerous grids with different spatial discretizations were generated for case study 1 last stages (for general meshing details, see section 3.2.2.1). The change in the number of cells among meshes was conducted as uniformly as possible, however keeping approximately 30 cells close to all walls to fully resolve the boundary layers. For succinctness, remarks will be made only regarding the configuration R6-S6, which can be extended for the

other setups. For steady state simulations performed independently for rotor and stator, Fig. 5.7 shows normalized values of isentropic efficiency and mass flow for several grids modeling R6 and S6.

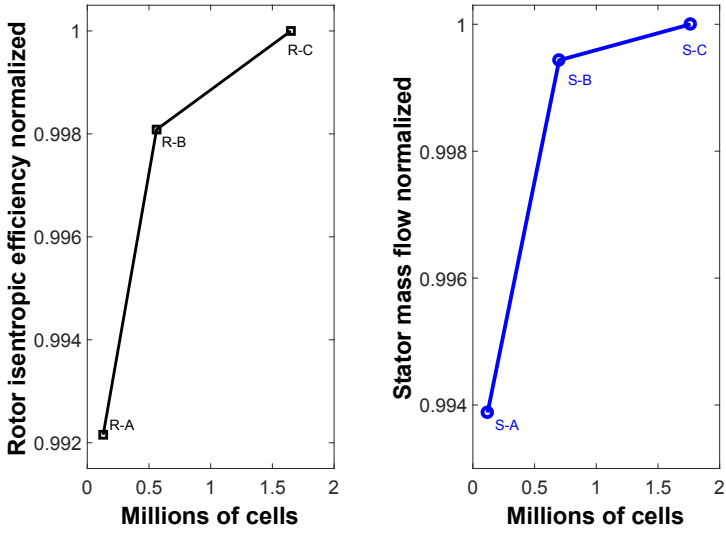

(a) Rotor R6

(b) Stator S6

Figure 5.7: Normalized scalars representing flow in the sixth stage of case study 1, showing grids with different spatial discretizations.

The first criteria to confirm grid trustworthiness is to compare the relative error between the quantities shown in each of the plots in Figure 5.7 for different meshes. For example, we notice in Fig. 5.7(a) that the relative change in isentropic efficiency between all rotor grids shown is less than 1%, which is deemed precise enough for the desired analyses. To further improve the local depiction of fine-scale phenomena and pressure distribution on the surfaces, grid R-B has been chosen for modeling the R6 passage. This choice implies a good trade-off between precision and computational requirements. With respect to the second convergence criteria, namely the GCI, the index between the

medium (B) and fine (C) grids in Fig. 5.7 is $\mathrm{GCI}_{\mathrm{BC}} = 0.24\%$. The apparent convergence order was 1.94, which matches well with the theoretical second order schemes employed.

Similar considerations are applied for the choice of the stator mesh. Grid S-B is deemed precise enough to model the S6 passage, even though the coarser mesh S-A also produced acceptable results. Grids R-B and S-B for the sixth stage are assembled together and depicted in Fig. (5.8). The displayed scale of this and all other figures in this section is different from the true original geometries for privacy reasons.

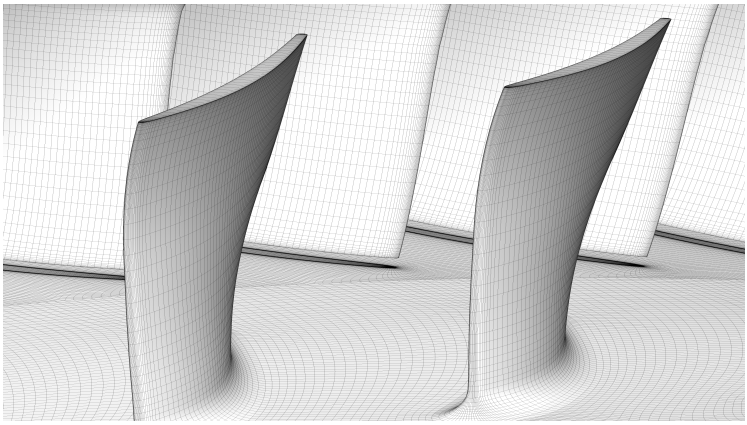

Figure 5.8: Meshes for the sixth stage (R6 at the front and S6 in the back), chosen according to grid independence study. Assembly showing R-B and S-B from Fig. 5.7. Geometries rescaled.

Analogously to the spatial discretization study just described, the precision with respect to the time domain was investigated. Initially, undisturbed unsteady computations were conducted until periodic convergence was obtained. More specifically, when the relative difference between two consecutive periods for some globally integrated parameter (such as compression ratio or efficiency) or pressure probe falls below 0.05%.

The choice of time step size depends on the time scales of the relevant phenomena occurring in the system. Typical events

include the blade or vane passing frequencies (BPF and VPF), flow instabilities and vortex shedding, and in our specific case the periodicity of the PGC processes. The number of time steps per rotor passing period (TSRPP) has been varied, with transient results for probes located between the R6 and S6 domains shown in Fig. 5.9. The probes are not located at the exact boundary, but inside the domains, next to each respective blade/vane, so that the normalization period in the horizontal axis matches each corresponding frame of reference. We notice that, beyond 50 TSRPP, further refinement in the time discretization incurs no significant change in the pressure coefficient for the probes. A slightly higher value of 55 has been chosen to carry the unsteady analyses.

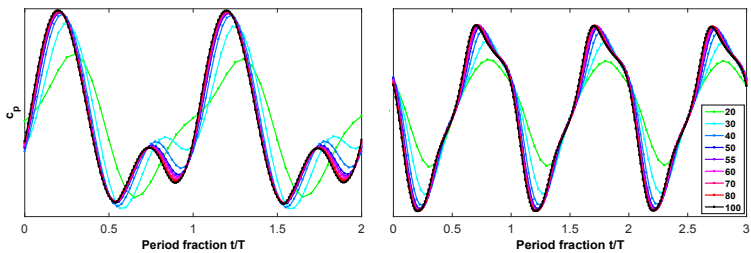

(a) Probe downstream of R6 blade (b) Probe upstream of S6 vane

Figure 5.9: Periodically-converged pressure coefficient c_p for point probes. Values represent the number of time steps per rotor passing period.

Additionally, to make sure that global scalars are also accurately represented by this time discretization, an extra simulation with halved time step (110 TSRPP) was conducted, for an extra full rotor revolution. In comparison with the 55 TSRPP setup, a relative difference of 0.09% and 0.005% respectively for isentropic efficiency and compression ratio was obtained. Other quantities such as unsteady damping and modal forcing yielded similar minimal changes. Therefore, the time resolution of 55 TSRPP was presumed precise enough for the unsteady runs with case study 1, taking also into account the PGC disturbance frequencies to be modeled.

It is relevant to mention that the case study 1 core compressor has not been specifically developed to be integrated with PGC systems, but rather to be installed right upstream of typical combustors working with constant deflagration. Therefore, we investigate how configurations such as case study 1, designed regarding conventional combustion constraints, would potentially react to novel unsteady combustion processes such as PGC.

Following the discussion in chapter 4, PGC is designed to work with periodic events occurring at high frequencies. Therefore, the most insightful boundary conditions to implement initially are harmonic fluctuations at the HPC outlet. Generally, static pressure and sometimes mass flow are employed as outlet boundary conditions for turbomachinery models. We favor here the static pressure over mass flow, since it promotes good numerical stability and may be more easily related to values obtained experimentally. Accordingly, the outlet boundary conditions, modeling PGC disturbance waves propagating upstream, are computed in the current section as

$$p(\mathbf{x}, t) = p(\mathbf{x}) \; [1 + A_d \cdot \sin(2\,\pi\, f_d\, t)] \,, \tag{5.10}$$

where A_d and f_d are the wave amplitude and frequency describing the harmonic change in the profile $p(\mathbf{x}, t)$. In the entire work, the disturbance frequency f_d will be given nondimensionally either as a multiple of the BPF or the St number (section 2.2.1.2). The simulated frequencies f_d are chosen far enough from the natural frequencies of the blades, motivated by the fact that a reasonable engine design would not have the PGC firing frequency matching the high-energy eigenvalues of the turbomachinery structure.

Furthermore, since the original boundary conditions are given as radial profiles, we implement for case study 1 the variations described by Eq. (5.10) as a function of the radius r, that is, $p(\mathbf{x}, t) = p(r, t)$. This approach presumes that the number of blades and vanes is considerably larger than the number of combustion units downstream (e.g. detonation tubes). That is, no disturbance wave circumferential interaction among combustor

units is initially modeled. More comments about this and other types of outlet conditions will be given later.

Referring back to Fig. 3.5 for an overview, this section is embedded within the CFD branch. More specifically, departing from steady state into the unsteady analyses. With the implementation of PGC disturbances (such as Eq. (5.10)) the simulations will deliver unsteady fluid dynamics and performance results, which will be compared with the undisturbed case. Additionally, the outcome will be then employed in the CSM assessments in order to obtain the aeroelastic results given in section 5.2.4.

5.2.3 Performance

We present initially the effects of PGC on case study 1 core compressor from the performance point of view. This is particularly relevant since, although these new combustion approaches promise significant increase in overall efficiency, potential component losses may be introduced, which could hinder the expected gains. Indeed, the establishment of PGC technologies integrated into gas turbines depends critically on the synergy between the combustion and turbomachinery systems.

The performance results will be presented sequentially for the different configurations given in Tab. 5.3. The outcome in the presence of PGC disturbances will be constantly contrasted with the so-called baseline case, which consists in an unsteady computation with constant boundary conditions (conversely, $A_d = 0$ in Eq. (5.10)).

5.2.3.1 R6

The most simple row setup from the analyzed configurations comprises only the rotor R6. Since just a single row is modeled, no rotor-stator interaction occurs, and we are able to understand how the PGC disturbances would directly affect the flow through the rotor blades only.

Total pressure loss

The total pressure loss ω for the R6 configuration is shown in Figure. 5.10, as a function of disturbance frequency given as a multiple of the BPF and the Strouhal number St. Values are shown for two different disturbance amplitudes A_d. As already stated, the normalization for the PGC-disturbed case is done with respect to the mean value for the undisturbed unsteady reference.

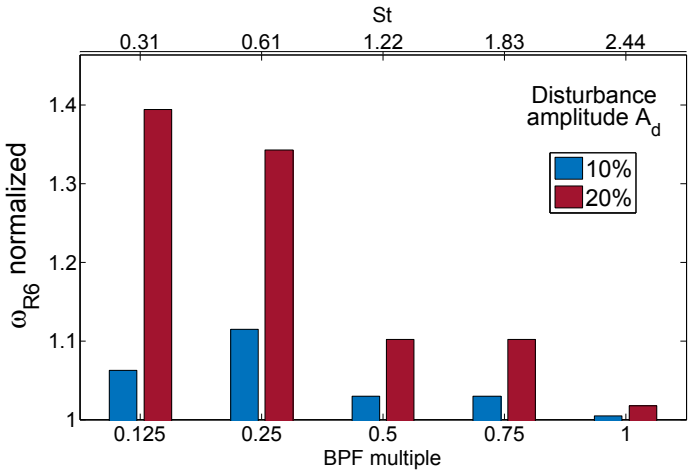

Figure 5.10: Normalized total pressure loss ω_{R6} for configuration R6, as a function of disturbance frequency f_d and amplitude A_d (see Eq. (5.10)).

Initially, we observe that lower disturbance frequencies incur higher losses in the system. For $f_d = 0.125$ BPF, an increase of almost 40% in loss occurs, for a disturbance amplitude $A_d = 20\%$. For $A_d = 10\%$, the increase in ω_{R6} was approximately 10% or less for all disturbance frequencies analyzed. Finally, for frequencies close to or higher than the BPF, no significant increment in ω_{R6} is observed.

These results can be explained by the duration of the interaction between the disturbance wave and the flow dynamics in the blade row. Indeed, the disturbance wave alters the mass flow periodically, offsetting the rotor from its baseline design condition. When the high-pressure half of the PGC wave

approaches the rotor trailing edge, an increase in the incidence angle occurs, provoking temporary separation on the suction side of the blade; the flow reattaches before the next PGC wave comes. Subsequentially, when the low-pressure half of the PGC wave approaches the trailing edge, small negative incidence angles occur, in a temporary behavior resembling choking. Both these departures from the design point explain the observed increase in total pressure loss. However, the necessary time for the blade to reestablish its "design-point flow" is shorter for the high-frequency disturbances, which explains the distribution in Fig. 5.10.

Unsteady damping

The unsteady damping presented in section 5.1 has been computed for all simulated configurations. According to its definition (Eqs. (5.1)), two planes are needed to define a domain. In the R6 case, the domain represents the blade passage, while planes 1 and 2 (or conversely AP B and AP C in Fig. 5.1) are located right upstream the leading edge and downstream the trailing edge, respectively. That is, the planes do not correspond to the inlet and outlet of the CFD domain, since at these locations some state variables are fixed a priori, and would not vary according to the system dynamics. Choosing planes close to the blade's leading and trailing edge allows the computation of the flow fluctuations without undesired interference of prescribed boundary conditions or numerical artifacts. This reasoning is applied for all configurations in this work.

The R6 unsteady damping will be denoted here, for simplicity, as ε_{R6}, considering that for all cases the PGC wave travels upstream, and the station position is clearly stated. The results for ε_{R6} are shown in Fig. 5.11 as a function of the disturbance frequency, for static pressure and temperature. Again, disturbance amplitudes of $A_d = 10\%$ and $A_d = 20\%$ are depicted. The outcome for total pressure and total temperature are very similar, and will not be shown here for brevity.

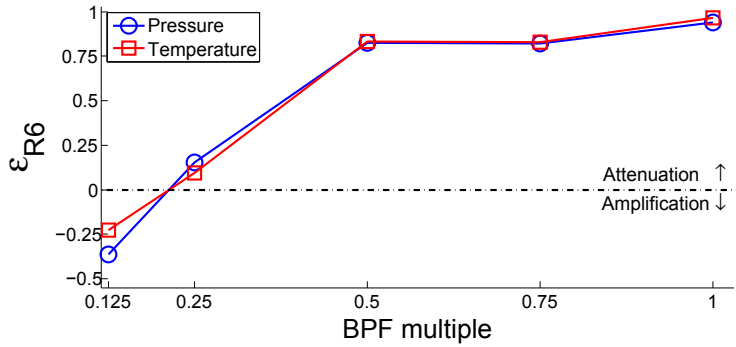

(a) Disturbance amplitude $A_d = 10\%$

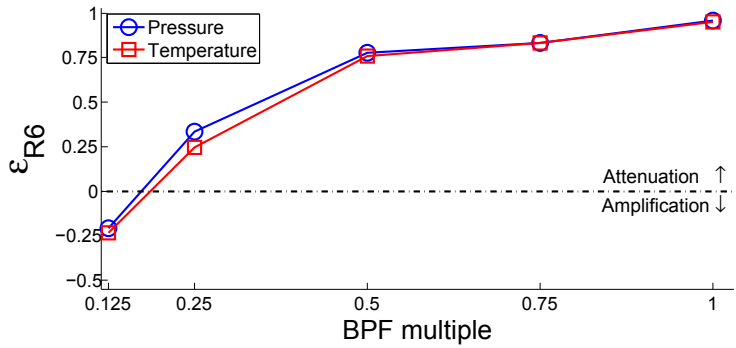

(b) Disturbance amplitude $A_d = 20\%$

Figure 5.11: Unsteady damping for configuration R6, depicting static pressure and temperature.

Considering frequency values of $f_d < 0.5$ BPF, a significant drop in ε_{R6} takes place, becoming even negative for $f_d = 0.125$ BPF. This implies that the rotor only was not capable of effectively chopping the disturbance wave, whose amplitude even increased. To the best of our knowledge, this situation had not been yet reported in the literature for such upstream propagating disturbances. This outcome advocates the importance of evaluating how farther these waves propagate, and motivates the assessment of multistage setups, as presented in the following sections.

5.2.3.2 R6-S6

Including the sixth stator in the computations allows us to understand how the presence of another row changes the way the PGC wave interacts with the rotor flow. It also makes the assessments more complex, since now rotor-stator interaction also occurs additionally to the PGC unsteadiness.

In order to prevent phasing and frequency errors inherent from non-unitary pitch ratios and approximated rotor-stator interfacing methods, the number of passages for the configuration R6-S6 has been slightly adjusted. Although simulating more passages implies higher computation costs, no scaling or time-lagging between domains must be employed. In the present case, the main advantage of unitary pitch ratio is preserving the real frequency content – from the R6-S6 interaction and the PGC.

Isentropic efficiency

The isentropic efficiency is essential when assessing how efficiently a compressor stage increases the fluid density without incurring excessive losses. Figure 5.12 shows the change in isentropic efficiency $\Delta\eta_{R6-S6}$ as a function of the disturbance frequency.

A substantial drop in efficiency of almost 25% takes place for $f_d = 0.25$ BPF. As discussed in section 5.2.3.1, the period when the row/stage remains far from its design point is directly linked to the increase in losses and corresponding decrease in efficiency. With respect to the frequencies shown in Figure 5.12, we notice that the drop in efficiency is greater for $f_d = 0.25$ BPF than $f_d = 0.125$ BPF. This is due to the fact that for the lowest frequency there is enough time for the flow around the blade to reestablish itself, back from partial separation, before the next PGC wave arrives. Since this interval is too short for $f_d = 0.25$ BPF, the system remains constantly disrupted from its design point, diminishing its isentropic efficiency. Figure 5.13 shows instantaneous flow snapshots for a cross section with entropy contours, for the undisturbed case and a disturbed

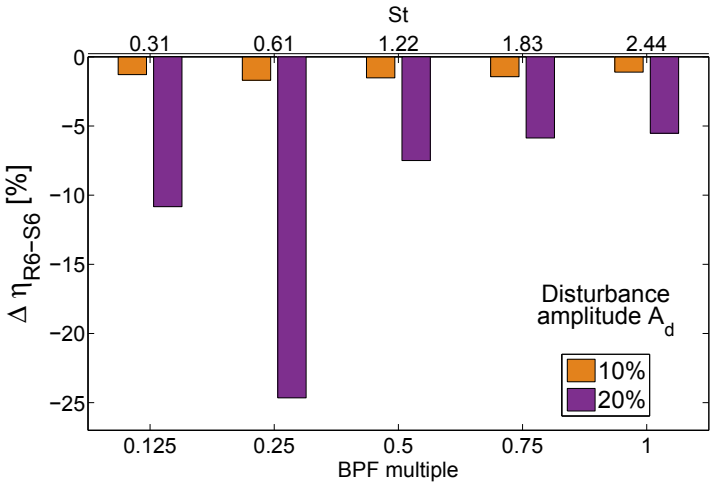

Figure 5.12: Normalized isentropic efficiency variation $\Delta\eta_{R6-S6}$ for configuration R6-S6, as a function of disturbance frequency f_d and amplitude A_d (see Eq. (5.10)).

scenario. The temporary recirculation zones just discussed are clearly seen close to the suction side, accompanied by high entropy regions.

A representation similar to Fig. 5.12, however with a higher density of computed disturbance amplitudes, is given in Fig. 5.14. This map is a function of the disturbance frequency and amplitude, and can be readily employed when assessing how particular PGC conditions shall affect the efficiency of a compressor stage. Darker regions at the top left corner indicate the higher drop in isentropic efficiency for low f_d and high A_d. The decrease in efficiency as a function of disturbance amplitude yielded a square dependency, with a coefficient of determination $R^2 > 0.98$.

Unsteady damping

Figure. 5.15 shows the unsteady damping for the R6-S6 configuration for static pressure and temperature. In this stage case, station 2 is located right downstream of S6, while station 1 right upstream of R6 (or respectively AP E and AP B in Fig. 5.1).

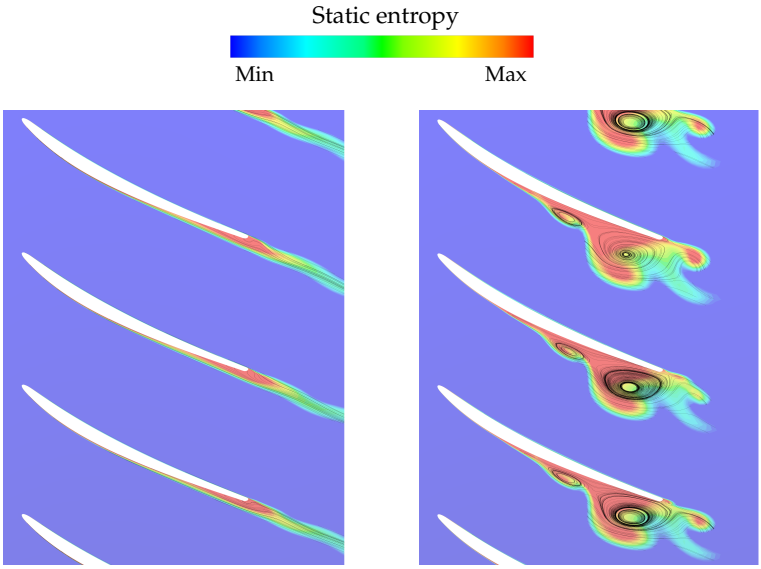

(b) Undisturbed (c) Disturbed

Figure 5.13: Selected instantaneous contours for static entropy and surface streamlines for rotor blade R6, cross section at 40% span. Simulated for configuration R6-S6, with $f_d = 0.25$ BPF and $A_d = 20\%$. The recirculation zones are clearly visible in the disturbed case. Geometries rescaled.

A distribution similar to the R6 configuration (Fig. 5.11) occurs. The lowest disturbance frequency shown, $f_d = 0.125$ BPF, produces a negative ε_{R6-S6} for static pressure with wave amplitude of $A_d = 10\%$, i.e., an increase along its journey. The unsteady damping for the static temperature is on the verge of crossing the border from attenuation to amplification; that is, the wave amplitude for he temperature virtually does not change along the stage.

We notice that, for this HPC, the presence of a stage dampens out the PGC waves for high disturbance frequencies, but was not capable of doing so for low PGC disturbance frequencies.

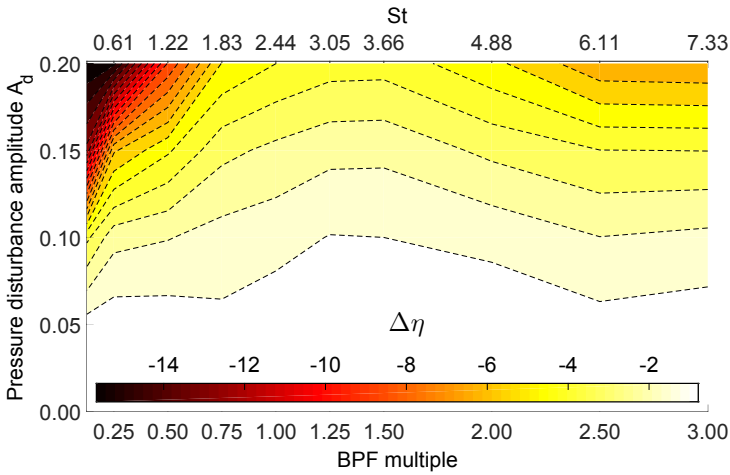

Figure 5.14: Isentropic efficiency η map, function of PGC disturbance frequency f_d and amplitude A_d (see Eq. (5.10)). The color shows the percentual variation in η.

5.2.3.3 R6-S6-R7-S7

In addition to the single-row and stage configurations, a multistage setup was simulated within the same PGC disturbance range. The seventh stage was modeled downstream, through which the PGC wave first travels before reaching the sixth stage. The results for performance, unsteady damping and also modal forcing (to be presented later) may be compared to the previous section outcome in order to understand how the addition of two more rows would influence the aerodynamic and aeroelastic response of one specific stage. Since in this case maintaining a unitary pitch ratio would be computationally prohibitive due to the specific blade count, the added stage comprises one passage per row, so that phase errors in the seventh stage may occur.

Isentropic efficiency

The variation in normalized isentropic efficiency is depicted in Fig. 5.16, separately for the sixth and seventh stages. Both plots have the same scale to ease the comparison.

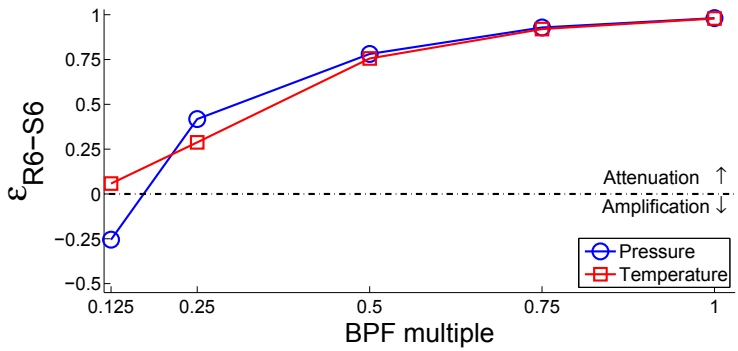

(a) Disturbance amplitude $A_d = 10\%$

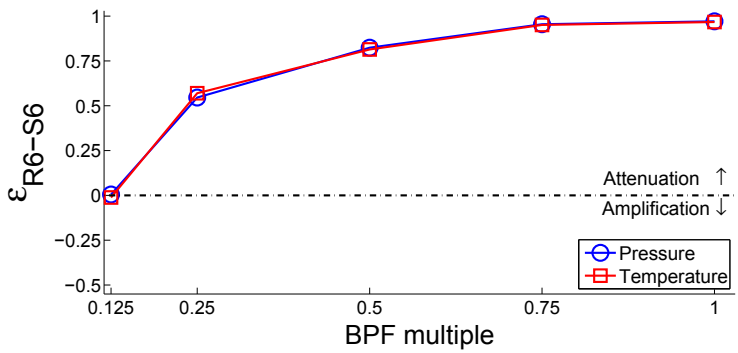

(b) Disturbance amplitude $A_d = 20\%$

Figure 5.15: Unsteady damping for configuration R6-S6, for static pressure and temperature.

According to Fig. 5.16(b), there is an evident strong drop in efficiency for the seventh stage, namely of $\Delta\eta_{R7-S7} = -25.4\%$ for a disturbance frequency of $f_d = 0.125$ BPF and amplitude $A_d = 20\%$. For all simulated frequencies at $A_d = 20\%$, the drop in $\Delta\eta_{R7-S7}$ always surpassed 10%. The decrease in η is more pronounced for the seventh in comparison to the sixth stage since the PGC wave first meets the most downstream rows before propagating further.

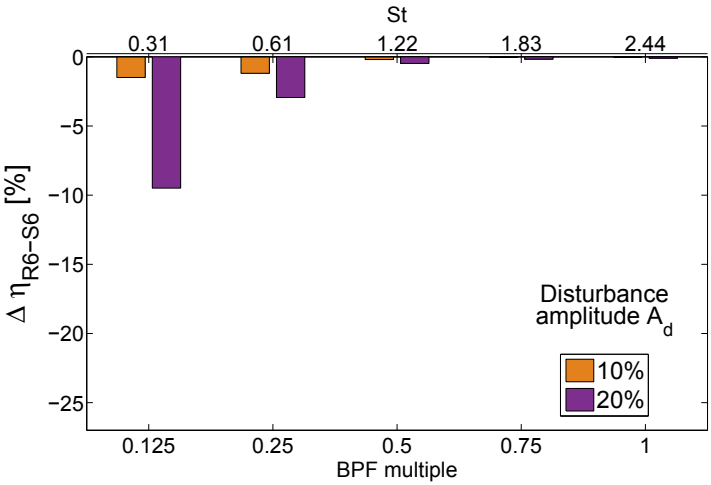

(a) Stage 6

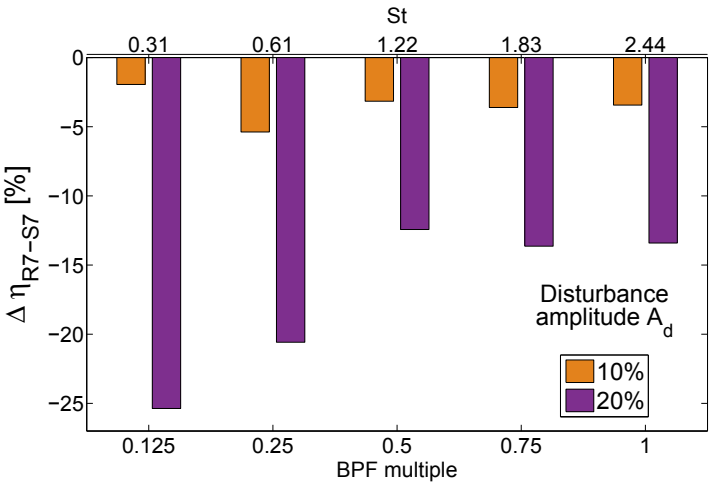

(b) Stage 7

Figure 5.16: Normalized isentropic efficiency variations $\Delta\eta_{R6-S6}$ and $\Delta\eta_{R7-S7}$ for configuration R6-S6-R7-S7, as a function of disturbance frequency f_d and amplitude A_d (see Eq. (5.10)).

Referring to Fig. 5.16(a), we notice that the efficiency reduction is mostly restricted to values less than 5%. The only exception is the case with $f_d = 0.125$ BPF and $A_d = 20\%$. The previously observed trend of higher losses for low disturbance frequencies is also kept for the R6-S6-R7-S7 configuration.

The worst outcome shown in Fig. 5.16(b) indicates that order of magnitude of the efficiency decrease is definitely not negligible from the performance point of view. However, the comparatively reduced values from Fig. 5.16(a) for stage 6 (especially in contrast with Fig. 5.12) hint that the presence of an extra stage downstream is directly responsible for attenuating the efficiency drop in the upstream rows.

Unsteady damping

The unsteady damping for this multistage setup is shown for the entire domain in Fig. 5.17. Similarly to previous results, high disturbance frequencies were strongly damped along the two stages, with $\varepsilon_{R6-S6-R7-S7} \approx 1$ for $f_d \geq 0.5$ BPF. However, visible decrease occurs for low disturbance frequencies, reaching $\varepsilon_{R6-S6-R7-S7} < 0$ for $f_d = 0.125$ BPF for all variables shown.

The temporal development of a specific case is depicted in Fig. 5.18. The static pressure is normalized by the mean value at the R6 inlet and is shown after periodic convergence has been reached. Fig. 5.18 can be interpreted analogously to Fig. 5.2(b), where the initial wave amplitude is increased after traveling through the domain.

The concept of cumulative unsteady damping developed in section 5.1.2 is numerically portrayed in Tab. 5.4. Values are shown for the sixth and seventh stages separately and also for the whole R6-S6-R7-S7 domain. It is straightforward to verify that Eqs. (5.5) fully hold, more specifically in the two-stage form $\varepsilon_{R6S6R7S7} = [1 - (1 - \varepsilon_{R6S6})\ (1 - \varepsilon_{R7S7})]$.

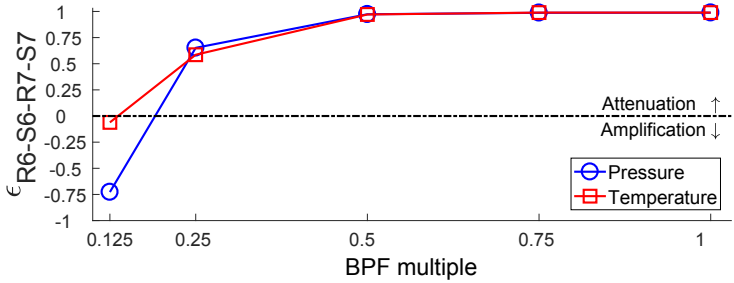

(a) Disturbance amplitude $A_d = 10\%$

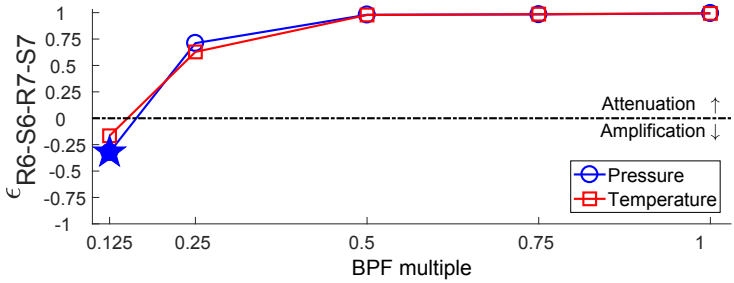

(b) Disturbance amplitude $A_d = 20\%$

Figure 5.17: Unsteady damping for configuration R6-S6-R7-S7, for static pressure and temperature. The time-domain behavior for the case shown with a star is depicted in Fig. 5.18.

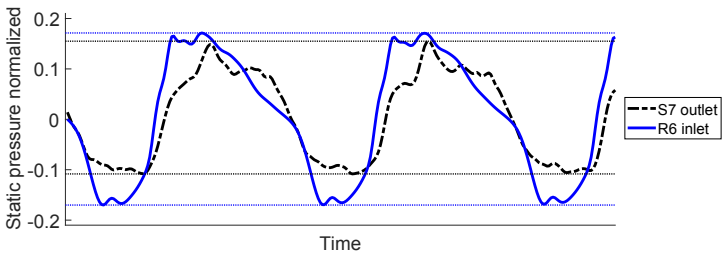

Figure 5.18: Static pressure variation used to compute the unsteady damping. The configuration is the R6-S6-R7-S7, with $f_d = 0.125$ BPF and $A_d = 20\%$ (shown with a star in Fig. 5.17). The unsteady damping is -0.322, indicating amplification of the PGC wave.

Table 5.4: Unsteady damping values for static pressure in the R6-S6-R7-S7 setup, disturbance amplitude $A_d = 20\%$. Stage and cumulative results for several disturbance frequencies.

Frequency f_d (BPF)	Stage 6 ε_{R6-S6}	Stage 7 ε_{R7-S7}	Stages 6 and 7 $\varepsilon_{R6-S6-R7-S7}$
0.125	-0.167	-0.133	-0.322
0.250	0.516	0.403	0.711
0.500	0.831	0.881	0.980
0.750	0.784	0.920	0.983
1.000	0.959	0.858	0.994

5.2.4 Aeroelasticity

The aeroelastic results presented in this section will be guided by the workflow described in section 3.2.3.1, summarized in Fig. 3.5. Therefore, the reader is invited to refer back to the previous discussion for details about the methodology.

The CSM analyses start with the working solid blade geometry (including disk), which through static analysis (section 3.2.1.1) is pre-stressed with mean loads and centrifugal forces. The mean loads are obtained by averaging the time-dependent results from the baseline unsteady case. The centrifugal forces are implemented according to the HPC rotational velocity at the chosen working conditions. The focus will be given here to the blade geometry, being sufficient to add that the disk displacement is fixed at the bore. That implies that shaft flexibility is ignored, as a standard practice in blisk assessments [251, 252]. The solid material is a typical industrial titanium alloy.

Similarly to the grid independence studies for the CFD model (presented in section 5.2.2), several meshes for the solid domain have been analyzed. They were generated in Ansys Mechanical, employing cyclic symmetry for a blade sector (see section 3.2.1.2 for more details). The unstructured grids were spawned by always keeping a high density of elements close to high-curvature regions, and particularly in areas with expected and empirically detected stress concentration. High-order

tetrahedra have been employed instead of hexaedra, wedges or pyramids. Although hexaedra could simplify the mapping between fluid and solid meshes, tetrahedra finite elements were shown to better model the problem's physics, particularly granting regions with high stress gradients a better meshing. The grids were then made coarser/finer as uniformly as practicable. The results for the static analyses differed so little among each other with the generated meshes (relative error less than 0.2%), so that a further study with the results from the modal analyses is justified.

After the static computations, pre-stressed modal analysis were conducted for all generated grids. The grid independence study for two selected natural modes is shown in Fig. 5.19, where the eigenfrequencies are normalized by the finest grid. Very similar behavior was obtained for the first 20 mode shapes, not shown here for brevity.

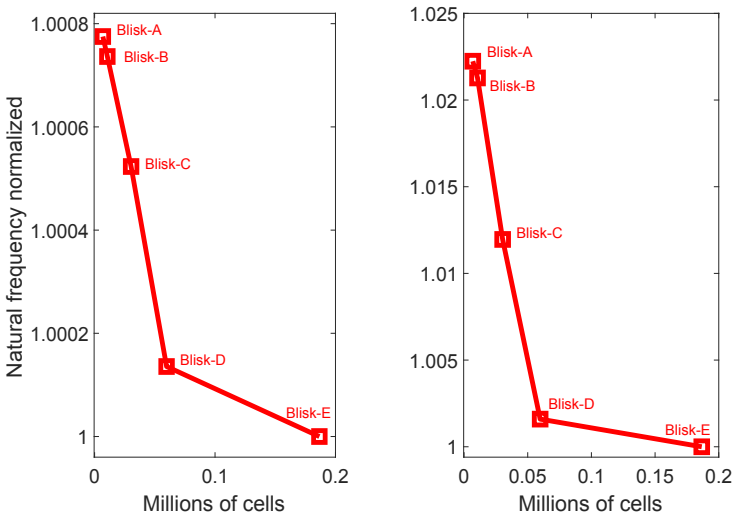

(a) Mode 2 (b) Mode 4

Figure 5.19: Natural frequencies for the analyzed rotor, with different spatial discretizations. Normalization with respect to finest grid.

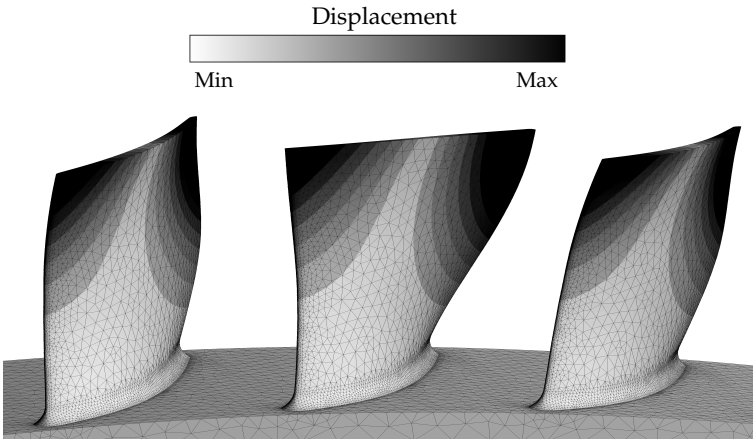

Figure 5.20: Solid mesh Blisk-D for the analyzed rotor. Full-annulus expansion for the first torsion mode displacement. Geometries rescaled.

Even the coarsest grid shown in Fig. 5.19 is able to model the natural modes with frequencies and shapes very close to the finest mesh. To guarantee good mapping between solid and fluid domains in the coming analyses, grid Blisk-D was chosen. One blade sector contains 96322 nodes and 70099 finite elements. The grid is shown for several sectors in Fig. 5.20, where the contours depict the second natural mode displacement in a specific nodal diameter count.

As discussed in sections 3.2.1.2 and 2.3.2, the natural modes of blisks are often depicted in interference diagrams. A sample diagram for the current rotor was shown in Fig. 2.5, with the first 10 mode families indicated. The blade-dominated modes are located on the right side, for higher nodal diameters, when the frequency of each mode family curve stabilizes; the disk-dominated are found on the left side, for lower nodal diameters.

The number of eigenvalues and eigenvectors computed should span over at least one and a half times the maximum external forcing frequency to be employed in the forced response analyses (section 5.2.4.2). This criteria is fulfilled for the present case by employing 117 mode shapes. Simulations with more modes have provided no significant change in the results. Thus, this number

of modes has been chosen to save computational resources. Additionally, modal participation factor and cumulative mass fraction were also controlled to make sure that the extracted modes properly represent the blade structure with respect to excitation in different directions.

5.2.4.1 Aerodynamic damping

Once the pre-stressed modal analyses are performed, the blade mode shapes are available so that the aerodynamic damping may be computed. For details on the numerical approach with the energy method, see section 3.2.2.3.

In this section, the NHB was employed to save computational resources when simulating the whole nodal diameter range. Discretization independence studies showed that 20 pseudo time steps per blade oscillation period were enough to guarantee convergence. Similarly, the blade displacement magnitude was varied, yielding reliable results for a maximum tip displacement of approximately 0.5% of the blade height.

Figure 5.21 shows an example of an aerodynamic damping computation with the NHB method. The contours depict the absolute value of the wall power density, which indicates with which magnitude the local displacement of infinitesimal surface element contributes to the integral yielding the aerodynamic work (Eq.(2.11)). The case shown corresponds to the first torsion mode, with an IBPA of approximately 177°. The CFD surface grid is also depicted. Comparing Fig. 5.20 for the solid domain and Fig. 5.21 for the fluid domain (both representing the same IBPA), a very good agreement between the interpolated results into the two meshes is observed.

Performing the same computation for different IBPA and for the first three mode shapes, we obtain the aerodynamic damping results shown in Fig. 5.22. The ζ values are normalized by the smallest result along the entire nodal diameter (or conversely IBPA) range.

No negative aerodynamic damping was obtained, implying, according to the energy method (see section 2.4.3), that no flutter

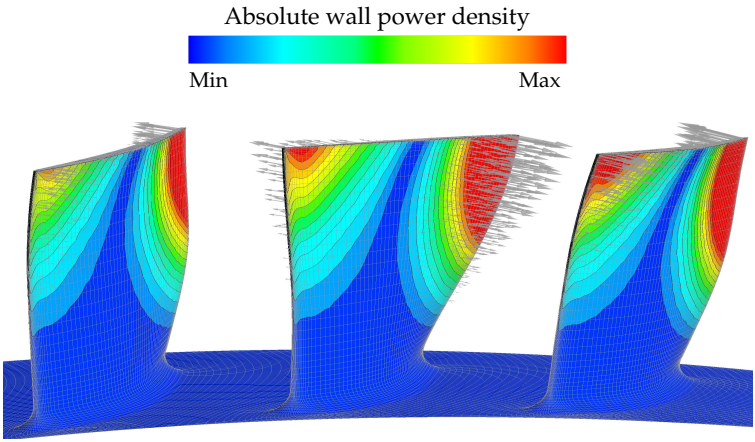

Figure 5.21: Absolute wall power density contours on rotor blades for the aerodynamic damping simulation. Vectors show the surface velocity for the first torsion mode (see Fig. 5.20). The blade displacement is magnified for visualization purposes, and the geometries are rescaled.

for this rotor and these modes is expected in this operating condition. We observe a relatively smooth harmonic behavior at the first oscillation order. This sinusoidal-like result can be related to the influence coefficient theory with traveling waves [24, 29, 48], with the vibrating blade exerting substantial more influence on the adjacent blades and much less on the far-located ones.

The aerodynamic damping corresponding to zero nodal diameter will be employed in the forced response computations in section 5.2.4.2. This damping value is located very near the minimum for the simulated modes, especially the first and the third. Additionally, it matches the implemented PGC excitation pattern and consists in a slightly conservative approach for the structural analyses.

5.2.4.2 Forced response

Referring back to the workflow in Fig. 3.5, at this point the modal decomposition, the aerodynamic modal damping and the

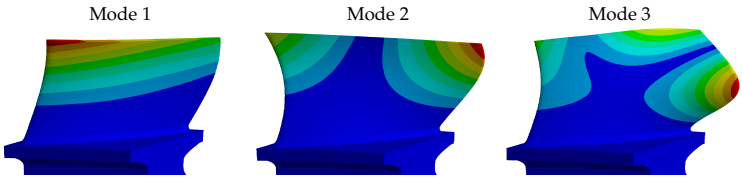

(a) Displacement of first blade-dominated mode shapes. Geometries rescaled.

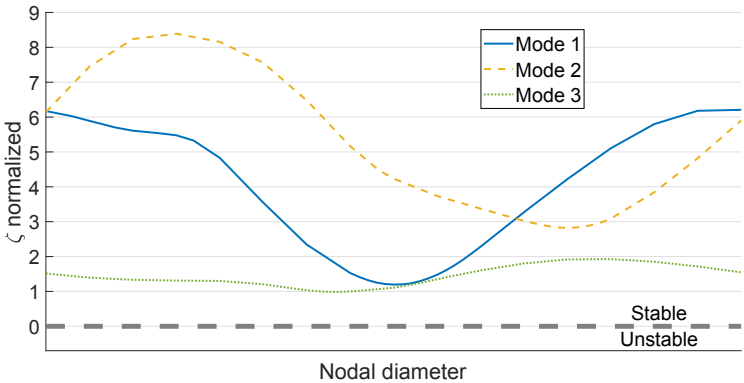

(b) Damping ratio ζ, normalized by the smallest value

Figure 5.22: Aerodynamic damping results for first blade mode shapes.

unsteady forcing from the CFD simulations are available. The mode-superposition harmonic response analyses can therefore be conducted for the baseline and PGC-disturbed cases. Indeed, the disturbed results will be always compared to the undisturbed, to give an idea of how the structural response of the HPC changes in the presence of PGC.

The CSM results shown in this work always refer to the design point rotational speed, that is, no part-speed state will be presented. Therefore, the inclination of the speed line in the interference diagram is fixed.

The unsteady CFD computations producing the dynamic loads for the forced response analyses have been carefully post-processed. This step is crucial to ensure that the transient signal adequately represents the excitation frequencies. For that,

the sampling rate and simulated interval must be adjusted to satisfy the Nyquist criterion in the Fourier decomposition. Initial convergence noise has been disregarded. Care was also taken with non-periodic data, by either choosing proper periodic intervals (generally encompassing multiple frequencies) or by employing windowing techniques.

As discussed in section 2.7, failure criteria are most often a function of mean and alternating stresses, which in turn are directly related to the minimum and maximum stresses. Therefore, we focus the presentation of CSM results on the limit values of the dynamic stresses. One particular scalar representing a general multi-axial stress state is the von-Mises (or equivalent) stress σ_{vm}, given by

$$\begin{aligned}\sigma_{vm}^2 =& \frac{1}{2}\Big[(\sigma_{xx}-\sigma_{yy})^2+(\sigma_{yy}-\sigma_{zz})^2+(\sigma_{zz}-\sigma_{xx})^2 \\ &+6(\tau_{xy}^2+\tau_{yz}^2+\tau_{xz}^2)\Big],\end{aligned} \tag{5.11}$$

where each of the terms correspond to normal and shear stress components in specific directions (see Eq. (3.35)). The von-Mises stress is related to one of the invariants of the deviatoric part of the Cauchy stress tensor (Eq. (3.2)). This means that the value of σ_{vm} is independent of coordinate system rotations, satisfying the principle of material frame indifference [253]. Generally, the von-Mises stress is a criterion employed for ductile materials by considering a critical value above which yield is expected to occur.

To illustrate how the stress distribution varies for a rotor blade in the forced response computations, Fig. 5.23 shows results for an undisturbed and a disturbed (with $f_d = 0.125$ BPF and $A_d = 20\%$) case. A single circumferential sector is shown, with the maximum stress obtained after a phase sweep (see section 3.2.1.3).

Much higher stresses occur for the disturbed case in comparison to the undisturbed, especially close to the leading edge root, above the fillet. For this load, the most excited mode is the first bending. Proceeding in a similar manner, we can compute the forced response for several disturbance frequencies in the undisturbed and the PGC-disturbed cases.

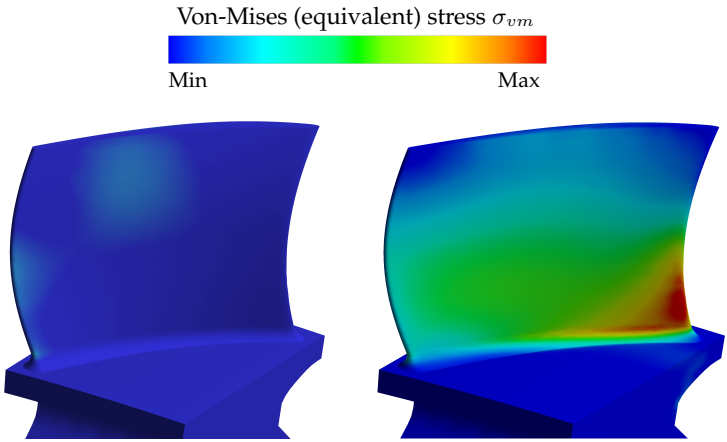

(a) Undisturbed (b) Disturbed

Figure 5.23: Von-Mises stress on rotor blade for setup R6-S6, for undisturbed and disturbed (Eq. (5.10) with $f_d = 0.125$ BPF and $A_d = 20\%$) cases. Maximum value over entire vibration cycle. Geometry rescaled.

5.2.4.3 R6

Figure 5.24 shows the forced response results for configuration R6 from Tab. 5.3. Two PGC disturbance amplitudes A_d are depicted. The normalization is conducted with respect to the stress value of the computation $f_d = 1$ BPF and $A_d = 20\%$.

The maximum equivalent stress reaches a level more than 150 times larger for $f_d = 0.25$ BPF in comparison to the disturbed case at $f_d = 1$ BPF. We also notice from Fig. 5.24 that an increase in the disturbance amplitude A_d from 10% to 20% amplifies the absolute stress observed on the blade, as expected.

It is possible to notice a qualitative correspondence between the von-Mises stress and performance indicator for the R6 setup. The total pressure losses (Fig. 5.10) are much higher for the lower disturbance frequencies than for the higher ones.

Interestingly, the unsteady damping presented for the R6 configuration in section 5.2.3.1 also depicted substantial change for low values of f_d. By the construction of the unsteady

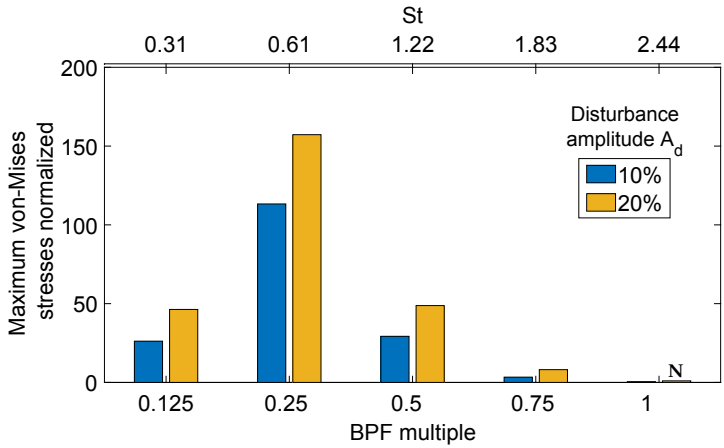

Figure 5.24: Maximum von-Mises stresses on R6 blade, for R6 configuration. Normalization conducted with respect to $f_d = 1$ BPF and $A_d = 20\%$ results (marked with **N**).

damping parameter, this result implies that the PGC wave "survives" longer as it travels axially, being able to excite the rotor blade with higher amplitudes than the high-frequency counterpart. In the present case, even though the unsteady damping value is lower for $f_d = 0.125$ BPF than $f_d = 0.25$ BPF (see Fig. 5.11), the latter excitation frequency is slightly closer to an eigenvalue (but still far from resonance ranges), explaining the higher stresses observed.

5.2.4.4 R6-S6

Similarly to configuration R6, Fig. 5.25 depicts the equivalent stresses for configuration R6-S6, subject to the same disturbance amplitudes A_d of 10% and 20%. Differently from section 5.2.4.3, in this setup the stator S6 is the first row affected by the upstream traveling PGC disturbances, followed by the structurally analyzed R6 blade.

An outcome similar to configuration R6 is obtained, with higher stresses for lower PGC frequencies. This behavior matches again well with the performance results from section 5.2.3.2. Compare

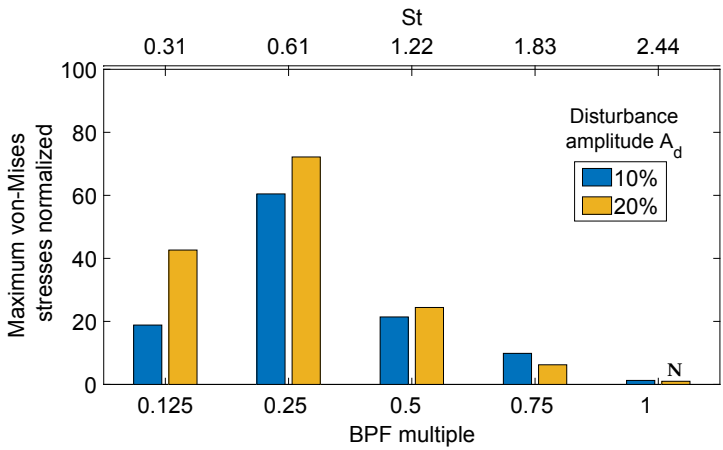

Figure 5.25: Maximum von-Mises stresses on R6 blade, for R6-S6 configuration. Normalization conducted with respect to $f_d = 1$ BPF and $A_d = 20\%$ results (marked with **N**).

for example Fig. 5.25 to Fig. 5.12, which also yields the highest decrease in isentropic efficiency for $f_d = 0.25$ BPF. Once more, the unsteady damping for R6-S6 (Fig. 5.15) also relates well to the stresses obtained in the forced response analyses.

When the normalization is conducted with respect to the von-Mises stresses obtained at the same forced response frequency in the baseline (undisturbed) simulation, the amplitude is much higher. This is shown in Fig. 5.26.

The distribution is quite similar to Fig. 5.25. However, the order of magnitude is three times higher. Although at the simulated frequencies the maximum von-Mises stress in the baseline case are quite small, posing no risk to the structure, a substantial amplification occurs with the PGC disturbances. This result quantitatively highlights the potential of PGC disturbances in enhancing aeroelastic response, serving as an alert to the structural designer.

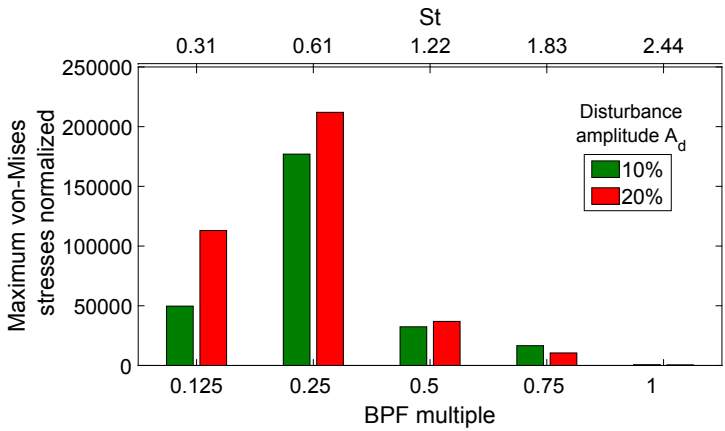

Figure 5.26: Maximum von-Mises stresses on R6 blade, for R6-S6 configuration. Normalization conducted concerning each respective baseline (undisturbed) result.

5.2.4.5 R6-S6-R7-S7

The maximum von-Mises stresses from the forced response analyses with the R6-S6-R7-S7 setup are shown in Fig. 5.27.

We see now a relative increase in the equivalent stress for the low frequencies even higher than for configurations R6 and R6-S6. More specifically, σ_{vm} is almost 250 times larger for $f_d = 0.25$ BPF than for $f_d = 1$ BPF, for a disturbance amplitude of $A_d = 20\%$. Again, the increase is more pronounced for the higher value of A_d shown.

There is also correspondence between the performance and forced response results for this configuration. That is, not only the equivalent stress (Fig. 5.27), but also the efficiency drop (Fig. 5.16) and unsteady damping (Fig. 5.17) yield much different values for the lowest two frequencies in comparison to $f_d \geq 0.5$ BPF.

When comparing the disturbed with the undisturbed case, relative increase occurs for all cases, as shown in Fig. 5.28.

This relative change varies from almost 4000 times higher stresses with PGC disturbances for $f_d = 0.125$ BPF, to simply 4 times in the $f_d = 1$ BPF case. The increment is definitely lower

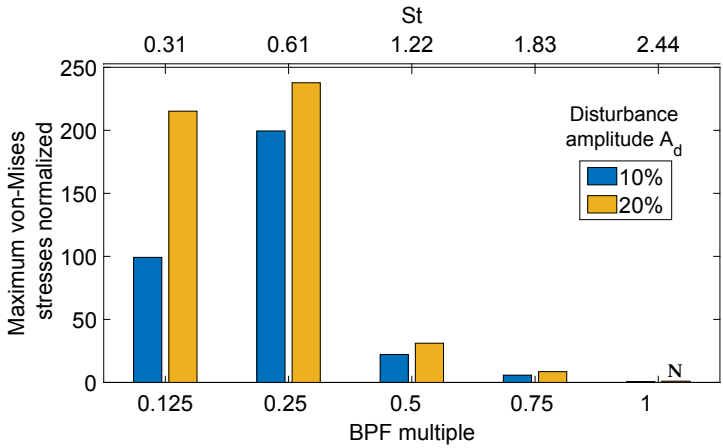

Figure 5.27: Maximum von-Mises stresses on R6 blade, for R6-S6-R7-S7 configuration. Normalization conducted with respect to $f_d = 1$ BPF and $A_d = 20\%$ results (marked with **N**).

than the values observed for configuration R6-S6 (Fig. 5.26), but still relevant. This happens because the undisturbed stresses are already higher for the R6-S6-R7-S7 in comparison to the undisturbed stresses for R6-S6, most likely due to the more complex dynamics brought by the presence of one further stage downstream.

The different stress distributions shown in Figs. 5.27 and 5.28 are directly related to how the amplitude of the unsteady loads acts on the blade. To get an idea of how the pressure distribution acts on each one of the blades and vanes in the R6-S6-R7-S7 configuration, Fig. 5.29 shows the probability density of the static pressure distribution *harmonic* corresponding to the $f_d = 0.25$ BPF and $A_d = 20\,\%$ disturbed case. These values are obtained by initially performing a Fourier decomposition of the surface pressure on each blade/vane and then fitting a normal distribution function into the data.

The goal of Fig. 5.29 is not to show a best fit for how the pressure varies for the node in the mesh, but rather to depict how

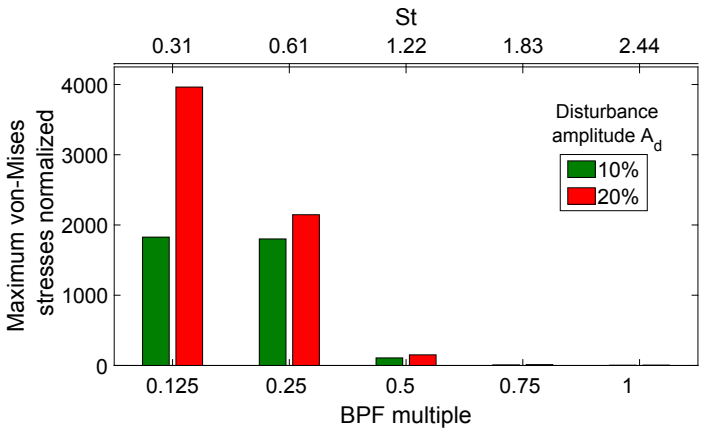

Figure 5.28: Maximum von-Mises stresses on R6 blade, for R6-S6-R7-S7 configuration. Normalization conducted concerning each respective baseline (undisturbed) result.

the pressure magnitude varies for each row. The downstream rows present a higher mean pressure for this harmonic, while the analyzed blade R6 perceives a comparatively lower mean pressure load but with a smaller variance. The monotonic decrease in the mean pressure from S7 to R6 (from right to left in Fig. 5.29) also matches with the unsteady damping results for this configuration (Fig. 5.17), which conveys a decrease in the PGC wave amplitude for $f_d = 0.25$ BPF and $A_d = 20\,\%$. Similar results are obtained for other values of f_d, not shown here for brevity.

5.2.5 Conclusions

This section numerically assessed a high pressure compressor subjected to boundary conditions representing PGC. Both unsteady performance and aeroelasticity analyses have been presented. Additionally, the concept of unsteady damping developed in section 5.1 was directly applied to the numerical results. Three model configurations were considered: a single rotor row (R6), a single stage (R6-S6) and two adjacent stages (R6-S6-R7-S7). The unsteady simulations presented in this section

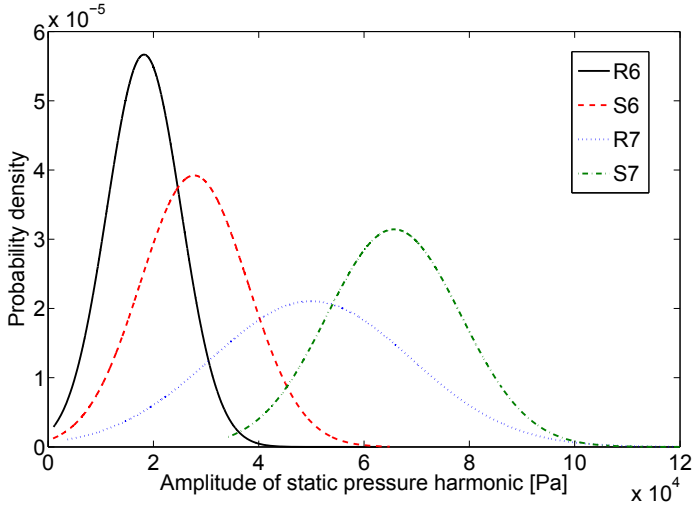

Figure 5.29: Probability density distribution of the static pressure harmonic of PGC-disturbed computation with $f_d = 0.25$ BPF and $A_d = 20\,\%$ (see Eq. (5.10)). Values are depicted for blades and vanes of the R6-S6-R7-S7 configuration.

considered PGC disturbances as changes in the outlet pressure following Eq. (5.10), with different disturbance amplitudes A_d and frequencies f_d.

Regarding the HPC performance subjected to PGC, a couple of results are worth mentioning. First, the amplitude A_d of the PGC wave was the most relevant factor when determining the total number of rows to be modeled. This outcome is conveyed in Figs. 5.10, 5.12 and 5.16, which respectively depict how an increase in total pressure loss and a decrease in isentropic efficiency are effectively minimized by the presence of additional rows between the PGC device and the analyzed domain. For disturbance amplitudes less than or equal to $A_d = 10\%$ of the mean outlet pressure, a rather small decrease in isentropic efficiency was noticed (less than 3%, as shown in Fig. 5.14). Once comparatively larger PGC amplitudes are present, such as $A_d = 20\%$, a reduction of up to 25% in the stage isentropic

efficiency took place. A square dependency of efficiency drop as a function of disturbance amplitude was obtained. Finally, the appearance and strengthening of temporary recirculation areas close to the blade surface have been detected (see Fig. 5.13), especially for lower values of f_d; this behavior is linked to the increase in the adverse pressure gradient downstream of the stage, due to the approach of the PGC wave. The time scale taken by the passage flow to reestablish itself after a PGC wave goes through turned out to be a relevant aspect, especially when directly contrasted with the period of a PGC wave itself.

The unsteady damping was computed for all configurations, so to assess how the wave amplitude varies as it axially travels along the HPC. For all row setups, a larger damping (attenuation) of the PGC wave followed for high f_d values. However, an amplification of the PGC wave occurred for a disturbance frequency of $f_d = 0.125$ BPF (see Figs. 5.11, 5.15 and 5.17). This large drop in the unsteady damping occurred independently of the disturbance amplitude. This behavior highlights the importance of quantitatively assessing the propagation persistence of PGC waves in turbomachinery components. Up to our knowledge, such an outcome had not yet been reported in the literature considering upstream-propagating waves.

With respect to the aeroelasticity results, no negative aerodynamic damping was obtained for the first rotor natural modes, under the simulated operating conditions. This is summarized in Fig. 5.22. Since the considered design consists of a blisk, no additional damping is considered. According to the energy method, this outcome implies that no flutter behavior is expected for the analyzed rotor in the selected operating point.

The damping ratio obtained in the flutter analyses was then employed in the computations considering PGC forced response. A substantial increase in the displacements and stresses on the rotor blade occurred in the presence of PGC disturbances. A much higher impact on the structure was seen for lower disturbance frequencies. For instance, the equivalent stress was almost 250 times larger for the case with $f_d = 0.25$ BPF in

comparison to $f_d = 1$ BPF, for the same disturbance amplitude (see Fig. 5.27). Additionally, comparing the disturbed with the unsteady baseline results for each single frequency, a similar distribution with respect to f_d occurs, however with a much larger amplification (see Figs. 5.26 and 5.28). On the one hand, this is expected since the stresses in the baseline case are comparatively very small. On the other hand, the larger amplification shows the latent danger of ignoring the structural excitation potential of PGC disturbances within turbomachinery.

The forced response trend with respect to f_d was similar to the unsteady damping results, clearly producing a higher impact for lower frequencies. This good qualitative agreement between the unsteady damping (obtained solely with CFD computations) and the forced response outcome (which requires a more involved workflow) indicates that the former may be used as a preliminary design predictor for structural response whenever axially traveling disturbances should be present in the system. Certainly, detailed computational mechanics assessments should be carried out for critical operating ranges or when precise stress values are sought.

5.3 Case study 2

5.3.1 Case description

The second case study employed in this work stems from the Energy Efficient Engine (EEE) program, covered by the comprehensive Aircraft Energy Efficiency scheme. A diagram representing the engine is shown in Fig. 5.30. This initiative, coordinated by the National Aeronautics and Space Administration (NASA), took place in the late 1970s and 1980s, aiming at developing new technology standards for turbofans employed in commercial aviation in the decades to come. Pragmatic goals with respect to existing representative figures were set, such as a 12% reduction in installed specific fuel consumption, when compared to a CF6-50C engine at maximum cruise thrust. Decrease in performance deterioration by 50% as well as meeting noise and emission standards were also covered [254]. The four main parts of the NASA EEE program were: (i) propulsion system analysis, design and integration; (ii) component analysis, design, and integration; (iii) core test and (iv) integrated core/low spool test.

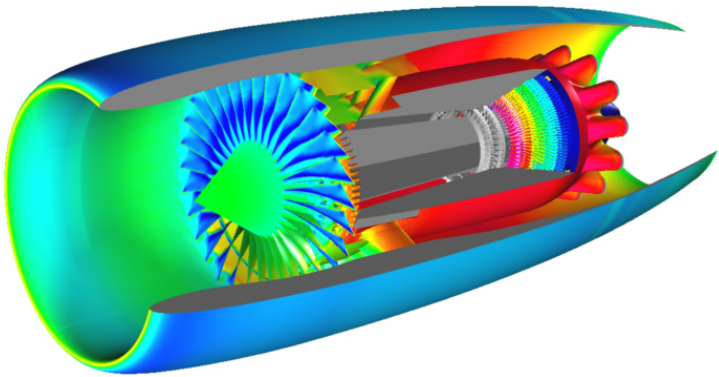

Figure 5.30: NASA Energy Efficient Engine representation [254].

Figure 5.31: Modern application of the NASA EEE core engine [258].

Contracts for development and production were awarded to General Electric and Pratt & Whitney. The data used in this work is extracted from the GE HPC design from [255], with corrected geometries provided by [256]. The EEE core was employed in later models such as GE90 and GEnx engines (see Fig. 5.31). An overview about the whole EEE program is given by [257].

The main operation requirements for the NASA EEE core compressor were the development of a pressure ratio of 23 within 10 stages while providing adiabatic and polytropic efficiencies of 86.1% and 90.5% respectively. The corrected mass flow at cruise is 53.5 kg/s.

Differently from case study 1, the NASA EEE comprises no rotor blisk. Therefore, the last stage, namely the tenth, has been chosen for the analyses in this section, due to its direct adjacency to the combustion system. The last rotor is named here R10, while the outlet guide vane, or last stator, is termed S10.

5.3.2 Numerical aspects

Similarly to the grid independence studies for the case study 1 (section 5.2.2), we start by ensuring that the generated meshes

properly represent the model. The details about meshing parameters will not be repeated in this section, since the process of generating the grids is alike for both case studies. It is sufficient to mention that the boundary layers have been modeled for all walls, including tip gaps and fillets.

Figure 5.32 shows the grid independence study for the EEE HPC tenth stage. The scalar values shown are normalized by the finest grid displayed.

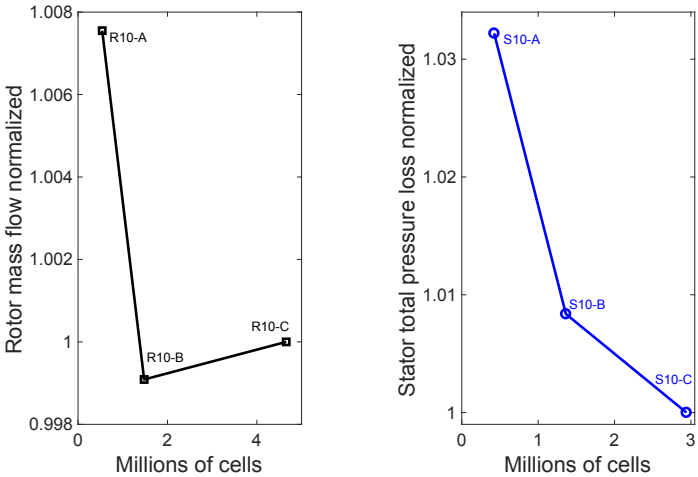

(a) Rotor R10

(b) Stator S10

Figure 5.32: Normalized scalars representing flow in the EEE HPC tenth stage, showing grids with different spatial discretizations.

The grid convergence index (see Appendix A.1) obtained for the loss coefficient, considering the finest and medium meshes (B and C), was $\mathrm{GCI}_{\mathrm{BC}} = 1.64\,\%$ with apparent convergence order of 1.937. It is relevant to say that the GCI and the apparent convergence order may vary substantially when considering different globally integrated parameters. But in any case, the relative difference between the scalars considered was below 0.8% (and often much smaller) for all cases. This threshold has been deemed sufficient for the desired precision for this work.

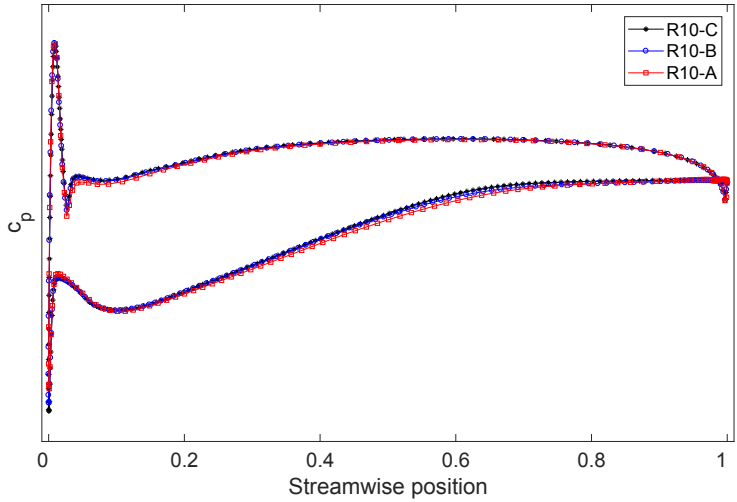

Figure 5.33: Pressure coefficient c_p for a rotor cross section at $50\,\%$ span. Same grids as in Fig. 5.32(a) (A: coarse; B: medium; C: fine).

To further investigate each of the generated grids, Fig. 5.33 depicts the pressure coefficient c_p on the R10 blade, for a cross section at half span.

Minimal discrepancies occur in the pressure distribution, which are considered insignificant for the desired numerical precision. Similar results are obtained for the stator vanes, not shown here for brevity. The medium grids (R10-B and S10-B) are chosen for further unsteady simulations. These are depicted in Fig. 5.34.

In order to obtain a unitary pitch ratio for the tenth stage numerical model, the number of rotor blades is slightly altered from 140 to 141 (0.7% change) and the number of stator vanes from 96 to 94 (2%). With that, modeling two rotor and three vane passages yields the same circumferential length. This modification did not imply substantial change in the design point and avoids frequency and phase errors when analyzing the unsteady PGC disturbances (similar discussion in section 5.2.3.2). The rotor domain in this setup has 3.5 million nodes, while the stator domain has 4.2 million, in a total of 7.7 million nodes for the simulated stage.

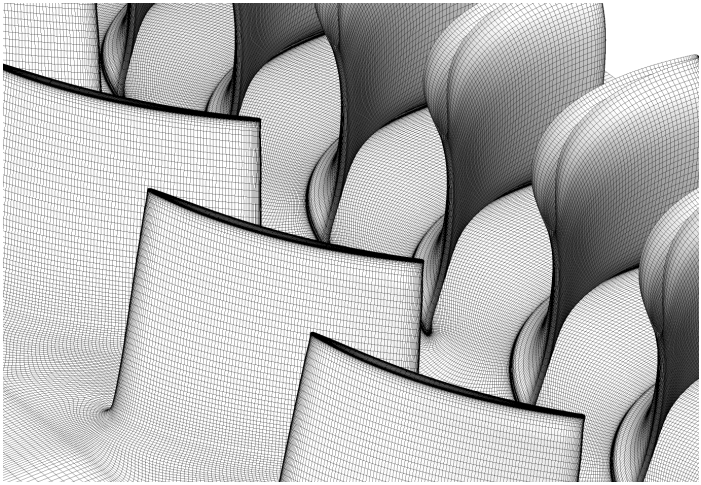

Figure 5.34: Grids for the analyzed tenth stage assembled together (R10-B and S10-B from Fig. 5.32).

A time discretization study was also conducted, to make sure the size of the time step is suitable for the expected simulations. Figure 5.35 shows pressure probes located in both R10 and S10 domains, between the rotors and vanes, for different time discretizations.

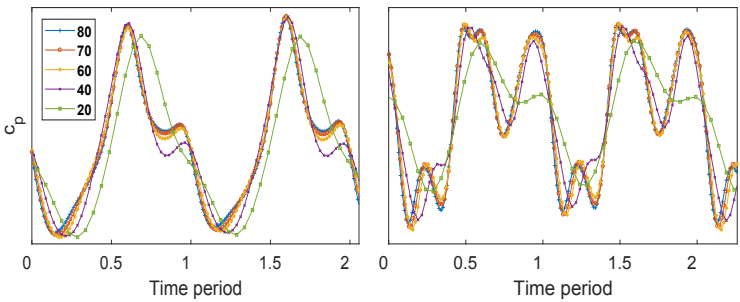

(a) Probe downstream of R10 blade (b) Probe upstream of S10 vane

Figure 5.35: Periodically-converged pressure coefficient c_p for point probes. Values represent the number of time steps per rotor passing period.

All the PGC frequencies simulated for the NASA EEE are lower than or equal to the BPF, making sure that the rotor-stator interaction is sufficiently discretized in time. According to the behavior shown in Fig. 5.35 and the confirmation of quasi-periodic convergence of global scalars (such as compression ratio or isentropic efficiency), the value of 70 time steps per rotor passing period was chosen. With that, adequate time discretization is expected while keeping the computational demand under a reasonable limit, considering the fine spatial discretization.

The setup just described (named here *standard*) does not contemplate the effective modeling of PGC waves varying in the circumferential direction θ. This would be the case, for example, when several PGC units are distributed around the whole annulus. However, the firing of a single PGC device may also generate higher wave harmonics that propagate around the annulus (see, e.g., [208] for similar spatial patterns with RDC). Such a situation is illustrated in Fig. 5.36, considering the fourth annulus harmonic (circumferential order) propagating in the opposite direction of the blade rotation.

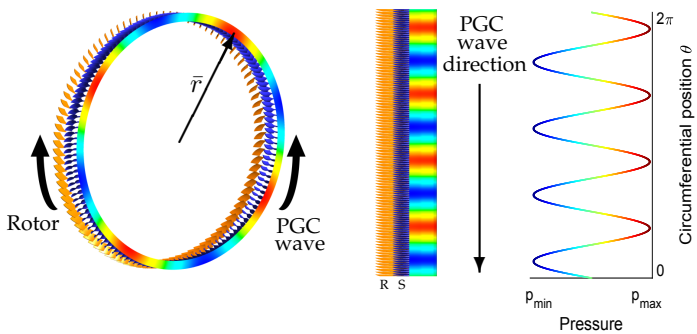

(a) 3D and θ-transformed views (b) θ distribution

Figure 5.36: Boundary condition at the stage outlet for a PGC wave propagating circumferentially. The pressure pattern shows the fourth annulus harmonic (circumferential order n_c) rotating in the opposite direction of the rotor.

Consider a pressure wave with circumferential order n_c propagating at the speed of sound c in an annulus with mean radius $\bar{r}$. In this case, for a frame of reference traveling with the wave, no change in amplitude with time is considered, but rather its propagation in the circumferential direction θ. The blades rotate with linear frequency f_r. The pressure at the outlet can be then modeled as

$$p(r,\theta,t) = p(r)\left[1 + A_d \cdot \sin\left(\frac{c\,t}{\bar{r}} - n_c\,\theta\right)\right]. \tag{5.12}$$

That is, a radial pressure profile $p(r)$ rotates around the annulus with the amplitude varying harmonically with magnitude A_d. The effective excitation frequency $\hat{f}_r$ perceived by a blade rotating with linear frequency f_r will therefore be

$$\hat{f}_r = \left(n_c f_r - \frac{c}{2\pi\bar{r}}\right). \tag{5.13}$$

Note that, for consistency, PGC waves traveling in the opposite direction of the rotor have a negative c value (thus increasing $\hat{f}_r$).

To model these PGC waves traveling circumferentially, a second mesh setup is also implemented in this work. Since many more passages must be modeled, the computational resources would be prohibitive for transient simulations considering all rotor and stator passages. Therefore, only a quarter of the whole annulus was modeled. Of course, fluctuations with wavelength larger than a quarter of the annulus perimeter cannot be properly implemented with this mesh. However, the likely presence of more combustion units justifies higher n_c values, adequately captured by the quarter-annulus setup. For that, 24 rotor and 35 stator passages are meshed. Due to this large number of passages and unsteady requirements, the coarser grids from Fig. 5.32 were selected, enabling feasible computational time with reasonable accuracy. Whenever referred to in this work, this setup will be termed *quarter-annulus*.

5.3.3 Performance

For brevity, we draw upon the discussion about PGC and performance already presented in section 5.2.3. The results presented in the current section shed light on how the performance of the last stage of the HPC from the NASA EEE would react to PGC disturbances traveling upstream. Again, comparisons with the baseline, unsteady case will be conducted.

To compensate instantaneous fluctuations in mass flow in the inlet and outlet of the domain, an adapted definition for unsteady performance quantities is presented. This approach takes into account the implementation of boundary conditions which vary in time. It starts by weighting spatially-integrated quantities in each time step by the mass flow $\dot{m}(t)$ which traverses each axial plane (revisit Fig. 5.1). In that way, fluxes associated with higher mass flow bear more relative influence than fluxes with lower mass flow.

Consider a generic state variable $\phi(t)$ (pressure, temperature etc.), possibly fluctuating in time. The mass-flow-weighted time average $\hat{\phi}$ is defined in Eq. (5.14), for a single axial plane.

$$\hat{\phi} \triangleq \frac{\dfrac{1}{T}\displaystyle\int_t^{t+T} \dot{m}(t)\phi(t)\,dt}{\dfrac{1}{T}\displaystyle\int_t^{t+T} \dot{m}(t)\,dt} = \frac{\displaystyle\int_t^{t+T} \dot{m}(t)\phi(t)\,dt}{\displaystyle\int_t^{t+T} \dot{m}(t)\,dt}, \tag{5.14}$$

where T is the desired integration period, comprising at least both the blade passing and the disturbances periods. In the middle equality of Eq. (5.14), the denominator stands for a simple time-averaged mass flow at the chosen axial plane. Observe that $\hat{\phi}$ is not a spatial average (which must be conducted beforehand), but instead a time average weighted by the mass flow. The circumflex symbol will be dropped for derived quantities, since all unsteady performance parameters in this section will be computed employing this definition.

5.3.3.1 Standard setup

Initially, the PGC disturbances will be implemented as harmonic fluctuations as in the previously presented Eq. (5.10). The performance results to be presented in section 5.3.3 allow immediate comparison with the results from case study 1.

Subsequently, thorough analyses will be performed with the data-driven decompositions in section 5.3.4. For that, in addition to the harmonic fluctuations prescribed by Eq. (5.10), another set of boundary conditions is also implemented, namely a pressure pulse. This elementary rapid variation in pressure simulates the opening of a PGC valve which allows compressed air from the HPC to enter the combustion chamber. For most part of a classic PGC cycle, more specifically during the ignition, burning and purge phases, no mass flows into the combustion chamber [155]. For a sector of the HPC, that implies a long time with "constant" outlet boundary conditions, followed by a drop in pressure when the PGC inlet valve opens. Such a transient behavior in the outlet pressure $p(\mathbf{x}, t)$ is modeled here with an inverted Gaussian function $g(t)$ and an activation function $a(t)$ as

$$p(\mathbf{x}, t) = p(\mathbf{x}) \left[1 - a(t) g(t)\right], \tag{5.15}$$

with

$$\begin{aligned} g(t) =& A_p \, e^{\dfrac{-(t - t_s)^2}{2\sigma^2}}, \\ a(t) =& 1/2 \left[1 + \tanh\left(a_1 \, t - a_2\right)\right], \end{aligned}$$

where A_p is the pulse relative amplitude (corresponding to the trough depth shown in Fig. 5.37), σ the standard deviation and t_s a time delay. The constants a_1 and a_2 simply modulate the activation function dynamics, avoiding nonphysical numerical discontinuity when applying the boundary conditions. The use of a narrow (Gaussian) pulse is valuable when seeking to understand how the turbomachinery reacts to a single, sudden change in the

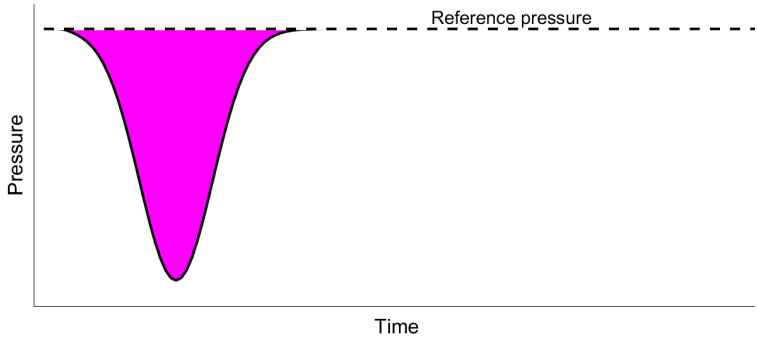

Figure 5.37: Representation of an inverted Gaussian pulse (Eq. (5.15)), employed as boundary condition to simulate the opening of a PGC valve.

outlet conditions, which is also convected upstream. Additionally, in contrast to single-frequency PGC disturbances, the frequency spectrum of a Gaussian function is also a Gaussian, meaning that a broad range of frequencies is excited simultaneously.

Total pressure loss

The loss for both the R10 and the S10 domains is depicted in Fig. 5.38, as a function of the harmonic disturbance frequency f_d, for an amplitude of $A_d = 10\%$. The loss is calculated at each respective frame of reference.

One notices a relative increase in the total pressure loss of up to 80% for S10 when comparing the PGC-disturbed with the baseline case. More specifically, the losses in the stator vane, the first row affected by the PGC waves, increase for higher disturbance frequencies f_d. For the R10 blade however, higher losses take place for lower f_d, reaching approximately 70% for $f_d = 0.125$ BPF. Similarly to the results observed in the case study 1 (section 5.2.3), the PGC wave is capable of traveling further upstream for lower frequencies. In this concrete case, it implies higher losses for the R10 row at low f_d values, when temporary flow separation occurs.

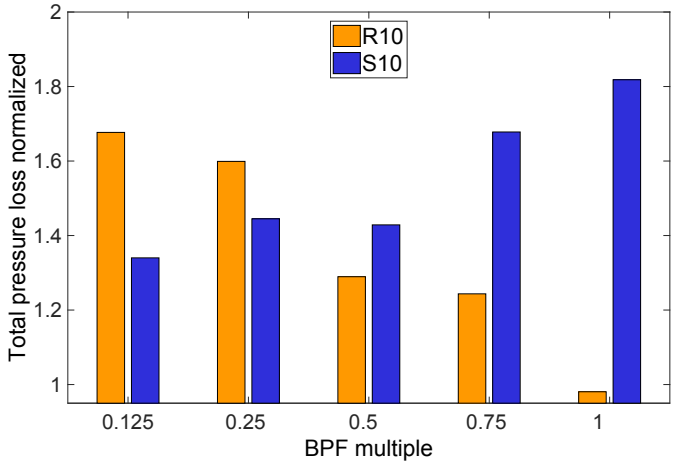

Figure 5.38: Normalized total pressure loss for rotor and stator, as a function of the disturbance frequency f_d and amplitude $A_d = 10\%$ (see Eq. (5.10)). Normalization with respect to the undisturbed case.

Unsteady damping

To assess how far and with which amplitude the PGC wave travels upstream, the unsteady damping for the tenth stage is depicted in Fig. 5.39. Values are shown for mass flow, static pressure and temperature for a disturbance amplitude $A_d = 10\%$.

Higher attenuation is obtained for higher disturbance frequencies, close to full damping for $f_d > 0.5$ BPF. Much lower attenuation occurs for lower f_d, reaching even $\varepsilon < 0$ for $f_d = 0.125$ BPF, considering the static pressure and mass flow. This implies an increase in the wave amplitude. To illustrate how the wave behaves in an amplification case, Fig. 5.40 shows the variation of static pressure for $f_d = 0.125$ BPF (marked with a star in Fig. 5.39).

These results are indeed very similar to the ones from case study 1 (see Figs. 5.11, 5.15 and 5.17). For both case studies, the PGC wave amplitude increased for $f_d = 0.125$ BPF as it traversed the system. Low-frequency PGC waves are able to travel further downstream, be it for setups with relatively lower or higher mass flow, respectively portrayed by case studies 1 and 2.

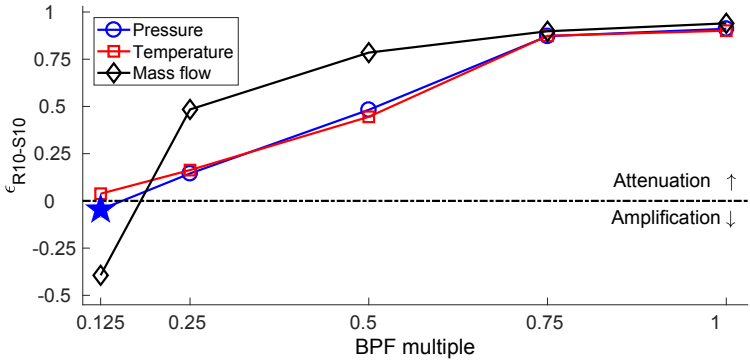

Figure 5.39: Unsteady damping for the tenth stage, with disturbance amplitude of $A_d = 10\,\%$. The time-domain behavior for the case shown with a star is depicted in Fig. 5.40.

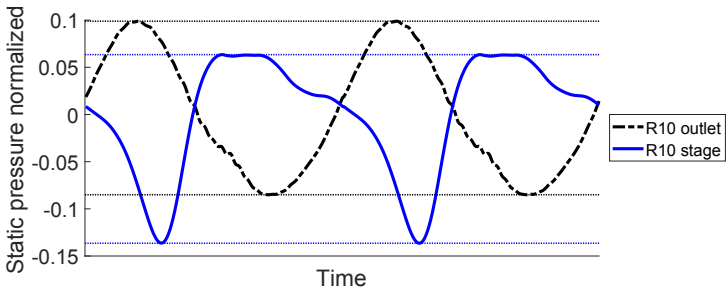

Figure 5.40: Static pressure variation at two stations to compute the unsteady damping. The disturbance parameters are $f_d = 0.125$ BPF and $A_d = 10\%$ (marked with a star in Fig. 5.39). The unsteady damping value is -0.046, indicating amplification of the PGC wave.

Isentropic efficiency

Finally, the variation in the isentropic efficiency comparing the undisturbed and the disturbed cases is shown in Fig. 5.41, for $A_d = 10\,\%$.

The drop in efficiency is limited to less than 7% for this setup. This magnitude is of the same order of the results shown for case study 1 in Fig. 5.12, however with less variation with respect to the disturbance frequency. This outcome allows the designer

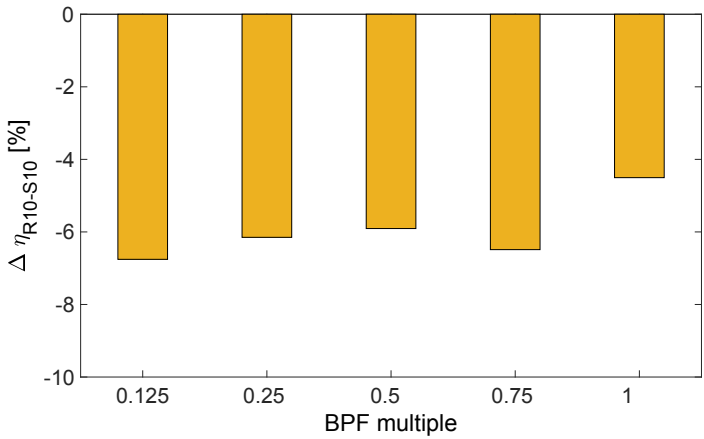

Figure 5.41: Variation in mass-flow-weighted isentropic efficiency as a function of disturbance frequency f_d, with $A_d = 10\,\%$ (see Eq. (5.10)).

to weight the potential gains obtained with the implementation of PGC against the decrease in stage efficiency occurring in the compressor last stages.

Since the mass-flow-weighted total pressure rise remains approximately unchanged in the presence of PGC disturbances, no results are shown here.

5.3.3.2 Quarter-annulus setup

Similarly to the standard setup, the unsteady performance and unsteady damping have been considered for the quarter-annulus setup. The mass-flow-weighted time average given by Eq. (5.14) is also employed here.

For the quarter-annulus setup, besides the undisturbed case, three values of circumferential order (n_c in Eq. (5.12)) have been considered: 4, 8 and 12. They all rotate in the opposite direction (counter-rotation) of the rotor so as to increase the relative excitation frequency perceived by the blades. Co-rotating cases with similar n_c values would promote effective excitation frequencies $\hat{f}_r$ (see Eq. (5.13)) so low that a quasi-steady flow

analysis would be instead justified. Additionally, the computation of a much longer time span would be necessary to obtain a stabilized flow behavior.

Total pressure loss

Figure 5.42 shows the total pressure loss for the rotor and stator domains with the quarter-annulus setup. Similarly to the standard setup (Fig. 5.38), an increase of up to 80% in relative losses occurs. The change pattern is also alike: higher losses in the S10 domain take place for higher circumferential order n_c (higher effective excitation frequency $\hat{f}_r$), while higher losses in the R10 domain occur for lower n_c. However, the two plots differ in that the losses for the rotor domain in the quarter-annulus setup do not increase by more than 20%, while in the standard setup they reach almost 70%.

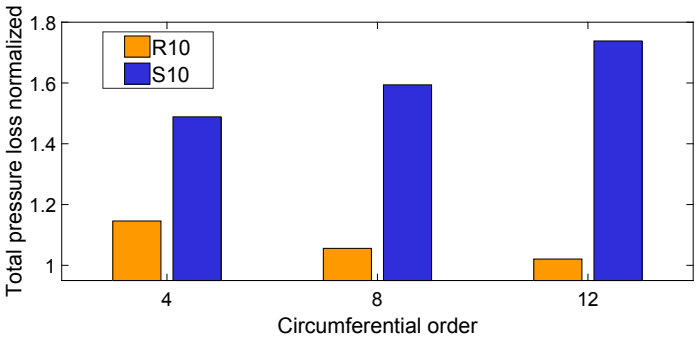

Figure 5.42: Total pressure loss for rotor and stator in quarter-annulus setup, as a function of the circumferential order n_c, for amplitude $A_d = 10\%$ (see Eq. (5.12)). Normalization with respect to the undisturbed case.

Unsteady damping

The attenuation or amplification of the PGC waves as they propagate axially can also be analyzed for the quarter-annulus case. Figure 5.43 depicts the unsteady damping for the same variables assessed with the standard setup (see Fig. 5.39). Once

again, a monotonic increase in ε proportional to n_c occurs for almost all cases. That is, fluctuations with larger circumferential wavelength (lower n_c) persisted longer than cases with lower wavelength.

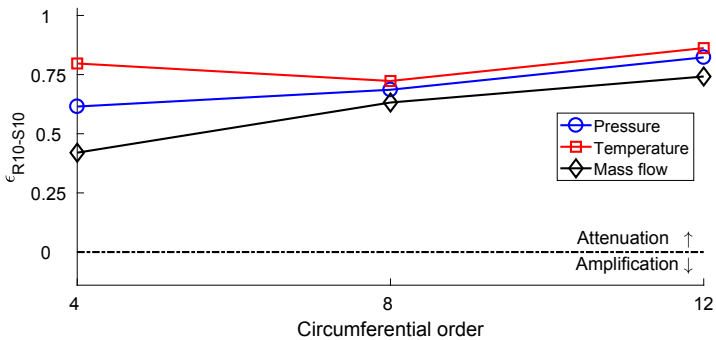

Figure 5.43: Unsteady damping for quarter-annulus setup, as a function of the circumferential order n_c (Eq. (5.12) with $A_d = 10\,\%$).

A reasonable amount of damping takes place for the circumferentially rotating waves, as they traveled axially through the stage. The fact that more damping followed from higher n_c advocates for the implementation of more combustion units, if the goal is reducing fluctuations effectively.

Isentropic efficiency

The drop in isentropic efficiency for the quarter-annulus case as a function of the circumferential order n_c is shown in Fig. 5.44(a). The order of magnitude is the same as in the standard case (compare with Fig. 5.41). Here, a slightly lower but still relevant decrease in η occurred, limited to less than 4%, for $A_d = 10\%$.

Substantial decrease in isentropic efficiency occurred by increasing the disturbance amplitude A_d, as shown in Fig. 5.44(b) for $n_c = 8$. Up to 15% drop took place for $A_d = 20\%$. These changes are similar to the values obtained with case study 1 with the same disturbance amplitude. They show, also in the quarter-annulus case, the extent with which PGC is able to affect the baseline performance values for the HPC.

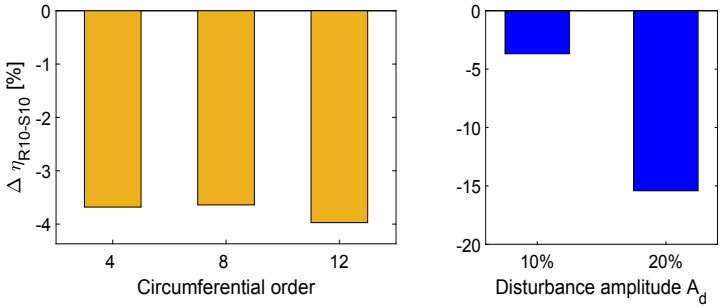

(a) Varying n_c for fixed $A_d = 10\%$ (b) Varying A_d for fixed $n_c = 8$

Figure 5.44: Variation in isentropic efficiency η for quarter-annulus setup, as a function of disturbance amplitude A_d and circumferential order n_c (see Eq. (5.12)).

5.3.4 Data-driven decompositions

The methods presented in section 3.3 will be employed in this section to analyze the flow in the tenth stage of the NASA EEE high pressure compressor in detail. The main idea is to identify relevant flow phenomena, coherent structures and which specific dynamic features influence the flow (and consequently the structure) most strongly. As usual, the unsteady baseline and the PGC-disturbed results will be compared.

From the three data-driven methods presented in section 3.3, only the Fourier decomposition has been employed up to this point, since it is a part of the aeroelastic workflow (Fig. 3.5). This section will focus on the other two methods, namely POD and DMD, however still relating to Fourier decompositions and phase averaging when relevant.

Three types of domains will be employed here for the POD and DMD investigations. The first is the axial plane already presented in Fig. 5.1. It corresponds simply to a cross section in the axial direction, perpendicular to the mainstream flow. The second type is the streamwise surface, which consists in a blade-to-blade cross section, i.e., a surface which varies in the circumferential and axial directions but has a single radius value. The third is the rotor

blade surface. Before presenting the results for these types of domains, some considerations will be made about the numerical discretization.

5.3.4.1 Numerical aspects

Analogously to the independence studies about time discretization previously conducted, we start by assessing whether the chosen time step and the total number of time samples (snapshots) provide reliable results. To illustrate how the POD singular values ($\mathbf{\Sigma}$ in Eq. (3.54)) behave, we consider initially a disturbed case in which complex flow dynamics at different frequencies occur. Namely, we perform a POD at the AP D (plane located between R10 and S10, see Fig. 5.1) for a harmonic disturbance of $f_d = 0.125$ BPF and $A_d = 10\%$. The singular value distribution for the POD of the velocity and vorticity magnitudes is depicted in Fig. 5.45, for the first nine unsteady modes[5]. The bar height represents the singular value normalized magnitude: in the velocity case in Fig. 5.45(a), twice the average kinetic energy; in the vorticity case in Fig. 5.45(b), the enstrophy. The colors for each bar represent the time step employed in the decomposition, normalized by the unsteady CFD value (70 time steps per rotor passing period).

As expected, we notice a monotonic decrease in the POD singular value for higher modes. Additionally, the decrease in the time step size (i.e., going from right to left for each POD mode) reaches a point where no significant change in the singular value occurs. More specifically, the relative change in the singular value is less than 0.5% for normalized time steps up to 3. Although this discretization could be chosen for the coming POD results, we employ the same time step from the CFD unsteady runs, since the processing time for these computations is not a critical resource. Similar orders of magnitude were found for other state variables, not shown here for the sake of brevity.

[5] As discussed in section 3.3.2, the first singular value, corresponding to the mean flow, is much larger than the following modes representing the unsteady flow. Therefore, when comparing magnitudes in Figs. 5.45 and 5.46, the singular value of POD mode 1 is omitted for scaling clarity.

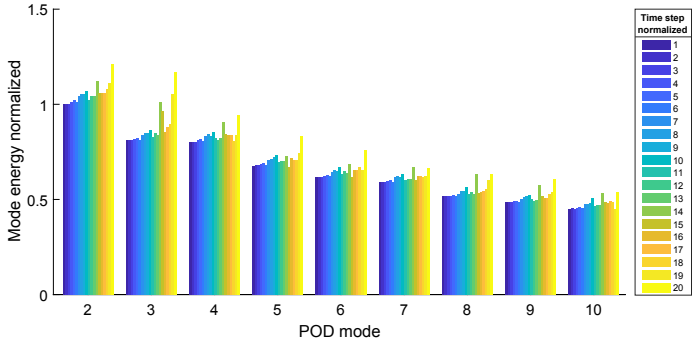

(a) Velocity magnitude $|\mathbf{v}|$

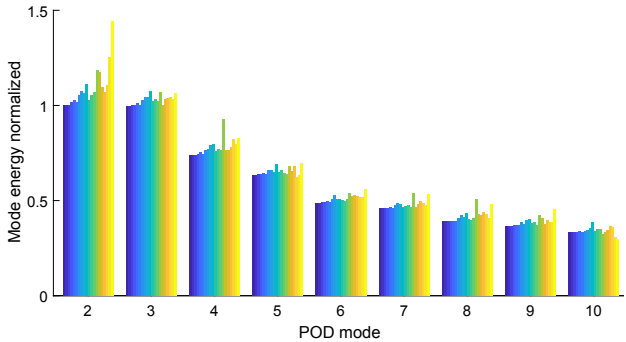

(b) Vorticity magnitude $|\nabla \times \mathbf{v}|$

Figure 5.45: Singular values from POD of disturbed flow (Eq. (5.10) with $f_d = 0.125$ BPF and $A_d = 10\%$) at station AP D (see Fig. 5.1). Time discretizations are shown normalized by the unsteady CFD time step.

To illustrate how the POD behaves for other axial positions, Fig. 5.46 shows the POD decomposition for the same fields of Fig. 5.45 now at AP A (see Fig. 5.1). It is clear that a faster decay in the singular value with increase in mode number occurs in Fig. 5.46 in comparison to Fig. 5.45. This happens with AP A because, although it still perceives the PGC wave fluctuation, it does not experience the complex dynamics of AP D, which includes not only the PGC wave but also rotor-stator interaction

phenomena. This faster decay means that fewer POD modes are necessary to convey most of the flow energy or to reconstruct the flow field in a reduced order model. Finally, the variation in the singular value with time discretization (height of bars) for AP A is also smaller than for AP D, meaning that simpler flow dynamics also demand lower snapshot sampling rate. However, the high sampling rate (conversely smaller time step) is still retained for all APs, to ensure quality in the POD and facilitate comparisons.

A similar study is performed with the total number of snapshots included in the analyses. This quantity (columns of matrix $\boldsymbol{\mathcal{X}}$ in Eq. (3.53)) was varied, with and without retaining an integer number of disturbance/blade passing periods. To ensure comparability between results with different f_d, the choice was made to always use an integer number of disturbance periods in the POD. This time, a threshold of less than 1% in the relative change in the first singular values has been employed. This requires the inclusion of 4 to 8 disturbance periods. Finally, no relevant changes in the singular values occurred by choosing different initial snapshots in the time series.

The most energetic POD modes themselves vary very little even when including less snapshots or for coarser time discretization; i.e., considering mostly the singular values as a verification criterion is a rather conservative but fast approach. The procedures just described for the time discretization in the POD were also conducted for the DMD analyses, including assessments of the decomposition residual. They will not be repeated here for the sake of brevity. In the following, axial planes, streamwise surfaces and finally blade surface will be assessed, for different flow variables.

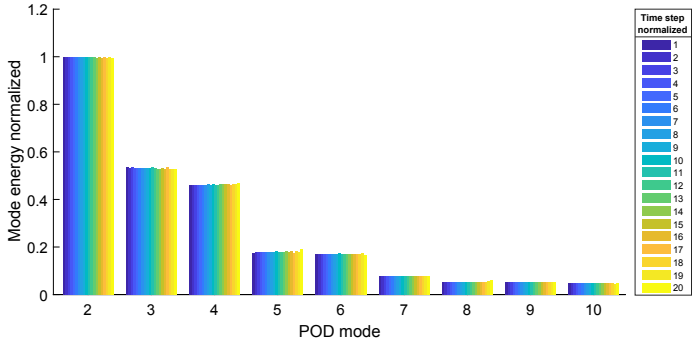

(a) Velocity magnitude $|\mathbf{v}|$

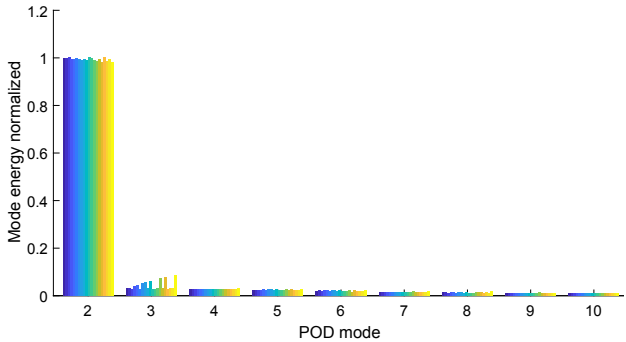

(b) Vorticity magnitude $|\nabla \times \mathbf{v}|$

Figure 5.46: Singular values from POD of disturbed flow (Eq. (5.10) with $f_d = 0.125$ BPF and $A_d = 10\%$) at station AP A (see Fig. 5.1). Time discretizations are shown normalized by the unsteady CFD time step.

5.3.4.2 Axial planes

Mass flow

As an initial overview on how the flow varies axially, we analyze the baseline, undisturbed case. The POD for mass flow $\dot{m}$ is shown for different APs in Fig. 5.47. Units are not depicted, due to the fact that the magnitude of each mode is already contained in the temporal coefficients matrix ($\mathbf{V}$ in Eq. (3.54)). In all POD depictions in this work, the superscript 'Energy' refers to

the ratio of the mode's singular value to the total decomposition energy (i.e., the sum of all singular values). Additionally, black dots are shown in the figures to symbolize the blades and vanes located close to the APs, which however do not intersect the cross sections (see again Fig. 5.1).

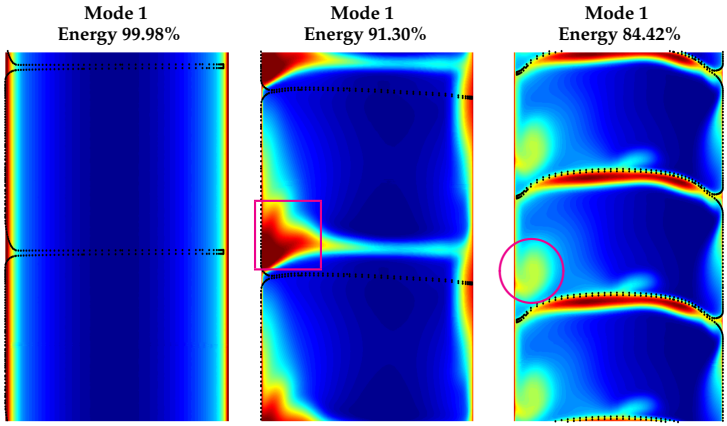

(a) AP A (b) AP C (aft R10) (c) AP E (aft S10)

Figure 5.47: POD mode 1 for mass flow, at different axial planes (see Fig. 5.1), for the undisturbed case. Horizontal: radial direction, vertical: circumferential direction. Although the APs do not intersect blades or vanes, their projection with black dots is shown for reference.

From the given energy levels shown in Fig. 5.47, we notice that, for all APs, the first POD mode (mean flow field) contains most of the decomposition energy. This outcome is recurrent in undisturbed cases. The mass flow modes are directly related to the blockage intensity at each axial position. The inlet radially uniform mass flow distribution (Fig. 5.47(a)) changes downstream each row, with specific flow phenomena clearly marking the mean flow. More specifically, the blade and vane wake is noticed by the horizontal lines close to the black dots. Areas of high blockage close to the walls occur: at the R10 hub, a corner vortex unrolls (shown with a rectangle in Fig. 5.47(b)); the vane tip clearance vortex is also depicted in the S10 domain (circle in Fig. 5.47(c)). Additionally, the modal energy linked to

the mean flow decreases from 99.98% for AP A to 84.42% for AP E, implying that traversing downstream and taking into account the flow phenomena developing in this stage promote a shift in the POD energy towards high-order modes. That is, analyzing further unsteady modes is necessary for a better understanding of the flow.

Still for the undisturbed case, the high-order POD modes 2–9 for the mass flow at AP D are shown in Fig. 5.48. Every two consecutive modes are paired and carry roughly the same energy, which is typical for the POD of periodic signals. This behavior is analogous to a decomposition into sines and cosines, functions which represent the same physical information, however phased by 90°. Indeed, the SVD is not efficient when representing translational invariance [140]. That is, whenever periodic traveling structures are present in the flow, the retainment of more POD modes is necessary, if flow reconstruction is pursued.

The main feature seen in Fig. 5.48 is the rotor wake convected downstream into the S10 domain. POD modes 2 and 3 (the first pair) show the exact R10 blade count. The following pairs depict the higher wake harmonics. To confirm this fact, the frequency spectrum (enclosed in matrix $\mathbf{V}$, from Eq. (3.56)) for this POD is exhibited in Fig. 5.49. The horizontal axis shows the frequency normalized by the BPF.

We observe clear frequency peaks at the BPF for the corresponding POD modes from Fig. 5.48. The paired modes, as predicted, have virtually the same frequency content. It is however not always the case in POD analyses that modes are linked to a single frequency. For example, pair modes 14 and 15 for the same run are shown in Fig. 5.50, whose spectrum is also depicted in Fig. 5.49. A frequency mixing is observed, which in the general case is inherent to the POD. The coherent structure shown in Fig. 5.50 originates from the R10 corner vortex as it convects downstream through the stator domain, and can be directly related to the marked area in Fig. 5.47(b). For this computation, other high-order modes also have their spatial support close to the vane tip, suggesting that, for AP D, most of

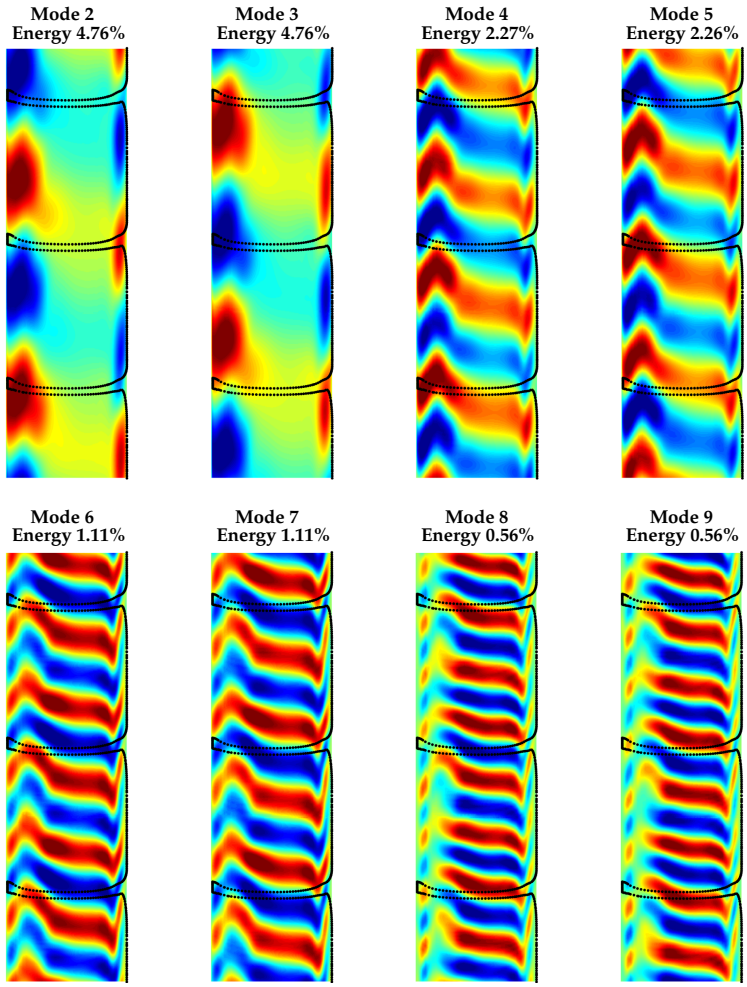

Figure 5.48: POD modes 2–9 for mass flow at AP D (see Fig. 5.1), for the undisturbed case. Every two consecutive modes are paired, with a 90° shift. Each pair represents successive harmonics, with corresponding frequency content given in Fig. 5.49.

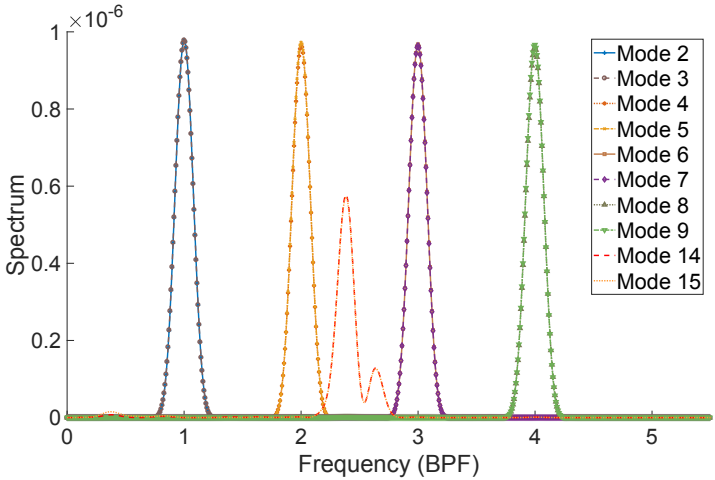

Figure 5.49: Frequency content of POD modes shown in Figs. 5.48 and 5.50. Frequencies are normalized by the BPF.

the POD energy and mass flow dynamics (related to axial velocity and blockage) are concentrated in this region.

Since in this work the mean flow is not subtracted before performing the POD, the first mode conveys the predominant energy share in a much higher proportion than a POD having the mean deducted. Therefore, the high-order modes display here a comparatively lower energy content. But even considering this fact, some high-order modes (such as the ones from Fig. 5.50) still contain a very small budget of the decomposition energy. If the focus were the implementation of a reduced order model, these high-order modes with low energy content would most likely be left out of a flow reconstruction. However, since this work aims at understanding the unsteady flow in the presence of PGC, some relevant high-order modes are still considered, as they may also convey relevant coherence information. For instance, it is insightful to understand which flow features become significant in a disturbed flow in comparison to the baseline state. The analysis of POD modes with higher index helps delimiting the

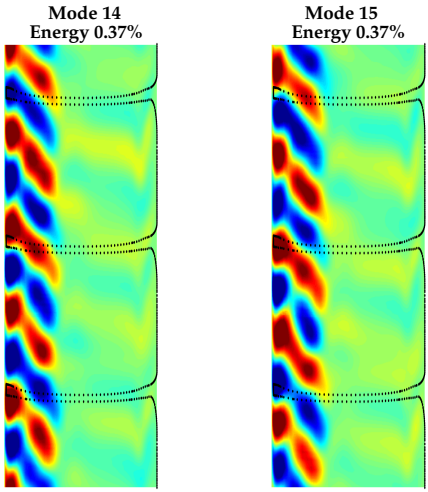

Figure 5.50: POD modes 14 and 15 for mass flow at AP D (see Fig. 5.1), for the undisturbed case. Coherent structure linked to the R10 corner vortex are observable close to the S10 vane tip. The frequency content for these modes is given in Fig. 5.49.

spatial support of these coherent structures and their relative energy content with respect to the low-order modes. This reasoning is also valid for later assessments with other state variables and decomposition domains.

Regarding the DMD results for the same computation, Fig. 5.51 depicts the continuous-system eigenvalues. Horizontal lines were added at the BPF and its high harmonics (more details about interpreting this type of figure were given in section 3.3.3).

High values for the coherence metric, depicted as color and size of each DMD mode in Fig. 5.51, hint the modes representing the most relevant flow features in the decomposition. Indeed, the DMD mode with highest coherence occurs at the BPF (label **B**). The high-coherence modes that follow occur at the higher harmonics of the BPF (labels **C** to **E**). The modes with very high frequency do not indicate the presence of long-lasting structures, yielding low coherence values.

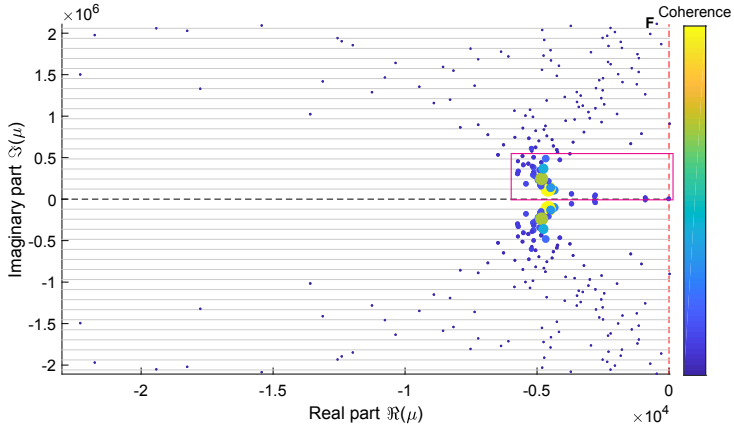

(a) DMD eigenvalues distribution

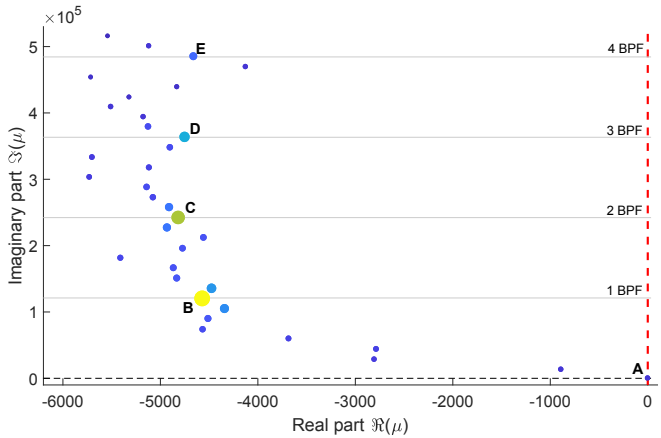

(b) Zoom on rectangle from Fig. 5.51(a)

Figure 5.51: DMD continuous-system eigenvalues for mass flow at AP D (see Fig. 5.1), for the undisturbed case. The horizontal lines correspond to the BPF and its higher harmonics, for reference. Label **A** represents the mean flow while the others correspond to the POD from Fig. 5.48 as: **B** with 2–3; **C** with 4–5, **D** with 6–7; **E** with 8–9. Label **F** represents a spurious DMD mode with high frequency, shown in Fig. 5.53.

Indeed, the DMD may identify similar flow structures as the POD, especially for convective flows (see [145]). To assess this relationship, consider a DMD mode given by $\mathbf{\Phi}$ (complex by construction, with phase $\boldsymbol{\Theta}$ and amplitude $\boldsymbol{\alpha}$) and a pair of real POD modes given by $\mathbf{X}_a$ and $\mathbf{X}_b$. These can be written as

$$\Re(\mathbf{\Phi}) + i\,\Im(\mathbf{\Phi}) = \boldsymbol{\alpha} e^{i\boldsymbol{\Theta}} = \mathbf{\Phi}, \tag{5.17a}$$

$$\mathbf{X}_a + i \quad \mathbf{X}_b = \mathbf{A} e^{i\mathbf{P}} = \hat{\mathbf{X}}_{a,b}, \tag{5.17b}$$

where the equivalent "complex" POD mode $\hat{\mathbf{X}}_{a,b}$ has amplitude $\mathbf{A} = \sqrt{\mathbf{X}_a^2 + \mathbf{X}_b^2}$ and phase $\mathbf{P} = \arg(\mathbf{X}_a + i\,\mathbf{X}_b)$. If the DMD and POD modes depict the same information, their amplitudes are expected to be equal, i.e., $\boldsymbol{\alpha} = \mathbf{A}$. To illustrate this similarity, the DMD mode labeled as $\mathbf{B}$ in Fig. 5.51(b) is shown in Fig. 5.52. Notice that the information contained in the real and imaginary parts of $\mathbf{\Phi}$ is virtually the same as depicted in the POD modes 2 and 3 shown in Fig. 5.48, up to a phase shift. Additionally, the DMD mode amplitude $\boldsymbol{\alpha}$ clearly indicates the areas with higher unsteady flow activity for the analyzed mode. It is however not always the case that POD and DMD provide the same information, since by construction they are different methods.

For completeness, a low-coherence DMD mode is shown in Fig. 5.53, for a very high frequency of approximately 17.4 times the BPF. Although large flow features may be partially observed in the real part of $\mathbf{\Phi}$, most of the oscillations represent spurious phenomena, which are not directly linked to relevant or large-scale physical phenomena. This outcome is linked both to the way the DMD concentrates most large flow structures in a couple of high-coherence modes and to numerical artifacts inherent to the limited discretization in space and time.

Up to this point, the POD and DMD results were shown only for the mass flow field. Other variables behave similarly, such as stagnation enthalpy (related to the energy change per unit mass), flow velocity (related to the turbulent kinetic energy), total pressure (related to entropy increase and passage losses), entropy and temperature – figures not shown.

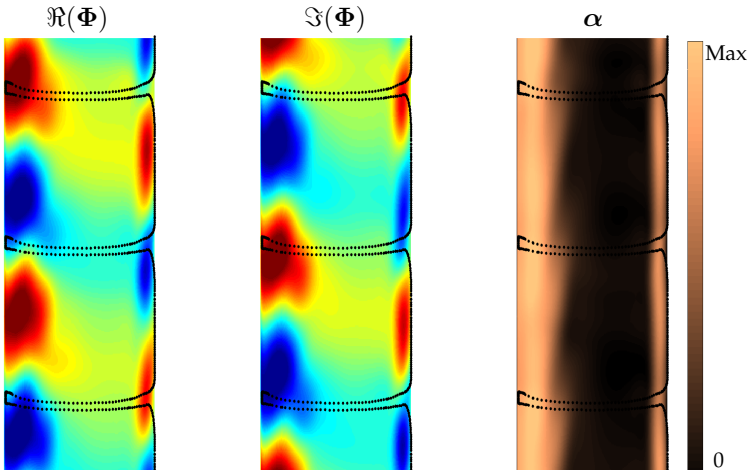

Figure 5.52: DMD mode $\mathbf{\Phi}$ for mass flow at AP D (see Fig. 5.1), for the undisturbed case. From left to right: real part, imaginary part and amplitude of $\mathbf{\Phi}$. Mode labeled as **B** in Fig. 5.51(b), with frequency corresponding to the R10 BPF.

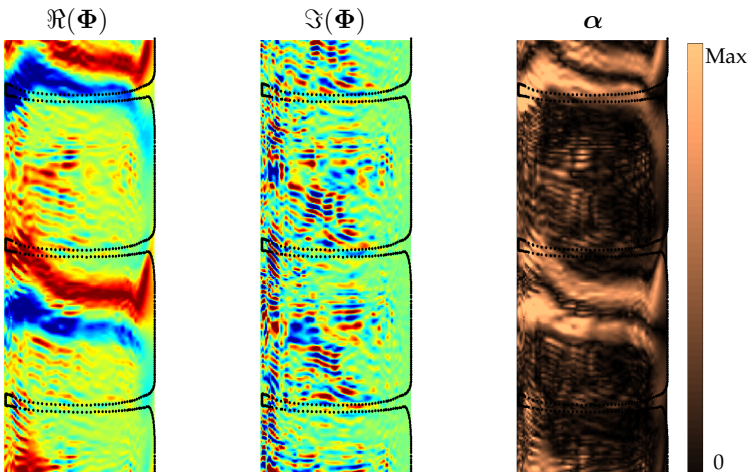

Figure 5.53: DMD mode $\mathbf{\Phi}$ for mass flow at AP D (see Fig. 5.1), for the undisturbed case. From left to right: real part, imaginary part and amplitude of $\mathbf{\Phi}$. Mode labeled as **F** in Fig. 5.51(a), with frequency of approximately 17.4 BPF.

Vorticity magnitude

Assessing the vorticity allows the identification of areas with high flow spinning and their development in time. This allows the analysis of how dynamic vortical structures already present in the baseline case are then affected by PGC disturbances.

The undisturbed results for the vorticity magnitude are shown downstream of S10 (AP E from Fig. 5.1), for a selected area close to the vane tip. Employing just a part of the spatial domain is a straightforward approach with the POD and DMD methods, allowing the identification of phenomena occurring locally without frequency-mixing effects from other regions. The selected domain chosen here is seen in Fig. 5.54(a). The phase average for the snapshot sequence employed is depicted in Fig. 5.54(b), considering a blade passing as the averaging period. POD modes 4 and 5 followed by their time dynamics are shown in Figs. 5.54(c) and 5.54(d). Although the absolute range for the vorticity is different in each plot, in all cases the same percentile interval[6] is chosen in order to keep the images comparable regarding pattern identification.

The vorticity phase average, shown in Fig. 5.54(b), indicates diffuse circular patterns close to the vane gap. However, it does not show the vortices as explicitly as the POD modes 4 and 5 from Fig. 5.54(c), from which the vortex center and its size can be extracted. This structure is originated from the convection of the R10 wakes into the S10 domain. There, the wakes encounter the vane tip clearance vortex, yielding periodic changes in vorticity (and, due to high convection velocities, helicity). The vane tip clearance vortex increases slightly in size as the stator diffuses the flow, producing the vorticity behavior observed in Fig. 5.54(c).

To confirm this fact, a detailed 3D view is shown in Fig. 5.55(a), with streamlines starting at one of the vane's tip, close to the leading edge. The pink surface corresponds to a constant, negative value of the λ_2 criterion, directly indicating the presence of the tip

[6]That is, extreme values are excluded in the same proportion for all figures. For example, the color legend ignores the smallest and highest 5% values, showing only the 90% range in between.

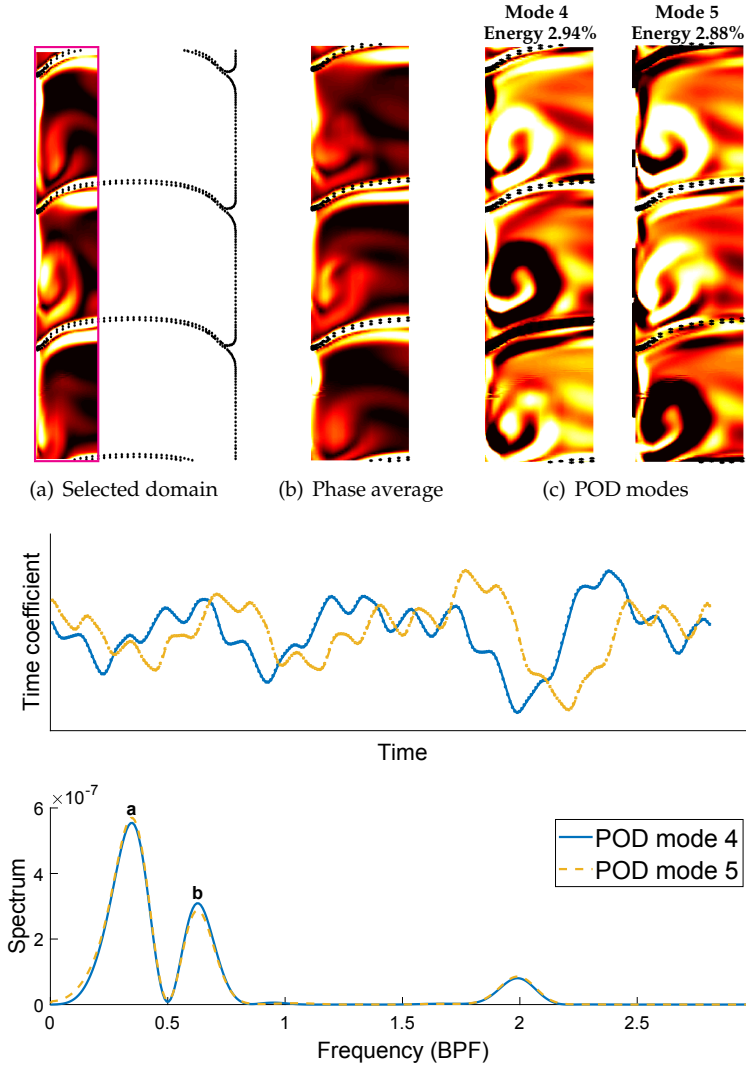

(a) Selected domain (b) Phase average (c) POD modes

(d) POD time dynamics

Figure 5.54: Phase average and POD for vorticity at part of AP E (see Fig. 5.1), for the undisturbed case. Labels **a** at $f \approx 0.35$ BPF and **b** at $f \approx 0.63$ BPF indicate the most pronounced modal frequencies.

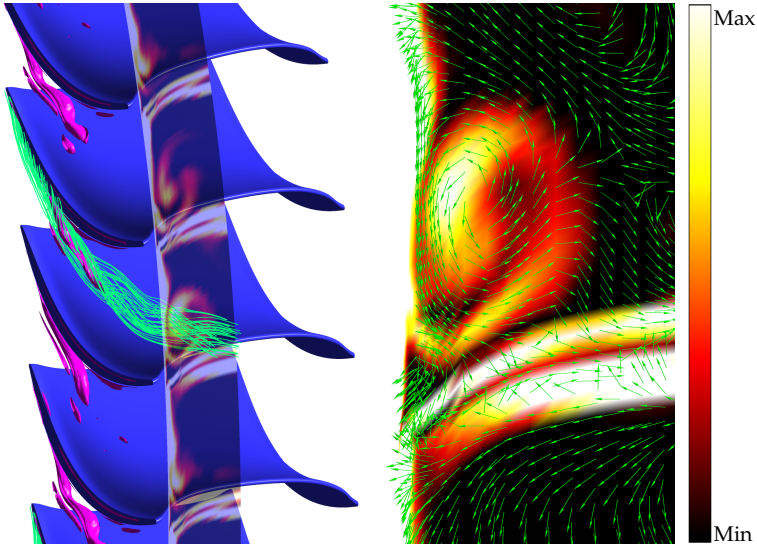

(a) Vane tip streamlines and λ_2 surface (b) Vorticity and velocity vectors

Figure 5.55: S10 vanes and part of AP E (see Fig. 5.54(a)) colored with the vorticity for a specific snapshot from the undisturbed case. Vane tip streamlines and velocity vectors are shown in green. Pink surface represents a negative λ_2 value for vortex identification.

clearance vortex[7]. The velocity vectors in Fig. 5.55(b) clearly show the tip clearance vortex, which rotates in the opposite direction of the rotor. The streamlines and λ_2 surface starting from the vane tip testify the origin of the patch with high vorticity.

The main frequencies linked to the POD modes shown in Fig. 5.54(d) are labeled with **a** at $f \approx 0.35$ BPF and **b** at $f \approx 0.63$ BPF. A smaller local peak also occurs at $f \approx 2$ BPF, related to the second harmonic of the R10 wake. However, it represents no relevant coherent structure in this case.

[7]The λ_2 vortex criterion is locally computed as the second smallest eigenvalue of the tensor $\left[\frac{1}{2}(\boldsymbol{\nabla}\mathbf{v} + \boldsymbol{\nabla}\mathbf{v}^T)\right]^2 + \left[\frac{1}{2}(\boldsymbol{\nabla}\mathbf{v} - \boldsymbol{\nabla}\mathbf{v}^T)\right]^2$, i.e., the sum of half the squares of the symmetric and antisymmetric parts of the velocity gradient tensor. Vortex cores are expected when $\lambda_2 < 0$, incurring from the Navier-Stokes equations a local minimum in pressure [259].

The DMD results for the same undisturbed case are shown in Fig. 5.56. The continuous-system eigenvalues displayed in Fig. 5.56(a) indicate that the frequencies of high coherence modes are the BPF and its higher harmonics. The real part and amplitude of DMD modes labeled **A** and **B** in Fig. 5.56(a) are displayed in Figs. 5.56(b) and 5.56(c), respectively. These modes capture basically the same phenomena portrayed in POD modes 4 and 5 (see Fig. 5.54), with good agreement on the vortex frequencies (less than 3% in relative error).

As discussed before, POD modes 4 and 5 contain mixed frequencies (see spectrum in Fig. 5.54(d)). Each DMD mode, on the other hand, is always linked to a single frequency (which is indicated in Fig. 5.56). While mode **A** represents the 'fundamental' vane tip clearance vortex shape (convected onto AP E), mode **B** shows some traces of a higher-order vortical structure. This can be seen, e.g., in the DMD mode amplitude $\boldsymbol{\alpha}$ in Fig. 5.56(c), where a more complex spiral pattern occurs, in comparison to Fig. 5.56(b). However, mode **B** is not the exact second harmonic of mode **A**, as the frequency ratio between them is not an integer.

To compare the undisturbed results with a disturbed case, Fig. 5.57 depicts the phase average and POD results for the disturbed case with $f_d = 0.125$ BPF and $A_d = 10\,\%$.

The phase average is similar to the undisturbed case (Fig. 5.54(b)), again not being able to explicitly represent coherent structures, except for a diffuse vortex pattern close to the vane tip. POD mode 2, shown in Fig. 5.57(b), contains the highest (unsteady) decomposition energy; the mode discloses, in addition to the vane tip clearance vortex, another structure at mid span, namely a high-vorticity volume which originates at the leading edge of S10. As this volume convects downstream in the passage, it detaches itself from the pressure side and produces a plume-like pattern. This flow event occurs specifically at the low-pressure part of the PGC wave, that is, in a condition resembling throttling, from the stage perspective.

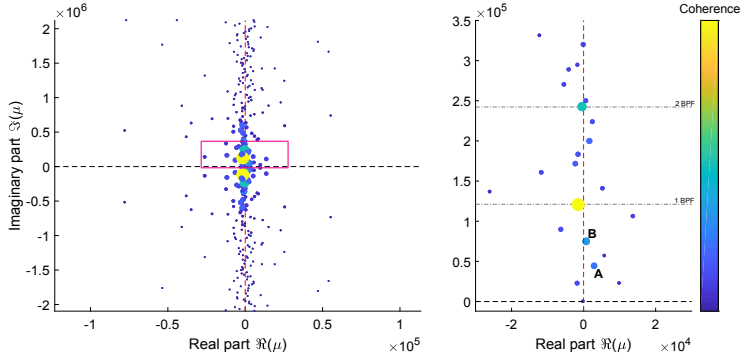

(a) DMD continuous-system eigenvalues. Right: zoom on rectangle

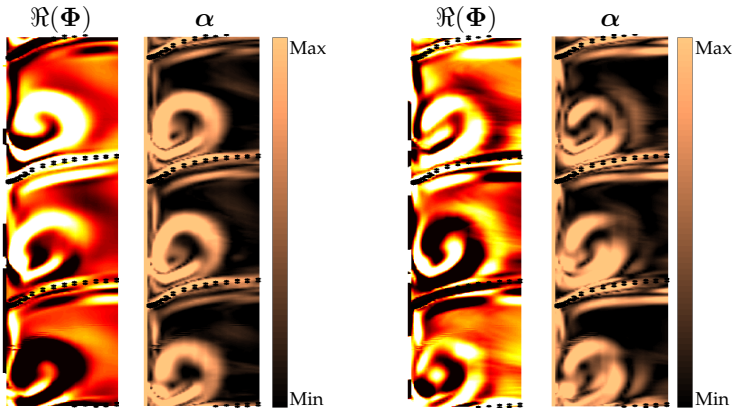

(b) Mode **A**: $f = 0.36$ BPF (c) Mode **B**: $f = 0.62$ BPF

Figure 5.56: DMD for vorticity at part of AP E (see Fig. 5.54(a)), for the undisturbed case. The real part $\Re(\mathbf{\Phi})$ and amplitude $\boldsymbol{\alpha}$ are shown for DMD modes labeled **A** and **B**.

To make this plume structure more evident, a snapshot is shown in Fig. 5.58. This time, two streamlines are shown: one originating from the vane tip and another from the leading edge, around mid span. This last streamline bundle curves away from the vane pressure side, indicating flow detachment. It then traverses AP E in the middle of the high-vorticity region. The velocity vectors in Fig. 5.58(b) indicate two flow circulation areas in the plume lobes.

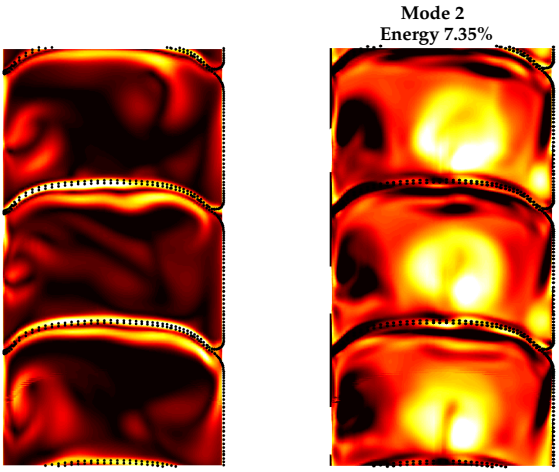

(a) Phase average (b) POD

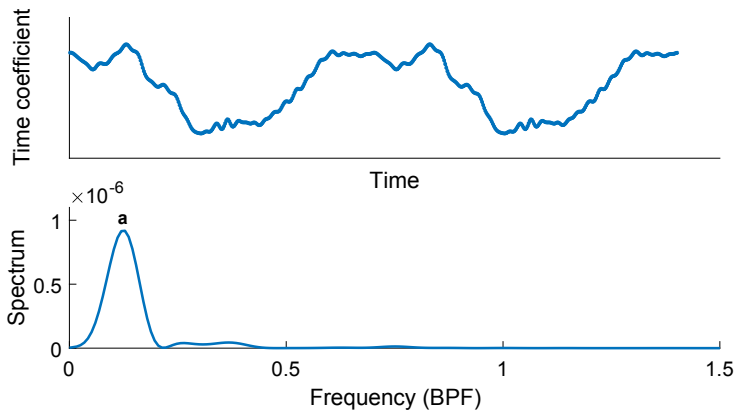

(c) Time dynamics for POD mode 2

Figure 5.57: Phase average and POD for vorticity at part of AP E (see Fig. 5.1), for the disturbed case (Eq. (5.10) with $f_d = 0.125$ BPF and $A_d = 10\,\%$). Label **a** indicates the most pronounced modal frequency.

For this disturbed case, the DMD results are shown in Fig. 5.59. Differently from the eigenvalue distribution in the undisturbed case (Fig. 5.56(a)), where substantial dispersion occurs, here the eigenvalues are much more concentrated in the dominant

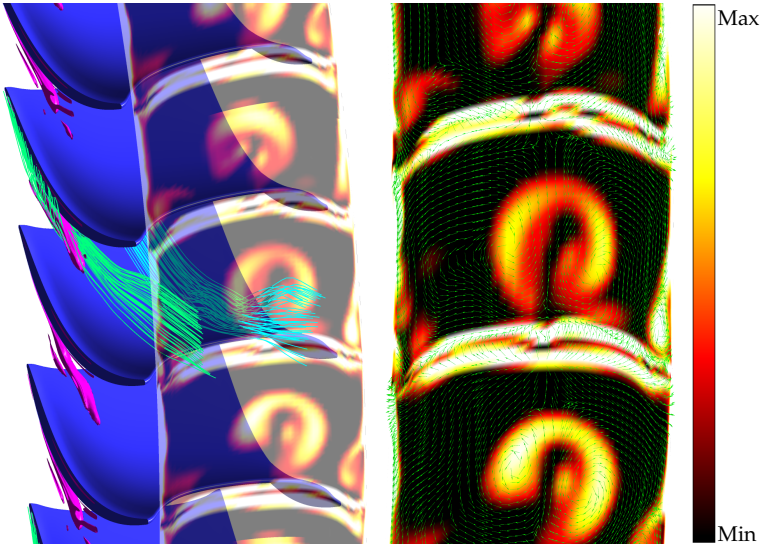

(a) Vane tip streamlines and λ_2 surface (b) Vorticity and velocity vectors

Figure 5.58: S10 vanes and AP E (see Fig. 5.1) colored with the vorticity for a specific snapshot from disturbed case (Eq. (5.10) with $f_d = 0.125$ BPF and $A_d = 10\,\%$). Vane tip streamlines and velocity vectors are shown in green. Pink surface represents a negative λ_2 value for vortex identification.

frequencies (f_d and the BPF). Again, high coherence is linked to modes matching the disturbance frequency and its harmonics, while the remaining modes yield very low coherence values (see Fig. 5.59(a)) and do not represent relevant flow features.

The real and imaginary parts, as well as the amplitude of the DMD mode labeled **A** in Fig. 5.59(a) are shown in Fig. 5.59(b). The DMD frequency matches f_d, that is, the main disturbance introduced by the PGC. The plume flow feature captured by the POD is also clearly observable in $\Re(\mathbf{\Phi})$ and $\boldsymbol{\alpha}$. Although diffuse, the vane tip clearance vortex is also present in $\Re(\mathbf{\Phi})$, however with a different sign in when compared to the plume region. This indicates that, for this specific DMD mode, these two structures occur out of phase with respect to each other, as a snapshot investigation shows.

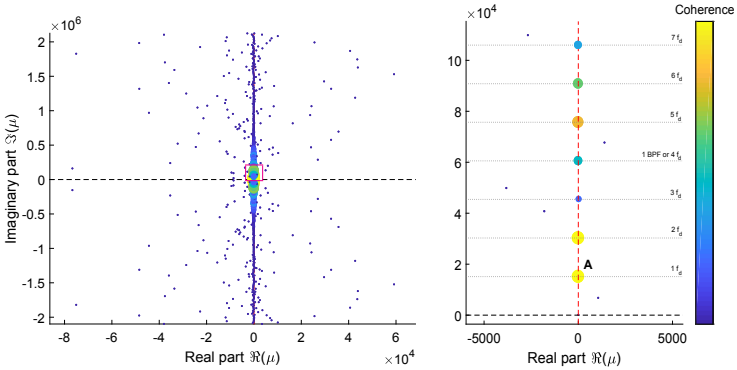

(a) DMD continuous-system eigenvalues. Right: zoom on rectangle

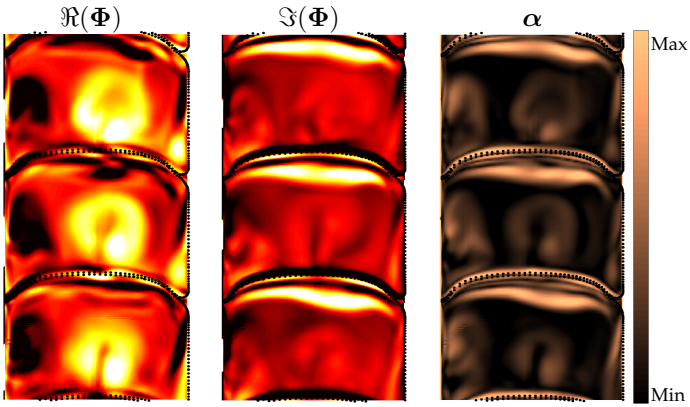

(b) Mode **A**: $f = f_d$

Figure 5.59: DMD for vorticity at AP E (see Fig. 5.1), for the disturbed case (Eq. (5.10) with $f_d = 0.125$ BPF and $A_d = 10\,\%$). The real part $\Re(\mathbf{\Phi})$, imaginary part $\Im(\mathbf{\Phi})$ and amplitude $\boldsymbol{\alpha}$ are shown for DMD mode **A**.

In order to understand how a variation in the disturbance amplitude A_d influences the flow, its value was changed while maintaining the same disturbance frequencies f_d presented up to now. Figure 5.60 shows the POD mode 3 for the disturbed flow with $f_d = 0.25$ BPF, with two different disturbance amplitudes. This POD mode is chosen since it represents a structure similar to the one shown in Fig. 5.57. The phase-average plot is not shown,

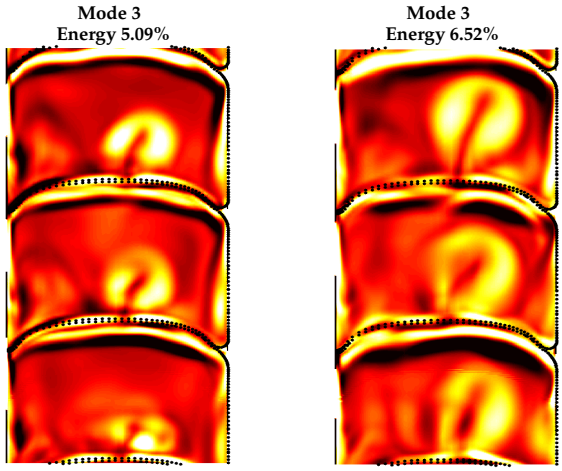

(a) $A_d = 5\%$ (b) $A_d = 10\%$

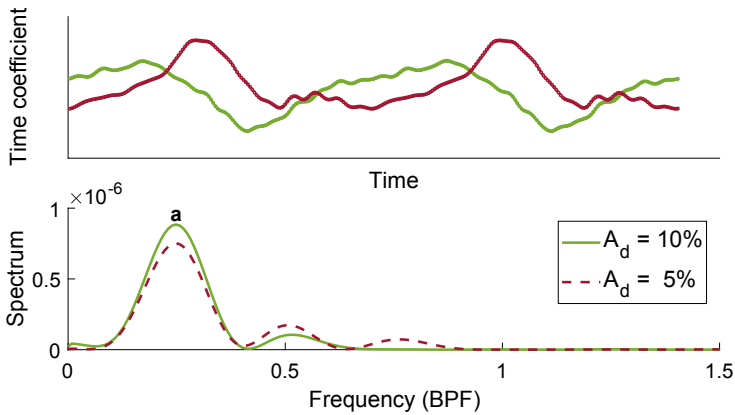

(c) Time dynamics

Figure 5.60: POD mode 3 for vorticity at part of AP E (see Fig. 5.1), for the disturbed case $f_d = 0.25$ BPF with different disturbance amplitudes A_d (see Eq. (5.10)). Label **a** indicates the most pronounced modal frequency.

since it does not reveal relevant flow structures nor adds insight to the analysis.

Initially, we notice from Figs. 5.60(a) and 5.60(b) that the separation plume detaching from the pressure side of S10 is

present in the POD mode 3 for both A_d values shown. Its size is however smaller for $A_d = 5\%$ than for $A_d = 10\%$. Turning towards Fig. 5.60(c), the time dynamics for both cases are similar, where the highest spectrum value, labeled **a**, matches f_d. Finally, the vane tip clearance vortex is not so strong as in the $f_d = 0.125$ BPF case depicted in Fig. 5.57.

Relevant information can also be extracted with other types of disturbances. Employing the inverted Gaussian pulse given by Eq. (5.15), coherent structures are obtained with POD and DMD which often relate to the flow features observed in the single-frequency cases. These structures may occur, however, in different frequency bands.

Figure 5.61 shows an insightful snapshot for the vorticity magnitude, for the inverted Gaussian pulse case[8]. This figure captures a moment after the low-pressure pulse has traversed the S10 domain upstream, which caused the temporary flow separation on the vane pressure side.

Focusing on the plume-like, high-vorticity region, we notice a similarity between this simulation and Figs. 5.57 to 5.59 (disturbed case with $f_d = 0.125$ BPF and $A_d = 10\,\%$). This region was also seen, with a different dimension, at the DMD results shown in Fig. 5.60 (disturbed case with $f_d = 0.25$ BPF). However, due to the significant amplitude of the inverted Gaussian pulse, the plume height fills virtually the entire passage pitch. A similar behavior occurs for the entropy and velocity magnitude fields.

A selected result for the DMD for the inverted Gaussian pulse is depicted in Fig. 5.62, for a mode with $f = 0.11$ BPF. Both the vane tip clearance vortex identified in the undisturbed case (Figs. 5.54 to 5.56) and the pressure side temporary separation are portrayed. Indeed, this smaller separation bubble observed adjacent to the vane in the real part of the DMD mode shown in Fig. 5.62 persists for the entire analyzed period, long after the large plume shown in Fig. 5.61 dissipates.

[8]The value of A_p in Eq. (5.15), for short-duration pulses, did not have a pivotal effect on the different coherent structures obtained with the data-driven decompositions. In this work, it was set to approximately 0.9.

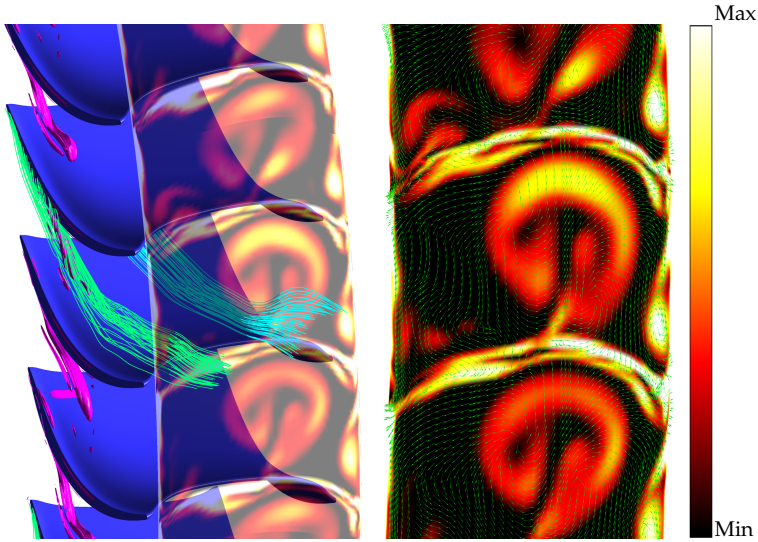

(a) Vane tip streamlines and λ_2 surface (b) Vorticity and velocity vectors

Figure 5.61: S10 vanes and AP E (see Fig. 5.1) colored with the vorticity for a specific snapshot from the inverted Gaussian pulse case (Eq. (5.15)). Vane tip streamlines and velocity vectors are shown in green. The pink surface represents a negative λ_2 value for vortex identification.

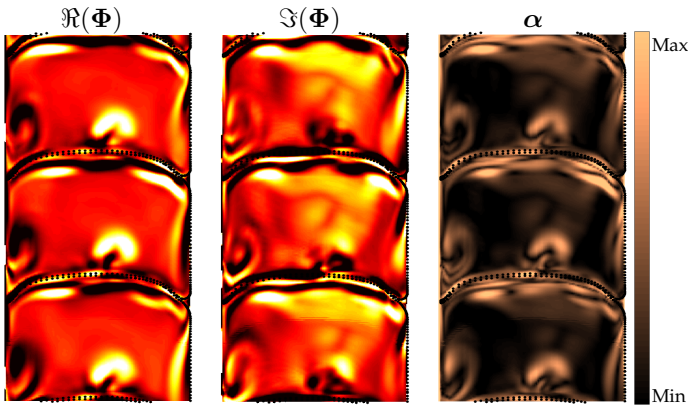

Figure 5.62: DMD for vorticity at AP E (see Fig. 5.1), for the inverted Gaussian pulse case (Eq. (5.15)). The real part $\Re(\mathbf{\Phi})$, imaginary part $\Im(\mathbf{\Phi})$ and amplitude $\boldsymbol{\alpha}$ are shown for DMD mode with $f = 0.11$ BPF.

Density gradient magnitude

We consider now changes in the decomposition of the density gradient magnitude field, contrasting the baseline with PGC-disturbed scenarios. As Figs. 5.45 and 5.46 previously hinted, an energy spread occurs in the presence of PGC disturbances, linked to a loss in coherence. Figure 5.63 depicts POD modes at AP C for the density gradient magnitude $|\boldsymbol{\nabla}\rho|$ (emulating classic Schlieren images, indicating however no shock waves here).

For the undisturbed case shown in Fig. 5.63(a), the R10 wake and corner vortex are evident in modes 2 and 3 respectively. In contrast, these structures appear spatially 'diffused' in the disturbed case shown in Fig. 5.63(b). Moreover for these disturbed case, the energy content is further shifted towards higher modes in comparison to the undisturbed computation.

Helicity

The spread of energy into high-order modes is also observed by analyzing the helicity. This scalar is an invariant in the Euler equations [260], which represent inviscid flows. Although the computations here include viscosity, the helicity still sheds light into how vortical structures unwound out when subjected to traveling disturbance waves. The helicity H is defined locally as the dot product between the velocity and its curl (or vorticity), i.e., $H = \mathbf{v} \cdot (\boldsymbol{\nabla} \times \mathbf{v})$.

Figure 5.64 shows POD modes for the helicity field at AP D[9]. Although from Fig. 5.64(a) the first POD mode (mean flow) does not disclose large coherent structures, the high-order modes 3, 7 and 13 depict periodic flow dynamics close to hub and tip. When comparing these unsteady modes for baseline case with the disturbed results from Fig. 5.64(b), again a spread in coherence is observed. The conform periodic patterns, once restricted to areas adjacent to the walls, are broken and dispersed throughout the entire plane in the presence of PGC disturbances.

[9]From now on, just one of two paired POD modes will be shown for the sake of brevity. For instance, if modes 2 and 3 are paired, only mode 3 will be shown.

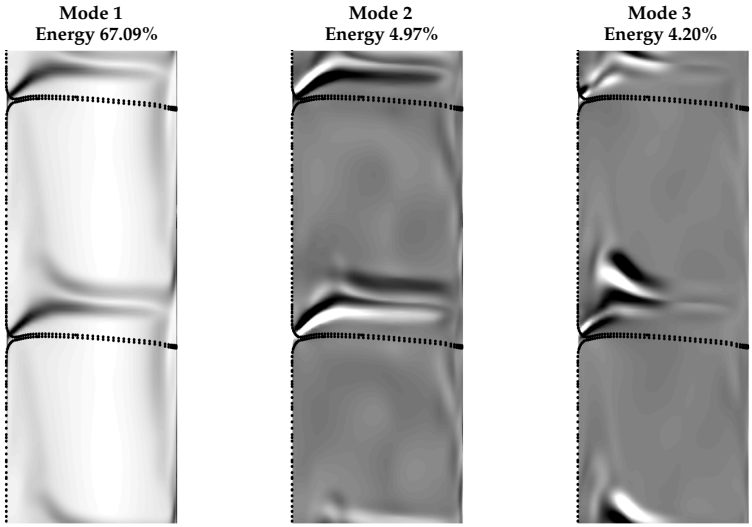

(a) Undisturbed case

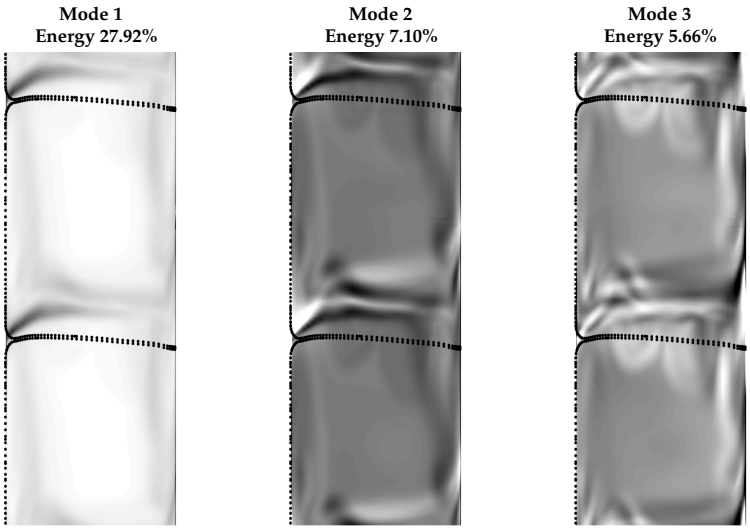

(b) Disturbed case (Eq. (5.10) with $f_d = 0.25$ BPF and $A_d = 10\,\%$)

Figure 5.63: POD modes 1–3 for density gradient magnitude at AP C (see Fig. 5.1).

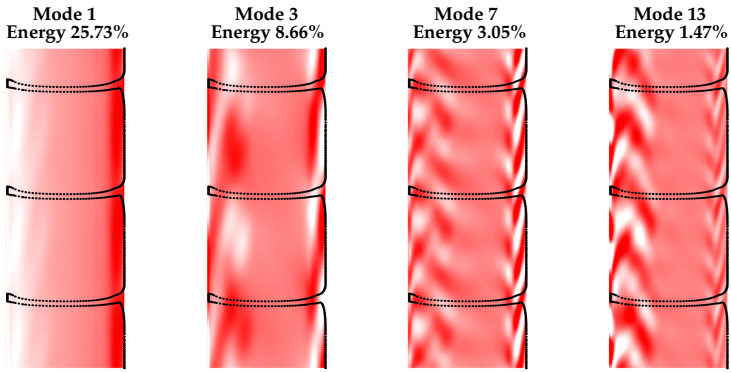

(a) Undisturbed case

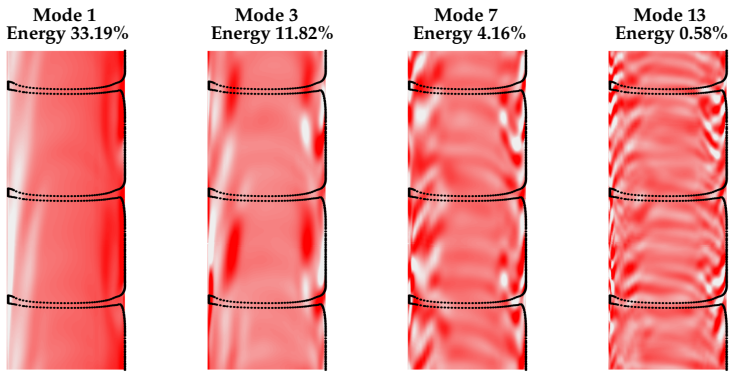

(b) Disturbed case (Eq. (5.10) with $f_d = 1$ BPF and $A_d = 10\,\%$)

Figure 5.64: POD modes 1–3 for helicity at AP D (see Fig. 5.1).

To contrast the POD with the DMD method, we analyze a more involved case, in regard to frequency content. More specifically, the disturbance frequency is set to $f_d = e^{-1/\pi}$ BPF ≈ 0.727 BPF, which is neither a multiple nor submultiple of the BPF[10]. Figure 5.65 shows POD mode 6 for the helicity field, with $A_d = 10\%$. The time coefficient linked to the POD mode is also presented, with its corresponding frequency spectrum.

[10]The total number of time steps for this computation comprises 16 blade passing periods to possibly accommodate nonlinear frequency interactions between the BPF and f_d.

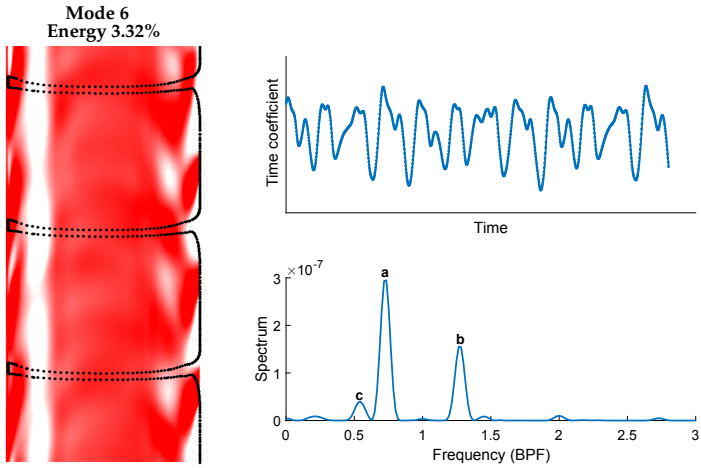

(a) Spatial mode (b) Time dynamics

Figure 5.65: POD mode 6 for helicity at AP D (see Fig. 5.1). Disturbed case (Eq. (5.10) with $f_d = e^{-1/\pi}$ BPF ≈ 0.727 BPF and $A_d = 10\,\%$). Labels **a**, **b** and **c** indicate the most pronounced modal frequencies.

The POD mode shown in Fig. 5.65 has mixed frequencies, with the most pronounced spectrum values labeled in Fig. 5.65(b) in a descending fashion from **a** to **c**. Figure 5.65(a) also indicates that flow phenomena in different spatial scales occur simultaneously in the same POD mode. Namely, a long circumferential wake line (vertical in Fig. 5.65(a)) is observed on the left, close to the vane tip. The same mode shows however smaller periodic vortical structures on the right, close to the vane root.

Now we contrast the POD with the DMD results for the same disturbed case shown above. Figure 5.66 shows the continuous-system eigenvalues for this computation. A closer view is shown in Fig. 5.66(b), where it is clear that both the BPF, the disturbance frequency f_d as well as cross-interactions are relevant for this flow. Most high-coherence modes occur with frequencies less than $3f_d$.

The DMD modes labeled with **A**, **B** and **C** in Fig. 5.66(b) are depicted in Fig. 5.67. Only the real part is shown for simplicity. The frequency of each DMD mode is given as a function of the BPF and f_d. These three modes were specifically chosen because

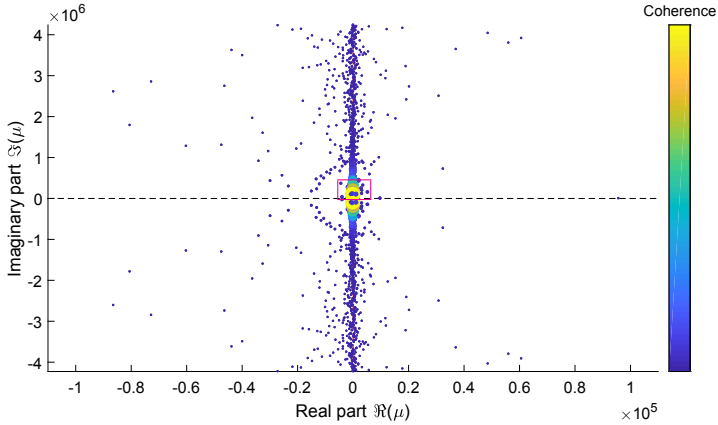

(a) DMD eigenvalues distribution

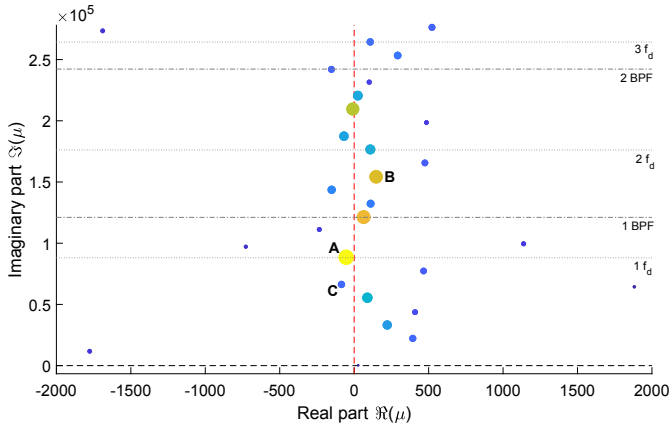

(b) Zoom on rectangle from Fig. 5.66(a)

Figure 5.66: DMD continuous-system eigenvalues for helicity at AP D (see Fig. 5.1), for the disturbed case (Eq. (5.10) with $f_d = e^{-1/\pi}$ BPF ≈ 0.727 BPF and $A_d = 10\,\%$). The horizontal lines indicate the BPF, f_d and their higher harmonics. Modes labeled **A**, **B** and **C** shown in Fig. 5.67.

their DMD frequency coincide with the three peaks shown in the spectrum of POD mode 6 (labeled correspondingly with **a**, **b** and **c** in Fig. 5.65(b)).

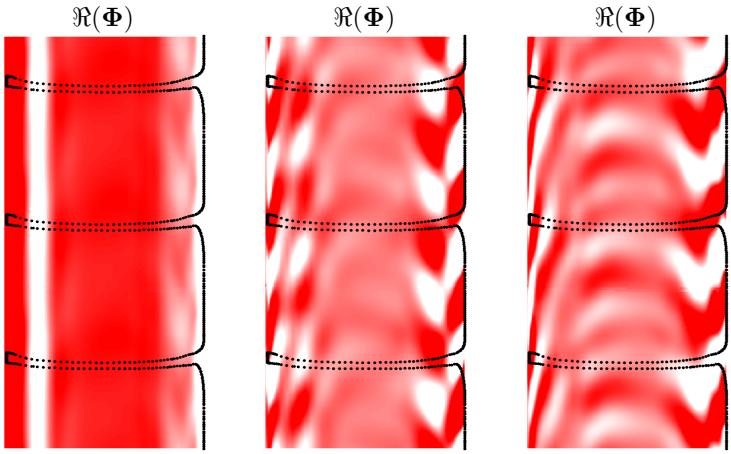

(a) **A**: $f = f_d$ (b) **B**: $f = 2\,\mathrm{BPF} - f_d$ (c) **C**: $f = 2(\mathrm{BPF} - f_d)$

Figure 5.67: Real part of DMD mode $\mathbf{\Phi}$ for helicity at AP D (see Fig. 5.1) for the disturbed case (Eq. (5.10) with $f_d = e^{-1/\pi}$ BPF ≈ 0.727 BPF and $A_d = 10\,\%$). Labels **A**, **B** and **C** from Fig. 5.66(b). For each mode, the respective DMD frequencies are shown, as a function of disturbance and blade passing frequencies, respectively f_d and BPF.

The mode linked to the fundamental disturbance frequency (label **A**, Fig. 5.67(a)) portraits dynamic behavior as a circumferential white stripe (vertical in this view) close to the vane tip, with weaker influence close to the vane hub. This feature was also recognized in the corresponding POD mode 6 (Fig. 5.65(a)), and is linked to how the R10 corner vortex is periodically chopped by the upstream-traveling PGC wave. However, differently from the POD, the DMD shows no flow structures between this wake stripe and the hub (far left border).

Furthermore, the DMD mode with frequency $f = 2\,\mathrm{BPF} - f_d$ (label **B**, Fig. 5.67(b)) conveys the interaction between the BPF and the PGC disturbance. It manages to capture the small-scale structures close to the walls much more clearly than the POD mode 6. Indeed, the two phenomena close to the vane tip which were mixed in the POD mode 6 are well separated in the DMD. This is a useful feature of the DMD method, enabling the

identification of coherent structures at a specific, single frequency, which is often proportional to the resulting spatial scales.

For completeness, the DMD mode labeled **C** in Fig. 5.67(b) and frequency $f = 2(\text{BPF} - f_d)$ is shown in Fig. 5.67(c). From the three DMD modes linked to most pronounced frequencies of POD mode 6, this one has the least coherence, and is associated with the smallest labeled peak (**c** in Fig. 5.65(b)).

5.3.4.3 Streamwise surfaces

Following the results presented for axial planes in section 5.3.4.2, we now show decomposition assessments for streamwise surfaces. These are blade-to-blade (alternatively, cylindrical) cuts at different radial positions. That is, the free variables are now the axial coordinate and the circumferential angle, for fixed span values. The mainstream flow goes from left to right.

Entropy

Initially, the POD results for entropy are shown in Fig. 5.68, for the undisturbed case at a mid-span cross section in the S10 domain. Paired modes are not shown for brevity.

POD modes 3, 5, 7, 9 and 15 portray the R10 wake, as it convects downstream through the S10 domain. They represent the ascending BPF harmonics, with a regular spectrum similar to the one depicted in Fig. 5.49. The number of alternating low and high entropy stripes present in each mode increases in direct proportion to the BPF harmonic. For example, POD mode 3 contains four stripes along the vane, POD mode 5 contains eight stripes, and so on.

The first unsteady instances containing structures not directly affiliated with the BPF are POD modes 11 and 13, already with a very low energy content. These modes are linked to flow separation on the pressure side, with a frequency peak of 0.37 BPF and 0.61 BPF, respectively. Note that, for the first 16 POD modes, this is the only high-coherence phenomenon occurring at frequencies lower than the BPF. Furthermore, these frequencies match with the POD and DMD results obtained for the vorticity

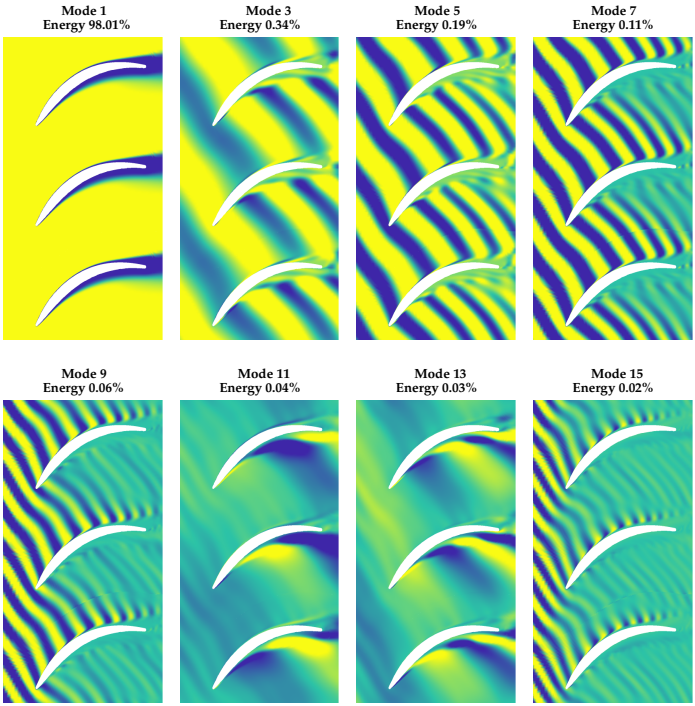

Figure 5.68: POD modes 1–15 for entropy on the mid-span streamwise surface in the S10 domain, for the undisturbed case. Horizontal: axial direction, vertical: circumferential direction. Paired modes not shown.

magnitude at AP E, shown in Figs. 5.54 and 5.56. Although the decomposition region employed in the vorticity results does not intersect the mid-span cut shown in Fig. 5.68, the radial influence of the vane tip clearance vortex is also observed in the entropy POD, when considering the frequency content.

Now we consider for the same mid-span surface a disturbed case with $f_d = 0.75$ BPF and $A_d = 10\,\%$. Figure 5.69 depicts the same POD mode indexes shown for the undisturbed case. This time, each of the POD modes contains mixed frequencies. For example, the BPF and its harmonics are observed in the spectrum of several modes. Indeed, the first instance portraying the R10 wake convection partially clearly is the POD mode 9, however

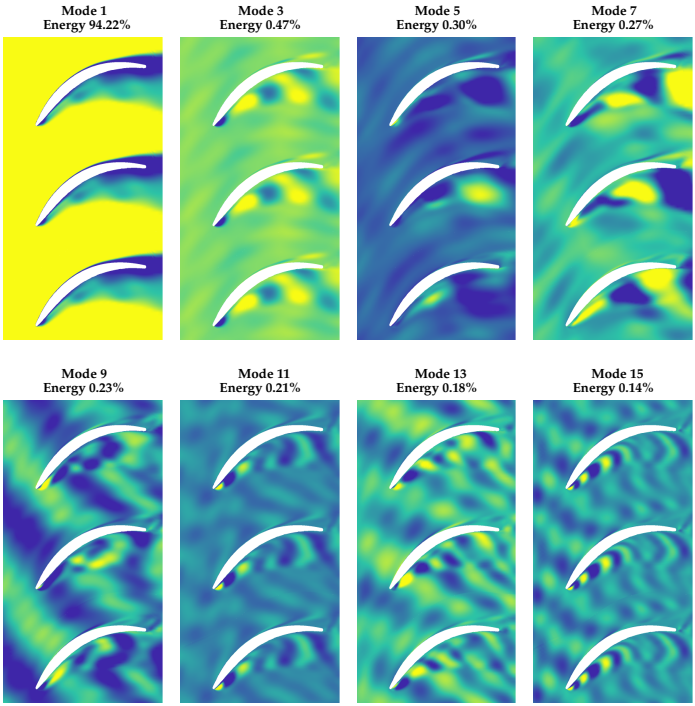

Figure 5.69: POD modes 1–15 for entropy on the mid-span streamwise surface in the S10 domain, for the disturbed case (Eq. (5.10) with $f_d = 0.75$ BPF and $A_d = 10\,\%$). Paired modes not shown.

certainly not as evident as in Fig. 5.68. All unsteady modes represent flow features mainly linked to temporary separation on the pressure side and its corresponding vortex street.

The POD is able, in this case, to directly rank physical phenomena according to their importance in reconstructing the unsteady flow. Relevant change in entropy in the undisturbed case was linked to wake convection, while in the presence of PGC disturbances, pressure side temporary separation plays a much more significant role. Also relevant is the fact that the modal energy decays more slowly for the disturbed case, revealing that important flow information is distributed among more modes in comparison to the undisturbed case.

Another remark about Fig. 5.69 is that modes linked to higher frequency phenomena ("fast mode") do not necessarily have a lower energy than modes depicting large-scale coherent structures associated with lower frequencies ("slow mode"). For example, mode 3 (with frequency peak at $f_d = 0.75$ BPF) has a larger singular value than mode 5 (peak at 0.5 BPF) and mode 7 (peak at 0.25 BPF).

Finally, the mean flow depicted in POD mode 1 contains decidedly the largest energy share and provides the spatial support of the pressure side separation area. This region is much larger for the disturbed case in contrast with the baseline flow. This outcome substantiates the increase in total pressure loss in the S10 domain, displayed in Fig. 5.38. The connection between the increase in entropy and loss in total pressure is obtained by the Gibbs equation[11], given in the rotor frame by

$$\frac{p_{t2}}{p_{t1}} = e^{-\Delta s/R}, \tag{5.18}$$

where p_{t2} and p_{t1} are the total pressure values at states 2 and 1, $\Delta s = s_2 - s_1$ the entropy change, and R the specific gas constant. That is, for an adiabatic flow with losses, the total pressure always decreases, since the entropy change must be positive.

After traveling the S10 domain, the disturbance wave reaches the R10 blades. However, before turning towards the disturbed cases, the undisturbed results for the rotor domain are shown for reference in Fig. 5.70. The blade wake oscillates minimally in the circumferential direction, producing a pattern similar to a Kármán vortex street for flow around a cylinder (e.g., [135, 141, 261]) or an airfoil (e.g., [262]). The POD of this oscillating wake produces the alternating lobe structures shown in Fig. 5.70. An increase in lobe count occurs for higher harmonics.

Similarly to the analyses in the S10 domain, we compare the undisturbed with the same disturbed case ($f_d = 0.75$ BPF and $A_d = 10\,\%$), whose POD is depicted in Fig. 5.71. This time, in

[11] The Gibbs relation merges the first and second laws of thermodynamics. It is given in the differential form by $Tds = de + p\,d(1/\rho)$.

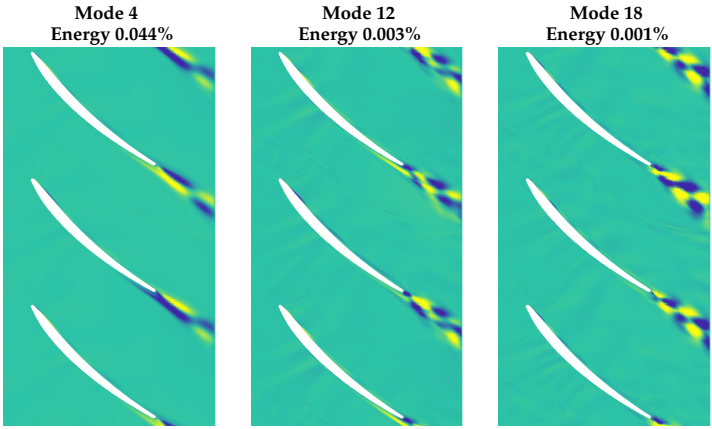

Figure 5.70: POD modes 4, 12 and 18 for entropy on the mid-span streamwise surface in the R10 domain, for the undisturbed case.

addition to the R10 wake downstream the trailing edge, small vortices originated at the leading edge travel adjacently to the blade pressure side. These vortices leave a footprint in all modes shown, specifically in the form of alternating stretched entropy spots. We seek to compare how this specific mode varies for different disturbance frequencies. For that, Fig. 5.72 contrasts the POD mode 4 between undisturbed and disturbed cases, for several values of f_d, with $A_d = 10\%$.

The thickness of the area linked to periodic entropy fluctuation on the pressure side clearly increases from the undisturbed case (Fig. 5.72(a)) towards the lowest disturbance frequency (Fig. 5.72(f)). This behavior, for the different disturbance frequencies simulated, matches qualitatively with and justifies the increase in total pressure loss in the R10 domain shown in Fig. 5.38. Finally, the relative energy associated with POD mode 4 also increases towards lower values of f_d (from 0.044% to 0.65%), once again indicating that, in the presence of PGC-disturbances, higher-order modes convey more relevance regarding unsteady phenomena.

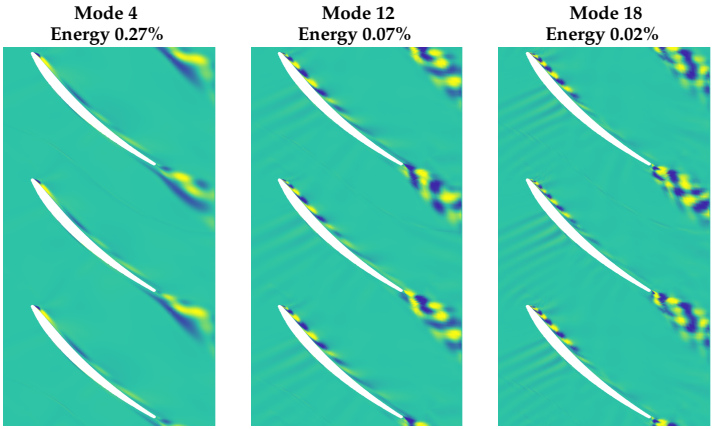

Figure 5.71: POD modes 4, 12 and 18 for entropy on the mid-span streamwise surface in the R10 domain, for the disturbed case (Eq. (5.10) with $f_d = 0.75$ BPF and $A_d = 10\,\%$).

The entropy distribution at the R10 blade tip shows an interesting pattern. For a streamwise surface at the tip gap (99% span), a representative snapshot is shown in Fig. 5.73(a), where the pink surface indicates the λ_2 vortex criterion. The projection of the R10 camber line at the blade tip is represented in orange, to ease visualization.

The streamlines originate at the tip gap, close to the leading edge of exactly one of the blades. They form a straight vortex tube which does not intersect with the adjacent (here, lower) blade projection. Although a couple of single streamlines do traverse towards the next blade and join its tip clearance vortex, their bulk remain intertwined in the main vortex body.

Fig. 5.73(b) depicts the two most energetic unsteady POD modes, for the undisturbed case. The alternating high and low entropy areas are directly linked to the downstream presence of the stator vanes (which is confirmed by the POD frequency spectrum, restricted simply to the vane passing frequency (VPF)). As will be shown in section 5.3.4.4, the pressure distribution on the rotor blade relates to the potential field from the downstream vanes with the same alternating pattern depicted here.

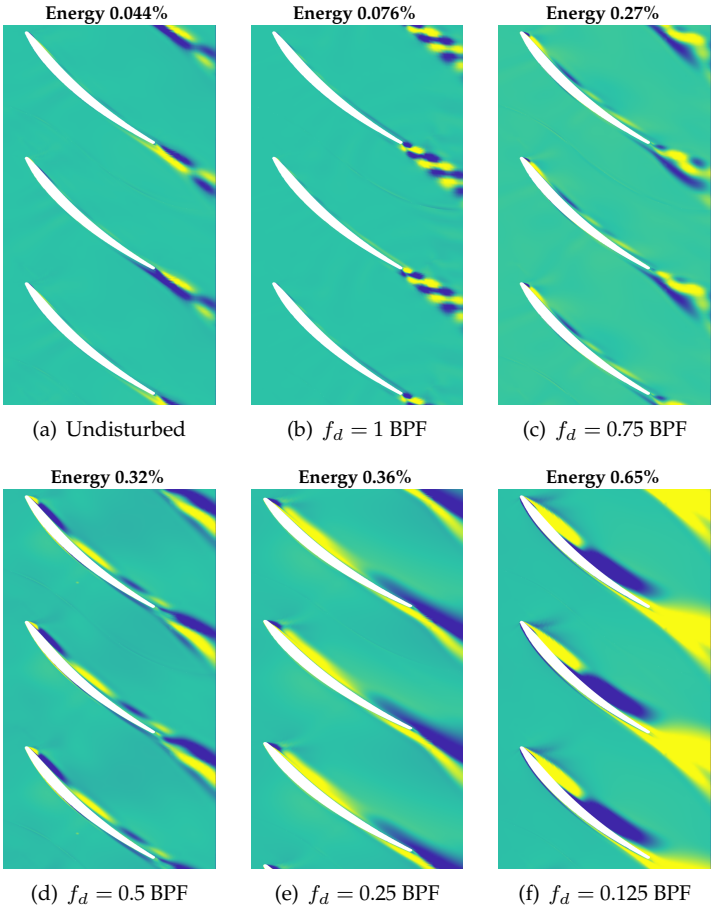

(a) Undisturbed (b) $f_d = 1$ BPF (c) $f_d = 0.75$ BPF

(d) $f_d = 0.5$ BPF (e) $f_d = 0.25$ BPF (f) $f_d = 0.125$ BPF

Figure 5.72: POD mode 4 for entropy on the mid-span streamwise surface in the R10 domain, for the undisturbed and disturbed cases, for different disturbance frequencies f_d with amplitude $A_d = 10\%$ (see Eq. (5.10)).

The DMD eigenvalue distribution for this case is also shown in Fig. 5.73(c). The frequency of the most coherent DMD mode matches the VPF. It is labeled **A**, with real and imaginary parts corresponding respectively to POD modes 2 and 3 from Fig. 5.73(b).

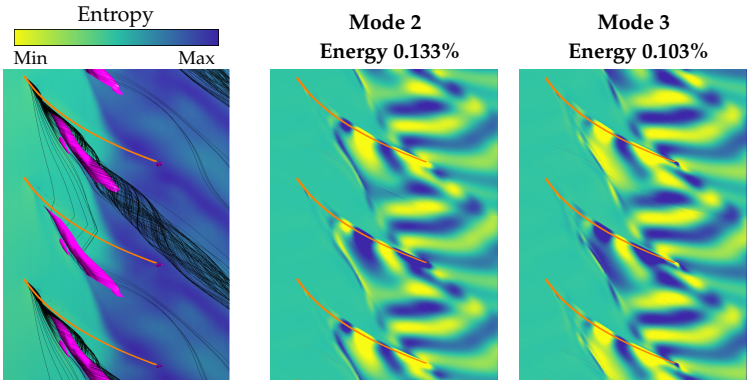

(a) Sample snapshot (b) POD

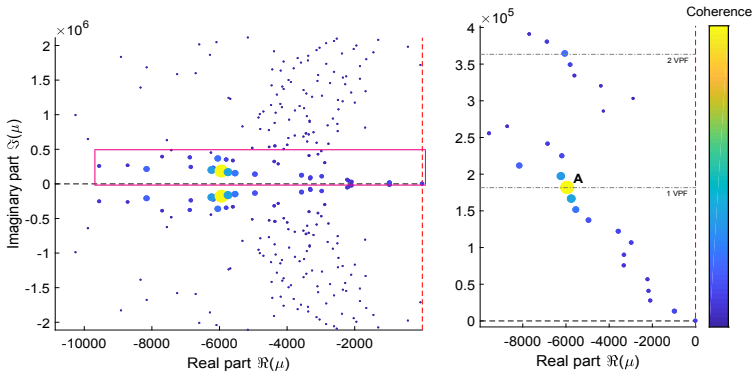

(c) DMD continuous-system eigenvalues. Right: zoom on rectangle

Figure 5.73: Representative snapshot and data-driven decompositions for entropy at the R10 tip gap (99% span), for the undisturbed case. The pink surface represents a negative λ_2 value for vortex identification, while the blade camber line is projected in orange for clarity. The POD modes correspond to the real and imaginary parts of the most coherent DMD mode, labeled **A**.

Additionally, the tip clearance vortex influence area, manifested here in the entropy distribution, can be readily obtained from the POD/DMD modes. Its upstream boundary starts from the leading edge and extends almost up to the trailing edge of the adjacent

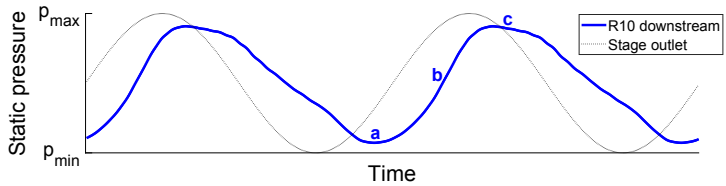

Figure 5.74: Static pressure averaged spatially, downstream R10 (at AP C, see Fig. 5.1) and at the stage outlet, for the disturbed case with $f_d = 0.125$ BPF and $A_d = 10\,\%$ (see Eq. (5.10)). Snapshots labeled **a**, **b** and **c** shown in Fig. 5.75.

blade's pressure side, in an impingement-like fashion (since this surface does not intersect the blade walls, no true impingement occurs).

To further investigate the tip gap behavior of entropy for the disturbed case, transient data is collected on the same streamwise surface (R10 tip gap at 99% span), for a run with $f_d = 0.125$ BPF and $A_d = 10\,\%$. Representative snapshots were selected within one disturbance cycle. They were extracted at the instants labeled **a**, **b** and **c** in Fig. 5.74, which shows the static pressure averaged on a plane downstream R10 (AP C, see Fig. 5.1) and at the stage outlet. For the current purposes, AP C can be understood as a surrogate to the R10 outlet; indeed, the flow dynamics in the rotor domain are vastly dependent on the pressure value at AP C, i.e., the R10 back pressure.

The selected snapshots are depicted in Fig. 5.75, portraying next to the entropy the static pressure field, hinting the back pressure value from the rotor perspective. Snapshot **a** (Fig. 5.75(a)) is termed[12] here "negative stall phase". This is justified by the fact that, for lower back pressure, lower incidence angles develop in the rotor, increasing the risk of flow separation on the pressure side. Additionally, a higher inlet Mach number occurs. Especially downstream the mid chord on the suction side, the helical streamlines embody a rather thin and uniform conical

[12]The nomenclature employed here draws from the seminal work with cascade flow from [263].

surface around the tip clearance vortex. Its core rests approximately in a straight line. Another set of streamlines remains close to the R10 pressure side, substantiating the low-incidence angles typical from the negative stall phase. Although for a very brief time interval, they disclose the presence of a pressure side vortex of short length. From this second streamline set, a couple of lines "cross" into the suction side and merge with the first set.

Moving towards the "unstalled phase", snapshot **b** (Fig. 5.75(b)), we notice no occurrence of low-incidence streamlines on the pressure side. Furthermore, the tip clearance vortex identified by the curved streamlines and the λ_2 surface increases in diameter, whose core loses the straight-line character from snapshot **a**. Differently from the negative stall case, some streamlines reach the adjacent blade, crossing towards the suction side and merging with its tip clearance vortex. Finally, the vortex angle (with respect to the axial direction) does not change significantly from the negative stall to the unstalled phase.

The last snapshot shown, labeled **c** (Fig. 5.75(c)), corresponds to the "positive stall phase". It is characterized by high-incidence angles and a tendency towards flow separation on the suction side. Initially, the incidence angle at the beginning of the vortex core line increases (i.e., the λ_2 surface leans towards the lower blade). Then, the tip clearance vortex swirls downstream, where the flow behaves much more irregularly than in snapshots **a** and **b**. This core precession behavior is typical of spiral vortices [264]. The increase in the incidence angle with higher back pressure is even enough to provoke flow spillage at the blade leading edge. This is clear from the streamlines located right upstream the camber line, which are indeed perpendicular to the axial direction. Even though this spillage does not last long, it shows to which extent the PGC disturbances are able to alter the design operation and produce new flow phenomena.

In classic steady state assessments in turbomachinery, flow regimes linked to negative and positive stalls are directly related to higher losses in comparison to the design point performance.

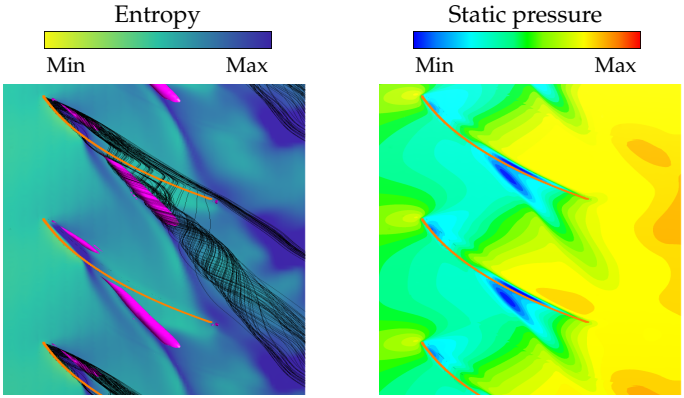

(a) Snapshot **a**: negative stall phase

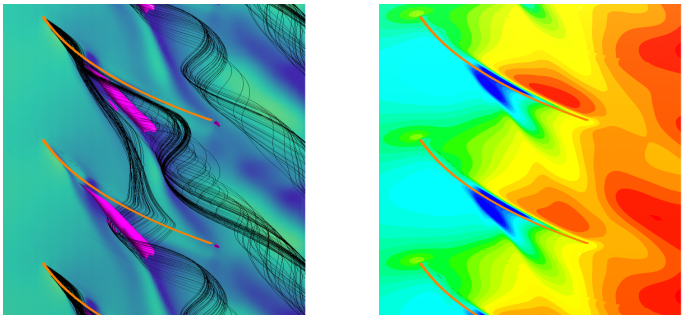

(b) Snapshot **b**: unstalled phase

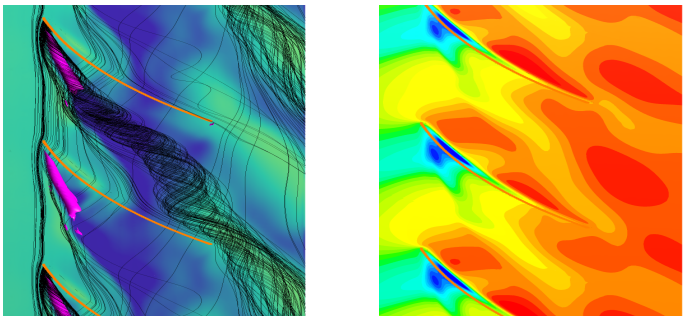

(c) Snapshot **c**: positive stall phase

Figure 5.75: Snapshots of entropy and static pressure at the R10 tip gap (99% span), for instants labeled as **a**, **b** and **c** in Fig. 5.74. Disturbed case with $f_d = 0.125$ BPF and $A_d = 10\,\%$ (see Eq. (5.10)). The pink surface represents a negative λ_2 value for vortex identification. The blade camber line is projected in orange for clarity.

Although here the whole transition from negative to positive stall regimes is contained within a single transient case, the high- and low-incidence losses explain the performance results from section 5.3.3 in a detailed manner. More specifically, the lower values of f_d imply that the rotor (and also for that matter the stator) domain remain for a longer period "off design". As exposed in Fig. 5.75, this departure from the design point incurs local increase in entropy and therefore decrease in isentropic efficiency.

5.3.4.4 Blade surface

The last type of domain employed in the data-driven analyses is the blade surface. The manner the flow interacts with the solid walls is a key aspect of turbomachinery design. It determines not only how the fluid is "guided" through the engine (producing, e.g., thrust), but also directly relates to the aeroelastic response of each component (see section 3.1.3).

Initially, we compare the data-driven techniques for the baseline, undisturbed case. Figure 5.76 shows the Fourier decomposition (real part of mode with $f = \text{VPF}$), the POD and DMD (imaginary part of mode with $f = \text{VPF}$) for the R10 blade surface. There is no substantial difference between the decompositions.

An alternating pressure pattern occurs on the suction side, especially close to the blade tip. This periodic disposition is explained by the combination of two features: the tip leakage from the pressure to the suction side and rotor-stator interaction. Although mass flows continuously (but not uniformly) through the gap due to the pressure difference between each side of the blade, the potential field from the vanes downstream varies periodically, "pushing" and "pulling" the tip gap flow in the axial direction. This recurring behavior is translated into the data-driven decompositions as the alternating patches observed in the upper part of Fig. 5.76.

This behavior can also be observed for other state variables. For instance, the POD of entropy at the tip gap (see Fig. 5.73(b)) also indicated this wavering pattern, with the same number of

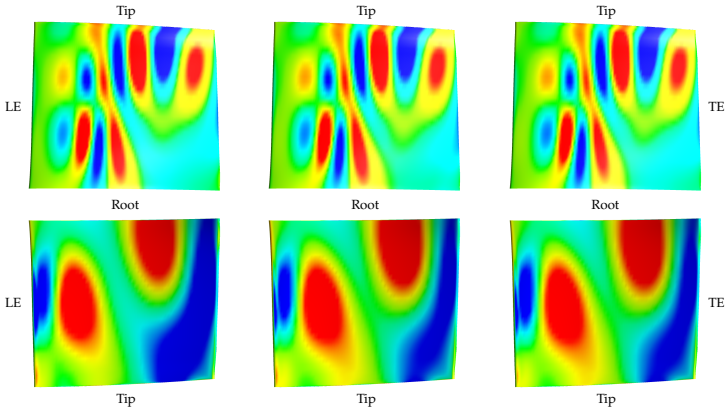

(a) Fourier $f = \text{VPF}$ (b) POD mode 3 (c) DMD $f = \text{VPF}$

Figure 5.76: Data-driven decompositions for the pressure on the R10 blade, for the undisturbed case. Top: suction side; bottom: pressure side.

alternating lobes at the rotor tip depicted in Fig. 5.76. The tip gap streamwise entropy distribution from Fig. 5.73(b) also indicates that this pattern with small alternating patches linked to the VPF is not present on the pressure side. This is again confirmed by analyzing the lower part of Fig. 5.76, where pressure variations occur rather at larger spatial scales.

The reason why all decompositions from Fig. 5.76 show virtually the same pattern is that this case not only has a single principal periodic event (the vane passing), but also the number of snapshots employed in the decomposition is very high, nearing periodic saturation (refer back to Eq. (3.60) for details in the DMD framework). In other words, adding more snapshots to the decomposition should not disclose insightful information.

This fact is confirmed in Fig. 5.77, comparing the DMD continuous-system eigenvalues for two data sets with different numbers of total snapshots. Although many more low-coherence DMD modes are present in the case with 80 rotor passing periods, the few high-coherence ones remain almost unchanged (both with respect to the empirical frequency and the spatial shape).

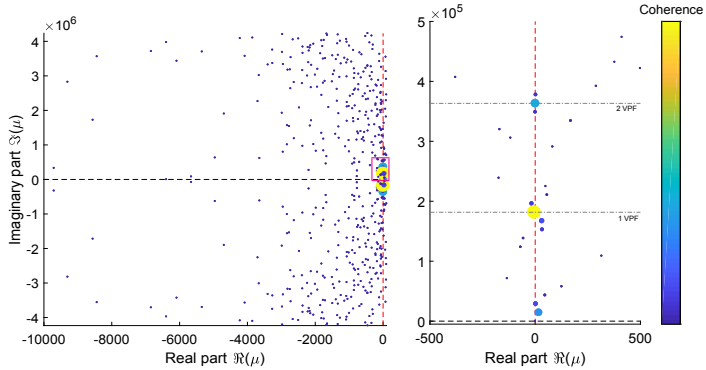

(a) 10 rotor passing periods

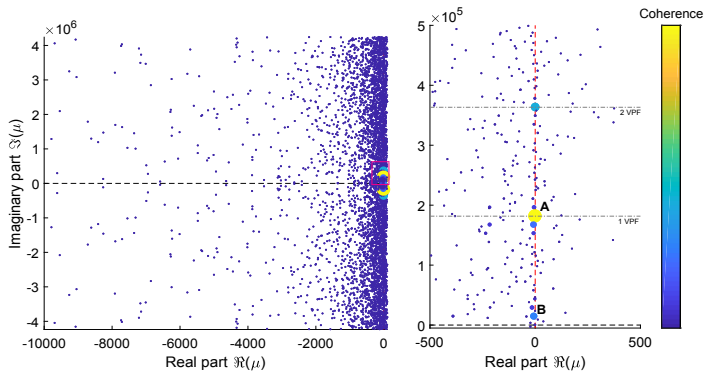

(b) 80 rotor passing periods

Figure 5.77: DMD continuous-system eigenvalues for pressure on the R10 blade surface. Undisturbed case shown for two different numbers of total snapshots. High-coherence modes labeled **A** and **B** depicted respectively in Figs. 5.76(c) and 5.78.

For instance, the DMD mode matching the VPF (labeled **A** and shown in Fig. 5.76(c)) remains the most coherent in both cases.

Similarly, the low-frequency DMD mode labeled **B** in Fig. 5.77(b) is the third most coherent, regardless of the total number of snapshots considered here. As shown in Fig. 5.78, it identifies the R10 corner vortex upstream the trailing edge.

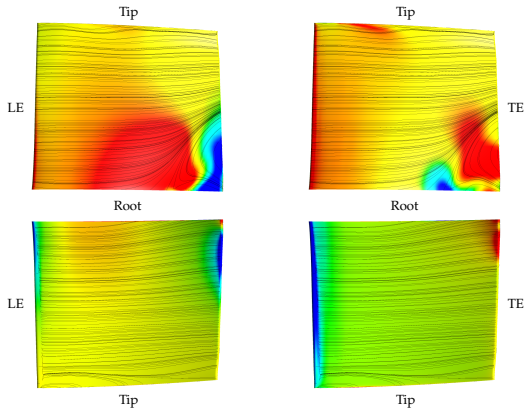

(a) Real part (b) Imaginary part

Figure 5.78: DMD mode with $f = 0.119$ BPF for pressure on the R10 blade for the undisturbed case, labeled as **B** in Fig. 5.77(b). Top: suction side; bottom: pressure side.

Among the flow structures with frequency lower than the VPF, this is the most relevant for this case, as conveyed by the DMD coherence metric (this outcome could also be seen at the mass flow decomposition presented in Fig. 5.47(b)). As illustrated for the present case case, the DMD allows easy extraction of low-frequency phenomena, clearly indicating its periodicity and spatial support.

These flow structures change considerably in the presence of PGC disturbances. Indeed, phenomena like the corner vortex (Fig. 5.78) identified in the undisturbed case are subsumed. For all disturbed cases with single PGC frequency f_d, the predominant flow features on the blade surface were directly linked to the periodic traveling waves. The main spatial length, however, differed among the cases inversely proportional to the f_d values. This can be seen in Fig. 5.79, which shows POD mode 2 for three different disturbance frequencies. Indeed, the higher the value of f_d, the shorter the spatial wavelength of the pressure pattern on the blade surface. This outcome is particularly evident

on the suction side. The time dynamics of POD mode 2 (Fig. 5.79(d)) also indicate the strong predominance of f_d in the respective spectrum for each setup.

The DMD sheds additional light into the relative importance of phenomena at specific frequencies for disturbed cases. The DMD continuous-system eigenvalues are shown in Fig. 5.80 for the disturbed case with $f_d = 0.125$ BPF and $A_d = 10\,\%$.

It is evident that one set of modes, with relative higher coherence, lies close to the stability line, with the real part of the

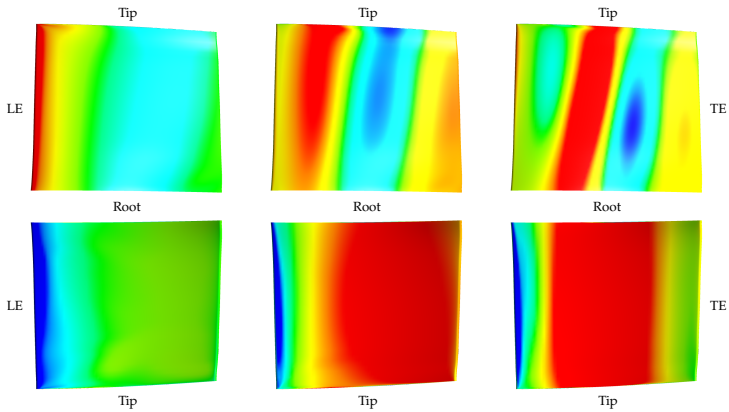

(a) $f_d = 0.125$ BPF (b) $f_d = 0.5$ BPF (c) $f_d = 0.75$ BPF

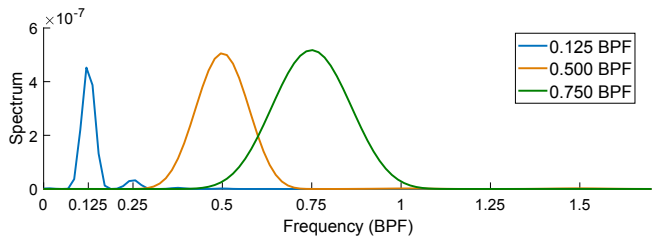

(d) Time dynamics

Figure 5.79: POD mode 2 for pressure on the R10 blade surface, for disturbed cases with $A_d = 10\%$ and different disturbance frequencies f_d (see Eq. (5.10)). For spatial modes, top: suction side; bottom: pressure side.

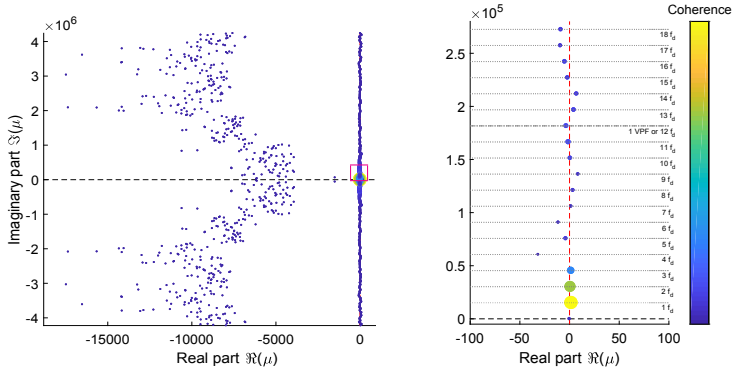

Figure 5.80: DMD continuous-system eigenvalues for pressure on the R10 blade surface, for the disturbed case with $f_d = 0.125$ BPF and $A_d = 10\,\%$ (see Eq. (5.10)).

eigenvalue in the range $|\Re(\mu)| \leq 100$. This indicates that the depicted phenomena are well characterized, with further addition of snapshots bringing the decomposition closer to dynamic saturation. The other set comprises DMD modes mostly with $\Re(\mu) < -4000$. That is, with a really strong and fast transient decay, not playing a relevant role when reconstructing the original, quasi-periodic flow.

It is also helpful to consider the effect of the inverted Gaussian pulse (Eq. (5.15)) in the pressure distribution on the R10 blade. Differently from the constant-frequency excitation with f_d, the pulse excites a continuous frequency range simultaneously. This brings up the question whether new flow features arise, which may dominate the flow dynamics (and consequently the data-driven decompositions). The DMD continuous-system eigenvalues for this case are shown in Fig. 5.81(a). This time a spread of coherence occurs among several DMD modes with frequency lower than the VPF.

Indeed, the dynamic information contained in these high-coherence modes is quite similar to the spatial patterns obtained with single-frequency excitation (Fig. 5.79). To avoid repetition, Figs. 5.81(b) to 5.81(d) depict, instead of the real and

imaginary parts, the DMD phase angle $\boldsymbol{\Theta}$ (see Eq. (5.17)) of the modes labeled **A**, **B** and **C** in Fig. 5.81(a). The repetition of the alternating pressure pattern from the PGC wave is evident from its phase angle distribution. Again, the higher the frequency, the smaller the spatial periodicity.

The DMD modes adjacent to the ones shown in Figs. 5.81(b) to 5.81(d) contain similar spatial information, however with slightly varying spatial length. These results indicate that no novel phenomena occurs on the R10 blade pressure distribution, whose pattern varies significantly from the information obtained with the single-frequency simulations. A similar conclusion can be drawn when simulating with linear and exponential sweeps (chirp) as outlet boundary condition, not shown here for brevity. That is, not only the Gaussian pulse, but also sine sweeps may be employed as representative inputs when searching for relevant flow excitation structures in the presence of PGC disturbances.

In summary, the pressure distribution on the R10 surface is directly linked in space and spectrum to the upstream traveling waves from the PGC. The frequency content of the aeroelastic excitation is dominated by the main disturbance frequency f_d and its multiples. More specifically, regarding the pressure distribution on the rotor blade, no novel unexpected phenomena occurred in the cases considered in this work.

Finally for completeness, the pressure distribution linked to the VPF for the undisturbed case may also be recovered from the inverted Gaussian pulse run. This is shown in Fig. 5.82, which compares the DMD mode (imaginary part) at $f = \text{VPF}$ from the undisturbed with the disturbed run. The similarity of the structures is strong, indicating once again that the decomposition of the inverted Gaussian pulse not only contains the main "disturbed" flow features, but also retains the baseline flow dynamics.

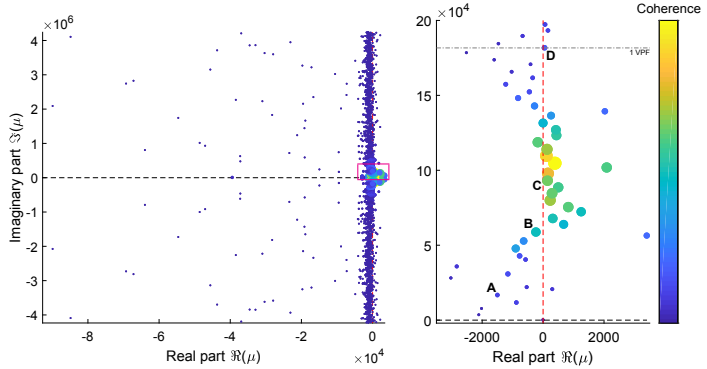

(a) DMD continuous-system eigenvalues

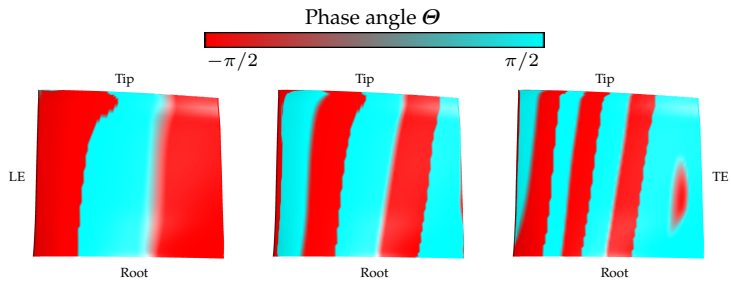

(b) **A**: $f = 0.137$ BPF (c) **B**: $f = 0.484$ BPF (d) **C**: $f = 0.767$ BPF

Figure 5.81: DMD for pressure on the R10 blade surface, for the disturbed case with inverted Gaussian pulse (Eq. (5.15)). Bottom: DMD phase angle Θ on pressure side for modes labeled **A**, **B** and **C**.

5.3.5 Aeroelasticity

In this section, the R10 blade from the NASA EEE high pressure compressor will be aeroelastically assessed. The analyses presented here follow the workflow from section 3.2.3.1 (see also Fig. 3.5). Additionally, many numerical considerations about the methods have already been presented in the case study 1 in section 5.2. Therefore, only the main practical matters will be examined here, for the sake of brevity.

Grids have been generated with specifications similar to the ones from section 5.2, however without a blisk geometry.

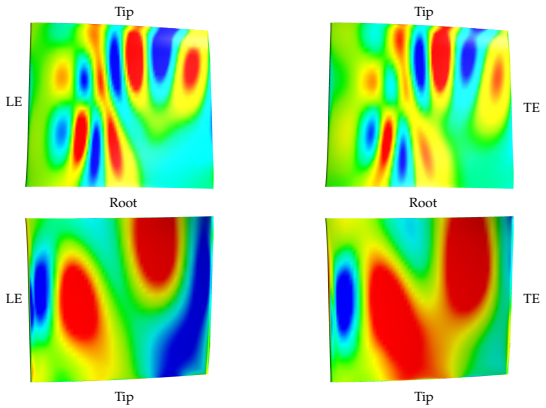

(a) Undisturbed (b) Inverted Gaussian pulse

Figure 5.82: Imaginary part of DMD mode with f = VPF, for different cases. Top: suction side; bottom: pressure side.

Differently from case study 1, the NASA EEE high pressure compressor comprises traditional bladed disks. The detailed root geometry has not been modeled in this work, but rather a fixed platform underneath the rotor blade. Although this simplification would indeed produce results slightly different from the real eigenfrequencies and stresses, the present aeroelastic focus on directly comparing the PGC-disturbed case with the undisturbed justifies this modeling approach. Details about damping in this bladed disk setup will be given later. Unstructured meshes with tetrahedra elements were spawned, with higher node density next to high-curvature areas. For the grid independence study, scalars for three representative discretizations are shown in Fig. 5.83, ranging from coarse (R-A) to fine (R-C).

From Fig. 5.83(a), the natural frequency for the first two modes changes minimally among the employed discretizations, namely less than 0.03%. Values of the same order occur for higher modes. In principle, all grids could be deemed precise enough for the simulations. To make sure other types of analyses also express grid-independence, Figs. 5.83(b) and 5.83(c) portray the results for static and forced response analyses. For all meshes, variations

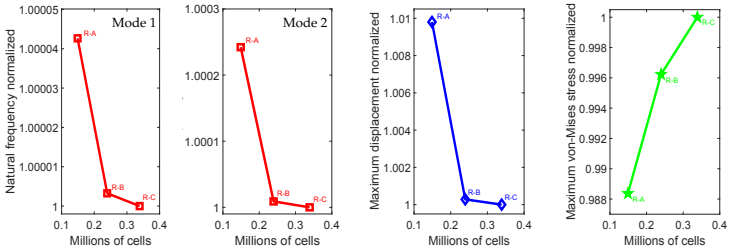

(a) Modal (b) Static (c) Forced response

Figure 5.83: Grid independence study for R10 solid domain, for different types of mechanical analyses. Normalization with respect to finest grid.

of less than 2% occur. When comparing the middle with the fine discretizations, a relative change of less than 0.5% is obtained. This value is judged precise enough for the desired computations. Thus, grid R-B is selected for the CSM studies, consisting of 387767 nodes and 239612 elements. One blade sector is shown in Fig. 5.84.

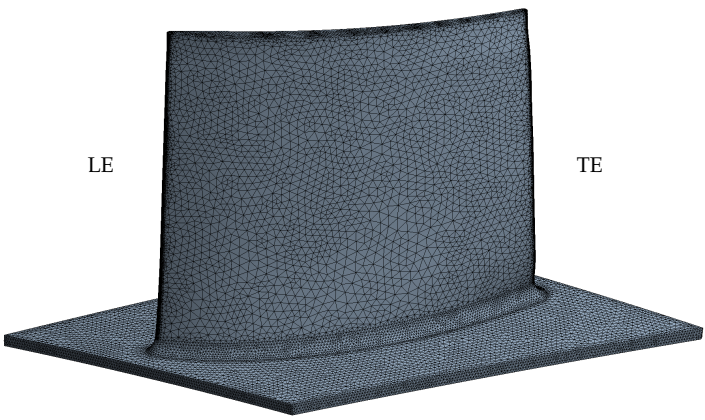

Figure 5.84: Sector of grid R-B for the R10 blade solid domain, chosen after independence study for the CSM analyses. Suction side shown.

5.3.5.1 Damping

The aerodynamic damping computation makes use of the first mode shapes of the rotor blade. These came from a pre-stressed modal analysis, performed with enough eigenvectors so that the highest eigenvalue is a couple of times higher than the expected maximum excitation frequency. In the current case, retaining the first 86 mode shapes in the eigenvalue decomposition was sufficient, covering more than 8 times the VPF but still enabling computations with feasible processing time.

Once the mode shapes are available, we proceed towards the aerodynamic damping computations. The numerical method employed in this section was the Fourier transformation[13]. This approach is based on the energy method, and was described in section 3.2.2.3. The periodic displacement magnitude at the blade tip was kept below 0.1% of the blade height. Lastly, after appropriate time independence assessments, the number of time steps per vibration period was set to 100.

The aerodynamic damping results for the R10 blade are depicted in Fig. 5.85. While the blade displacements for the first three mode shapes are shown in Fig. 5.85(a), the damping ratio is displayed in Fig. 5.85(b), for the whole nodal diameter range.

No negative damping ratio was obtained, indicating, according to the energy method, no flutter behavior, independently of the mechanical damping present (considered always positive). The smallest reduced frequency is $f = 1.4$ for the first bending mode. As discussed in section 2.4.4, published values for critical reduced frequency in axial compressors often focus on the first stages. The present results refer to the last stage of a HPC and should be compared with caution. In any case, the current reduced frequency is relatively larger than the upper flutter bounds indicated by [20, 47, 48], indicating at least a preliminary agreement with the critical flutter ranges from the mentioned literature.

[13]The nonlinear harmonic balance, employed in the aerodynamic damping calculations for case study 1, was not used in this section since it produced oscillatory solutions. That did not occur with the Fourier transformation method, which however demands higher computational resources.

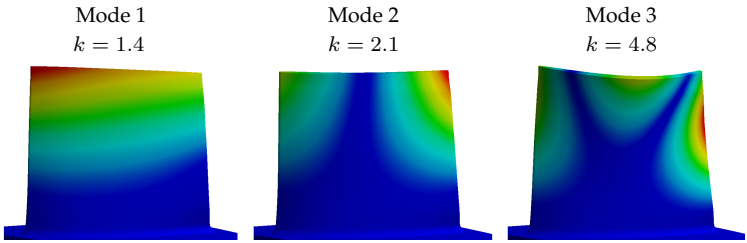

(a) Displacement of blade mode shapes with corresponding reduced frequency k

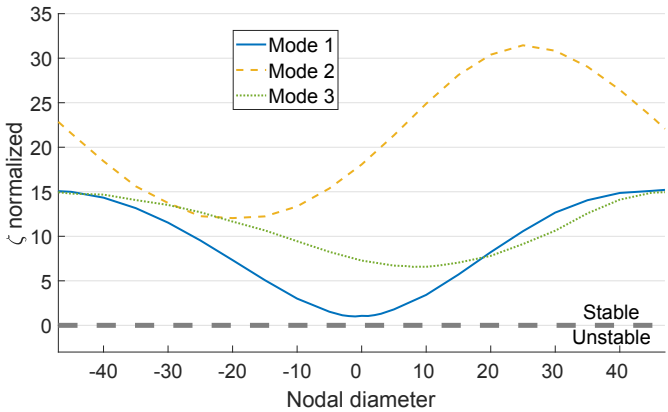

(b) Damping ratio ζ, normalized by the smallest value

Figure 5.85: Aerodynamic damping results for first blade mode shapes of the R10 blade.

From Fig. 5.85(b), the smallest damping ratio ζ occurred for the first mode shape, with nodal diameter -1, with $\zeta = 0.093\%$. Some values of ζ were computed for higher modes, with frequencies close to the VPF. The damping ratio range obtained was similar to that of mode 3. Therefore, in a slightly conservative approach, the minimum value shown in Fig. 5.85 was chosen as the representative aerodynamic damping figure.

As discussed in section 2.4, in addition to the aerodynamic, the material and structural parts also contribute towards the total damping in traditional bladed disks. The material damping is negligible for the material employed. The mechanical damping

was not simulated, but rather set according to typical values from the literature (see, e.g., [12, 38, 39, 265]). The three cases employed in this section are shown in Tab. 5.6. Case A ignores any mechanical damping, being comparable to a modern blisk geometry lacking friction damping. Cases B and C include lower and higher levels of structural damping, respectively.

Table 5.6: Total damping ratio ζ employed in the forced response computations, considering aerodynamic and structural shares.

	Case name	Total damping ratio ζ
A	Only aerodynamic damping	0.093%
B	With low mechanical damping	1.1 %
C	With high mechanical damping	3.0 %

5.3.5.2 Forced response

After the unsteady forces, pre-stressed modes and total damping have been obtained, we proceed to the forced response computations. Here, a single value is provided as excitation and vibration frequency at a time, appropriately matching the previously employed f_d. Special attention is given to the VPF, which often represents the strongest excitation source for rotor blades.

This is indeed the situation in the baseline (undisturbed) case, which exhibited maximum dynamic stresses at the frequency matching the vane excitation. That is conveyed by Fig. 5.86. More specifically, Fig. 5.86(a) depicts the von-Mises (equivalent) stress at R10 for a chosen vibration temporal phase angle[14]. This depiction artificially reconstructs the harmonic motion in time, clearly showing the periodic deformation of the blade surface (here exaggerated for clarity). The damping ratio corresponds to the more critical case (**A** from Tab. 5.6). The maximum stress occurs at the tip, slightly upstream of the trailing edge.

[14]The phase angle linked with time corresponds to ωt in Eq. (3.40) (derived for the displacement, with an analogous form for the equivalent stress).

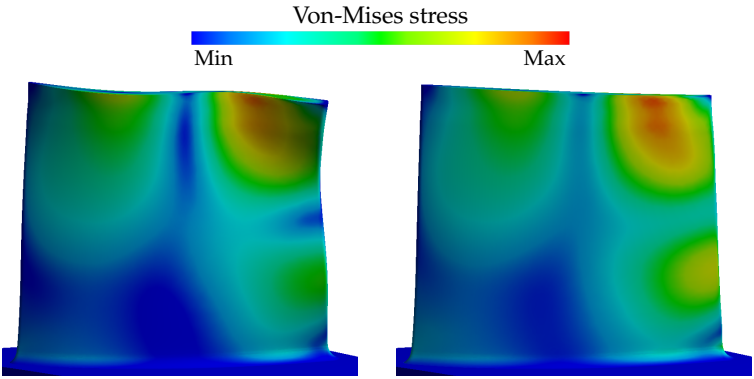

(a) Stress at temporal phase of 120°

(b) Maximum over vibration cycle

Figure 5.86: Von-Mises stresses on rotor blade suction side for baseline case, at f = VPF. Exaggerated deformation for clarity.

While Fig. 5.86(a) shows the value of the von-Mises stress at a specific temporal phase angle ωt, Fig. 5.86(b) depicts the maximum stress for each finite element[15]. This approach ensures the acquisition of the highest stress over the vibration period.

The VPF excitation lies between the blade natural frequencies 8 and 9. This is asserted by Fig. 5.87, which shows the maximum displacement over the vibration cycle next to blade mode shapes 8 and 9. It is clear that the resulting displacement in Fig. 5.87(a) consists in a linear combination of (mainly) modes 8 and 9. Furthermore, the excitation effectiveness from the patterns shown in Fig. 5.76 is made clearer: the alternating pressure arrangements have a similar wavelength to mode shape 8 and act precisely close to the trailing edge tip, where the highest displacement occurs.

To understand how the stresses vary for different query frequencies[16], Fig. 5.88(a) displays the maximum von-Mises

[15] This maximum value corresponds to the quantity in parenthesis in Eq. (3.40) (derived for the displacement, with an analogous form for the equivalent stress).

[16] For the undisturbed case, $A_d = 0\%$ in Eq. (5.10) and the query frequencies shown are chosen to match f_d from the disturbed runs, enabling direct comparison.

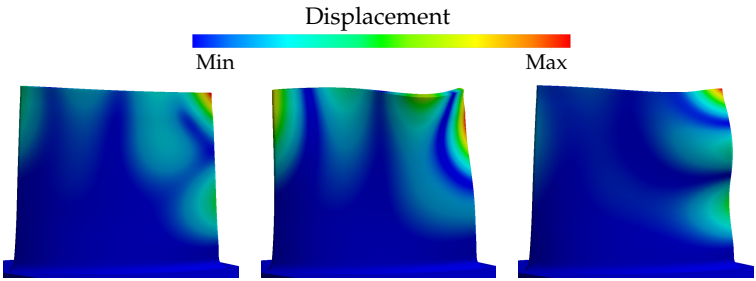

(a) Maximum over cycle (b) Mode shape 8 (c) Mode shape 9

Figure 5.87: Displacement of rotor blade suction side for baseline case, at $f = \text{VPF}$. The VPF is located between the natural frequency corresponding to the eigenmodes shown.

stresses for the undisturbed case, normalized by the value at $f = \text{VPF} = 1.5$ BPF and $\zeta = 0.093\%$. This value is marked with **N** and corresponds to the σ_{vm} spatial distribution from Fig. 5.86.

As anticipated for the undisturbed case, the vane presence incurs the highest stresses, followed by the case with $f = 0.125$ BPF. The latter behavior is directly linked to the unsteady fluid forcing, more specifically, to the suction side corner vortex. To investigate that, the previous DMD provides valuable assistance. Referring back to Fig. 5.77(b), the second most coherent DMD mode (labeled **B**) has a frequency of $f_{cv} = 0.119$ BPF, less than 5% off from the simulated value of $f = 0.125$ BPF. This mode was shown in Fig. 5.78, identifying flow dynamics linked to the corner vortex.

The variation in the pressure amplitude at f_{cv} is reflected in the Fourier decomposition. Indeed, for the undisturbed case the pressure load for $f = 0.125$ BPF is two orders of magnitude higher than for 0.25 BPF $\leq f \leq 1$ BPF, ramping up again towards the VPF. This is confirmed by Fig. 5.89, which shows the spectral content of the mean pressure on the rotor blade, employed as load in the forced response workflow. The nonlinear interactions between the VPF, f_{cv} and their harmonics are clearly depicted.

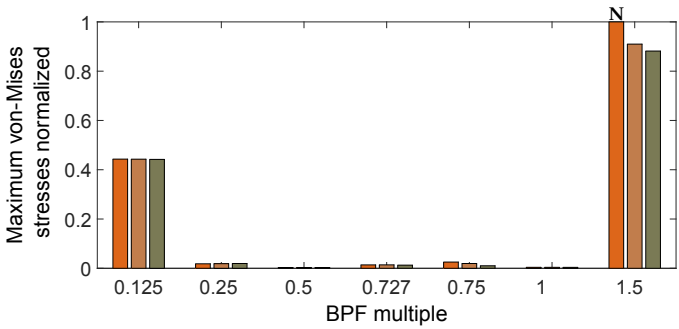

(a) Undisturbed

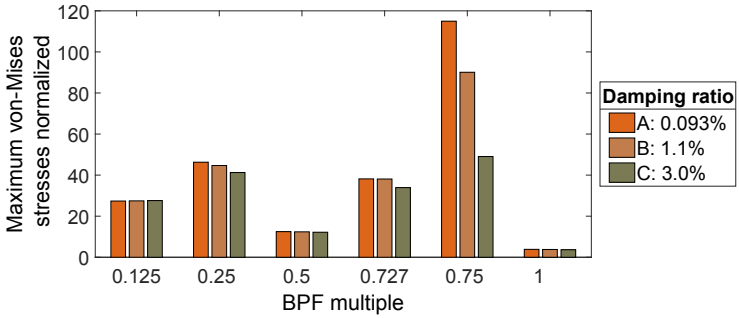

(b) Disturbed

Figure 5.88: Maximum von-Mises stresses on rotor blade as a function of excitation frequencies (f_d in Eq. (5.10)), for different damping ratios ζ. The undisturbed case has no excitation, while for the disturbed case, $A_d = 10\%$. Normalization conducted with respect to the undisturbed case at $f =$ VPF and $\zeta = 0.093\%$ (marked with **N**).

Regarding the disturbed cases, Fig. 5.88(b) shows the equivalent stresses for simulations at different disturbance frequencies f_d. The stresses are normalized by the same undisturbed value marked with **N** in Fig. 5.88(a), for comparison. For most f_d instances, an increase of up to 50 times occurs, in comparison to the maximum stress due to the vane passing. A steady decrease in amplitude occurs for larger damping ratios, however not changing the order of magnitude.

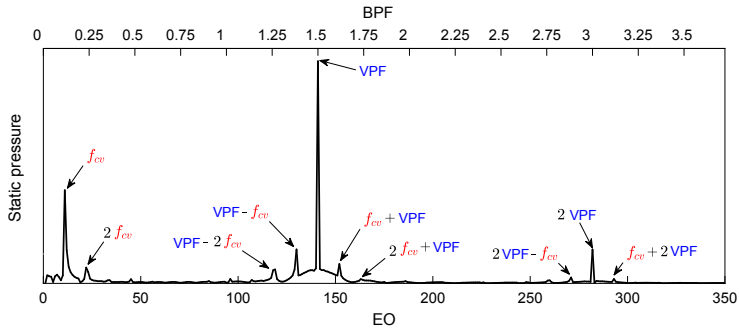

Figure 5.89: Pressure spectrum (spacial average) on R10 as a function of engine order (EO) and blade passing frequency (BPF), used as load for the undisturbed case. The corner vortex fundamental frequency and the vane passing frequency are labeled f_{cv} and VPF respectively.

The single case with substantially higher equivalent stress corresponds to the $f_d = 0.75$ BPF excitation. Up to almost 120-fold amplification occurred, with a steeper decrease in stress for higher damping than for other f_d instances. This behavior is typical of points located close to resonance frequencies. Indeed, mode shape 4 vibrates with a frequency of approximately 14.7 kHz, which is less than 2% apart from 0.75 BPF. This proximity is confirmed by the Bode stress amplitude diagram shown in Fig. 5.90. The von-Mises stress distribution as a function of frequency for the undisturbed case intersects with the query frequency $f = 0.75$ BPF very close to a resonance point. This crossing, labeled **A**, explains the large forced response at $f_d = 0.75$ BPF[17]. The fact that a similar increase in the stresses does not occur for the undisturbed case at $f = 0.75$ BPF (even though it is close to a natural frequency, as label **B** shows) is directly related to the very low forcing level (two orders of magnitude lower than for 0.125 BPF or VPF, as previously described).

[17] A reasonable aeroelastic design considering PGC would actively avoid setting the combustion frequency close to the first blade eigenvalues; therefore, aeroelastic results linked to $f_d = 0.75$ BPF will not receive further structural attention in this section.

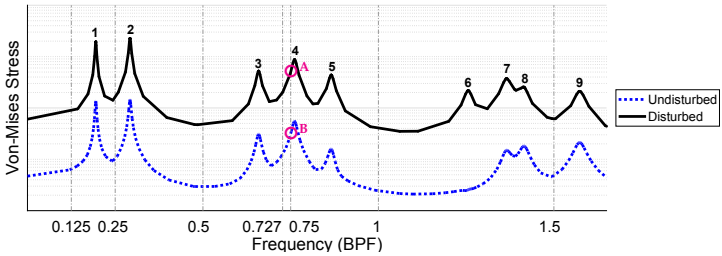

Figure 5.90: Bode magnitude plot for von-Mises stress on the R10 blade. Undisturbed case with VPF forcing; disturbed case with $f_d = 0.75$ BPF and $A_d = 10\%$ (Eq. (5.10)). Eigenfrequencies marked from 1 to 9. Labels **A** and **B** indicate crossings of the harmonic response with $f = 0.75$ BPF.

One further result from Fig. 5.88(b) deserves attention, namely the $f_d = 0.25$ BPF case. It has the highest relative stresses from the simulated cases (apart from the discarded $f_d = 0.75$ BPF, as discussed before). A tip view with (exaggerated) displacement within a vibration cycle of R10 is shown in Fig. 5.91(a). The phase angle goes through a complete cycle (360°) in a period of exactly $1/(0.25\,\text{BPF})$. In this interval, two main vibration modes are observed: bending (e.g. at opposite phases 90° and 270°) and torsion (e.g. at phases 0° and 180°). Referring back to Fig. 5.85(a), these shapes correspond the first and second natural modes, which indeed neighbor the excitation frequency $f_d = 0.25$ BPF, as clearly depicted by the Bode magnitude plot from Fig. 5.90. The maximum displacement over the entire cycle is shown in Fig. 5.91(b), combining the bending and torsion modes.

To understand the vibration relative amplification for the $f_d = 0.25$ BPF case, POD modes 2 and 3 for the pressure are shown in Fig. 5.91(c). The decomposition of the pressure field is of high aeroelastic importance, since it is directly related to the effective forcing experienced by the rotor blade. In the current case, the two most energetic unsteady POD modes indicate a pressure load whose wavelength has the same order of magnitude as the displacement pattern wavelength of the mode shapes most prone to be excited. Remember that POD modes 2

and 3 describe the PGC wave traveling upstream and contain the same information up to a 90° phase offset (paired, traveling modes). The matching between forcing and displacement on the upper part of the blade is especially clear when comparing the torsion mode with POD mode 3.

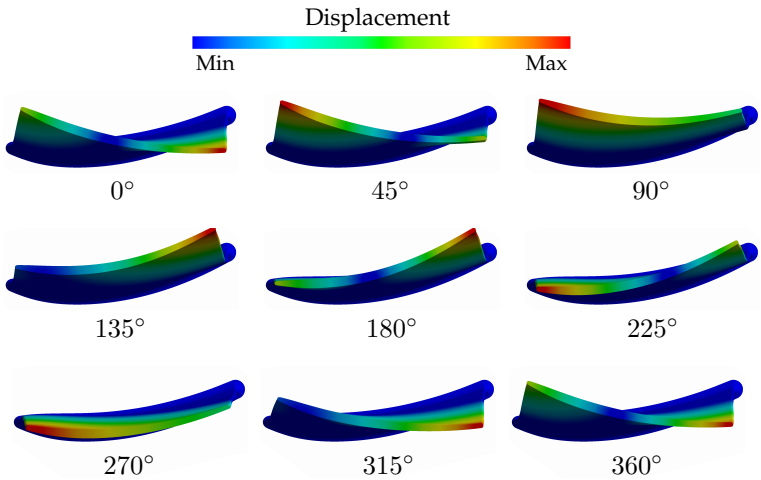

(a) Displacement within a vibration period (tip view)

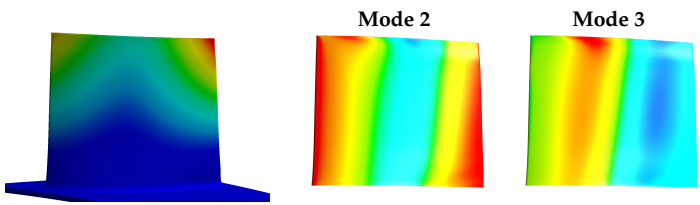

(b) Maximum displacement (c) Pressure POD

Figure 5.91: Harmonic analysis for displacement and POD for pressure on rotor blade for the disturbed case with $f_d = 0.25$ BPF and $A_d = 10\%$ (see Eq. (5.10)). Bottom: suction side view.

Indeed, similar wavelength matching between forcing and adjacently-excitable mode shapes occurs for other f_d values (see Figs. 5.79 and 5.81). The exception is natural mode 6 (not shown here), whose chord, especially for large span, does not vibrate

with a pattern similar to the pressure load distribution. This is then reflected in the lower equivalent stresses obtained for the disturbed case with $f_d = 1$ BPF shown in Fig. 5.88(b).

Turning towards the quarter-annulus case described in section 5.3.2, Fig. 5.92 shows the R10 pressure spectrum (spatial average) employed as excitation in the forced response assessments[18]. For a fixed disturbance amplitude of $A_d = 10\%$, Fig. 5.92(a) shows how the forcing in the frequency domain is distributed for the undisturbed case and for different values of circumferential order n_c. Indeed, the empirical peak matches the effective excitation frequency $\hat{f}_r$ described by Eq. (5.13), for each respective n_c. The maximum value in the disturbed cases is definitely much larger than the peak for the undisturbed case, located at the VPF. Additional local peaks are related to nonlinear combinations of $\hat{f}_r$ and the VPF, but no relevant flow phenomena in other frequencies occurred.

For the quarter-annulus setup, the equivalent stresses on the R10 blade as a function of the circumferential order n_c are shown in Fig. 5.93, considering a normalization to the undisturbed case at $f = \text{VPF}$ and $\zeta = 0.093\%$. The undisturbed stresses from Fig. 5.93(a) are negligible, bounded to less than 1% of the VPF maximum stress. This happens because the corresponding effective excitation frequencies for the analyzed cases are rather far from the first eigenfrequency (analogously to the bottom, leftmost part of the undisturbed response from Fig. 5.90).

The disturbed counterpart shown in Fig. 5.93(b) indicates von-Mises stresses between 20 and 35 times the undisturbed VPF response. These values match indeed with the low-frequency stresses from the standard case (see response magnitude at $f_d = 0.125$ BPF in Fig. 5.88(b)).

Finally, the stresses normalized by each respective undisturbed value are shown in Fig. 5.94. Amplifications of almost 6000 times

[18]The variation in the spectrum and Fourier modes among blades in different circumferential positions in the quarter-annulus setup was negligible for the undisturbed and all disturbed cases simulated. Therefore, just a single result representing the R10 blades is considered here.

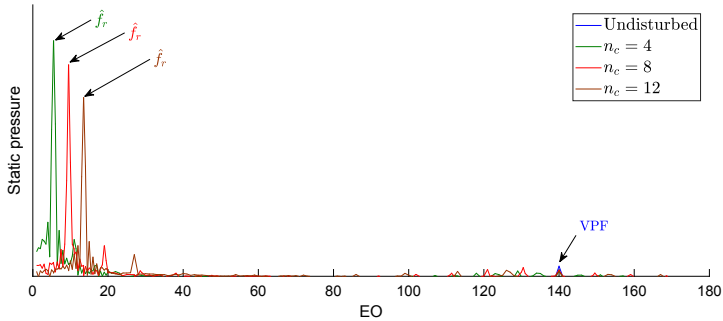

(a) Varying n_c for fixed $A_d = 10\%$

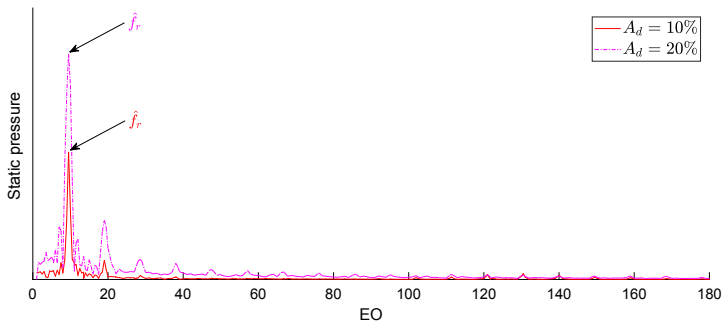

(b) Varying A_d for fixed $n_c = 8$

Figure 5.92: Pressure spectrum (spacial average) at R10 as a function of engine order (EO) in the quarter-annulus setup. Disturbed cases with different circumferential orders n_c and disturbance amplitude A_d (see Eq. 5.12). The vane passing frequency and the effective excitation frequency (see Eq. (5.13)) are labeled respectively VPF and $\hat{f}_r$.

occur. Although it is true that the stresses for the undisturbed case are rather low at these query frequencies (explaining the high amplification), it is relevant to point out that substantial increase in relative response occurs in the presence of PGC. That is, even for large safety margins, this augment in vibration could potentially exceed materials limits if not taken into account during design.

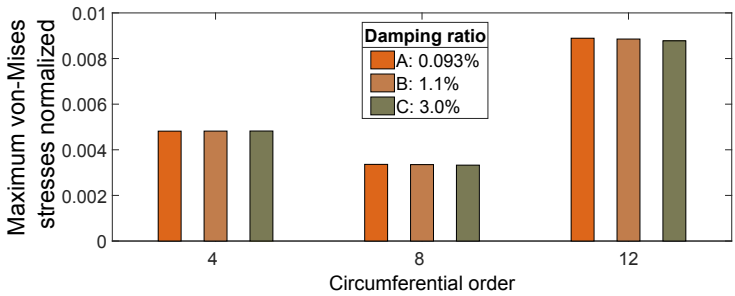

(a) Undisturbed

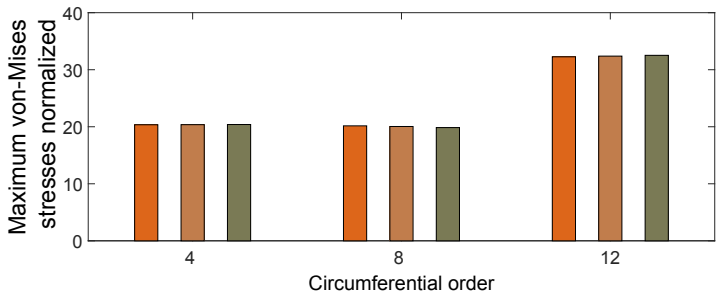

(b) Disturbed

Figure 5.93: Maximum von-Mises stresses on rotor blade as a function of circumferential order n_c, for different damping ratios ζ in the quarter-annulus setup. The undisturbed case has no excitation, while for the disturbed case, $A_d = 10\%$ (see Eq. (5.12)). Normalization conducted with respect to the undisturbed case at $f =$ VPF and $\zeta = 0.093\%$.

The maximum stress over the vibration cycle in the disturbed case $n_c = 8$ in the damping case A ($\zeta = 0.093\%$) is shown in Fig. 5.95. The areas with highest equivalent stress are located at the hub fillet. They indeed justify the denser mesh discretization in this high stress gradient surface. In this case, the forcing with spatial pattern similar to the first (bending) mode shape is partially effective in exciting the blade tip (with higher absolute displacement). As a consequence, stresses increase close to the hub, comparably to a classic cantilever case, clamped at one end.

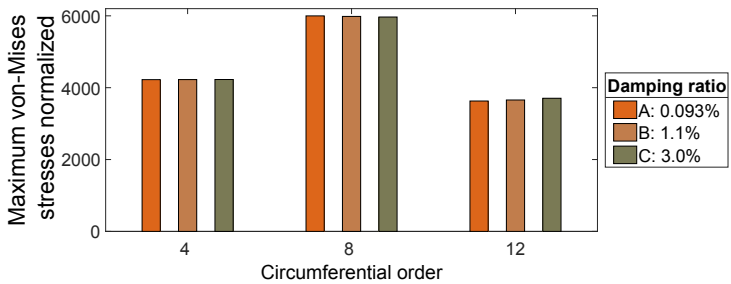

Figure 5.94: Maximum von-Mises stresses on rotor blade as a function of circumferential order n_c, for different damping ratios ζ in the quarter-annulus setup. The disturbance amplitude is $A_d = 10\%$ (see Eq. (5.12)). Normalization conducted concerning each respective undisturbed case.

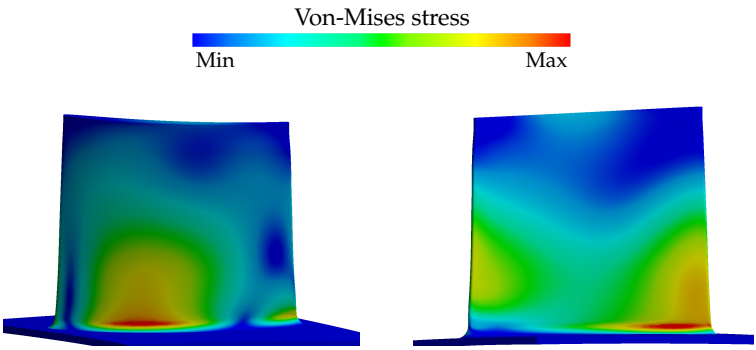

(a) Suction side (b) Pressure side

Figure 5.95: Von-Mises stresses on rotor blade in the quarter-annulus setup for the disturbed case with $n_c = 8$ and $A_d = 10\%$ (see Eq. (5.12)). The damping ratio is $\zeta = 0.093\%$. Maximum value over cycle shown.

5.3.6 Conclusions

The present section numerically analyzed the effects of PGC on a high pressure compressor from a large-scale turbofan, namely the NASA EEE. This engine is an open test case, well established in the turbomachinery literature. More specifically, the investigations in this section were concentrated on the last (tenth) HPC stage. As with case study 1 (section 5.2), single-frequency

PGC disturbances were initially considered (as in Eq. (5.10)); subsequently, boundary conditions simulating a valve-opening event (in the form of an inverted Gaussian pulse) were also implemented (according to Eq. (5.15)).

Regarding the number of passages modeled, two different stage setups were explored: the *standard*, which contains only a few rotor and stator passages; and the *quarter-annulus*, which models one quarter of the circumference. In the latter case, the PGC disturbances were implemented according to Eq. (5.12) (see also Fig. 5.36). Both standard and quarter-annulus numerical setups yield a unitary pitch ratio, so to prevent frequency errors as the PGC waves traverse the stage.

The stage performance under PGC disturbances showed a clear depreciation in comparison to the baseline unsteady reference. Considering the standard setup, the total pressure loss was up to 80% larger than the undisturbed counterpart (see Fig. 5.38 for the rotor and stator domains). The drop in the stage isentropic efficiency was restricted to less than 7% (see Fig. 5.41). This value is similar to the ranges obtained with case study 1, when considering the same disturbance amplitude of $A_d = 10\%$ of the mean outlet pressure.

The quarter-annulus setup considered PGC waves which travel not only axially but also in the circumferential direction. The performance deterioration, considering total pressure loss and efficiency drop, was in the same order of magnitude of the standard setup, for the simulated circumferential orders. This outcome is depicted in Figs. 5.42 and 5.44. Once again, an increase in the disturbance amplitude A_d induced a relative sharp drop in the isentropic efficiency, as shown in Fig. 5.44(b).

Also for the present case study the unsteady damping formulated in section 5.1 was computed. In the standard setup for the low disturbance frequency of $f_d = 0.125$ BPF, the PGC wave amplitude increased as it moved axially upstream (see Fig. 5.39). This range matches very well with the unsteady damping obtained for case study 1, which also produced negative values for the same disturbance frequency f_d (compare Fig. 5.39

with Figs. 5.11, 5.15 and 5.17). In contrast, the quarter-annulus setup produced strictly positive unsteady damping values for the simulated circumferential orders (see Fig. 5.43). This indicates that the PGC waves which also travel circumferentially have a lower amplification potential. However, further investigations with other circumferential orders and amplitude variation patterns should be carried out for a more general understanding.

The data-driven decompositions applied to the unsteady results provided relevant insights into the undisturbed and PGC-disturbed flows, not obtained with classic techniques such as Fourier decomposition or phase averaging. The performance losses could be directly linked to specific flow phenomena, including blade wake, tip and corner vortices, as well as temporary separation zones (see, for instance, Figs. 5.47 to 5.50 and 5.68 to 5.72 for decompositions of the mass flow and entropy fields). These phenomena were not only exposed, but also ranked according to the energetic and coherence content of each spatial mode. Furthermore, a spread of coherence into high-order modes was observed in the presence of PGC disturbances (see, e.g., Figs. 5.63 and 5.64 for the density gradient and helicity fields).

The relative energetic importance of distinct flow phenomena could be clearly determined from the POD and DMD analyses, when comparing the baseline with the disturbed cases. For instance, the unsteady flow feature containing more energy in the stator domain in the absence of PGC waves was the vane tip clearance vortex (as shown in Figs. 5.54 to 5.56 for the vorticity field). In the presence of PGC disturbances, an energetic and coherence shift occurs, namely from the vane tip clearance vortex towards temporary pressure side separation, which then produces a plume-like flow structure covering almost the entire passage (as depicted in Figs. 5.57 to 5.61).

A detailed assessment of the entropy field at the rotor tip clearance was able to link local flow structures with the performance losses obtained for the stage. More specifically, the well-behaved tip clearance vortex in the baseline case (characterized in Fig. 5.73) experiences intense periodic change

when subject to PGC waves. This behavior is conveyed in Fig. 5.75, indicating an increase in the vortex diameter accompanied by an irregular precession of its core. Additionally, a short-lived, negative-incidence vortex, as well as flow spillage at the leading edge, occur periodically. The "off-design" unsteady phases portrayed in Fig. 5.75 are traced back to the change in back pressure promoted by the PGC wave and, when accumulated within the disturbance cycle, justify the performance depreciation previously obtained.

The unsteady pressure distribution on the rotor blade was also investigated in detail with the aid of data-driven decompositions. Three main results are worth mentioning. First, the decompositions of the undisturbed case indicated clear preponderance of the vane passing frequency, manifested in the presence of alternating lobes on the suction side (see Fig. 5.76); indeed, this result matches the entropy decomposition of streamwise surfaces at the rotor blade tip clearance (see Fig. 5.73(b)). Second, the presence of PGC disturbances dominated the blade pressure decomposition, for all frequencies considered. That is, flow features linked to the undisturbed case, such as the vane passing, were wholly energetically overshadowed by behavior directly related to the PGC waves (see Fig. 5.79 for wavelength and spectra matching the f_d and Fig. 5.80 for the clustering of modes around f_d and its multiples). Third, employing a single pulse (or sine sweeps) as a PGC excitation function was also successful to obtain the main flow features present in the unsteady flow (refer to Figs. 5.81 and 5.82). These patterns had also been independently acquired when running several computations with different f_d values. This pulse approach (with adequate parameters) turns out to be very effective when considering general PGC disturbances since it excites a broad frequency range, therefore avoiding the execution of multiple unsteady runs.

The aerodynamic damping computed for the rotor blade's first modes yielded no negative values (see Fig. 5.85), indicating flutter stability for the simulated operating point. The first mode

(bending) showed the lowest absolute value of aerodynamic work. Additionally, to compute the total damping, two different shares of mechanical damping are considered, termed in this work "low" and "high" (see Tab. 5.6). The total damping was then employed in the subsequent forced response analyses.

The displacement and stresses on the rotor blade were obtained employing the forced response workflow given in section 3.2.3.1 (see also Fig. 3.5). As expected for the undisturbed case, the stator vane consists in the strongest forcing source for the rotor, with natural modes 8 and 9 being the most excited (see Fig. 5.87). Indeed, these modes present larger displacement at the rotor tip, with a pattern and wavelength similar to the pressure decompositions previously obtained, shown in Fig. 5.76. This pattern matching between the excitable areas (antinodes from natural modes) and the forcing decompositions (POD and DMD of pressure field), justify the high stresses obtained for the VPF in the forced response analysis (see Fig. 5.88(a)). The decompositions also helped explain the second largest stresses experienced by the rotor blade. In short, they occur at $f_d = 0.125$ BPF, which is 5% close to the low-frequency DMD mode with large coherence, portraying the corner vortex upstream the trailing edge (labeled **B** in Fig. 5.77(b) and shown in Fig. 5.78).

For the standard setup, the maximum stresses in the presence of PGC waves exceeded the undisturbed case for all simulated frequencies. This behavior is depicted in Fig. 5.88(b), with up to 50 times amplification in stresses in comparison to the largest (VPF) excitation at baseline operation. The disturbance frequency of $f_d = 0.75$ BPF produces even higher stress levels, specifically due to its proximity to a blade natural frequency (see Fig. 5.90).

Considering from Fig. 5.88(b) the largest stresses not neighboring a natural mode ($f_d = 0.25$ BPF), a situation similar to the undisturbed case occurs. The mode shapes subject to the strongest excitation are the first bending and first torsion (1 and 2 in Fig. 5.90). Additionally, the pressure load obtained from the POD decomposition at $f = 0.25$ BPF, depicted in Fig. 5.91(c),

matches the natural modes with a very similar spatial pattern. This situation explains the amplification in equivalent stresses observed in this PGC-disturbed case.

The quarter-annulus setup produced forced response levels in a very similar range to the standard setup (see Fig. 5.93(b)). This outcome is justified by the effective excitation frequencies obtained with the simulated circumferential orders n_c, which are rather low in comparison to the first blade natural modes. When normalizing the disturbed results with respect to their corresponding undisturbed counterpart (as in Fig. 5.94), large amplification factors are obtained, up to almost 6000-fold. This indicates, also for the quarter-annulus case, that PGC disturbances are capable of influencing the aeroelastic response drastically. Generally, these results call for (i) detail assessments of the mode shapes most likely to be excited by specific PGC disturbance frequencies; (ii) a broad estimation of the damping mechanisms at the blade; and (iii) thorough analyses of the PGC forcing patterns, possibly with the help of data-driven decompositions.

6

Conclusions and outlook

Reducing fuel consumption in aero engines and gas turbines is indispensable in the contemporary transition from societies grounded on fossil fuel to new realities bearing more environmental and social responsibility. To do so, not only a drastic curtail in demand is unavoidable, but also the development of novel technology able to radically improve the overall efficiency of turbomachines. One of these emerging approaches is pressure gain combustion (PGC). It aims at improving the engine's thermal efficiency by substituting the (ideally) constant-pressure with a pressure-gain combustion process. However, this modification comes at the price of unsteady combustion, with potentially severe consequences for turbomachinery components.

This thesis attempted to throw light on the effects of PGC on axial compressors with numerical methods, more explicitly, unsteady fluid dynamics and solid mechanics computations. First, a generic analytical model was presented, able to quantitatively assess the amplification or damping of waves traveling axially through (multiple) fluid domains. Afterwards, PGC waves varying in form, frequency and amplitude were implemented as unsteady boundary conditions for numerical simulations, considering two case studies. Finally, time- and frequency-domain methods, along with data-driven decompositions, delivered relevant insight into the repercussions of PGC on unsteady aerodynamic and aeroelastic behavior of a few stages of the two high pressure compressors investigated.

The introduced analytical model defined the "unsteady damping" as a scalar describing the spatial extent to which potentially harmful PGC waves traverse turbomachinery components. This flexible metric can be employed to any fluid state variable fluctuating in time, although here the focus was placed on pressure, temperature and mass flow. In this work, the single-domain unsteady damping formulation was extended to the generic cumulative case, which becomes suitable when several rows or stages are involved. Two special instances were derived from the generic cumulative form, the homogeneous and

the alternating models. In the PGC context, the unsteady damping becomes a valuable tool when estimating, either from experiments or simulations, how many rows should be affected by axially traveling waves. With it, aerodynamics and aeroelasticity designers are able to evaluate to which degree PGC disturbances impact the flow and possibly the mechanical response of blades and vanes.

When applied to the unsteady fluid dynamic results, the unsteady damping metric produced similar scenarios for both case studies considered here. In the presence of PGC disturbances with rather high frequencies – equal to or larger than half the rotor blade passing frequency (BPF) –, a strong damping of the wave amplitude occurred. However, for lower disturbance frequencies, such as 0.125 BPF, an amplification of the PGC wave ensued, during its upstream journey through the high pressure compressor. Such an outcome appears to be new in the turbomachinery literature considering upstream-traveling pressure waves. The results clearly draw attention to the potential risks of neglecting PGC unsteady effects and to the importance of modeling enough rows according to the expected disturbance frequencies. The quarter-annulus setup, which considered PGC waves moving also in the circumferential direction, produced a less alarming scenario. Now, also the low-frequency waves were reasonably damped, preliminarily indicating that this type of wave propagation could have a lower amplification potential.

Another relevant aspect concerning the integration of PGC into turbomachines is the depreciation of performance caused by the combustion unsteadiness. In both case studies assessed, a considerable increase in component losses ensued due to PGC waves. A mapping of isentropic efficiency decrease as a function of the disturbance amplitude and frequency was assembled from numerical results. For instance, a stage subjected to a PGC wave amplitude of 20% of the mean outlet pressure experienced up to 25% decrease in isentropic efficiency. When exposed to amplitudes equal to or lower than 10%, the drop in efficiency was

restricted to 7% or less, for all disturbance frequencies considered. The increase in total pressure loss per row was also evaluated: up to 80% higher values were reported due to the disturbance waves. This deterioration in performance in the presence of PGC should be diligently estimated for each specific design since, for a successful integration of novel combustion devices into gas turbines, the thermodynamic improvement must definitely not be hindered by local component losses.

Data-driven decompositions of the unsteady flow cast light into the most relevant coherent structures identifiable in the absence and presence of PGC. More specifically, proper orthogonal decomposition and dynamic mode decomposition were insightful approaches to disclose flow structures not accessible with conventional techniques such as Fourier decomposition or phase averaging. Specific unsteady phenomena such as wakes, tip and corner vortices, but also temporary separation, could be efficiently ranked according to their energy and coherence content. Furthermore, the identified flow structures were directly linked to stage losses from previous analyses, providing physical justifications for the performance deterioration. For instance, the analysis of the entropy field at the rotor blade tip gap was able to clearly identify temporary "negative-" and "positive-stall" phases experience by a stage, as a function of the back pressure variation promoted by the PGC waves. The accumulation of these off-design phases within the disturbance cycle explains the efficiency drop outcome.

Moreover, the data-driven decompositions showed that, in the presence of PGC disturbances, a spread of coherence into high-order modes ensued, confirmed by the decomposition of several state variables at different spatial locations. Additionally, specific flow features dominating the baseline unsteady flow subsumed in the PGC-disturbed scenario. For instance, the vane tip clearance vortex in the stator domain of case study 2, bearing the highest decomposition energy content, was overshadowed by periodic flow separation on the vane pressure side, followed by a plume-like detached volume covering the entire passage.

This dynamics domination by PGC-induced phenomena was also observed in the pressure decompositions on the rotor blade. That occurred for all frequencies simulated and was distinctly corroborated by the clustering of dynamic modes at the disturbance frequency and its multiples. Indeed, the pressure decomposition produced alternating patterns on the blade precisely related to the respective PGC disturbance wavelength. Employing as boundary conditions functions such as the inverted Gaussian pulse (simulating the opening of a PGC valve) or sine sweeps was also effective in disclosing the same pressure patterns obtained with several single-frequency simulations.

The aeroelasticity assessments predicted no flutter for both case studies, following the energy method. The forced response analyses indicated a substantial increase in displacement and stresses in the PGC-disturbed response, when contrasted with the baseline operation. For instance, the dynamic stress due to PGC for case study 2 was 50 times larger than the maximum stresses in the baseline case (due to rotor-stator interaction), even when relatively far from the blade natural frequencies. When regarding the ratio of PGC-disturbed stresses to the baseline case for the same query frequency, the amplification becomes thousandfold. Although this large rise is partially explained by the very small absolute stresses in the baseline case, such a major relative increase should not be understated. These results circumstantiate the relevance of precisely estimating the forced response for the main PGC frequencies and amplitudes expected to reach the turbomachinery components.

The harmonic response results for the rotor blade of case study 2 could also be interpreted with the aid of data-driven decompositions and modal analyses. Both for undisturbed and disturbed scenarios, particularly higher stresses ensued on the rotor when the forcing function spatial pattern matched the blade mode shapes. That is, whenever the pressure distribution of high-energy modes coincides in space with the blade natural modes displacement, for frequencies close to the PGC excitation, more intense blade vibration followed.

Finally, qualitative agreement was observed between the unsteady damping metric and the stresses on the rotor blades subject to PGC disturbances. For both case studies, the PGC waves produced a higher impact for lower frequencies, meaning that the strength of axially traveling waves persisted even after traversing some rows. Since the unsteady damping computation requires solely CFD runs (in comparison to a more involved workflow for forced response), it is recommended as a exploratory predictor of the potential impact of PGC disturbances in turbomachinery.

The contributions from this thesis should encourage further research concerning the integration of PGC into gas turbines. For instance, other combustion disturbances profiles could be employed, preferably based on PGC experimental data specifically contemplating turbomachinery integration. Further investigations of PGC disturbances with diverse circumferential patterns, including the cross-interaction of multiple combustors, should enhance the understanding on the potentially hazardous effects of PGC on compressors and turbines. Clarifications on plena located between combustor and adjacent components is also required. Among other additional challenges, only after the performance depreciation is precisely estimated (and remains limited to small values) and structural risks are out of the way, PGC may be successfully incorporated into gas turbines so to effectively improve their overall efficiency and reduce fuel consumption.

A

Appendix

A.1 Grid independence index

The grid independence index (GCI) is an attempt to provide a single scalar which quantitatively conveys the convergence of a set of different numerical discretizations. It is based on the Richardson extrapolation method, and presented here oriented towards direct implementation, according to the framework of [250].

The GCI computation starts by defining a representative discretization metric h (e.g., average numerical cell length, cubic root of the average cell volume). This metric should be computed for all grids analyzed, ordered here from finer to coarser such that $h_1 < h_2 < h_3$ for three meshes, ideally systematically refined/coarsed. Define the ratio r between two adjacent discretizations as

$$r_{21} = h_2/h_1, \tag{A.1a}$$

$$r_{32} = h_3/h_2. \tag{A.1b}$$

Subsequently, extract from the solution with each discretization a scalar θ, which represents a relevant quantity in the targeted analysis. Compute the finite variation $\Delta\theta$ between adjacent discretizations as

$$\Delta\theta_{21} = \theta_2 - \theta_1, \tag{A.2a}$$

$$\Delta\theta_{32} = \theta_3 - \theta_2. \tag{A.2b}$$

The apparent order p is then evaluated as

$$p = \frac{1}{\ln(r_{21})} \left| \ln \left| \Delta\theta_{32}/\Delta\theta_{21} \right| + q(p) \right|, \tag{A.3}$$

where

$$q(p) = \ln\left(\frac{r_{21}^p - s}{r_{32}^p - s}\right), \tag{A.4a}$$

$$s = \operatorname{sgn}\left(\Delta\theta_{32}/\Delta\theta_{21}\right). \tag{A.4b}$$

Negative values of s indicate oscillatory convergence. Note that Eqs. (A.3) and (A.4) must be computed recursively (e.g., by fixed-point iteration). If the apparent order p obtained consistently matches the numerical scheme discretization order, the values and discretizations are understood to be in the asymptotic regime.

The extrapolated scalar $\check{\theta}$ may then be computed as

$$\check{\theta}_{21} = \frac{r_{21}^p \theta_1 - \theta_2}{r_{21}^p - 1}, \tag{A.5a}$$

$$\check{\theta}_{32} = \frac{r_{32}^p \theta_1 - \theta_2}{r_{32}^p - 1}. \tag{A.5b}$$

The approximate relative error between discretizations 2 and 1 is computed as

$$e_{21} = \left|\frac{\theta_1 - \theta_2}{\theta_1}\right|. \tag{A.6}$$

Finally, the GCI between discretizations 2 and 1 (fine) is computed as

$$\mathrm{GCI}_{21} = \frac{n\, e_{21}}{r_{21}^p - 1}, \tag{A.7}$$

where n is a safety factor (usually assuming the value of 1.25).

A.2 Cumulative unsteady damping

The identity between Eqs. (5.5a) and (5.5b) for the cumulative unsteady damping from section 5.1.2 can be demonstrated by an inductive argument. The case with $n = 1$ is trivially satisfied. Supposing the identity is true for n and expanding Eq. (5.5b) for $n + 1$:

$$
\begin{aligned}
&1 - \prod_{k=1}^{n+1}(1 - {}^{k}\varepsilon) \\
&= 1 - (1 - {}^{n+1}\varepsilon)\prod_{k=1}^{n}(1 - {}^{k}\varepsilon) \\
&= 1 - \prod_{k=1}^{n}(1 - {}^{k}\varepsilon) + {}^{n+1}\varepsilon\prod_{k=1}^{n}(1 - {}^{k}\varepsilon) \\
&= \sum_{k=1}^{n}\sum_{\substack{i_1,\ldots,i_k\in\{1,\ldots,n\}\\ i_1<\cdots<i_k}}(-1)^{k+1}\prod_{j=1}^{k}{}^{i_j}\varepsilon + {}^{n+1}\varepsilon\prod_{k=1}^{n}(1 - {}^{k}\varepsilon) \qquad \text{(A.8)}
\end{aligned}
$$

Note that the strict inequalities in the second sum ($i_1 < \cdots < i_k$) in Eq. (A.8) imply that the products of ${}^{i_k}\varepsilon$ do not have repeated indexes i_k. Applying again the inductive hypothesis, the last term in (A.8) is expanded as

$$
\begin{aligned}
&{}^{n+1}\varepsilon \prod_{k=1}^{n} (1 - {}^{k}\varepsilon) \\
&= {}^{n+1}\varepsilon \left[1 - \sum_{k=1}^{n} \sum_{\substack{i_1,\ldots,i_k \in \{1,\ldots,n\} \\ i_1 < \cdots < i_k}} (-1)^{k+1} \prod_{j=1}^{k} {}^{i_j}\varepsilon \right] \\
&= {}^{n+1}\varepsilon - \sum_{k=1}^{n} \sum_{\substack{i_1,\ldots,i_k \in \{1,\ldots,n\} \\ i_1 < \cdots < i_k}} (-1)^{k+1} \prod_{j=1}^{k} {}^{i_j}\varepsilon \; {}^{n+1}\varepsilon \\
&= {}^{n+1}\varepsilon - \sum_{k=1}^{n} \sum_{\substack{i_1,\ldots,i_k \in \{1,\ldots,n\} \\ i_{k+1} = n+1 \\ i_1 < \cdots < i_k}} (-1)^{k+1} \prod_{j=1}^{k+1} {}^{i_j}\varepsilon \\
&= {}^{n+1}\varepsilon - \sum_{k=2}^{n+1} \sum_{\substack{i_1,\ldots,i_{k-1} \in \{1,\ldots,n\} \\ i_k = n+1 \\ i_1 < \cdots < i_{k-1}}} (-1)^{k} \prod_{j=1}^{k} {}^{i_j}\varepsilon \\
&= {}^{n+1}\varepsilon + \sum_{k=2}^{n+1} \sum_{\substack{i_1,\ldots,i_{k-1} \in \{1,\ldots,n\} \\ i_k = n+1 \\ i_1 < \cdots < i_{k-1}}} (-1)^{k+1} \prod_{j=1}^{k} {}^{i_j}\varepsilon \\
&= \sum_{k=1}^{n+1} \sum_{\substack{i_1,\ldots,i_{k-1} \in \{1,\ldots,n\} \\ i_k = n+1 \\ i_1 < \cdots < i_{k-1}}} (-1)^{k+1} \prod_{j=1}^{k} {}^{i_j}\varepsilon \qquad \text{(A.9)}
\end{aligned}
$$

Substituting this term in expression (A.8), we obtain

$$
\begin{aligned}
1-\prod_{k=1}^{n+1}(1-{}^{k}\varepsilon) &= \sum_{k=1}^{n} \sum_{\substack{i_1,\ldots,i_k\in\{1,\ldots,n\}\\ i_1<\cdots<i_k}} (-1)^{k+1}\prod_{j=1}^{k} {}^{i_j}\varepsilon \\
&+ \sum_{k=1}^{n+1} \sum_{\substack{i_1,\ldots,i_{k-1}\in\{1,\ldots,n\}\\ i_k=n+1\\ i_1<\cdots<i_{k-1}}} (-1)^{k+1}\prod_{j=1}^{k} {}^{i_j}\varepsilon \\
&= \sum_{k=1}^{n+1} \sum_{\substack{i_1,\ldots,i_k\in\{1,\ldots,n+1\}\\ i_1<\cdots<i_k}} (-1)^{k+1}\prod_{j=1}^{k} {}^{i_j}\varepsilon \qquad \text{(A.10)}
\end{aligned}
$$

completing the proof.

BIBLIOGRAPHY

[1] V. Masson-Delmotte, P. Zhai, H.-O. Pörtner, D. Roberts, J. Skea, P. Shukla, A. Pirani, W. Moufouma-Okia, C. Péan, R. Pidcock, et al. *Global Warming of 1.5°C: An IPCC Special Report on the Impacts of Global Warming of 1.5°C Above Pre-industrial Levels and Related Global Greenhouse Gas Emission Pathways, in the Context of Strengthening the Global Response to the Threat of Climate Change, Sustainable Development, and Efforts to Eradicate Poverty*. World Meteorological Organization Geneva, Switzerland, 2018.

[2] European Environment Agency, European Aviation Safety Agency, & Eurocontrol. European Aviation Environmental Report. 2019.

[3] International Civil Aviation Organization. Long-Term Traffic Forecasts, Passenger and Cargo. 2018.

[4] Advisory Council for Aeronautics Research in Europe. Strategic Research and Innovation Agenda (SRIA) Vol. 1, Realizing Europe's vision for aviation. 5(5.6):132–137, 2012.

[5] N. T. S. Board. Left Engine Failure and Subsequent Depressurization, Southwest Airlines Flight 1380, Boeing 737-7H4, N772SW. Technical Report NTSB/AAR-19/03 PB2019-101439, 2019.

[6] W. Frank. Schaden Spiegel. 25(1):20, 1982.

[7] J. S. Rao. Application of fracture mechanics in the failure analysis of a last stage steam turbine blade. *Mechanism and Machine Theory*, 33(5):599–609, 1998.

[8] Examination of a Failed Fan Blade. Rolls-Royce RB211 Trent 892, Turbofan Engine, Boeing 777-300, A6-EMM. Technical Report 8/01, Australian Transport Safety Bureau, 2001.

[9] H. R. Simmons, K. Brun, and S. Cheruvu. Aerodynamic Instability Effects on Compressor Blade Failure: A Root Cause Failure Analysis. In *Volume 5: Marine; Microturbines and Small Turbomachinery; Oil and Gas Applications; Structures and Dynamics, Parts A and B*. ASME, 2006.

[10] R. K. Mishra and K. Srinivasan. Failure of Low-Pressure Turbine Blades in Military Turbofan Engines: Causes and Remedies. *Journal of Failure Analysis and Prevention*, 16(4):622–628, 2016.

[11] B. A. Cowles. High cycle fatigue in aircraft gas turbines—an industry perspective. *International Journal of Fracture*, 80(2-3):147–163, 1996.

[12] Y. El-Aini, R. deLaneuville, A. Stoner, and V. Capece. High cycle fatigue of turbomachinery components - Industry perspective. In *33rd Joint Propulsion Conference and Exhibit*. American Institute of Aeronautics and Astronautics, 1997.

[13] R. E. Dundas. A Statistical Study of Gas Turbine Losses and Analysis of Causes and Optimum Methods of Prevention. In *Volume 4: Heat Transfer, Electric Power, Industrial and Cogeneration*. American Society of Mechanical

Engineers, 1994.

[14] F. Kushner, R. A. Strickland, and J. Shurina. Rotating Component Modal Analysis and Resonance Avoidance – An Update. In *Proceedings of the Forty-Second Turbomachinery Symposium*, 2013.

[15] A. R. Collar. The Expanding Domain of Aeroelasticity. *The Journal of the Royal Aeronautical Society*, 50(428):613–636, 1946.

[16] D. L. Thomas. Dynamics of rotationally periodic structures. *International Journal for Numerical Methods in Engineering*, 14(1):81–102, 1979.

[17] V. Strouhal. Über eine besondere Art der Tonerregung. *Annalen der Physik und Chemie*, 241(10):216–251, 1878.

[18] Y. Fung. *An Introduction to the Theory of Aeroelasticity*. Dover Phoenix Edition: Engineering. Dover Publications, 2002.

[19] J. G. Marshall and M. Imregun. A review of aeroelasticity methods with emphasis on turbomachinery applications. *Journal of Fluids and Structures*, 10(3):237–267, 1996.

[20] A. V. Srinivasan. Flutter and Resonant Vibration Characteristics of Engine Blades. *Journal of Engineering for Gas Turbines and Power*, 119(4):742, 1997.

[21] M. Blocher and I. E. G. Fernández. Time-Linearized Forced Response Analysis of a Counter Rotating Fan: Part I — Theoretical Concept of a Fully Time-Linear Forced Response Analysis. In *Volume 7B: Structures and Dynamics*. ASME, 2014.

[22] L. E. Kinsler, A. R. Frey, A. B. Coppens, and J. V. Sanders. *Fundamentals of Acoustics*. Wiley India Pvt. Limited, New Delhi, 4th edition, 2009.

[23] H. Försching. Aeroelastic stability of cascades in turbomachinery. *Progress in Aerospace Sciences*, 30(3):213–266, 1994.

[24] M. Platzer, F. Carta, and North Atlantic Treaty Organization. *AGARD Manual on Aeroelasticity in Axial-flow Turbomachines: Structural dynamics and aeroelasticity*. AGARD Manual on Aeroelasticity in Axial-flow Turbomachines. North Atlantic Treaty Organization, Advisory Group for Aerospace Research and Development, 1987.

[25] W. Campbell. *Protection of Steam Turbine Disk Wheels from Axial Vibration*. General Electric Company, 1924.

[26] M. Jüngst, F. Holzinger, H.-P. Schiffer, and S. Leichtfuss. Analysing Non-Synchronous Blade Vibrations in a Transonic Compressor Rotor. In *11th European Conference on Turbomachinery Fluid dynamics & Thermodynamics*, number ETC2015-079, 2015.

[27] H. Lamb and R. V. Southwell. The Vibrations of a Spinning Disk. *Proceedings of the Royal Society of London. Series A, Containing Papers of a Mathematical and Physical Character*, 99(699):272–280, 1921.

[28] E. Dowell. *A Modern Course in Aeroelasticity*. Springer International Publishing, 5th edition, 2015.

[29] O. Bendiksen, R. E. Kielb, and K. C. Hall. *Encyclopedia of Aerospace Engineering - Turbomachinery Aeroelasticity*. John Wiley & Sons, Ltd, 2010.

[30] S. J. Wildheim. Excitation of Rotationally Periodic Structures. *Journal of Applied Mechanics*, 46(4):878, 1979.

[31] L. Bertini, P. Neri, C. Santus, A. Guglielmo, and G. Mariotti. Analytical investigation of the SAFE diagram for bladed wheels, numerical and experimental validation. *Journal of Sound and Vibration*, 333(19):4771–4788, 2014.

[32] A. Srinivasan, D. Cutts, and S. Sridhar. Turbojet Engine Blade Damping. Technical Report 165406, National Aeronautics and Space Administration, Lewis Research Center, 1981.

[33] J. Sun and L. Kari. Coating Methods to Increase Material Damping of Compressor Blades: Measurements and Modeling. In *Volume 6: Structures and Dynamics, Parts A and B*. ASMEDC, 2010.

[34] C. Gastaldi, A. Fantetti, and T. Berruti. Forced Response Prediction of Turbine Blades with Flexible Dampers: The Impact of Engineering Modelling Choices. *Applied Sciences*, 8(1):34, 2017.

[35] K. Y. Sanliturk, D. J. Ewins, and A. B. Stanbridge. Underplatform Dampers for Turbine Blades: Theoretical Modeling, Analysis, and Comparison With Experimental Data. *Journal of Engineering for Gas Turbines and Power*, 123(4):919–929, 1998.

[36] E. P. Petrov. Explicit Finite Element Models of Friction Dampers in Forced Response Analysis of Bladed Disks. *Journal of Engineering for Gas Turbines and Power*, 130(2), 2008.

[37] J. Gross, M. Krack, and H. Schoenenborn. Analysis of the Effect of Multi-Row and Multi-Passage Aerodynamic Interaction on the Forced Response Variation in a Compressor Configuration: Part 2 — Effects of Additional Structural Mistuning. In *Volume 7B: Structures and Dynamics*. ASME, 2017.

[38] H.-S. Im and G.-C. Zha. Simulation of Non-Synchronous Blade Vibration of an Axial Compressor Using a Fully Coupled Fluid/Structure Interaction. In *Volume 7: Structures and Dynamics, Parts A and B*. ASME International, 2012.

[39] S. Moffatt and L. He. Blade Forced Response Prediction for Industrial Gas Turbines. Part 1: Methodologies. In *Volume 4: Turbo Expo 2003*. ASME International, 2003.

[40] A. Torkaman. *Flutter Stability of Shrouded Turbomachinery Cascades with Nonlinear Frictional Damping*. PhD thesis, College of Engineering and Computer Science, University of Central Florida, 2018.

[41] O. J. Poudou. *Modeling and Analysis of The Dynamics of Dry-Friction-Damped Structural Systems*. PhD thesis, University of Michigan, 2007.

[42] F. O. Carta. Coupled Blade-Disk-Shroud Flutter Instabilities in Turbojet Engine Rotors. *Journal of Engineering for Power*, 89(3):419–426, 1967.

[43] F. Lane. System Mode Shapes in the Flutter of Compressor Blade Rows.

Journal of the Aeronautical Sciences, 23(1):54–66, 1956.

[44] S. V. Borbély. Über die Luftkräfte, die auf einen harmonisch schwingenden zweidimensionalen Flügel bei Überschallgeschwindigkeit wirken . *ZAMM - Zeitschrift für Angewandte Mathematik und Mechanik*, 22(4):190–205, 1942.

[45] E. F. Crawley and K. C. Hall. Optimization and Mechanisms of Mistuning in Cascades. *Journal of Engineering for Gas Turbines and Power*, 107(2):418, 1985.

[46] T. Reddy, M. Bakhle, and R. Srivastava. Review of Recent Aeroelastic Analysis Methods for Propulsion at NASA Lewis Research Center. Technical Report 19940023724, NASA Lewis Research Center, 1993.

[47] O. Bendiksen. Aeroelastic problems in turbomachines. In *31st Structures, Structural Dynamics and Materials Conference*. American Institute of Aeronautics and Astronautics (AIAA), 1990.

[48] D. Vogt. *Experimental Investigation of Three-Dimensional Mechanisms in Low-Pressure Turbine Flutter*. PhD thesis, Royal Institute of Technology, 2005.

[49] T. Fransson. Aeroelasticity in Axial-Flow Turbomachines. *Von Karman Institute for Fluid Dynamics Lecture Series*, 2005.

[50] F. Holzinger, F. Wartzek, H.-P. Schiffer, S. Leichtfuss, and M. Nestle. Self-Excited Blade Vibration Experimentally Investigated in Transonic Compressors: Acoustic Resonance. *Journal of Turbomachinery*, 138(4), 2015.

[51] R. Kielb, K. Hall, M. Spiker, J. Thomas, E. T. Pratt, and R. Jeffries. Non-Synchronous Vibration of Turbomachinery Airfoils. Technical Report AFOSR Contract F49620-03-1-0204, Duke University, 2006.

[52] M. Jüngst, D. Franke, H.-P. Schiffer, and T. Giersch. Aeroelastic Effects in a Transonic Compressor with Nonaxisymmetric Tip Clearance. In *Proceedings of GPPS Forum 18, Global Power and Propulsion Society*, 2018.

[53] M. P. Castanier and C. Pierre. Modeling and Analysis of Mistuned Bladed Disk Vibration: Current Status and Emerging Directions. *Journal of Propulsion and Power*, 22(2):384–396, 2006.

[54] J. C. Slater, G. R. Minkiewicz, and A. J. Blair. Forced Response of Bladed Disk Assemblies–A Survey. *The Shock and Vibration Digest*, 31(1):17–24, 1999.

[55] R. E. Kielb and K. R. V. Kaza. Aeroelastic Characteristics of a Cascade of Mistuned Blades in Subsonic and Supersonic Flows. *Journal of Vibration Acoustics Stress and Reliability in Design*, 105(4):425, 1983.

[56] E. P. Petrov. A Method for Forced Response Analysis of Mistuned Bladed Disks With Aerodynamic Effects Included. *Journal of Engineering for Gas Turbines and Power*, 132(6), 2010.

[57] E. P. Petrov. Reduction of Forced Response Levels for Bladed Discs by Mistuning: Overview of the Phenomenon. In *Volume 6: Structures and Dynamics, Parts A and B*. ASMEDC, 2010.

[58] D. J. Ewins. *The effects of detuning upon the vibration of bladed discs*. PhD thesis, University of Cambridge, 1966.

[59] D. S. Whitehead. Effect of mistuning on the vibration of turbo-machine blades induced by wakes. *Journal of Mechanical Engineering Science*, 8(1):15–21, 1966.

[60] D. S. Whitehead. The Maximum Factor by Which Forced Vibration of Blades Can Increase Due to Mistuning. *Journal of Engineering for Gas Turbines and Power*, 120(1):115–119, 1998.

[61] O. Bendiksen. Localization phenomena in structural dynamics. *Chaos, Solitons & Fractals*, 11(10):1621–1660, 2000.

[62] R. Bladh, C. Pierre, M. P. Castanier, and M. J. Kruse. Dynamic Response Predictions for a Mistuned Industrial Turbomachinery Rotor Using Reduced-Order Modeling. *Journal of Engineering for Gas Turbines and Power*, 124(2):311, 2002.

[63] M. P. Castanier and C. Pierre. Using Intentional Mistuning in the Design of Turbomachinery Rotors. *AIAA Journal*, 40(10):2077–2086, 2002.

[64] E. P. Petrov and D. J. Ewins. Analysis of the Worst Mistuning Patterns in Bladed Disc Assemblies. In *Volume 4: Manufacturing Materials and Metallurgy; Ceramics; Structures and Dynamics, Controls, Diagnostics and Instrumentation; Education; IGTI Scholar Award*. American Society of Mechanical Engineers, 2001.

[65] D. J. Ewins. Further studies of bladed disc vibration: effects of packeting. In *International conference of Vibrations in rotating machinery*, 1980.

[66] J. H. Griffin and T. M. Hoosac. Model Development and Statistical Investigation of Turbine Blade Mistuning. *Journal of Vibration and Acoustics*, 106(2):204–210, 1984.

[67] C. Martel, R. Corral, and J. M. Llorens. Stability Increase of Aerodynamically Unstable Rotors Using Intentional Mistuning. *Journal of Turbomachinery*, 130(1), 2007.

[68] R. Budynas. *Shigley's Mechanical Engineering Design*. McGraw-Hill series in mechanical engineering. McGraw-Hill Higher Education, 2014.

[69] J. Goodman. *Mechanics applied to engineering*. Longmans, Green, 1899.

[70] R. C. Batra. *Elements of Continuum Mechanics*. American Institute of Aeronautics and Astronautics, 2006.

[71] L. Malvern. *Introduction to the Mechanics of a Continuous Medium*. Englewood Cliffs, 1977.

[72] P. K. Kundu, I. M. Cohen, and D. R. Dowling. *Fluid Mechanics*. Academic Press, Amsterdam, Boston, Heidelberg, 2012.

[73] G. Batchelor. *An Introduction to Fluid Dynamics*. First Cambridge Mathematical Library, 2000.

[74] S. B. Pope. *Turbulent Flows*. Cambridge University Press, 2000.

[75] D. Wilcox. *Turbulence modeling for CFD*. DCW Industries, La Canada, Calif, 1998.

[76] J. Donea, A. Huerta, J.-P. Ponthot, and A. Rodríguez-Ferran. Arbitrary Lagrangian-Eulerian methods. In *Encyclopedia of Computational Mechanics*. Wiley-Blackwell, 2004.

[77] S. C. Brenner and L. R. Scott. *The Mathematical Theory of Finite Element Methods*. Springer New York, 1994.

[78] K. Bathe. *Finite Element Procedures*. Klaus-Jürgen Bathe, 2007.

[79] O. C. Zienkiewicz, R. L. Taylor, and J. Z. Zhu. *The Finite Element Method: Its Basis and Fundamentals*. Elsevier LTD, Oxford, 2013.

[80] ANSYS, Inc. *ANSYS Academic Research, Release 19.2*.

[81] J. Fish and T. Belytschko. *A First Course in Finite Elements*. John Wiley & Sons, 2007.

[82] Z.-F. Fu and J. He. *Modal Analysis*. Butterworth-Heinemann, 2001.

[83] P. Balasubramanian, J. G. Jagadeesh, H. K. Suhas, and V. Ramamurti. Free-vibration analysis of cyclic symmetric structures. *Communications in Applied Numerical Methods*, 7(2):131–139, 1991.

[84] G. W. Stewart. A Krylov–Schur Algorithm for Large Eigenproblems. *SIAM Journal on Matrix Analysis and Applications*, 23(3):601–614, 2002.

[85] N. M. Newmark. A Method of Computation for Structural Dynamics. *ASCE Journal of the Engineering Mechanics Division*, 85:67–94, 1959.

[86] J. Chung and G. M. Hulbert. A Time Integration Algorithm for Structural Dynamics With Improved Numerical Dissipation: The Generalized-Alpha Method. *Journal of Applied Mechanics*, 60(2):371–375, 1993.

[87] D. Soares and V. B. C. de Almeida. An effective adaptive time domain formulation to analyse acoustic-elastodynamic coupled models. *Computers & Structures*, 189:1–11, 2017.

[88] B. Leonard. The ULTIMATE conservative difference scheme applied to unsteady one-dimensional advection. *Computer Methods in Applied Mechanics and Engineering*, 88(1):17–74, 1991.

[89] *IGG™/AutoGrid5™ v13.1*.

[90] J. Tu, G.-H. Yeoh, and C. Liu. *Computational Fluid Dynamics: A Practical Approach*. Elsevier LTD, Oxford, 2018.

[91] R. Courant, K. Friedrichs, and H. Lewy. Über die partiellen Differenzengleichungen der mathematischen Physik. *Mathematische Annalen*, 100:32–74, 1928.

[92] L. He. An Euler Solution for Unsteady Flows Around Oscillating Blades. *Journal of Turbomachinery*, 112(4):714, 1990.

[93] L. He. A method of simulating unsteady turbomachinery flows with multiple perturbations. *AIAA Journal*, 30(11):2730–2735, 1992.

[94] G. A. Gerolymos, G. J. Michon, and J. Neubauer. Analysis and Application of Chorochronic Periodicity in Turbomachinery Rotor/Stator Interaction Computations. *Journal of Propulsion and Power*, 18(6):1139–1152, 2002.

[95] W. Ning and L. He. Computation of Unsteady Flows Around Oscillating Blades Using Linear and Nonlinear Harmonic Euler Methods. *Journal of Turbomachinery*, 120(3):508, 1998.

[96] J. Adamczyk. Model equation for simulating flows in multistage turbomachinery. In *ASME, International Gas Turbine Conference and Exhibit, 30th, Houston, TX*, 1985.

[97] K. C. Hall, J. P. Thomas, and W. S. Clark. Computation of Unsteady Nonlinear Flows in Cascades Using a Harmonic Balance Technique. *AIAA Journal*, 40(5):879–886, 2002.

[98] J. Boussinesq. *Essai sur la théorie des eaux courantes*. Paris: Imprimerie Nationale, 1877.

[99] P. Spalart and S. Allmaras. A one-equation turbulence model for aerodynamic flows. In *30th Aerospace Sciences Meeting and Exhibit*. American Institute of Aeronautics and Astronautics, 1992.

[100] K. Hanjalić and B. E. Launder. A Reynolds stress model of turbulence and its application to thin shear flows. *Journal of Fluid Mechanics*, 52(4):609–638, 1972.

[101] D. C. Wilcox. Formulation of the k-w Turbulence Model Revisited. *AIAA Journal*, 46(11):2823–2838, 2008.

[102] F. R. Menter. Two-equation eddy-viscosity turbulence models for engineering applications. *AIAA Journal*, 32(8):1598–1605, 1994.

[103] E. Akcayoz, H. D. Vo, and A. Mahallati. Controlling Corner Stall Separation With Plasma Actuators in a Compressor Cascade. *Journal of Turbomachinery*, 138(8):081008, 2016.

[104] M. C. Keerthi, S. Shubham, and A. Kushari. Aerodynamic Influence of Oscillating Adjacent Airfoils in a Linear Compressor Cascade. *AIAA Journal*, 55(12):4113–4126, 2017.

[105] R. Chow and C. P. van Dam. Verification of computational simulations of the NREL 5 MW rotor with a focus on inboard flow separation. *Wind Energy*, 15(8):967–981, 2011.

[106] J. Siemann and J. R. Seume. Design of an Aspirated Compressor Stator by Means of DoE. In *Volume 2A: Turbomachinery*. ASME, 2015.

[107] K. Auchoybur and R. Miller. The sensitivity of 3D separations in multi-stage compressors. *Journal of the Global Power and Propulsion Society*, 2:34C05T, 2018.

[108] F. M. Besem, R. E. Kielb, P. Galpin, L. Zori, and N. L. Key. Mistuned Forced Response Predictions of an Embedded Rotor in a Multistage Compressor. *Journal of Turbomachinery*, 138(6):061003, 2016.

[109] J. Smagorinsky. General Circulation Experiments with the Primitive Equations. *Monthly Weather Review*, 91(3):99–164, 1963.

[110] D. K. Lilly. A proposed modification of the Germano subgrid-scale closure method. *Physics of Fluids A: Fluid Dynamics*, 4(3):633–635, 1992.

[111] P. Spalart, W.-H. Jou, M. Strelets, and S. Allmaras. Comments on the Feasibility of LES for Wings, and on a Hybrid RANS/LES Approach. In *Advances in DNS/LES: Direct numerical simulation and large eddy simulation*, 1997.

[112] P. B. Ryzhakov, R. Rossi, S. R. Idelsohn, and E. Oñate. A monolithic Lagrangian approach for fluid-structure interaction problems. *Computational Mechanics*, 46(6):883–899, 2010.

[113] C. Michler, S. Hulshoff, E. van Brummelen, and R. de Borst. A monolithic approach to fluid-structure interaction. *Computers & Fluids*, 33(5-6):839–848, 2004.

[114] B. Hübner, E. Walhorn, and D. Dinkler. A monolithic approach to fluid-structure interaction using space-time finite elements. *Computer Methods in Applied Mechanics and Engineering*, 193(23-26):2087–2104, 2004.

[115] K.-J. B. S. Rugonyi. On the analysis of fully-coupled fluid flows with structural interactions. *International Journal for Computational Civil and Structural Engineering*, 1:29–41, 2000.

[116] M. A. Storti, N. M. Nigro, R. R. Paz, and L. D. Dalcín. Strong coupling strategy for fluid-structure interaction problems in supersonic regime via fixed point iteration. *Journal of Sound and Vibration*, 320(4-5):859–877, 2009.

[117] G. Link. *A Finite Element Scheme for Fluid–Solid–Acoustics Interactions and its Application to Human Phonation*. PhD thesis, Technischen Fakultät der Universität Erlangen-Nürnberg, 2008.

[118] S. Moffatt. *Forced response prediction for industrial gas turbine blades*. PhD thesis, Durham University, 2006.

[119] W. Ning, S. Moffatt, Y. Li, and R. G. Wells. Blade Forced Response Prediction for Industrial Gas Turbines. Part 2: Verification and Application. In *Volume 4: Turbo Expo 2003*. ASME International, 2003.

[120] I. E. G. Fernández and M. Blocher. Time-Linearized Forced Response Analysis of a Counter Rotating Fan: Part II — Analysis of the DLR CRISP2 Model. In *Volume 7B: Structures and Dynamics*. ASME, 2014.

[121] S. L. Bittner, C. Keller, C. E. Meinzer, and J. R. Seume. Experimental Validation of a Forced Response Analysis Using a Time-Linearized Method. In *2018 AIAA/ASCE/AHS/ASC Structures, Structural Dynamics, and Materials Conference*. American Institute of Aeronautics and Astronautics, 2018.

[122] J. W. Cooley and J. W. Tukey. An algorithm for the machine calculation of complex Fourier series. *Mathematics of Computation*, 19(90):297–297, 1965.

[123] R. Bracewell. *The Fourier transform and its applications*. McGraw Hill, Boston, 2000.

[124] K. Pearson. On lines and planes of closest fit to systems of points in space. *The London, Edinburgh, and Dublin Philosophical Magazine and Journal of Science*, 2(11):559–572, 1901.

[125] H. Hotelling. Simplified calculation of principal components. *Psychometrika*,

1(1):27–35, 1936.

[126] K. Karhunen. Zur Spektraltheorie stochastischer Prozesse. *Ann. Acad. Sci. Finnicae, Ser. A*, 1:34, 1946.

[127] M. Loève. *Fonctions aléatoires du second ordre*. Revue, Processus Stochastiques et Mouvement Brownien, Paris, 1948.

[128] E. N. Lorenz. Empirical orthogonal functions and statistical weather prediction. *Statistical Forecasting Project, Scientific Report No. 1*, 1956.

[129] I. T. Jolliffe. *Principal Component Analysis*. Springer-Verlag, 2002.

[130] J. L. Lumley. The Structure of Inhomogeneous Turbulence. In I. A. M. Yaglom and E. V. I. Tatarski, editors, *Atmospheric Turbulence and Wave Propagation*, pages 166–178, Nauka, Moscow, 1967.

[131] P. Holmes, J. L. Lumley, G. Berkooz, and C. W. Rowley. *Turbulence, Coherent Structures, Dynamical Systems and Symmetry*. Cambridge University Press, 2009.

[132] K. Taira, S. L. Brunton, S. T. M. Dawson, C. W. Rowley, T. Colonius, B. J. McKeon, O. T. Schmidt, S. Gordeyev, V. Theofilis, and L. S. Ukeiley. Modal Analysis of Fluid Flows: An Overview. *AIAA Journal*, 55(12):4013–4041, 2017.

[133] C. Eckart and G. Young. The approximation of one matrix by another of lower rank. *Psychometrika*, 1(3):211–218, 1936.

[134] L. Sirovich. Turbulence and the dynamics of coherent structures. I - Coherent structures. II - Symmetries and transformations. III - Dynamics and scaling. *Quarterly of Applied Mathematics*, 45(3):573–582, 1987.

[135] O. Lehmann, M. Luchtenburg, B. Noack, R. King, M. Morzynski, and G. Tadmor. Wake stabilization using POD Galerkin models with interpolated modes. In *Proceedings of the 44th IEEE Conference on Decision and Control*. IEEE, 2005.

[136] T. K. Sengupta, H. Singh, S. Bhaumik, and R. R. Chowdhury. Diffusion in inhomogeneous flows: Unique equilibrium state in an internal flow. *Computers & Fluids*, 88:440–451, 2013.

[137] B. O. Koopman. Hamiltonian Systems and Transformation in Hilbert Space. *Proceedings of the National Academy of Sciences*, 17(5):315–318, 1931.

[138] P. J. Schmid. Dynamic mode decomposition of numerical and experimental data. *Journal of Fluid Mechanics*, 656:5–28, 2010.

[139] C. W. Rowley, I. Mezić, S. Bagheri, P. Schlatter, and S. S. Henningson. Spectral analysis of nonlinear flows. *Journal of Fluid Mechanics*, 641:115, 2009.

[140] J. Kutz. *Dynamic mode decomposition : data-driven modeling of complex systems*. Society for Industrial and Applied Mathematics, Philadelphia, 2016.

[141] J. H. Tu, C. W. Rowley, D. M. Luchtenburg, S. L. Brunton, and J. N. Kutz. On dynamic mode decomposition: Theory and applications. *Journal of*

Computational Dynamics, 1(2):391–421, 2014.

[142] R. Penrose. A generalized inverse for matrices. *Mathematical Proceedings of the Cambridge Philosophical Society*, 51(3):406–413, 1955.

[143] M. R. Jovanović, P. J. Schmid, and J. W. Nichols. Sparsity-promoting dynamic mode decomposition. *Physics of Fluids*, 26(2):024103, 2014.

[144] G. W. Stewart. *Matrix algorithms*. Society for Industrial and Applied Mathematics, Philadelphia, 1998.

[145] P. J. Schmid, D. Violato, and F. Scarano. Decomposition of time-resolved tomographic PIV. *Experiments in Fluids*, 52(6):1567–1579, 2012.

[146] S. Farokhi. *Aircraft Propulsion*. Wiley, 2nd edition, 2014.

[147] T. Grönstedt, M. Irannezhad, X. Lei, O. Thulin, and A. Lundbladh. First and Second Law Analysis of Future Aircraft Engines. In *Volume 2: Aircraft Engine; Coal, Biomass and Alternative Fuels; Cycle Innovations*. ASME, 2013.

[148] H. Holzwarth. *Die Gasturbine: Theorie, Konstruktion und Betriebsergebnisse von zwei ausgeführten Maschinen*. Oldenbourg Wissenschaftsverlag, 1911.

[149] F. K. Lu, R. Miller, M. R. Nalim, and K. H. Yu. Introduction: Special Section on Pressure Gain Combustion. *Journal of Propulsion and Power*, 33(1):16–16, 2017.

[150] D. Paxson. Resonant Pulse Combustors: A Reliable Route to Practical Pressure Gain Combustion. Technical Report GRC-E-DAA-TN58478, NASA Glenn Research Center Cleveland, 2017.

[151] P. Berndt. *Mathematical Modeling of the Shockless Explosion Combustion*. Phd, Freie Universität Berlin, Mathematik und Informatik, 2016.

[152] W. H. Heiser and D. T. Pratt. Thermodynamic Cycle Analysis of Pulse Detonation Engines. *Journal of Propulsion and Power*, 18(1):68–76, 2002.

[153] A. H. Lefebvre and D. R. Ballal. *Gas Turbine Combustion: Alternative Fuels and Emissions*. CRC Press, 3rd edition, 2010.

[154] E. Wintenberger and J. Shepherd. The performance of steady detonation engines. In *41st Aerospace Sciences Meeting and Exhibit*. American Institute of Aeronautics and Astronautics (AIAA), 2003.

[155] K. P. Rouser, P. I. King, F. R. Schauer, R. Sondergaard, and J. L. Hoke. Performance Evaluation of an Unsteady Turbine Driven by a Pulsed Detonation Combustor. In *Volume 7: Turbomachinery, Parts A, B, and C*. ASME International, 2011.

[156] G. Roy, S. Frolov, A. Borisov, and D. Netzer. Pulse detonation propulsion: challenges, current status, and future perspective. *Progress in Energy and Combustion Science*, 30(6):545–672, 2004.

[157] K. Matsuoka, H. Taki, J. Kasahara, H. Watanabe, A. Matsuo, and T. Endo. Pulse Detonation Cycle at Kilohertz Frequency. In *Shock Wave and High Pressure Phenomena*, pages 183–198. Springer International Publishing, 2017.

[158] K. Kailasanath. Review of Propulsion Applications of Detonation Waves.

AIAA Journal, 38(9):1698–1708, 2000.

[159] K. Kailasanath. Recent Developments in the Research on Pulse Detonation Engines. *AIAA Journal*, 41(2):145–159, 2003.

[160] K. M. Pandey and P. Debnath. Review on Recent Advances in Pulse Detonation Engines. *Journal of Combustion*, 2016:1–16, 2016.

[161] X. Meng, W. de Jong, and T. Kudra. A state-of-the-art review of pulse combustion: Principles, modeling, applications and R&D issues. *Renewable and Sustainable Energy Reviews*, 55:73–114, 2016.

[162] J. M. Clarke and J. H. Horlock. Availability and Propulsion. *Journal of Mechanical Engineering Science*, 17(4):223–232, 1975.

[163] C. Xisto, F. Ali, O. Petit, T. Grönstedt, A. Rolt, and A. Lundbladh. Analytical Model for the Performance Estimation of Pre-Cooled Pulse Detonation Turbofan Engines. In *Volume 1: Aircraft Engine, Fans and Blowers, Marine, Honors and Awards*. ASME, 2017.

[164] E. Wintenberger and J. E. Shepherd. Thermodynamic Cycle Analysis for Propagating Detonations. *Journal of Propulsion and Power*, 22(3):694–698, 2006.

[165] J. A. T. Gray, J. Vinkeloe, J. Moeck, C. O. Paschereit, P. Stathopoulos, P. Berndt, and R. Klein. Thermodynamic Evaluation of Pulse Detonation Combustion for Gas Turbine Power Cycles. In *Volume 4B: Combustion, Fuels and Emissions*. ASME International, 2016.

[166] J. Goldmeer, V. Tangirala, and A. Dean. System-Level Performance Estimation of a Pulse Detonation Based Hybrid Engine. *Journal of Engineering for Gas Turbines and Power*, 130(1), 2007.

[167] A. Rasheed, A. H. Furman, and A. J. Dean. Experimental Investigations of the Performance of a Multitube Pulse Detonation Turbine System. *Journal of Propulsion and Power*, 27(3):586–596, 2011.

[168] H. Qiu, C. Xiong, C. J. Yan, and W. Fan. Propulsive Performance of Ideal Detonation Turbine Based Combined Cycle Engine. *Journal of Engineering for Gas Turbines and Power*, 134(8), 2012.

[169] S. M. Jones and D. E. Paxson. Potential Benefits to Commercial Propulsion Systems from Pressure Gain Combustion. In *49th AIAA/ASME/SAE/ASEE Joint Propulsion Conference*. American Institute of Aeronautics and Astronautics, 2013.

[170] S. C. Gülen. Pressure gain combustion advantage in land-based electric power generation. *Journal of the Global Power and Propulsion Society*, 2017.

[171] N. Zhao, H. Zheng, X. Wen, and D. Xiao. Thermodynamic Performance Enhancement of Marine Gas Turbine by Using Detonation Combustion. In *Volume 1: Aircraft Engine, Fans and Blowers, Marine*. American Society of Mechanical Engineers, 2018.

[172] J. A. C. Kentfield, M. Rehman, and E. S. Marzouk. A Simple Pressure-Gain Combustor for Gas Turbines. *Journal of Engineering for Power*, 99(2):153, 1977.

[173] A. Rasheed, V. Tangirala, A. Dean, C. L. Vandervort, and C. Haubert. Interactions of a Pulsed Detonation Engine with a 2D Blade Cascade. In *42nd AIAA Aerospace Sciences Meeting and Exhibit*. American Institute of Aeronautics and Astronautics (AIAA), 2004.

[174] J. Hoke, R. Bradley, J. Stutrud, and F. Schauer. Integration of a pulsed detonation engine with an ejector pump and with a turbo-charger as methods to self-aspirate. In *40th AIAA Aerospace Sciences Meeting & Exhibit*. American Institute of Aeronautics and Astronautics (AIAA), 2002.

[175] F. Schauer, R. Bradley, and J. Hoke. Interaction of a Pulsed Detonation Engine with a Turbine. In *41st Aerospace Sciences Meeting and Exhibit*. American Institute of Aeronautics and Astronautics (AIAA), 2003.

[176] T. Sakurai, T. Obara, S. Ohyagi, and M. Murayama. Experimental Study of Pulse Detonation Turbine Engine Toward Power Generator. In *Proceedings of the 20th International Colloquium on the Dynamics of Explosion and Reactive Systems*, 2005.

[177] T. Tsuji, S. Shirakawa, T. Yoshihashi, T. Obara, and S. Ohyagi. Interaction Between Two Cylinders in a Pulse Detonation Engine. *International Journal of Energetic Materials and Chemical Propulsion*, 8(6):489–500, 2009.

[178] J. Deng, L. Zheng, C. Yan, L. Jlang, C. Xiong, and N. Li. Experimental Investigations of a Pulsed Detonation Combustor-Turbine Hybrid System. In *47th AIAA Aerospace Sciences Meeting including The New Horizons Forum and Aerospace Exposition*. American Institute of Aeronautics and Astronautics (AIAA), 2009.

[179] K. Rouser, P. King, F. Schauer, R. Sondergaard, and J. Hoke. Experimental Performance Evaluation of a Turbine Driven by Pulsed Detonations. In *51st AIAA Aerospace Sciences Meeting including the New Horizons Forum and Aerospace Exposition*. American Institute of Aeronautics and Astronautics, 2013.

[180] H. Qiu, C. Xiong, and L. Zheng. Experimental investigation of an air-breathing pulse detonation turbine prototype engine. *Applied Thermal Engineering*, 104:596–602, 2016.

[181] D. Petters and J. Felder. Engine System Performance of Pulse Detonation Concepts Using the NPSS Program. In *38th AIAA/ASME/SAE/ASEE Joint Propulsion Conference Exhibit*. American Institute of Aeronautics and Astronautics (AIAA), 2002.

[182] N. Caldwell, A. Glaser, R. Dimicco, and E. Gutmark. Acoustic Measurements of an Integrated Pulse Detonation Engine with Gas Turbine System. In *43rd AIAA Aerospace Sciences Meeting and Exhibit*. American Institute of Aeronautics and Astronautics (AIAA), 2005.

[183] N. Caldwell, A. Glaser, and E. Gutmark. Acoustic Interactions of a Pulse Detonation Engine Array with a Gas Turbine. In *44th AIAA Aerospace Sciences Meeting and Exhibit*, 2006.

[184] A. Glaser, N. Caldwell, and E. Gutmark. Performance of an Axial Flow

Turbine Driven by Multiple Pulse Detonation Combustors. In *45th AIAA Aerospace Sciences Meeting and Exhibit*. American Institute of Aeronautics and Astronautics (AIAA), 2007.

[185] N. Caldwell and E. Gutmark. A Review of Pulse Detonation Engine Research at the University of Cincinnati. *43rd AIAA/ASME/SAE/ASEE Joint Propulsion Conference Exhibit*, 2007.

[186] A. C. S. George, R. B. Driscoll, D. E. Munday, and E. J. Gutmark. Experimental Comparison of Axial Turbine Performance Under Pulsed-Air and Pulsed-Detonation Flows. In *49th AIAA/ASME/SAE/ASEE Joint Propulsion Conference*. American Institute of Aeronautics and Astronautics, 2013.

[187] A. Rasheed, A. Furman, and A. Dean. Experimental Investigations of an Axial Turbine Driven by a Multi-Tube Pulsed Detonation Combustor System. In *41st AIAA/ASME/SAE/ASEE Joint Propulsion Conference & Exhibit*. American Institute of Aeronautics and Astronautics (AIAA), 2005.

[188] M. Baptista, A. Rasheed, B. Badding, O. Velagandula, and A. Dean. Mechanical Response in a Multi-tube Pulsed Detonation Combustor-Turbine Hybrid System. In *44th AIAA Aerospace Sciences Meeting and Exhibit*. American Institute of Aeronautics and Astronautics (AIAA), 2006.

[189] A. Rasheed, A. H. Furman, and A. J. Dean. Pressure Measurements and Attenuation in a Hybrid Multitube Pulse Detonation Turbine System. *Journal of Propulsion and Power*, 25(1):148–161, 2009.

[190] A. Rasheed, A. Furman, and A. Dean. Wave Attenuation and Interactions in a Pulsed Detonation Combustor-Turbine Hybrid System. In *44th AIAA Aerospace Sciences Meeting and Exhibit*. American Institute of Aeronautics and Astronautics (AIAA), 2006.

[191] B. K. Kan, S. D. Heister, and D. E. Paxson. Experimental Study of Pressure Gain Combustion with Hypergolic Rocket Propellants. *Journal of Propulsion and Power*, 33(1):112–120, 2017.

[192] D. Van Zante, E. Envia, and M. G. Turner. The Attenuation of a Detonation Wave by an Aircraft Engine Axial Turbine Stage. In *18th AIAA International Symposium on Air-Breathing Engines*, 2007.

[193] G. Xia, D. Li, and C. Merkle. Modeling of Pulsed Detonation Tubes in Turbine Systems. In *43rd AIAA Aerospace Sciences Meeting and Exhibit*. American Institute of Aeronautics and Astronautics (AIAA), 2005.

[194] C. Brück, C. Tiedemann, and D. Peitsch. Experimental Investigations on Highly Loaded Compressor Airfoils With Active Flow Control Under Non-Steady Flow Conditions in a 3D-Annular Low-Speed Cascade. In *Volume 2A: Turbomachinery*, Seoul, South Korea, 2016. ASME International.

[195] M. Staats, J. Mihalyovics, and D. Peitsch. A Qualitative Comparison of Unsteady Operated Compressor Stator Cascades with Active Flow Control. In *Notes on Numerical Fluid Mechanics and Multidisciplinary Design*, pages 91–104. Springer International Publishing, 2018.

[196] C. Brück, J. Mihalyovics, and D. Peitsch. Experimental Investigations On Highly Loaded Compressor Airfoils With Different Active Flow Control Parameters Under Unsteady Flow Conditions. *Global Power and Propulsion Society Forum 18*, 2018.

[197] J. Mihalyovics, J. Gambel, and D. Peitsch. 3D Profile Design and Optimization of a Rotor for a Low Speed Axial Compressor Wind Tunnel. *Deutscher Luft- und Raumfahrtkongress 2019, Darmstadt*, 2020.

[198] F. K. Lu and E. M. Braun. Rotating Detonation Wave Propulsion: Experimental Challenges, Modeling, and Engine Concepts. *Journal of Propulsion and Power*, 30(5):1125–1142, 2014.

[199] K. Kailasanath. Recent Developments in the Research on Rotating-Detonation-Wave Engines. In *55th AIAA Aerospace Sciences Meeting*. American Institute of Aeronautics and Astronautics (AIAA), 2017.

[200] J. Z. Ma, S. Zhang, M. Luan, and J. Wang. Experimental investigation on delay time phenomenon in rotating detonation engine. *Aerospace Science and Technology*, 88:395–404, 2019.

[201] C. Sonwane, S. Claflin, E. Lynch, and J. Stout. Recent advances in power cycles using rotating detonation engines with subcritical and supercritical CO2. In *The 4th International Symposium - Supercritical CO2 Power Cycles*, 2014.

[202] P. Wolański. Application of the Continuous Rotating Detonation to Gas Turbine. *Applied Mechanics and Materials*, 782:3–12, 2015.

[203] J. Sousa, G. Paniagua, and E. C. Morata. Thermodynamic analysis of a gas turbine engine with a rotating detonation combustor. *Applied Energy*, 195:247–256, 2017.

[204] F. A. Bykovskii and S. A. Zhdan. Current status of research of continuous detonation in fuel-air mixtures (Review). *Combustion, Explosion, and Shock Waves*, 51(1):21–35, 2015.

[205] V. Anand and E. Gutmark. Rotating Detonation Combustor Research at the University of Cincinnati. *Flow, Turbulence and Combustion*, 2018.

[206] E. Bach, P. Stathopoulos, C. O. Paschereit, and M. D. Bohon. Performance analysis of a rotating detonation combustor based on stagnation pressure measurements. *Combustion and Flame*, 217:21–36, 2020.

[207] R. Bluemner, M. D. Bohon, C. O. Paschereit, and E. J. Gutmark. Single and Counter-Rotating Wave Modes in an RDC. In *2018 AIAA Aerospace Sciences Meeting*. American Institute of Aeronautics and Astronautics, 2018.

[208] M. D. Bohon, A. Orchini, R. Bluemner, C. O. Paschereit, and E. J. Gutmark. Dynamic mode decomposition analysis of rotating detonation waves. *Shock Waves*, 2020.

[209] D. Schwer and K. Kailasanath. Feedback into Mixture Plenums in Rotating Detonation Engines. In *50th AIAA Aerospace Sciences Meeting including the New Horizons Forum and Aerospace Exposition*. American Institute of

Aeronautics and Astronautics, 2012.

[210] E. Bach, M. Bohon, C. O. Paschereit, and P. Stathopoulos. Development of an Instrumented Guide Vane Set for RDC Exhaust Flow Characterization. In *2018 Joint Propulsion Conference*. American Institute of Aeronautics and Astronautics, 2018.

[211] M. Asli, C. Cuciumita, P. Stathopoulos, and C. O. Paschereit. Numerical Investigation of a Turbine Guide Vane Exposed to Rotating Detonation Exhaust Flow. In *Proceedings of ASME Turbo Expo 2019: Turbomachinery Technical Conference and Exposition*, 2019.

[212] M. Asli, P. Stathopoulos, and C. O. Paschereit. Effect of Blade Setting Angle on Damping Role of Turbine Guide Vanes Downstream of an RDC. In *IGTC 2019*, Tokyo, Japan, 2019.

[213] M. Asli, P. Stathopoulos, and C. O. Paschereit. Aerodynamic Investigation of Guide Vane Configurations Downstream a Rotating Detonation Combustor. *Journal of Engineering for Gas Turbines and Power*, 2020.

[214] B. C. Bobusch, P. Berndt, C. O. Paschereit, and R. Klein. Shockless Explosion Combustion: An Innovative Way of Efficient Constant Volume Combustion in Gas Turbines. *Combustion Science and Technology*, 186(10-11):1680–1689, 2014.

[215] P. Berndt and R. Klein. Modeling the kinetics of the Shockless Explosion Combustion. *Combustion and Flame*, 175:16–26, 2017.

[216] J.-S. Schäpel, T. Reichel, R. Klein, C. Paschereit, and R. King. Online Optimization Applied to a Shockless Explosion Combustor. *Processes*, 4(4):48, 2016.

[217] T. G. Reichel, J. Schäpel, B. C. Bobusch, R. Klein, R. King, and C. O. Paschereit. Shockless Explosion Combustion: Experimental Investigation of a New Approximate Constant Volume Combustion Process. *Journal of Engineering for Gas Turbines and Power*, 139(2):021504, 2016.

[218] T. S. Rähse, C. O. Paschereit, P. Stathopoulos, P. Berndt, and R. Klein. Gas Dynamic Simulation of Shockless Explosion Combustion for Gas Turbine Power Cycles. In *Volume 3: Coal, Biomass and Alternative Fuels, Cycle Innovations, Electric Power, Industrial and Cogeneration Applications, Organic Rankine Cycle Power Systems*. ASME, 2017.

[219] P. Stathopoulos, T. Rähse, J. Vinkeloe, and N. Djordjevic. Steam injected Humphrey cycle for gas turbines with pressure gain combustion. *Energy*, 188:116020, 2019.

[220] P. Stathopoulos, T. Rähse, J. Vinkeloe, and N. Djordjevic. First law thermodynamic analysis of the recuperated humphrey cycle for gas turbines with pressure gain combustion. *Energy*, 200:117492, 2020.

[221] D. E. Paxson and K. T. Dougherty. Ejector Enhanced Pulsejet Based Pressure Gain Combustors: An Old Idea With a New Twist. Technical Report NASA/TM—2005-213854, National Aeronautics and Space Administration,

Glenn Research Center, 2005.

[222] D. Paxson and K. Dougherry. Operability of an Ejector Enhanced Pulse Combustor in a Gas Turbine Environment. In *46th AIAA Aerospace Sciences Meeting and Exhibit*. American Institute of Aeronautics and Astronautics, 2008.

[223] S. Yungster, D. E. Paxson, and H. Perkins. Numerical Evaluation of an Ejector-Enhanced Resonant Pulse Combustor with a Poppet Inlet Valve and a Converging Exhaust Nozzle. In *52nd AIAA/SAE/ASEE Joint Propulsion Conference*. American Institute of Aeronautics and Astronautics, 2016.

[224] J. C. Lisanti, X. Zhu, and W. L. Roberts. Improving the Performance of an Active Valve Resonant Pulse Combustor. In *AIAA Propulsion and Energy 2019 Forum*. American Institute of Aeronautics and Astronautics, 2019.

[225] V. Anand, J. Jodele, E. Knight, E. Prisell, O. Lyrsell, and E. Gutmark. Dependence of Pressure, Combustion and Frequency Characteristics on Valved Pulsejet Combustor Geometries. *Flow, Turbulence and Combustion*, 100(3):829–848, 2017.

[226] M. J. McClearn, M. D. Polanka, M. R. Mataczynski, F. Schauer, and D. E. Paxson. The Design of a Small-Scale Wave Rotor for Use As a Modified Brayton-Cycle Engine. In *54th AIAA Aerospace Sciences Meeting*. American Institute of Aeronautics and Astronautics (AIAA), 2016.

[227] M. J. McClearn, M. D. Polanka, K. Lapp, M. R. Mataczynski, F. R. Schauer, and D. E. Paxson. The Testing of a Small-Scale Wave Rotor for Use as a Modified Brayton-Cycle Engine. In *52nd AIAA/SAE/ASEE Joint Propulsion Conference*. American Institute of Aeronautics and Astronautics (AIAA), 2016.

[228] P. Akbari and R. Nalim. Review of Recent Developments in Wave Rotor Combustion Technology. *Journal of Propulsion and Power*, 25(4):833–844, 2009.

[229] M. R. Nalim, P. H. Snyder, and M. Kowalkowski. Experimental Test, Model Validation, and Viability Assessment of a Wave-Rotor Constant-Volume Combustor. *Journal of Propulsion and Power*, 33(1):163–175, 2017.

[230] P. Snyder, T. Elharis, S. Wijeyakulasuriya, M. Nalim, Y. Matsutomi, and S. Meyer. Pressure Gain Combustor Component Viability Assessment Based on Initial Testing. In *47th AIAA/ASME/SAE/ASEE Joint Propulsion Conference & Exhibit*. American Institute of Aeronautics and Astronautics, 2011.

[231] S. Tüchler and C. D. Copeland. Experimental and numerical assessment of an optimised, non-axial wave rotor turbine. *Applied Energy*, 268:115013, 2020.

[232] S. Kaiser, S. Donnerhack, A. Lundbladh, and A. Seitz. A Composite Cycle Engine Concept with Hecto-Pressure Ratio. In *51st AIAA/SAE/ASEE Joint Propulsion Conference*. American Institute of Aeronautics and Astronautics, 2015.

[233] M. Nickl and S. Kaiser. Evaluation of piston engine modes and

configurations in composite cycle engine architectures. *CEAS Aeronautical Journal*, 2019.

[234] P. Akbari, C. J. Tait, M. D. Polanka, and B. C. Sell. Development and Initial Testing of a Radial Wave Engine. In *Proceedings of ASME Turbo Expo 2019: Turbomachinery Technical Conference and Exposition*, 2019.

[235] J. Sebastiampillai, A. M. Rolt, F. Jacob, D. Nalianda, and V. Sethi. Thermodynamic analysis of nutating disc engine topping cycles for aero-engine applications. *Energy*, 2019.

[236] M. Kiesner and R. King. Closed-Loop Active Flow Control of the Wake of a Compressor Blade by Trailing-Edge Blowing. In *Volume 2A: Turbomachinery*. ASME, 2015.

[237] C. Xisto, O. Petit, T. Grönstedt, A. Rolt, A. Lundbladh, and G. Paniagua. The efficiency of a pulsed detonation combustor-axial turbine integration. *Aerospace Science and Technology*, 2018.

[238] M. Staats and W. Nitsche. Active Control of the Corner Separation on a Highly Loaded Compressor Cascade With Periodic Non-Steady Boundary Conditions by Means of Fluidic Actuators. In *Volume 2A: Turbomachinery*. ASME International, 2015.

[239] A. Rasheed, T. Furman, and A. Dean. Wave Interactions in a Multi-Tube Pulsed Detonation Combustor-Turbine Hybrid System. In *42nd AIAA / ASME / SAE / ASEE Joint Propulsion Conference & Exhibit*. American Institute of Aeronautics and Astronautics, 2006.

[240] J. Lu, L. Zheng, Z. Wang, C. Peng, and X. Chen. Operating characteristics and propagation of back-pressure waves in a multi-tube two-phase valveless air-breathing pulse detonation combustor. *Experimental Thermal and Fluid Science*, 61:12–23, 2015.

[241] F. Bakhtiari and H.-P. Schiffer. Numerical approach to the modelling of transient interaction of prospective combustor concepts and conventional high pressure turbines. *Propulsion and Power Research*, 2019.

[242] D. Topalovic, S. Wolff, A. Heinrich, D. Peitsch, and R. King. Minimization of Pressure Fluctuations in an Axial Turbine Stage Under Periodic Inflow Conditions. In *AIAA Propulsion and Energy 2019 Forum*. American Institute of Aeronautics and Astronautics, 2019.

[243] A. S. George and E. Gutmark. Trends in Pulsating Turbine Performance: Pulse-Detonation Driven Axial Flow Turbine. In *50th AIAA Aerospace Sciences Meeting including the New Horizons Forum and Aerospace Exposition*. American Institute of Aeronautics and Astronautics, 2012.

[244] A. Naples, J. Hoke, R. T. Battelle, M. Wagner, and F. R. Schauer. RDE Implementation into an Open-Loop T63 Gas Turbine Engine. In *55th AIAA Aerospace Sciences Meeting*. American Institute of Aeronautics and Astronautics, 2017.

[245] F. E. Habicht. *Towards the implementation of a pulse detonation combustor into a*

gas turbine. Doctoral thesis, Technische Universität Berlin, Berlin, 2021.

[246] Y. Matsutomi and S. Heister. Entropy Considerations on Integration of Pressure Gain Combustors. In *46th AIAA/ASME/SAE/ASEE Joint Propulsion Conference & Exhibit*. American Institute of Aeronautics and Astronautics, 2010.

[247] M. R. Haghdoost, B. S. Thethy, D. Edgington-Mitchell, F. Habicht, J. Vinkeloe, N. Djordjevic, C. O. Paschereit, and K. Oberleithner. Mitigation of Pressure Fluctuations From an Array of Pulse Detonation Combustors. *Journal of Engineering for Gas Turbines and Power*, 2021.

[248] Z. Liu, J. Braun, and G. Paniagua. Performance of axial turbines exposed to large fluctuations. In *53rd AIAA/SAE/ASEE Joint Propulsion Conference*. American Institute of Aeronautics and Astronautics, 2017.

[249] H. Klinger, W. Lazik, and T. Wunderlich. The Engine 3E Core Engine. In *Volume 1: Aircraft Engine; Ceramics; Coal, Biomass and Alternative Fuels; Manufacturing, Materials and Metallurgy; Microturbines and Small Turbomachinery*. ASME International, 2008.

[250] I. B. Celik. Procedure for Estimation and Reporting of Uncertainty Due to Discretization in CFD Applications. *Journal of Fluids Engineering Editorial Policy*, 2008.

[251] I. A. Sever. *Experimental Validation of Turbomachinery Blade Vibration Predictions*. PhD thesis, Department of Mechanical Engineering, Imperial College London, 2004.

[252] Z. Li, W. Yang, and H. Yuan. Vibration Analysis of Aeroengine Blisk Structure Based on a Prestressed CMS Super-Element Method. *Shock and Vibration*, 2016:1–10, 2016.

[253] C. T. Walter Noll. *The Non-Linear Field Theories of Mechanics*. Springer Berlin Heidelberg, 2004.

[254] E. J. Hall and P. Owen. NASA Contract NAS3-27394, NASA Contractor Report CR-0000000, Task 17 - Energy Efficient Engine HP/LP Spool Analysis. Technical report, NASA Glenn Research Center, 2000.

[255] P. R. Holloway, G. L. Knight, C. C. Koch, and S. J. Shaffer. Energy efficient engine. High pressure compressor detail design report, Contract NAS3-20643. Technical report, General Electric Company, NASA-Lewis Research Center, 1982.

[256] R. W. Claus, T. Beach, M. Turner, K. Siddappaj, and E. S. Hendricks. Geometry and Simulation Results for a Gas Turbine Representative of the Energy Efficient Engine (EEE). Technical Report 2015-218408, NASA, 2015.

[257] C. C. Ciepluch, D. Y. Davis, and D. E. Gray. Results of NASA's Energy Efficient Engine Program. *Journal of Propulsion and Power*, 3(6):560–568, 1987.

[258] GE90-115BL - Engine Lease Finance Corporation. `https://elfc.com/engines/ge90-115bl/`, 2020. Last accessed on 20/8/2020.

[259] J. Jeong and F. Hussain. On the identification of a vortex. *Journal of Fluid*

Mechanics, 285(-1):69, 1995.

[260] A. L. B. Andrew J. Majda. *Vorticity and Incompressible Flow*. Cambridge University Press, 2007.

[261] J. Higham, W. Brevis, and C. Keylock. Implications of the selection of a particular modal decomposition technique for the analysis of shallow flows. *Journal of Hydraulic Research*, 56(6):796–805, 2018.

[262] T. Kajishima and K. Taira. *Computational Fluid Dynamics: Incompressible Turbulent Flows*. Springer International Publishing, 2017.

[263] G. Mellor. *The Aerodynamic Performance of Axial Compressor Cascades with Application to Machine Design*. Report (Massachusetts Institute of Technology. Gas Turbine Laboratory). Massachusetts Institute of Technology, Department of Mechanical Engineering, 1957.

[264] O. Lucca-Negro and T. O'Doherty. Vortex breakdown: a review. *Progress in Energy and Combustion Science*, 27(4):431–481, 2001.

[265] E. Petrov, L. D. Mare, H. Hennings, and R. Elliott. Forced Response of Mistuned Bladed Disks in Gas Flow: A Comparative Study of Predictions and Full-Scale Experimental Results. *Journal of Engineering for Gas Turbines and Power*, 132(5):052504, 2010.